High Optical Throughput and Low-Cost Spectral Sensing Using Photonic Structures

by

Iman Khodadadzadeh

A thesis
presented to the University of Waterloo
in fulfillment of the
thesis requirement for the degree of
Doctor of Philosophy
in
Electrical and Computer Engineering (Nanotechnology)

Waterloo, Ontario, Canada, 2016

Abstract

Spectral sensing is an accurate means of probing the environment in a non-invasive manner. One of the most common instruments to acquire spectral data is a spectrometer. Spectrometers continue to improve in throughput and resolution while becoming smaller in size. However, the improvements in optics, gratings and detector performance have plateaued in free-space spectrometers due to fundamental trade-off between the spectral resolution and throughput of the spectrometer slit. Free space optical slicers on the other hand, have shown that this trade off can be broken using a complex optical setup. With the advent of nanophotonics and integrated optics, light can be routed and interact in a much smaller footprint. While integrated optics approach provides a more robust and smaller footprint, the throughput is still an issue since most designs only work with a very narrow band and single mode input. In this thesis, the concept of far-field beam forming is explored using mode coupling principles to increase the throughput of a spectrometer using photonic structures and waveguides. Three designs are provided that use the interaction between the modes to couple light between different size apertures at input and output. These designs use multi-mode input fibers and could operate on a wider wavelength range since they are not wavelength specific resonant based structures. They are fabricated and experimentally tested to measure their performance against a conventional free space slit.

While spectrometers provide the full-range spectral information, application specific photonic sensors that use multi-spectral sensing approach are also promising fields of research. In this thesis, two such sensor designs are discussed. A multi-slot bio-sensor design is proposed as well as its optimization procedure to increase the refractive index sensitivity by 3×. Due to similarities between this design and the tapered waveguide designs for the spectrometer, the fabrication techniques developed for the photonic slit concept can be extended and applied for fabrication of this sensor. In addition, to avoid the system design and measurement complexities of a spectrometer or a ring resonator based sensor, a simple periodic array of silicon nanowire is proposed as a refractive index sensor. By considering the movement of diffraction spots at multiple wavelengths, refractive index resolution of 10^{-5} or higher can be achieved.

Acknowledgements

There is an interesting African proverb saying; “It takes a village to raise a child!” I am not an exclusion and I would like to acknowledge all those who have supported and helped me through this work. First and foremost, I would like to express my sincerest gratitude to my supervisors, Dr. Dale Henneke, Dr. Arsen Hajian and Dr. Simarjeet S. Saini. They tirelessly mentored me academically, professionally and personally throughout the past couple of years. Their passion, vision and mission to make this world a better place for everyone has always guided me through the various steps of this painstaking research.

I would also like to thank the members of my committee, Dr. Safiedin Safavi-Naeini, Dr. Dyan Ban, Dr. Alex Wong at University of Waterloo, and Dr. Nazir Kherani at University of Toronto for their invaluable comments and feedbacks. Their individual view of my project helped me widen my view and probe the matter at hand from various angles.Dr. Ban’s frequent follow up on the state of my project through these years and his experience with surface coupling helped me improve the coupling ratio which I greatly appreciate.

In addition, I need to express my greatest thanks to the scientific team at Tornado Spectral Systems. This work would not have been possible without their utmost support throughout the project. The discussions I had with Dr. Brad Schmidt, Dr. Jeff Meade, Dr. Andrew Cenko, Dr. Art Nitkowski, Dr. Kyle Preston, Dr. Nicholas Sherwood and Dr. Bradford Behr on several occasions were the most fruitful and enlightening. Their passion and dedication to probe and understand the unknowns have always been inspiring for me.

I also need to acknowledge the help and support of the scientific team at Raith America. The discussions I had with Dr. Kevin Burcham and the support of Dr. Michael Kahl were instrumental in understanding the limitations current system and developing new FBMS modes of writing.

Last but not least, this work would not have been possible without the help and support of the scientific team at university of Waterloo including my colleagues and lab mates. I would like to express my humble thanks to Dr. Nathan Fitzpatrick, Dr. Reza khorasaninejad and Dr. Anita Roudsari for mentoring me through the fabrication stages of my project. I have a special thanks for my dearest lab buddy, Dr. Farnoud Kazemzadeh. He is a curious researcher with a wonderful personality with whom I shared the everyday pains and mysteries of research. I will never forget his help and support. I also want to thank my group members, Dr. Jaspreet Walia and Navneet Dhindsa for sharing the fun of research and discovery with me on a number of other projects involving Nanowires.

Dedication

I want to dedicate this work to:

- *my parents for their unconditioned love and care. I am grateful for their uninterrupted support for every second of the past 30 years*
- *the memory of my two grandfathers whose wisdom taught me purpose in life*
- *my lovely wife Nazila. Her utmost love, support and care gave me the strength to excel!*

Table of Contents

List of Tables

List of Figures

Nomenclature

MEMS	Micro-Electromechanical System
SNR	Signal-to-Noise Ratio
HTPS	High Throughput Integrated Photonic Slit
FTS	Fourier-Transform Spectroscopy
FWHM	Full-Width at Half Maximum
BPM	Beam Propagation Method
PIC	Photonic Integrated Circuit
EP	Entrance Pupil
XP	Exit Pupil
CMT	Coupled Mode Theory
MMT	Multiple Mirror Telescope
ELT	Extremely Large Telescopes
MOEMS	Mico-Opto-Electro-Mechanical Systems
SiON	Silicon-Oxi-Nitride
NIR	Near Infrared
IPS	Integrated Photonic Spectrographs
AWG	Arrayed Waveguide Grating
FPR	Free-Propagation Region
2D	Two Dimensional
3D	Three Dimensional
PD	Photonic Dicer
RI	Refractive Index
HTVS	High Throughput Virtual Slit
FEM	Finite Element Method
TE	Transverse Electric
TM	Transverse Magnetic
EBL	Electron Beam Lithography

HF	Hydrofluoric Acid
PECVD	Plasma Enhanced Chemical Vapor Deposition
SCCM	Standard Cubic Centimeters per Minute
FBMS	Fixed Beam Moving Stage Method
MBMS	Modulated Beam Moving Stage
SEM	Scanning Electron Microscopy
ICP	Inductively Coupled Plasma
DRIE	Deep Reactive Ion Etching
SOG	Spin-on-Glass
CMP	Chemical and Mechanical Polishing
SLED	Super-Luminescent Diode
SOI	Silicon-on-Insulator
SNOW	Silicon Nanowire Optical Waveguide
FDTD	Finite Difference Time Domain
SiNW	Silicon Nanowire
RCWA	Rigorous Coupled Wave Analysis
BSDF	Bi-Directional Scattering Distribution Function

Chapter 1

Introduction

Integrated silicon photonic devices offer modular, robust and low cost solutions for applications ranging from telecommunications to remote sensing and environmental monitoring. In addition, their compatibility with IC and micro-electromechanical system (MEMS) fabrication technology enables us to implement a variety of solutions in a single integrated package while reducing development and packaging costs. Hence, integrated photonic solutions have stimulated a significant amount of research and attention during the past decade while continuing to find its way to revolutionize devices and instruments.

The stated goal being investigated in this dissertation is to develop high performance and low cost spectral sensing solutions. One of the devices used increasingly over the past decade in many scientific applications is a spectrometer which studies light and matter interactions and provides a remote and non-invasive way of probing a target. Conventionally, the quality of spectrometers have been considered to be proportional to their size such that "X-meter spectrometers" were considered natural for high resolution spectroscopy in applications such as astrophysics. While reduction in size has its own challenges with regards to aberrations and focal ratio degradation, there has been constant improvements towards producing smaller and yet high resolution spectrometers over the past decade. Another conventional belief in spectroscopy is the trade-off present between resolution and throughput. Slit has been a key component in spectrometer design where the slit width determines the spectral line width and hence the resolution. While smaller slit width increases the resolution, it also blocks a bigger portion of the incoming light and hence the throughput reduces drastically. Having high resolution spectrometers with reasonable signal-to-noise ratios (SNR) requires bulky optics which adds to the alignment and design complexity and therefore cost.

In this dissertation, the possibility of eliminating the slit by introducing a high throughput integrated photonic slit (HTPS) is investigated. A number of photonic structures are proposed, fabricated and characterized which can be extended and used in completely integrated spectrometers in the future designs. During the course of this thesis, some of the developed fabrication methods were also useful in realizing new classes of spectral sensing units. Design and characterization of these photonic structures are also provided at the end of this thesis.

1.1 Spectroscopy

Spectral analysis has been used during the past few decades in areas of physics, chemistry and biology for remote sensing applications. Especially in fields such as astrophysics, it has been the only source of information about our surrounding world. Spectroscopic information from a distant planetary system or a batch of cell culture provides valuable details about the band structure, topology, composition and even concentration of the remotely sensed medium. Various types of spectrometers have been built over the years with early versions having a slit, a prism and a screen as a registering element. The registering element recorded the wavelength which became an electronic detector later on. Spectrometer is known to be invented by Gustav Kirchhoff and Robert Bunsen around 1860 [1]. However, it has been evolving ever since with increasing speeds over the past few years with the advent of integrated photonics technology.

In terms of operations principle, spectrometers can be grouped into three categories: dispersive, filter-based and Fourier-transform (FTS) based. Dispersive spectrometers generate spectra by means of dispersive elements such as a prism or a grating. Filter-based spectrometers use either absorption or interference based processes to transmit a selection of wavelengths. Due to the requirement for a stable source in FT based spectrometers which makes them cost prohibitive for small size portable applications, filter-based and dispersive spectrometers are the focus of this dissertation [2].

Two key specification of any spectrometer are their throughput and spectral resolving power. Throughput is the product of $A\Omega$ in which A is the area of the limiting aperture and Ω is the solid angle formed by the focusing or collimating optics. The systems throughput in a spectrometer can be limited either by the collimating optics or by the detection optics. The collimating optics also determines the resolution of the spectrometer. Hence, fixing either of the throughput or the resolution would limit the other factor [2]. The spectral resolving power R is defined as the ratio $(\lambda/d\lambda)$, where λ is the operating wavelength and $d\lambda$ is the wavelength difference between two adjacent spectral lines. Resolution is the ability of the instrument to separate two adjacent spectral lines. The shape of the lines which affects the final resolution is a function of various parameters such as entrance slit width, exit slit width or the pixel width of the detector, diffraction phenomena from the grating, aberrations, alignment and quality of the optical components [3]. Each of the mentioned parameters may broaden the line profile individually and some of these factors may dominate others. In practice, the full-width at half maximum (FWHM) is the convolution of a set of line broadening parameters. Assuming a Gaussian line profile, an approximation to FWHM can be written as [3]:

$$FWHM \cong \sqrt{d\lambda_{slits}^2 + d\lambda_{resolution}^2 + d\lambda_{line}^2} \tag{1.1}$$

where $d\lambda_{resolution}$ refers to the limiting resolution of the spectrometer depending on the instrument line profile and imperfections such as aberrations and diffraction effects; $d\lambda_{line}$ is the natural line width of the source and $d\lambda_{slits}$ is the bandpass imposed by finite slit widths. In practice, however, spectrometers are not used that often at their resolution limit so the slit bandpass may dominate the line profile and ultimately the resolving power of a spectrometer. Hence, slit width has an essential role in determining the resolving power and throughput of a spectrometer.

There have been several spectrometer designs proposed over the years for applications ranging from astronomy to bio-chemical sensing. For astronomical studies, high-performance macroscopic spectrometers have been proposed and built with resolutions exceeding $R = 10^6$. While such designs are extremely bulky and expensive, they are not needed in industrial applications where size and cost is of importance. There has been a series of efforts in academia and industry over the past decade to produce low cost hand-held devices considering the advancements in optical component design and manufacturing. Also, with the advancements in MEMS fabrication and integrated photonics, there has been a great push towards novel micro-spectrometer designs [4]. Despite these efforts toward reducing the size, the proposed designs have relatively low resolution and throughput and there has not been much fundamental work done in breaking the trade-off between the resolution and throughput. There are only a few studies done over the years from the invention of spectrometers which shows that the resolution and throughput trade-off can be broken in certain conditions. In 1938, Bowen introduced the concept of image slicing for spectrometers used with large telescopes and showed that the efficiency can be increased to 75%-90% [5]. This was followed by the concept of pupil slicing in 1961 and a few more designs that are explained further in the future chapters which are mostly based on free space optical elements [6,7,8,9]. In 2006, Bland-Howthorn *et. al* proposed an integrated photonic spectrograph for application in astronomy which was used along with a multi-mode to single mode fiber splitter called Photonic Lantern [10,11]. By rearranging the single mode fibers into a slit shape, one can retain higher throughput while having the resolution of a slit. Although the proposed structure showed promising results for use with large telescopes, there are concerns regarding practical implementation of such scenarios especially in the form factor for the fiber couplers used to build Photonic Lantern. In this work, we intend to investigate how and why the resolution and throughput trade-off can be broken and propose a candidate photonic structure to realize a virtual slit which has the resolution of a slit while it reshapes the beam and retains its power in a planar lightwave circuit.

1.2 Motivation

Developments in integrated photonics and its fabrication technologies have provided a unique platform for emerging concepts and devices. As light can be manipulated at much smaller length scales than with conventional bulk optical elements, a broad range of functionalities can be achieved. The inherent advantages of integrated photonic spectrographs make this venue extremely interesting. Some of these advantages can be named as [12]:

- Modular design: Modular components can be built to enable low-cost, low-maintenance and expandable instruments. This can be achieved by breaking the system into smaller functional elements.
- Miniaturization: by minimizing the size of each spectrograph a large multiplexing capability becomes available. Hence, going toward on-chip spectrographs would help with multiplexed sensing platforms at different operation wavelengths and different modalities.
- Mass production: relying on the fabrication techniques developed by the telecommunication industry, the initial cost of research and development of such instruments would not be a major barrier.

The conventional market for spectrometers has been towards research applications in two main venues which are astrophysics and bio-chemical sensing to find the constructing elements of compounds. Hence, traditionally there has not been much of a demand on reducing the size and cost of spectrometers. However, with the advancement of photonic and MEMS technology, the idea of having affordable hand-held spectrometers for a variety of environmental sensing applications is becoming more popular. Already, there are commercial spectrometer packages available in the market which are small enough to carry around with portable battery packs for its circuitry [13]. Since they use bulk optical components, they are prone to failure due to mechanical vibrations, thermal fluctuations and alignment related issues. Hence, an integrated photonic spectrometer would be an interesting alternative to make a robust, low cost and small sized device. Applications of miniature and highly efficient spectrometers can be an extended list of areas such as airborne systems for environmental sensing applications in vegetation, forestry and carbon emissions. Other applications with a broader usage pool include food safety, process control, defense and security and health-care. In such applications, specialized spectral sensing units can also be envisioned and designed which are highly sensitive, low cost and application specific. For instance, if the sensory unit is responsible for detecting nitride and nitrates, the absorption lines of these two solutions can be used from which one can determine their presence as well as quantify the concentration levels. Therefore, there can be a large number of these application specific photonic chips designed, fabricated and deployed in the field to check for environmental contaminants or hazards.

1.3 Scope and Structure

This dissertation has a very specific goal: investigating low-cost and high-performance spectral sensing solutions for remote sensing applications. In spectrometers as a general sensing tool, we want to investigate how the trade-off between spectral resolution and throughput can be broken by use of a photonic integrated circuit (PIC). Seeking an answer using concepts from photonics, helps us in downsizing the design and potentially move toward an efficient fully photonic (i.e. on chip) solution. This would additionally result in breaking the size-quality proportionality considered conventionally for spectrometers. The topics and materials provided in the body of the thesis presents the essential background needed to understand the problem and solution provided which includes optical invariant, numerical aperture, radiometry concepts, coupled mode theory, coupling into and out of waveguides and its governing relations. A commercial software package (Rsoft [14]) including a beam propagation (BPM) module has been used for numerical simulation in most of the structures. Additional Matlab codes along with necessary post processing might have been used to interpret or validate the results in some cases. However, the numerical simulation techniques for light propagation in optical waveguides are not in the scope of this proposal.

A solution shown in block diagrams in Figure 1.1 is proposed, fabricated and tested. We will investigate a PIC based mode converter as HTPS. The HTPS converts light from a multi-mode fiber into a slit like output with minimal loss. The output will be a few

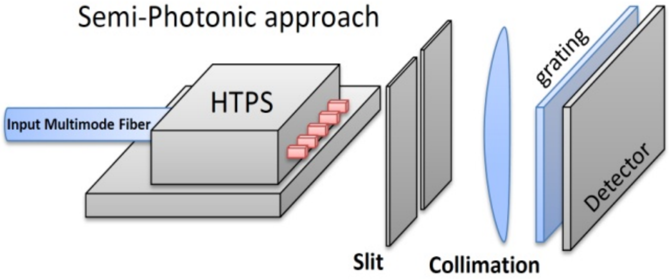

Figure 1.1: Photonic slit based spectrometer design showing a semi-photonic approach to spectroscopy.

mode in vertical direction while being a Gaussian type supermode in the lateral one. HTPS will be evaluated and bench-marked to slits in a conventional spectrometer with the goal to increase the throughput while maintaining the spectral resolution. To our knowledge no such mode conversion has been in achieved in PICs dealing with multi-mode inputs with such large modal mismatch. Thus, the proposed concepts will add to the knowledge of coupling systems for PICs while trying to achieve specific goals in enhancing spectrometers throughput. Integration of optical filters (like ring resonators) can be considered to remove the undesired spectral components. The knowledge generated could also be useful for applications in biochemical sensing assays whereby the output of the HTPS can be integrated with multiple single mode devices each integrated with an optical sensor.

The rest of this proposal is structured as follows: Chapter 2 provides the background information regarding free space optical systems, radiometry and guided wave concepts including coupled mode theory. If the reader is already familiar with free space optical concepts or guided wave optical theories, these sections can be quickly skimmed for brevity. In the end of chapter 2, a literature survey of spectrometer designs is presented with greater emphasis on micro-spectrometers. Chapter 3 presents the idea of far-field beam shaping using mode coupling within waveguides of dissimilar cross sections. This has been used to change the far-field beam shape and effectively produce a virtual slit with HTPS. A figure of merit is introduced for the first time using the *etendue* principle to quantify the performance of the proposed devices against a slit and other potential architectures. Three different structures have been proposed, simulated and evaluated in this chapter. Chapter 4 includes fabrication methods and developed recipes and processes for the selected designs as well as post fabrication procedures to make the sample ready for lab experiments. Chapter 5 provides the details of measurement methods and procedures and the respective setup used to characterize the performance of the photonic slicer coupler system. The experimental results are discussed in depth within this chapter. During the development of the fabrication methods for long coupled channel waveguides, we realized that some of the methods can be extended to silicon-based coupled multi-slot waveguides for applications in bio-chemical sensing. Therefore, a multi-slot Si based waveguide was designed and optimized for sensing application in Chapter 6. This device can be easily fabricated in the future using the fabrication methods developed in Chapter 4. One other photonic sensing platform that was developed and tested during the course of this project, is a nanowire based multi-spectral sensing unit. Instead of having separate dispersive elements, the diffraction properties of a two dimensional Si nanowire array is used to eliminate the need for external spectrometers in performing refractive index sensing. The design and experimental results of this photonic sensor is given in Chapter 7. Concluding remarks and future work are provided within the final chapter.

Chapter 2

Background Information

This chapter provides a theoretical background on the topics discussed in the rest of the dissertation and then provides a brief literature review on state of the art related to the topic of this dissertation. The theoretical background presented here briefly covers the topics of interest and it can be divided into two sections of free space optical relations and integrated optics or wave optics formulations. Geometrical optics provides a simplified description of light propagation in an optical system which serves as a powerful engineering model to describe light propagation and interaction with different materials. The subjects of optical invariance and radiometry are presented under the framework of geometrical optics which includes fundamental definitions of interest such as focal ratio, numerical aperture and irradiance in a system. The integrated optics concepts are based on wave optics formulations in which mode coupling, supermodes and beam propagation within optical waveguides can be explained and discussed more accurately. This chapter serves as a basis for further developments in the theory and concepts discussed in the rest of this dissertation and further topics will refer to concepts presented in this chapter. If the reader is already familiar with concepts of radiometry and optical wave-guiding theory, then this chapter can be skipped for brevity and the reader may continue with Chapter 3.

2.1 Geometrical optics

Geometrical optics or ray optics is a simpler form of the more general wave treatment of optics in which the propagating waves are described as rays that are perpendicular to phase fronts and propagate in space as straight lines. Optical phenomena can mostly be described in this framework and to first order approximation, optical path in a system can be explained by the model of rays. In this section, some of the ray optics concepts presented are of key importance in comprehending the results from the integrated optical system. As the core focus of this dissertation is on integrated optical systems, the presented concepts are for review purposes and the interested reader is referred to the literature for more in depth discussions. The measurement of electromagnetic radiation in optics is referred to as radiometry. Radiometry is a vast enough concept on its own which would need an individual section for review. However, since the approximate geometrical picture provides a sufficiently simplified model for radiometric investigations, it is appropriate to present this concept within the geometrical optics category.

2.1.1 Optical invariant in a system

The number of rays that are able to pass through any optical system is limited due to the systems finite size. An aperture in an optical system is the opening from which rays pass through. An aperture stop is however, an aperture that limits the portion of light that passes through the system from an axial objects point. The stop can be either a lens aperture or a separate aperture such as an iris diaphragm that is placed within the system. The entrance pupil (EP) and the exit pupil (XP) are the images of the stop in the object and image spaces [15].

Due to linearity of rays in paraxial optics, in which all angles are assumed to be close to the optical axis (i.e. less than 10° in 1^{st} approximation), heights and angles of any two rays propagating through the system are related. Using two rays of an optical system, an invariant or constant of a system can be written as [16]:

$$O_{1,2}(\omega) = n(\omega)(\theta_1 h_2 - \theta_2 h_{1)} \tag{2.1}$$

in which θ_1 and h_1 are the paraxial angle and height of the first ray and θ_2 and h_1 are the paraxial angle and height of the second ray at any location through the system with refractive index of $n(\omega)$. To describe an image at any point of the system, two types of rays called the marginal and chief rays maybe used. The marginal ray starts from an axial point and goes through the edge of the entrance pupil, stop and the exit pupil. The chief ray on the other hand, starts from the edge of the object and goes through the center of the entrance pupil. If the two rays are the chief and marginal rays, then the optical invariant is called the Lagrange invariant of the system. The value of the optical or Lagrange invariant should remain constant at any axial position along the system, but in reality it would degrade due to optical losses in the system. The throughput, *etendue* or AΩ product in radiometry is related to the square of the Lagrange invariant which is explained further in Section 2.1.3.

2.1.2 Numerical aperture and F-number

Numerical aperture and F-number ($f/\#$) are widely used in optics describing the light collecting capability of the system or lenses. In an optical system, the axial cone of light can be described in terms of the real marginal ray angle with the optical axis and the refractive index of the space n(Ω). Hence, the numerical aperture can be described as:

$$NA(\omega) = n(\omega).|sin(\theta_m)| \tag{2.2}$$

in which, using small angle paraxial approximation one can estimate the value to be $NA \approx n(\omega).|\theta_m|$.

The ($f/\#$) on the other hand, describes the image cone of light for an object at infinity. For a single lens serving as the system stop, it can be defined as the ratio of focal length of the system to the diameter of the entrance pupil:

$$f/\#(\omega) = \frac{f_L(\omega)}{D_{EP}} \tag{2.3}$$

Both $f/\#$ and NA values are common parameters which are used interchangeably in practice (e.g. an $f/2$ lens or a lens with $NA = 0.25$). Therefore if a thin lens is used in air, both values can be related as follows:

$$f/\# = \frac{1}{2NA} \tag{2.4}$$

2.1.3 Radiometry

In this section, the geometrical optics model is used in which light is considered as flow of energy along geometrical rays. It is shown that this flow of energy is subjected to geometrical law of conservation of energy [15]. This law states that the energy transmitted in unit time through any cross section of the system remains constant when there are no losses. Therefore in radiometry, the light energy emitting from an area of a surface is considered in which the surface can be any sort of a radiating surface or aperture. One of the key elements in radiometry is the definition of solid angle (commonly shown with the symbol Ω). Solid angle extends the definition of plane angle (i.e. θ=l/r) into three dimensions.If the element of solid angle subtended by dA_{sp} is defined as $d\Omega{=}dA_{sp}/r^2$ in a spherical system, the solid angle is found as [17]:

$$\Omega = \int_{\phi_{min}}^{\phi_{max}} \int_{\theta_{min}}^{\theta_{max}} sin\theta d\theta d\phi \tag{2.5}$$

While the above formula is for a spherical case, the solid angle can subtend any arbitrary surface. In general, most objects do not have a spherical curvature to them so the above formula would be too complicated to compute. In many cases, one can approximate the solid angle by using the 2D area of the object, A_{2D}, and its distance from the observation point, d_o, as follows:

$$\Omega = \frac{A_{2D}}{d_0} \tag{2.6}$$

This approximation is valid only when the distance of the object from the observation point is much larger than the height of the object. As mentioned in the beginning of this section, the throughput of the system can be defined as area of the cross-section of the beam times its solid angle. In the case of a non-lossy medium, the throughput should remain constant throughout the system. Between two differential surface areas separated by a distance d, one can consider the AΩ product the same for different parts of an optical system [17]. Therefore,

$$A_s\Omega_{os} = A_o\Omega_{so} = A_o\Omega_{do} = A_{sd}\Omega_{od} \tag{2.7}$$

in which the subscripts of s, o and d denote the source, optics and detector respectively and the throughput at each of these areas should remain constant through the system. Therefore, the total amount of light collected by an optical system can be calculated as the sum of differential element of areas multiplied by differential elements of solid angle. The resulting value is called *etendue* (Ξ) and it can be written as follows:

$$\Xi = \int_{\Omega_{min}}^{\Omega_{max}} \int_A dA_{EP} d\Omega \tag{2.8}$$

where the integration is calculated over the angular range of the source and the area of the entrance pupil. This is in fact summation over the source solid angle as seen from differential areas within the entrance pupil. In the small angle approximation, considering the emission of a finite source with area of A$_s$, at a distance d$_{EP}$ from the entrance pupil of area A$_{EP}$, the *etendue* can be written as:

$$\Xi = A_{EP}\Omega_s \cong A_{EP}\frac{A_s}{d^2} = A_s\Omega_{EP} \tag{2.9}$$

As seen, the *etendue* value or the light collection efficiency of the system remains constant over the source, entrance pupil, and detector as well as through the system.

In the next chapters, this characteristic of optical systems is used to develop a figure of merit for quantitative comparison of proposed structures with conventional spectrometers performance.

2.2 Guided Wave Optics

The wave theory of light is inclusive of the geometrical optics. In fact, the geometrical or ray optics is the limit of wave optics when the wavelength is infinitesimally short compared with the objects and mediums that light travels through and around. Wave optics is the basis for describing phenomena such as diffraction and interference that are not well defined by the conventional geometrical optics. Electromagnetic optics on the other hand, provides the vector wave theory description of light as an electromagnetic phenomenon. Therefore, electromagnetic optics is a vector theory comprising an electric and magnetic field that vary in time and space.

Electromagnetic optics is fundamentally constructed based on Maxwells equations in which there are two related vector fields that are functions of time and space: the electric field $\mathcal{E}(r,t)$ and the magnetic field $\mathcal{H}(\mathrm{r,t})$. The $\mathcal{E}$ and $\mathcal{H}$ wave functions that satisfy the Maxwell equations are found by solving the wave equation using the appropriate boundary conditions in the spatial domain of interest. The vector nature of electromagnetic field leads to the polarization phenomena. It also governs the amount of light that is reflected and transmitted at boundaries between two different mediums, and hence determines characteristics of light propagation in waveguides and layered media [18].

In traditional optical instruments, light propagates in forms of a collimated or focused beam. As the beam propagates through lenses, mirrors or prisms, it diffracts or broadens where it can get refocused or collimated again by means of lenses and mirrors. While bulk optical elements have been used extensively over the past decade, they are often large, expensive and too sensitive for field use. In many cases, it is beneficial to transmit optical beams through light guides within which the light is confined. Such light guides were initially designed to transmit light over long distances without the need to use relay lenses. These guides are called optical fibers and they are categorized in general as optical waveguides which can include any form of a channel, slab or a cylindrical dielectric guide. The fundamental principles describing light propagation in optical guides are known in literature as guided-wave optics [19]. Optical confinement in a guide is basically achieved by embedding a medium of refractive index n_1 in a medium of refractive index n_2 where $n_2 < n_1$. Hence, the light gets trapped in a higher refractive index region in one or two directions as it propagates through the medium.

Although optical waveguides were primarily developed for long-distance communication purposes, they are widely used in optical chips. Integrated optics is the technology of integrating different optical devices on a single chip which is heavily dependent on optical waveguides. These optical components can perform various tasks such as generating, focusing, splitting, combining, isolating, polarizing, coupling, switching, modulating and detecting light where optical waveguides provide the link between these various devices [18]. In the rest of this section, some of the concepts of interest in the area of waveguide optics are presented briefly which would relate to the topic of this dissertation.

2.2.1 Coupled Mode Theory

In many integrated optics phenomena, power is exchanged between modes within the waveguides. In most cases, the exchange of power can be described using coupled mode theory (CMT). Coupled mode theory is in fact a perturbation approach that analyzes the coupling of electromagnetic field in space and time in which it makes the assumption that energy is conserved in the system and the coupling is weak (i.e. small perturbation) [20]. Historically, mode coupling has found applications in various areas including modulators, switches, signal processing, ring resonators, slot waveguides, longitudinal mode control and phased arrays [21]. In the following section some of the main features of this formalism are reproduced and evaluated.

Consider two parallel dielectric waveguides such as "a" and "b" which may differ in shape, cross-section and refractive index. Hardy and Streifer developed a theory in 1985, known as $H-S$ theory, where they showed that conventional CMT methods were inconsistent in case of dissimilar waveguides which had shown asymmetric coupling coefficients between the waveguides [21], [22]. The formulation developed here is partly based on the general coupled mode theory and notation used by Kogelnik [23] and expands the methodology used in $H-S$ theory [21] to dissimilar waveguides with multiple modes. As for the two dissimilar and parallel waveguides of "a" and "b", the modal vectorial fields of each waveguide is designated by superscripts "a" and "b". A general electromagnetic field of $\mathbf{E}(x,y,z), \mathbf{H}(x,y,z)$, can be considered to satisfy Maxwells equations and boundary conditions in the whole structure. Such field would include the guided modes of the whole structure plus the radiation modes. Hence, the transverse fields maybe written as:

$$\mathbf{E}_t(x,y,z) = U(z)\mathbf{E}_t^a(x,y,z) + V(z)\mathbf{E}_t^b(x,y,z) + \mathbf{E}_r(x,y,z) \tag{2.10a}$$

$$\mathbf{H}_t(x,y,z) = U(z)\mathbf{H}_t^a(x,y,z) + V(z)\mathbf{H}_t^b(x,y,z) + \mathbf{H}_r(x,y,z) \tag{2.10b}$$

where $U(z)$ and $V(z)$ show the z dependence of the individual guided modes of the waveguides with transverse fields of $\{\mathbf{E}_t^{(a)}, \mathbf{H}_t^{(a)}\}$, $\{\mathbf{E}_t^{(b)}, \mathbf{H}_t^{(b)}\}$, and $\mathbf{E}_r$ and $\mathbf{H}_r$ represent the residual fields of the whole structure. In this derivation, we consider the residual fields to be orthogonal to the guided fields. The residual fields may or may not be guided by the whole structure depending on whether the total transverse mode is a guided mode of the system or not. In both cases, the residual fields maybe represented in terms of the radiation modes of either waveguides but they need to be calculated explicitly. In general, we are interested in systems where the modal transverse fields are well guided through the whole structure and hence the residual fields are small in comparison to other terms. However, the full forms are retained throughout the derivation and $\{\mathbf{E}_r, \mathbf{H}_r\}$ are only neglected at the very last stages. After substantial mathematical manipulations, we can derive differential equations relating $U(z)$ and $V(z)$ for multi-mode coupled waveguides as outlined in Appendix A. Hence, we obtain:

$$\frac{dU}{dz} = i\gamma^{(a)}U + ik_{ab}V \tag{2.11a}$$

$$\frac{dV}{dz} = i\gamma^{(b)}U + ik_{ba}U \tag{2.11b}$$

where the residual fields have been neglected only after the coefficients in the above equations have been derived. Therefore, the propagation constants $\gamma^{(a)}$ and $\gamma^{(b)}$ are given by:

$$\gamma^{(a)} = (\beta^{(a)} + \hat{k}_{aa} - D\beta^{(b)}C - \hat{k}_{ab}C)(1 - DC)^{-1} \tag{2.12a}$$

$$\gamma^{(b)} = (\beta^{(b)} + \hat{k}_{bb} - C\beta^{(a)}D - \hat{k}_{ba}D)(1 - CD)^{-1} \tag{2.12b}$$

The corrections to the individual modal propagation constants $\beta^{(a)}$ and $\beta^{(b)}$, describes the effects of the modal interactions. The coupling coefficients can also be written as:

$$K_{ab} = (C\beta^{(a)} + \hat{k}_{ab} - \beta^{(b)}C - \hat{k}_{bb}C)(1 - DC)^{-1} \tag{2.13a}$$

$$K_{ba} = (D\beta^{(a)} + \hat{k}_{ba} - \beta^{(a)}D - \hat{k}_{aa}D)(1 - CD)^{-1} \tag{2.13b}$$

The coefficients C_{ij} are the modal overlap integrals between multiple modes of different waveguides, i.e:

$$C_{ij} = 2\hat{z}.\int_{\infty}^{\infty}\int[\mathbf{E}_t^{(i)} \cdot \mathbf{H}_t^{(j)}]dxdy \tag{2.14}$$

the individual modes are normalized such that $C_{ii} = 1$.

The constants $\hat{k}_{pq}$ depend on perturbations to the individual waveguides and are defined by:

$$\hat{k}_{pq} = \omega\int\int_{-\infty}^{+\infty}[\Delta\epsilon^{(p)}[\mathbf{E}_t^{(p)} \cdot \mathbf{E}_t^{(q)} - \frac{\epsilon^q}{\epsilon_0 n^2}E_z^{(p)}E_z^{(q)}]dxdy \tag{2.15}$$

where $\epsilon^{(p)}$ refer to individual waveguides and $\Delta\epsilon^{(p)}$ are the perturbations to the respective guide. As an example, lets consider two parallel slab waveguides with similar refractive indices of $n_{core} = 1.7$ and $n_{clad} = 1.5$. The thickness of the first waveguide is 1.3 μm and the second waveguide is 0.3 μm wide while they are separated by 0.4 μm (as shown in Figure 2.1). Working at wavelength of $\lambda = 1$ μm, the first waveguide supports 3 modes while the second waveguide is single mode. Table 2.1 represents the computed effective modal indices from the H-S CMT in comparison to the values from numerical methods. As it can be seen, the percentage error of the values found are all less than 1%. For the highest mode there is a higher error present between the developed CMT method and the numerical simulations which is due to the higher perturbation effect it has on the second waveguide.

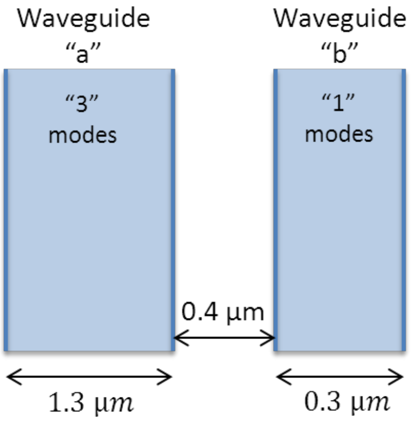

Figure 2.1: Coupling between two parallel and dissimilar slab waveguides

Modal Index	$\beta_1^{(a)}$	$\beta_2^{(a)}$	$\beta_3^{(a)}$	$\beta_1^{(b)}$
CMT	1.673162	1.593361	1.472544	1.546538
Numerical	1.673932	1.595093	1.463638	1.544094
Error %	0.046 %	0.108 %	0.608 %	0.158 %

Table 2.1: System Parameters

The calculated coupling coefficients from the extended H-S method are:

$$K_{ab} = \begin{bmatrix} 0.10264, 0.10606, 0.07323 \end{bmatrix}, \quad K_{ab} = \begin{bmatrix} 0.01954 \\ 0.05445 \\ 0.25249 \end{bmatrix} \tag{2.16}$$

the above results clearly show that the coupling coefficient is not symmetric for dissimilar waveguides (i.e. $k_{pq} \neq k^*_{qp}$). Also, it is evident that while the coupling coefficient is lower from one waveguide to the other, there is higher interaction between the third mode of the wider waveguide to the fundamental mode of the second waveguide. This would result in asymmetric coupling which would be beneficial in directional coupling of modes between dissimilar waveguides.

Haus *et. al* elaborated on the results of H-S theory and showed that this theory can follow from variational principles [24]. They introduced an eigenvalue problem from which the system's propagation constants are found while H-S method used mode expansion to find the corresponding coupling coefficients. Huang and Haus continued their work and expanded their results to waveguides with variations along z direction such as angled or tapered waveguides [25]. In a more generalized fashion, they formulated the evolution of an arbitrary number of modes through various coupling mechanisms as follows:

$$\mathbf{P}\frac{d\mathbf{A}}{dz} = -j\mathbf{HA} - \mathbf{FA} \tag{2.17}$$

from which $\mathbf{A}$ is a vector of system's modal amplitudes, $\mathbf{P}$ is the power matrix, $\mathbf{H}$ is the matrix including self and evanescent coupling coefficients and $\mathbf{F}$ shows taper induced coupling. Therefore through careful consideration of waveguide parameters and designed perturbations, one can induce directional coupling between arbitrary shaped waveguides.

2.2.2 Coupling light into and out of waveguides

While light propagation in the waveguide, through the crossings and modal interactions between the waveguides are of importance, the coupling of light into waveguides and the radiation from the waveguide should not be neglected. In order to couple light into a waveguide, a power overlap integral can determine the amount of coupled power. The type of incident field and its position with regards to the waveguide center would determine the type and number of modes excited within the waveguide. To find the amount of power coupled into each of the waveguide modes the following normalized overlap integral relation can be used where $\mathbf{E}_{inc}$ is the incident field and the $\mathbf{E}_{mod}$ is the waveguide mode field considered.

$$OI = \frac{|\int\int_S \mathbf{E}_{inc}(x,y)\cdot\mathbf{E}^*_{mod}(x,y)dxdy|^2}{\int\int_S |\mathbf{E}_{inc}(x,y)|^2dxdy\int\int_S |\mathbf{E}_{mod}(x,y)|^2dxdy} \tag{2.18}$$

In order to find the far-field radiation pattern from a waveguide, one can use Huygens-Fresnel principle with a number of approximations to drive a more usable formulation.

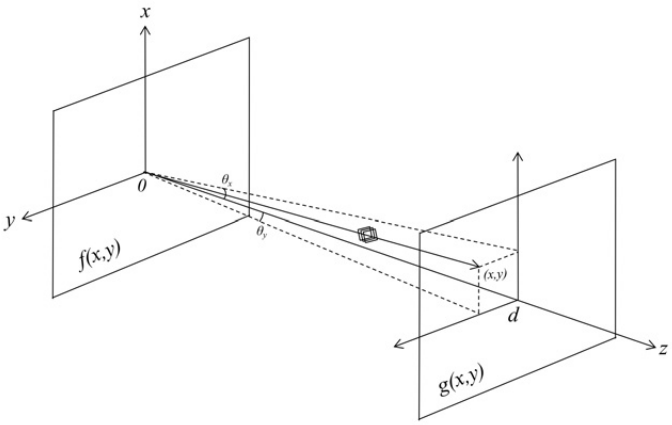

Figure 2.2: Far-field approximation at sufficiently large distances from the $z = 0$ plane. The complex amplitude at point (x, y) is proportional to the complex amplitude of a plane wave component with angles θ_x and θ_y [18]

First, the output wave is considered to be scalar. Then, it is assumed that the observation point is many wavelengths away from the aperture (i.e. $d \gg \lambda$). This allows for simplification of the phase term using a binomial expansion (as outlined in [26]). In addition, over large distances from the aperture and close to the optical axis, the quadratic phase function is approximated to be unity which is Fraunhoffer's diffraction approximation. As shown in Figure 2.2, for Fraunhofer approximation, the complex amplitude of a wave at $z = 0$ (i.e. $f(x, y)$) is related to its far-field amplitude $g(x, y)$ at a distance $z = d$ through Fourier transform. Hence, $g(x, y)$ is proportional to the Fourier transform of $f(x, y)$ (i.e. $F(v_x, v_y)$), which is evaluated at spatial frequencies of $v_x = x/\lambda d$ and $v_y = y/\lambda d$. Hence, the electric field amplitude can be written as:

$$E(x,y,z=d) \cong \frac{ie^{-ikd}e^{-i\frac{k}{2d}}(x^2+y^2)}{\lambda d}\int\int E(x',y',z=0)e^{i\frac{k}{d}(xx'+yy')}dx'dy' \tag{2.19}$$

Now, if the propagation distance d is sufficiently long compared with local coordinates of (x, y) the far-field position can be expressed in terms of the angles:

$$tan(\theta_x) = \frac{x}{d};\ tan(\theta_y) = \frac{y}{d} \tag{2.20}$$

Considering the above simplifications, the far-field radiation pattern can be simplified as:

$$E(\theta_x,\theta_y)\ \alpha \int\int E(x',y',z=0)e^{ik(x'tan(\theta_x)+y'tan(\theta_y))}dx'dy' \tag{2.21}$$

2.3 Literature Review

As briefly explained in the introduction, in 1938, Bowen showed that the efficiency of a spectrometer cannot be increased by introducing a condenser lens in front of a slit [5]. From thermodynamic point of view, it is argued that it would be impossible to reduce the area on which a given amount of radiant energy is concentrated without increasing the incident cone of light correspondingly. Since changes in the area of an image are not able to increase the efficiency, Bowen introduced the concept of changing the shape of the image without changing its area. Hence, the optimum shape would be a long narrow band whose width is equal to the slit. This method was called image slicing and proved to enhance the efficiency of the spectrometers especially in large telescopes. Bowen reports an improvement of efficiency up to 75%-90% compared with 5% for the initial case with a slit [5].

Another method of increasing the resolving power while maintaining the throughput was first proposed by W.G. Fastie in 1961 [6]. This method performed the previously mentioned slicing in the pupil space and showed that it can increase the sensitivity of astronomical spectral studies. In practice, the pupil slicing method was first used in the multiple mirror telescope (MMT) by 1982 and showed that the unusual optical configuration of the MMT improves the slit efficiency by a factor of 2.5 [7]. Another instance of using pupil slicers was reported by Beckers *et. al* for high-resolution spectroscopy in extremely large telescopes (ELTs) using adaptive optics [8]. While most of the pupil slicing was proposed for large telescopes in astronomical applications, Meade *et. al.* proposed another pupil slicing platform to improve the resolving power of a spectrometer without sacrificing throughput. A virtual slit was proposed which enabled high-performance, lowlight, and high-speed imaging instruments in a much smaller footprint based on a dispersive-type spectrometer [9]. The proposed virtual slit would reformat the pupil so that the image would be compressed in the dispersive direction without a corresponding increase on the exit cone angle [27,28]. All these recent approaches were deemed successful using free space optical components and they tend to break the size-quality factor relationship historically perceived to be true for spectrometers.

On the other frontier, with advancements in photonics and its fabrication processes that are compatible with IC manufacturing and MEMS technology, there has been a great push towards design and fabrication of micro-spectrometers. As discussed, spectrometers can be classified into three groups from an operation point of view: dispersive type, filter-based type and FT based spectrometers. On the other hand, from the fabrication of micro-spectrometers stand point, they can be categorized into the waveguide based (or PICs) and mico-opto-electro-mechanical (MOEMS) based systems. Here, a functional sample of

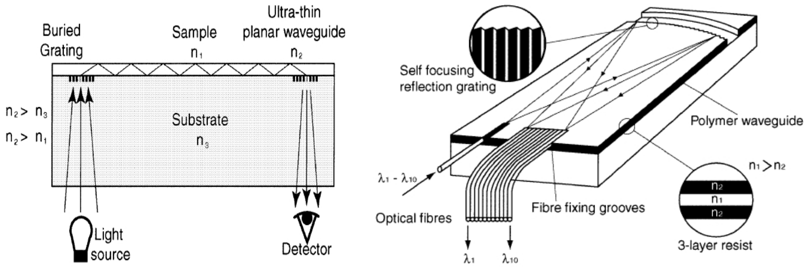

(a) (b)

Figure 2.3: Two of the very first waveguide based micro-spectrometers (a) Goldman et. al integrated spectrometer for chemical sensing application [29] (a) Mohr *et al* planar spectrometer with coupled input/output fibers [30].

each type is provided for review. Wolffenbuttel has also reviewed some of the proposed micro-spectrometers proposed by 2004 in literature [4]. From this review and considering the categories mentioned earlier, some of the distinct designs are revealed and expanded upon in the following pages.

One of the first few micro-spectrometers with on chip technology was presented by Goldman *et. al* in which a structure with a waveguide on top of a glass substrate was used for chemical sensing [29]. As shown in Figure 2.3(a), two buried gratings were used under the waveguide to allow coupling of light into and out of the waveguide. As the refractive index n_1 is changed on the liquid sample, the dispersion of the propagating wave changes and there would be a change in the resulting spectra that is coupled out in the output grating. Hence, a series of detectors would be able to register this change and hence detect certain chemical agents in the sample liquid.

Mohr *et. al* introduced another planar waveguide based spectrometer (shown in Figure 2.3(b)) shortly after Goldman in which the light from the input fiber is coupled into a waveguide which is then allowed to propagate freely until it hits a reflective grating made by deep reactive ion etching process [30]. The reflected and dispersed light is then coupled back into a series of fibers. Therefore, each of these fibers would carry a spectral component to a detector. While the size of such a chip was $18 \times 6.4\ mm^2$, its resolving power was reported to be 10 over the wavelength range of $700 - 900\ nm$. This approach can also be used with different materials as the waveguide core such as silicon-oxi-nitride (SiON) [31]. Based on Goldman methodology of grating couplers, Kwa and Wolfenbuttel also proposed to use bulk micromachining techniques to fabricate deep trenches in Si and allow the light to be reflected on angled Si surfaces until it reaches the grating [32]. While the proposed micro-spectrometer was one of the first kinds for visible/near infrared (NIR) which included a photodetector array, the surface roughness of the etched bulk Si caused high amount of scattering and therefore high losses. Later on, use of on-chip gratings was proposed for a variety of other micro-spectrometer designs. For instance, Chaganti *et. al*, proposed a miniature spectrometer with a thin-film planar waveguide grating coupler and a miniature focusing lens [33]. The resolving power was reported to be 700 and as stated, such waveguide based micro-spectrometers have the advantage of deviating from the throughput-resolution duality of conventional spectrometers.

Hence, one can increase the input slit width to increase the collected light without sacrificing the resolution. However, the total throughput of the whole system was reported to be only 0.94% which could be due to the efficiency of the grating coupler used. Grabarnik *et. al* have also introduced a planar spectrometer design with a concave micro-grating which uses a novel setup to totally reflect the light into the plane of the grating [34, 35]. The reported resolving power was about 100 whereas the efficiency was calculated to be about 28%-38%. Kumar *et. al* proposed a chirped waveguide coupler to couple the light in the waveguide out of plane and focus different wavelengths at different locations [36]. Ko and Lee have also proposed a micro-grating based micro-spectrometer using bulk micro machining techniques. While the proposed micro-grating presents a good resolving power of around 600 but there is no mention of the efficiency of such grating system [37].

Along with photonic integrated chips, there has been a series of advancements in the area of MOEMS which uses a system of moving mechanical arms or membranes by means of controllable electrical forces to achieve certain optical tasks. One example of such devices was proposed by Manzardo *et. al* in Figure 2.4(a) [38]. In this device, a Michelson interferometer was built by means of an electrostatic actuator in which a moving reflective arm would change the path difference between its two arms to perform Fourier transform spectroscopy (FTS). Another FT based micro-spectrometer was proposed by Kung *et. al* in which they proposed to sample a standing wave in the visible range to perform FTS [39]. A similar approach was also suggested by Stiebig *et. al* [40, 41], but both methods showed low resolving power which would be unacceptable for spectroscopy purposes.

Another type of MEMS structure which could be categorized as a filter-based spectrometer is a thermal bimorph arm (as illustrated in Figure 2.4(b)) which would scan the wavelength by varying the incidence angle of the multilayer cantilever acting as a filter [42]. Rissanen *et. al* also proposed a MEMS based tunable Fabry-Perot interferometer for central wavelengths of 420 nm and 670 nm for applications in diagnostics, healthcare and environmental monitoring [43]. The FWHMs of this design would vary from $4 - 9$ nm where for higher wavelengths the transmission peaks becomes wider. While this design claims to do imaging and point spectrometry at the same time, the transmission signal

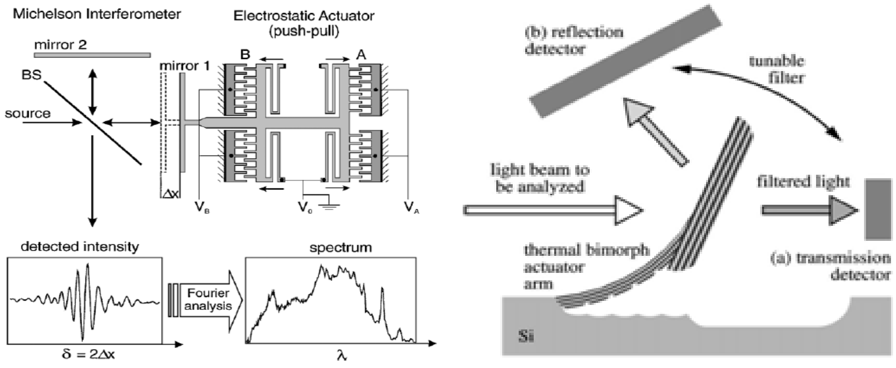

(a) (b)

Figure 2.4: MEMS based spectrometer designs (a) a Michelson interferometer to realize FTS [38] (b) A thermal cantilever to tune the transmission wavelength [42].

of less than 50% for smaller wavelengths and the maximum resolving power of 100 would limit its applications.

The low resolution in most of the above mentioned designs limits their use to specific applications in consumer products and inspection. However since the fabrication processes in some of the designs were not completely Si compatible, the researchers realized the need to shift towards Si compatible processes to reduce the initial costs of developing such devices for commercial use. Therefore, gratings and Fabry-Perot based resonance cavities were successfully fabricated in Si and designs were proposed for integrated micro-spectrometers in Si. Although, due to opacity of Si in visible wavelength ranges, they are mostly proposed for infrared ranges.

A Si based design was proposed by Correia *et. al* as shown in Figure 2.6. It uses a CMOS process to produce a chip with embedded photo-detectors and 16 channels of fixed-cavity Fabry-Perot filters on top. It was argued that having mechanically tunable parts in MOEMS based chips would reduce their reliability and limits the operation to certain bandwidth and hence the use of fixed cavities is plausible. However, the fabrication of a fixed cavity chip is extremely complex due to the number of steps needed in etching and lithography for each channel. For instance, in the chip fabricated by Correia *et. al*, 16 steps of lithography and etching was done to produce different cavity lengths for each channel. Therefore, in order to cover a wider range with better resolution, the number of channels or the number of fabrication steps becomes a critical bottleneck. It should be noted that any Fabry-Perot interferometer based design such as the one proposed by Kurth *et. al* for infrared filtering can be used in a similar setting to construct a micro-spectrometer [44].

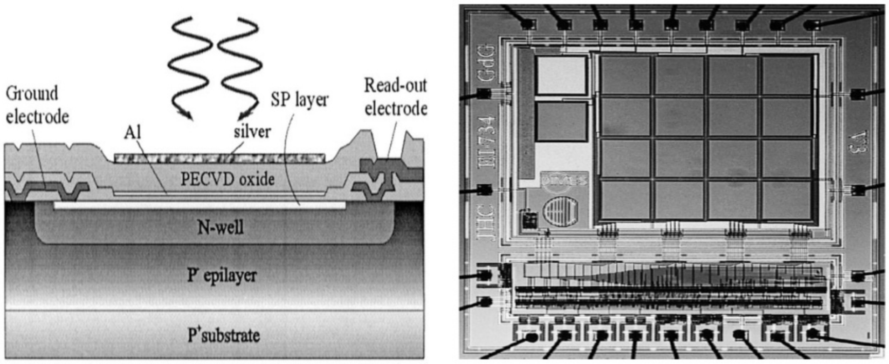

(a) (b)

Figure 2.5: CMOS based optical spectrometer (a) A cross-section of the Fabry-Perot etalon is presented on the left with the photodiode underneath (b) A top view of a 16 channel CMOS chip is shown on the right figure [45].

Another filter type on-chip spectrometer design is based on a large array of micro-donut resonators [46]. The designed structure by Xia *et. al* consists of 84 micro-donut resonators that resonate between the wavelengths of $1550 - 1610$ nm with 0.05 nm steps (as shown in Figure 2.6). While the quality factors of such micro-donuts are very high, implementation of such a design in the visible region would be challenging as the waveguides in the visible region are relatively weaker waveguides compared with Si counterparts. Also due to operation in single mode, the throughput of such designs is extremely low compared with free space spectrometers. Hence, the throughput is being trade-off for size in the process of miniaturization of spectrometers. This might not be an issue in regular bio-chemical sensing applications with high signal to noise (SNR) ratio but it would be a concern in applications such as Raman spectroscopy or Astronomy where there is limited number of photons to begin with.

Back in 1995, Watson was the first to suggest use of micro-spectrometers in astronomy [47, 48]. In conventional spectrometers used for astronomy, size of optical components scales with telescope diameter. Therefore, larger telescopes imply a much higher cost as sizes of the components are increased. The integrated photonic spectrographs (IPS) allow for more compact, modular and highly multiplexed systems while offering thermal and opto-mechanical stability especially for airborne systems. Bland-Hawthorn and Horton developed this concept further by proposing use of a telecommunication based arrayed waveguide grating (AWG) as the dispersive element in a micro-spectrometer [10]. The IPS outlined uses a single mode input fiber that feeds into an AWG very similar to the

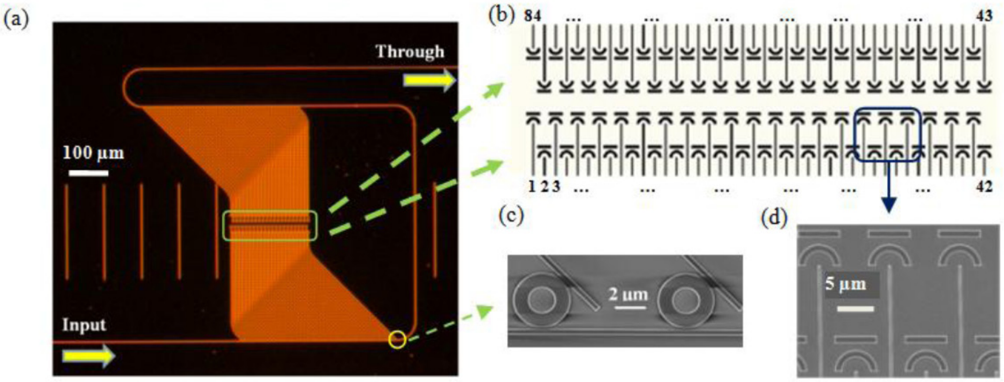

Figure 2.6: Micro-donut resonator array for high resolution spectroscopy. (a) an image of the proposed 84 channel resonating filters along with the 2D array of out of plane scattering elements. (b) The scattering array with their respective channel designations. (c) SEM image of the coupling region showing the mirco-donut resonators coupled with the input bus waveguide. (d) SEM image of the scattering elements [46].

one originally proposed by Smit [49, 50]. In the first free-propagation region (FPR), light diffracts in a slab region and gets coupled into an array of single mode waveguides. These waveguides differ in their path lengths by constant increments of Δx, which in the end is fed into the second FPR. The phase difference due to path length difference causes constructive interference of different wavelengths at different positions along the slab width in the end of the second FPR. In telecommunication applications, these discrete wavelengths are then coupled into waveguides in the end of the second FPR to be routed to different locations [51]. However, since the separated wavelengths are not individually needed in the micro-spectrometer case, the output waveguides of the second FPR are not needed in this design (as opposed to the AWG for telecommunication case). Hence, having a line of detecting pixels at the end of the second FPR, one can register the spectra of the incoming light. A spectrometer design based on AWG theory is shown in Figure 2.7 which shows how the light is dispersed at the second FPR. It is clear that overlap of higher order modes would contribute to the cross-talk noise on the detector which should be minimized during the design phase. As outlined by Bland-Hawthorn and Horton, one other issue with use of such micro-spectrometers is that while astronomical fibers are typically multi-mode, the micro-spectrometers are likely to operate with few-mode fibers [10]. Multi-mode fibers allow for much more light collection compared with single mode fibers and hence the throughput of such settings remains an issue.

Leon-Saval *et. al* proposed a device for the first time in 2005 that converted a multi-

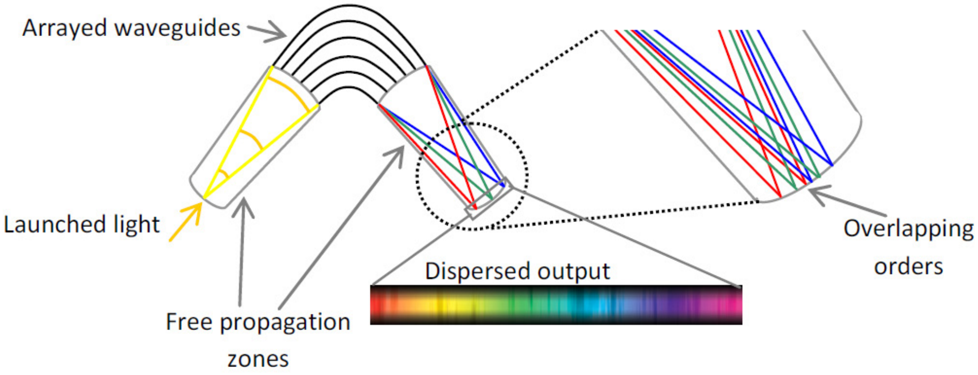

Figure 2.7: AWG based spectrometer [12].

mode fiber to a bundle of single mode fibers called a Photonic Lantern [52]. It included an array of single mode fibers surrounded by a low index jacket which were adiabatically tapered down to form a multi-mode fiber on the other end. The concept of adiabatic fiber tapers were investigated before by Love et. al where the criteria for adiabaticy was treated theoretically and experimentally [53, 54]. As it was shown, a near perfect coupling with minimum loss can happen between the fundamental mode and the cladding modes of the adiabatically tapered fiber core. The photonic Lantern is also based on similar principles; however, there was a series of studies published afterwards to explain the roots of such phenomena and its application in Astrophotonics [11, 55, 56, 57]. In the latest one, Bland-Hawthorn *et. al* make an analogy between the evolution of optical modes and eigen-states of electrons in quantum wells [58]. As shown in Figure 2.8, starting from the single mode fibers end on top, the modes in each core is strongly guided and uncoupled. As progressing along the taper, the modes become less confined in the core and start expanding in the cladding area. In an ideal case, there would be m cladding supermodes that would evolve to m modes of the multi-mode fiber.

The significance of Photonic Lantern is that it could be used to decompose the incoming light from a multi-mode fiber into a number of single mode fibers where they can be separately pre-filtered and fed to spectrometers. Bland-Howthorn *et. al* suggest two conceptual approaches, a semi integrated photonic case and a full integrated photonic device both of which are shown in Figure 2.9 [58]. In the semi-photonic approach, it is shown how the use of Photonic Lantern and changing the mode shape of a multi-mode fiber into a slit shape would increase the performance of a spectrometer without loss of power associated with conventional slit use. In the full photonic case, an AWG is used along with the Photonic Lantern to provide a fully photonic solution for modern spectrographs

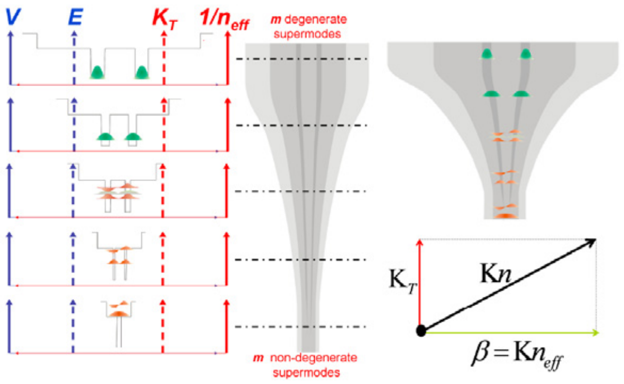

Figure 2.8: Evolution mode of single modes from a multi-mode optical fiber input [58].

used in astronomy. However, there are technological limitations to the solutions based on Photonic Lanterns. For ELTs, the primary mirror can get larger than 25 m and hence its point spread function can support thousands of modes. Therefore, a single observation requires handling of thousands of single mode fibers that has to be fed into AWGs. The technical difficulties of setting up such systems should obviously be considered. Therefore, Cvetojevic *et. al* suggested launching multiple fibers into one AWG and found that off-axis launch would shift the channels on the detector and hence increase the cross-talk between the channels [59]. Hence, depending on the number of input fibers, the FSR of the output would become greatly limited. To correct for this issue, the authors suggested to do cross dispersion on the output of AWG using additional bulk optics. Now, the detector needs to be a 2D array to be able to detect the entire cross dispersed spectra. While using multiple input AWGs would help with the large number of single mode fibers resulting from the Photonic Lanterns, there is an upper limit to the number of single mode fibers per AWG. Each standard single mode fiber has a minimum cladding of 125 μm, so their core have to be placed at least 125 μm apart. Hence, the size of the Photonic Lantern would become an issue along with the complexity of the overall system as there is a limit to the number of single mode fibers that could be fed into an AWG. Therefore, this would raise an interesting challenge to look for an alternative solution to this problem.

With the advances in three dimensional (3D) lithography, laser inscription can be used to pattern non-planar waveguides in fused silica [60, 61]. The photonic lantern concept was used again to transition the modes from a multi-mode input waveguide to multiple single-mode waveguides. Then, in order to address the shortcoming of photonic lanterns, the output single mode waveguides were reformatted into a quasi 1D slit-like output in a device called photonic dicer (PD) [62]. The slab size is about 30 mm for a system with

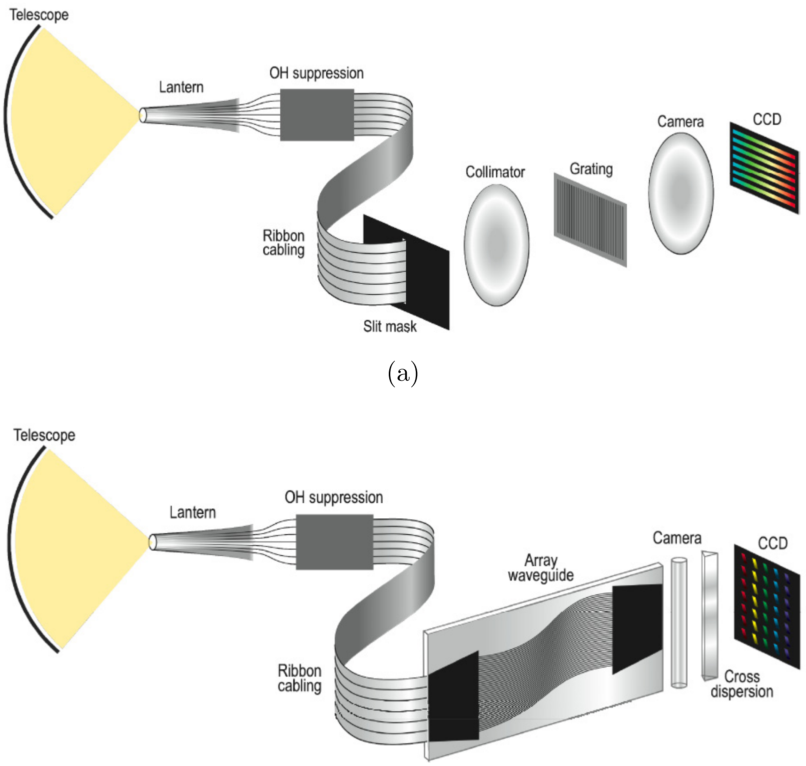

(a)

(b)

Figure 2.9: Use of Photonic Lantern with spectrometers. (a) the semi-photonic approach. (b) the full photonic approach with AWG [58].

multi-mode input fiber of 50 μm core. As shown in Figure 2.10(a), the waveguides are inscribed with soft transitions within the dielectric slab to minimize propagation losses. The input side is a square of size 50 μm which transitions into 36 single mode waveguides and then it would re-arrange into a diffraction limited psuedo-slit output. The dark field images of the fabricated device is shown in Figure 2.10(b). The scale bars are 50 μm and therefore the slit-like output is measured to be about 15 × 400 μm in size. At the designed operation wavelength of 1550 nm, the throughput is reported to be 50%-70% [62]. While the throughput has dropped considerably compared with the photonic lantern, the limitation of working only with the single mode fibers on the output is resolved. However, scalability of this solution to larger sized fibers is still a limiting factor. Having a larger size input, the number of waveguides needs to be increased which would result in longer and more complex waveguides routing and design.

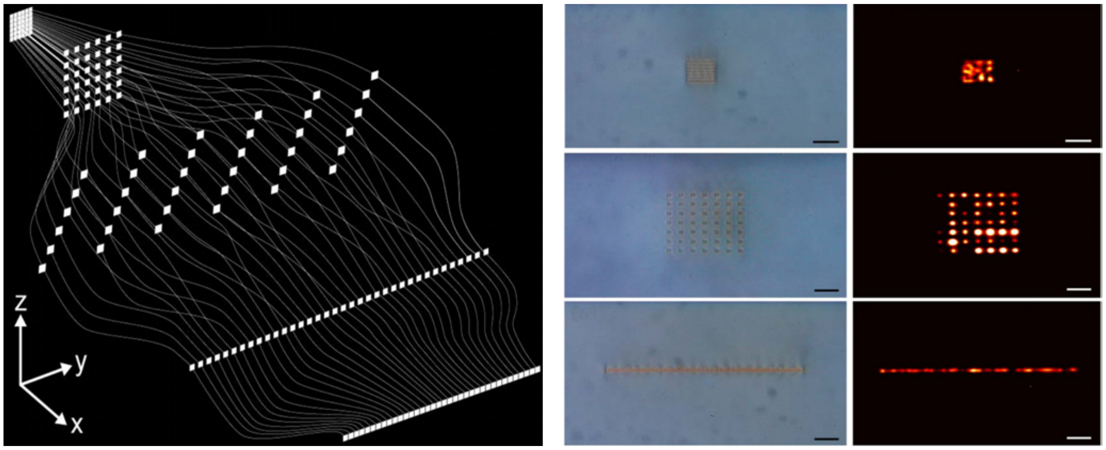

(a) (b)

Figure 2.10: Photonic dicer design, fabrication and output results (a) 3D sketch of a 6 × 6 photonic dicer system going from a multi-mode input to a diffraction limited pseudo-slit. (b) Images of the fabricated waveguide facets showing the transition from multi-mode input to single mode waveguides and then the diffraction limited pseudo slit output [62].

2.4 Conclusion

In this chapter, basic properties of geometrical optics and fundamental concepts of radiometry were introduced. Then, a brief discussion of mode coupling between dissimilar waveguides was presented along with radiation of light from waveguides and its governing equations.

An exhaustive list of prior art especially for micro-spectrometers were reviewed. While there are a variety of proposed structures in literature which have limited spectral/imaging interrogating capabilities, they are not completely universal in providing high-quality wide band spectral information. Comparing the throughput of the micro-spectrometers with their free space counterpart, one finds that most of the proposed solutions have very limited throughput. This might be due to coupling and alignment issues or surface roughness present in most applications due to the MEMS or Si fabrication processes. A rather novel concept called Photonic Lantern was briefly introduced to solve the problem of throughput by coupling of multi-mode input to a number of single mode outputs were they can be fed into the micro-spectrometers subsequently. While this approach seems promising, it does not solve the problem fundamentally. Another integrated approach based on the same principles of photonic lanterns were implemented recently using 3D lithography. However, there are still limitations with respect to scalability of this solution for larger input fibers. In the next chapter, the theoretical basis for a new approach is provided to reformat the input beam to a psuedo-slit like output in a planar platform.

Chapter 3

Design of Integrated Photonic Slits for a High Resolution-High Throughput Spectrometer

As discussed in earlier chapters, a trade-off exists between the resolution and throughput of a conventional spectrometer. These two parameters are inter-related based on *etendue* principle which has been discussed previously. In this chapter, the concept of increasing throughput in a spectrometer while maintaining the spectral resolution is introduced using integrated photonic elements in planar setups. A figure of merit developed for comparison purposes is suggested and three potential structures are proposed towards achieving an integrated photonic slit concept. These structures are based on the mode-coupling concept explained in previous chapters in which an arbitrary series of circular fiber modes are converted to modes of a structure that have a smaller output facet in the dispersive direction. The smaller output facet is chosen such that the far-field radiation pattern of the waveguide matches the output of the slit without much power loss compared to an actual slit. In the following, the integrated high-throughput photonic slit (HTPS) concept is discussed. Then, an adiabatic tapered waveguide, a ridge waveguide with sub-wavelength channels and a wedged fiber with sub-wavelength channels are proposed to realize the above mentioned goals. These designs are first explored using numerical simulations. However due to large number of variables involved in the design and fabrication steps, the simulations are used as guidance in the design to improve the optical throughput and quality of output beam and more accurate measurements are left to the experimental stages.

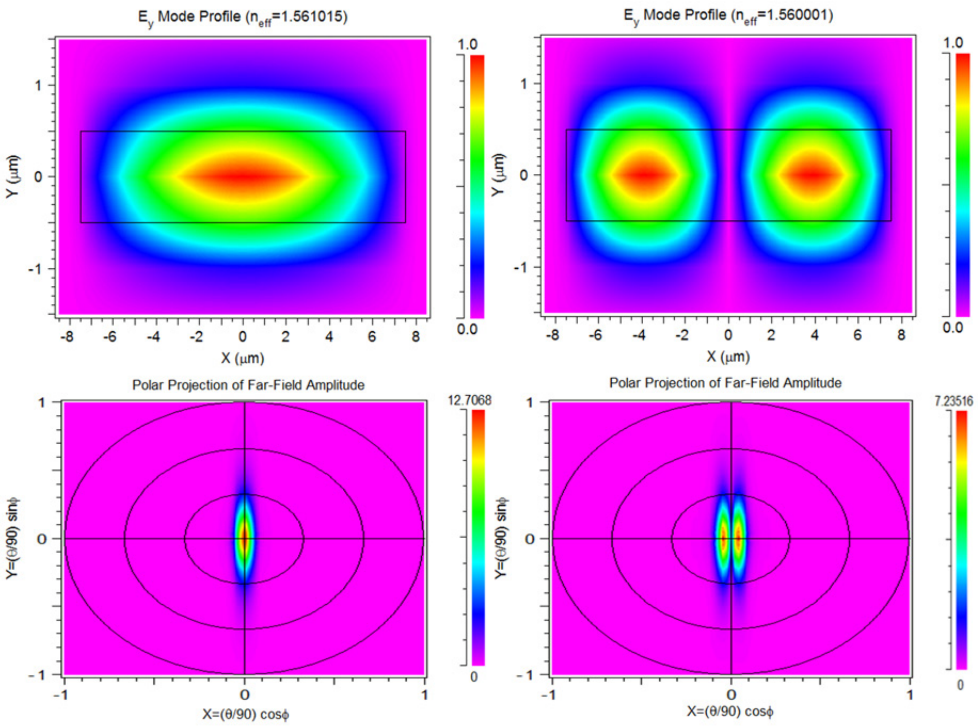

Figure 3.1: Modes of a rectangular waveguide with their equivalent far-field projections underneath them.

3.1 Controlling the far-field projections using mode conversion

As reviewed in Section 2.2.2, the far-field distribution emerging from of a waveguide depends on the aperture shape and the modal profile of the waveguide. Therefore from given waveguide geometry, different modes would produce different far-field projections. As an example, consider a simple rectangular $1 \times 15\ \mu m$ dielectric waveguide with core refractive index (RI) of 1.5 and cladding RI of 1.444. The first two modes are found using a finite element mode-solving method in RSoft. These modes are then excited and the far-field projections are calculated using the Fraunhofer diffraction method (illustrated in Figure 3.1). If a few-mode waveguide is designed and perturbed such that the first order mode is coupled to a higher order mode, one can achieve far-field beam reshaping with such a structure. This could prove useful in realizing specific free space optical systems with equivalent integrated photonic circuits. One of the areas of interest in this regard, is performing non-imaging tasks such as spectroscopy. In such cases, the spatial information is not of particular interest. Hence, a waveguide-based system would be a valuable solution since waveguides do not preserve spatial-phase information within them. While mode coupling within a waveguide would change the far-field projected pattern, coupling between non-identical waveguides or waveguides with different cross-sections can result in far-field projection patterns of interest.

To illustrate coupling between two waveguides of different cross-sections, consider the system shown in Figure 3.2. A 20 μm multi-mode slab waveguide is considered which is butt-coupled into another 2 μm wide slab waveguide. These slabs have a core RI of 1.5 surrounded by cladding RI of 1.444 and operation wavelength of 1 μm. Assuming that the wider waveguide is excited by a multi-mode input field with a random set of initial phases, the narrow waveguide center can be placed at the constructive interference point of the fields to maximize the coupling ratio. In the case illustrated in Figure 3.2, a maximum coupling ratio of 35% could be achieved going from a 20 μm waveguide to a 2 μm waveguide. It is worth noting that by decreasing an aperture by a factor of 10 in a free space setting, the output power would approximately reduce by a factor of 10. Hence,

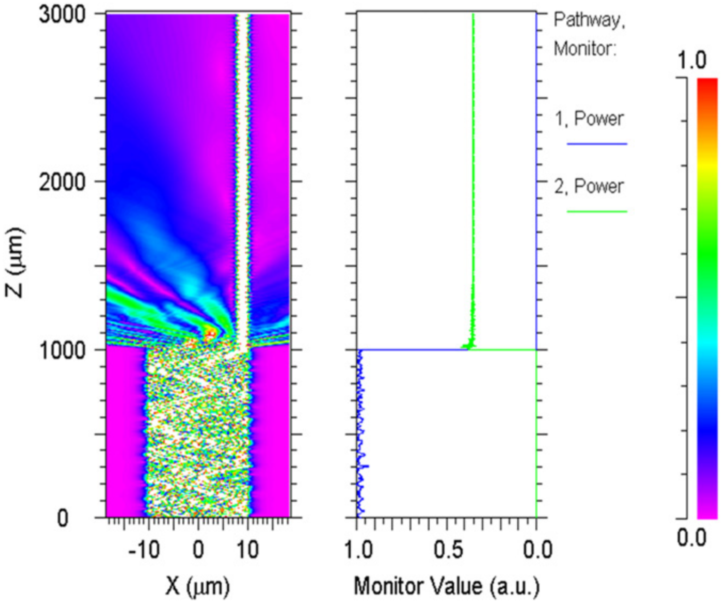

Figure 3.2: Intensity profile in the xz plane on the left, showing mode coupling from a 20 μm wide input waveguide that is butt-coupled to a 2 μm wide output waveguide. The plot on the right shows the power monitor as the optical field propagates in the z direction.

by exploiting the nature of light propagation in waveguides and appropriate constructive interference conditions, one can disrupt the inverse proportionality of aperture size (i.e. resolution) and throughput. However, due to the preservation of *etendue* (as explained in Section 2.1.3), when going from a 20 μm waveguide to a 2 μm waveguide the output beam becomes 10 times more divergent in a lossless optical system. Therefore, a figure of merit is needed to characterize and quantify the performance of different structures. The proposed figure of merit is explained more detail in the following section.

3.2 Figure of Merit - β Value

In order to characterize different optical systems, a figure of merit is proposed which takes into account the expected flux ratio and the throughput of the system. In an ideal case, for an optically invariant system, the input and output *etendue* should remain the same. Therefore, any change in *etendue* is related to net losses or generation in the system. In a spectrometer, as mentioned in previous chapters, the dispersive direction width is an important factor in the resolution of the acquired spectra. Therefore, use of narrow slits have been conventionally suggested for decades. Slits provide a trade-off between the resolution and throughput while keeping *etendue* constant. If one is able to reduce the beam width in the dispersive direction while maintaining the divergence angles approximately the same, there is the possibility of increasing throughput while maintaining the resolution. As mentioned in the previous chapter, the pupil slicing solution (as implemented in HTVS [27]) tends to decrease the beam width in the dispersive direction while keeping the NA constant. The slicing method increases the beam height in the non-dispersive direction and therefore, *etendue* value remains the same while the resolution remains the same. Now if we use the ratio of input/output beam dimensions times the ratio of input/output divergence angles, it would give us an estimate of the expected flux ratio through the system:

$$< \frac{f_{out}}{f_{in}} >= \frac{\Xi_{out}}{\Xi_{in}} = (\frac{A_{out}}{A_{in}}).(\frac{\theta_{out}}{\theta_{in}}) \tag{3.1}$$

In the case of a slit, the output divergence angle is inversely related to the slit width in the dispersive direction. As an example, let us assume that the slit width is 10 μm while it has been illuminated by a Gaussian beam of width 200 μm. As shown in Figure 3.3, the output beam gets diffracted. Using Fraunhofer diffraction theory, the intensity of the diffracted wave in the far-field can be approximated by the following formula considering a uniform field over the slit:

$$I(\theta) = I_0 sinc^2(\frac{\pi a}{\lambda} sin\theta) \tag{3.2}$$

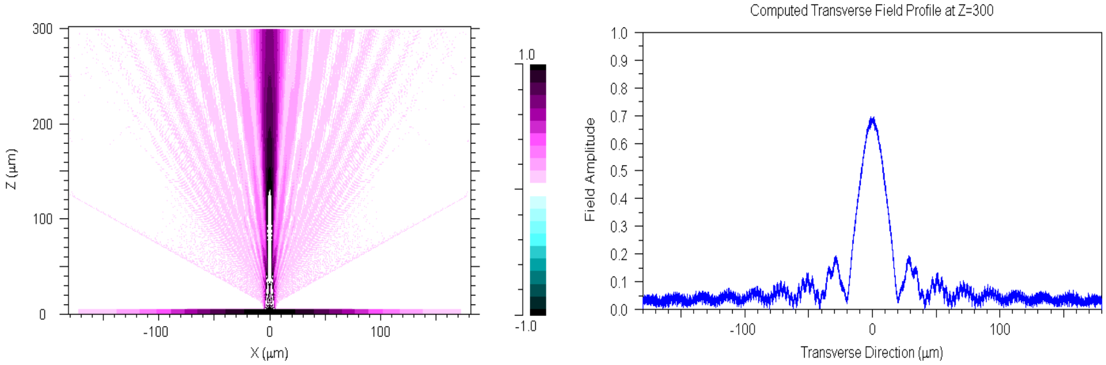

(a) (b)

Figure 3.3: Diffraction pattern from a 2D single slit simulation (a) Intensity at the xz plane as the field propagates along the z direction (b) The transverse intensity pattern plotting the *Sinc* function along x after propagating 300 μm in z.

Hence, by solving the above equation to find the FWHM (i.e. $\frac{I(\theta)}{I_0} = 0.5$) the θ_{out} would be 2.54°. The divergence angle of the input is simply the divergence of a Gaussian beam which is approximately:

$$\theta_{in} \approx \frac{\lambda}{\pi w_0} = \frac{1}{100\pi} = 0.18^{\circ}$$

Therefore the expected flux ratio can be calculated as:

$$< \frac{f_{out}}{f_{in}} >= (\frac{10 \times 200}{200 \times 200}).(\frac{2.54}{0.18}) = 0.695$$

But on the other hand, the actual throughput of the slit can be calculated by integrating the squared amplitude value of the Gaussian electric field distribution across the slit width for output and across all x for the input;

$$P_{out} = \int_{-d/2}^{d/2} e^{\frac{2x^2}{w_0^2}}\, dx = \int_{-5}^{5} e^{\frac{2x^2}{100^2}}\, dx = 9.983,$$

$$P_{in} = \int_{-\infty}^{\infty} e^{\frac{2x^2}{w_0^2}}\, dx = 125.331$$

Therefore, the throughput of the system is expected to be 7.9% at this spectral resolution. By introducing a new figure of merit called the β factor one can relate the throughput and resolution parameters of a spectrometer. The proposed β metric is the throughput of the system divided by the expected flux ratio from the *etendue* relation. While *etendue* describes the input/output relationship of a lossless optical system, the β value tends to relate the flux ratio changes of the system to the losses present. The β factor can be written as:

$$\beta = \frac{\left({}^{P_{out}}\!/_{P_{in}}\right)}{< {}^{f_{out}}\!/_{f_{in}} >} \tag{3.3}$$

As an example, lets consider a slit of width 10 μm, the calculated β factor becomes 0.114 according to the expected flux ratio and input/output powers calculated earlier. This is a very small value since the slit is physically blocking the input light in order to create the narrow beam profile needed for high resolution spectroscopy without making the beam divergent and thus showing the in-efficiency in using slits. The β factor depends on the slit width or the diffractive power of the slit and hence in case of a Gaussian beam is dependent to the ratio of the slit width to the Gaussian beam diameter. Since Gaussian beam is not uniform over the slit area, the Fraunhofer integral should be evaluated directly for the far-field FWHM of a certain Gaussian beam width and different slit widths. As shown in Figure 3.4, this integral is evaluated for various slit widths and input beam diameter of 200 μm. As the slit width is increased and hence the diffraction from the slit reduces, the divergence angle of the output converges to the divergence angle of the input and hence an upper bound can be considered for the β value of a slit. It should be noted that in practice, the output of the slit is collimated using additional optical elements and hence the upper bound is reached for smaller slit widths. However, since the addition of other optical elements makes the analysis of the proposed structures more complicated, the upper bound of the β value for the slit is compared with the β value calculated for the diffracted light from the proposed structures. Therefore, in a sample structure, if the β is less than one it

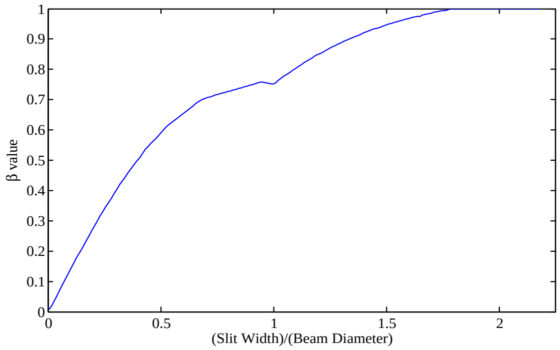

Figure 3.4: The β value curve for different slit widths to beam diameter ratios.

would mean that the structure delivers the output power like a slit or worse. Otherwise, the structure is performing better than a slit and hence there is a rationale to use the proposed structure.

Cases of improved β

In the case of HTVS, the following beam parameters were reported by Meade *et al.* [27]. While the input was a circular spot, it is reported that the output would be an elliptical spot with minor and major axis of 14 μm and 500 μm. Hence, the expected flux ratio could be approximated by,

$$< \frac{f_{out}}{f_{in}} >= (\frac{14\ \mu m \times 500\ \mu m}{200\ \mu m \times 200\ \mu m}).(\frac{0.25}{0.1}) = 0.437$$

In the above calculation, the beam area was approximated by a rectangle for both input and output beams. On the other hand, the throughput of the system is reported to be 0.98 in which the loss is mainly due to reflective optics surfaces. Using Equation 3.3, the β value is calculated to be 2.24 which is much greater than the value for a slit. This indicates that HTVS performs better than a slit in terms of maintaining throughput for a specific resolution. In general, when the expected flux ratio remains lower than the actual power throughput of the system, one can conclude that the studied system is performing better than a slit. Translating the proposed formulation for optical waveguides, one can use the ratio of the input-output apertures times the ratios of the corresponding divergence angles to find the expected flux ratio and from there, using the actual throughput of the integrated optical system, the final β value can be found which quantifies its performance with respect to a slit.

Considering the mode-coupling example proposed in section 3.1, the divergence angles can be calculated from the projected far-fields of the input and output beams using the far-field formulation given in Section 2.2.2. Figure 3.5 illustrates the input and output far-fields of the structure illustrated in Figure 3.2. As explained in the previous section, the input of the 20 μm waveguide is a mixture of high-order modes with a specific phase association between different modes as a case study. The resulting multi-mode field is excited using the illustrated far-field pattern shown in Figure 3.5. The calculated FWHM angle can therefore be considered as the input cone angle for that structure. On the output side, in case of efficient mode-coupling to the narrow waveguide, the fewer modes of the narrow waveguide are excited and hence the projected far-field would be much different than the input field pattern. The output far-field projection in the right-hand plot of

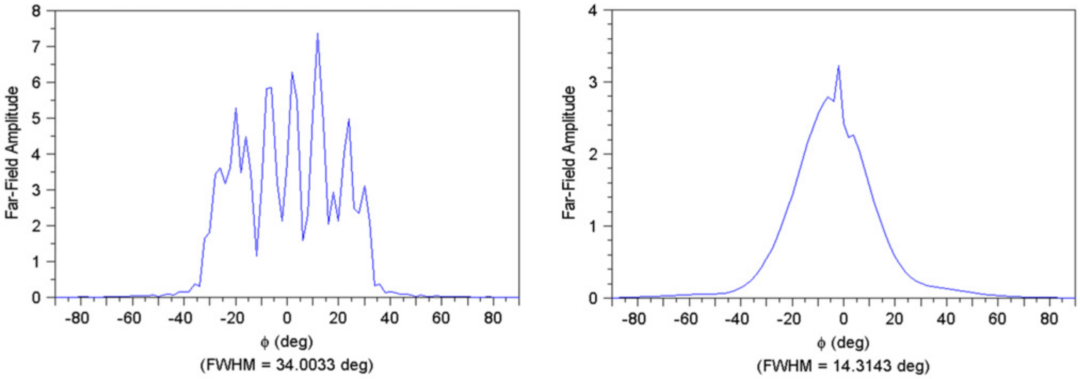

(a) (b)

Figure 3.5: Calculated far-field amplitudes and their corresponding FWHM measurements for waveguides of Figure 3.2. (a) Far-field amplitude of a mixture of higher order modes from the multi-mode waveguide (b) Far-field of the same high-order modes after being coupled to a narrower few-mode waveguide.

Figure 3.5 shows the calculated FWHM to be 14.31°. Considering these simulated values, the β value can be calculated as:

$$< \frac{f_{out}}{f_{in}} >= (\frac{2\ \mu m}{20\ \mu m}).(\frac{14.31}{34}) = 0.042,$$

$$(\frac{P_{out}}{P_{in}})_{simulated} = 0.35$$

$$\Rightarrow\ \beta = \frac{0.35}{0.042} = 8.33$$

Hence if an efficient mode-coupling system is used, one can effectively achieve better throughputs compared with conventional slits in a spectrometer for a specific width. In the following, lets consider the effect of β on the detected signal based on photon statistics.

Significance of β in SNR

Assuming that the HTPS design results in a β factor higher than one (i.e. β of an equivalent slit), an important aspect to explore is the relationship between the β and SNR values. If the output aperture of an HTPS has a fixed width, a two times improvement in β would mean the throughput should be increased by a factor of two. Therefore, it should be determined that whether this would lead to a two-fold improvement in SNR or not. Due to the quantized nature of light and the independence of photon detections, there is a natural uncertainty within the measurements of light which is known as photon noise. The photon noise is also known as Poisson noise and is a signal-dependent source and is a major source of image noise.

In electronic imaging sensors, the photoelectric effect is used to convert the number of incident photons into electrons which would translate into an electric signal. Photon noise is due to the independent photon arrival events that follow a random temporal distribution. Therefore, the photon counting is a classic Poisson process. If $\mathcal{N}$ is the number of photons measured by a pixel over time t, the probability of detecting k photons is [63]:

$$Pr(\mathcal{N}=k)=\frac{e^{-\lambda t}(\lambda t)^k}{k!}$$

where λ is the expected number of photons per unit time which is related to the incident irradiance. Since the incident photon count has a Poisson distribution, its variance is equal to its expectation value, $E[\mathcal{N}]=Var[\mathcal{N}]=\lambda t$. Hence, the photon noise is signal dependent and the standard deviation grows with the square root of the signal. As a result, the SNR would be [63]:

$$\frac{S}{N}=\frac{(\lambda t)}{\sigma_k}=\sqrt{\lambda t}$$

If the β value can be doubled in a prospective design while the output aperture remains the same size, it would result in an increase of throughput by approximately the same ratio. This would result in SNR improvement of $\sqrt{2}$ in a photon-limited system where other sources of noise (e.g. readout noise) are not considered.

Considering β as the figure of merit to compare various designs, in the remainder of this chapter three designs are proposed and evaluated. In these designs, the far-field shape is effectively changed through mode-coupling. The first designed structure is a simple adiabatic taper which goes from 50 μm width to 5 μm according to an exponentially decaying function. The other proposed designs use coupling between to dissimilar waveguides to reshape the far-field beam while achieving higher coupling power than simply using hard apertures like a slit. These structures are explored in more detail in the following sections.

3.3 Adiabatically-Tapered Waveguide

An adiabatically-tapered waveguide can be used to convert the distribution of modes by means of inter-modal coupling. A taper is considered adiabatic if the optical power is maintained within a particular number of modes with negligible coupling into other modes along its length [64]. In addition, adiabatic perturbation on waveguide boundaries warrants mode-coupling with minimum losses. However, one caveat is that the length of the taper would have to be longer and material losses would become prominent. Tapered waveguides have been long introduced in literature for applications such as mode-size conversion, sensing and couplers [65, 66]. By tapering the core of a single-mode waveguide, one can change the mode size and hence facilitate better mode coupling into and out of high index waveguides.

The proposed multi-mode tapered waveguide changes the mode size of a multi-mode fiber and matches it to the mode shape of a slit-like aperture. By performing this action, the throughput of a dispersive spectrograph can be increased while preserving its resolution. A sample structure is designed which was fabricated through a collaboration with IIT Bombay by their developed fabrication techniques for SU-8 [67]. The fabricated chip was then used to observe its output far field beam shape. A number of adiabatic taper profiles such as a linear or exponential profile can be used to taper down the waveguide width. However, for a low-loss transmission, the linear adiabatic taper should be long enough to achieve an adiabatic propagation. On the other hand, a longer taper leads to more propagation losses. This becomes more critical if the input and output apertures have large width mismatches which need longer linear tapers. In order to reduce the length of the taper, other profiles such as exponentially decaying profiles have been shown to be more efficient [68]. The adiabatic taper used in this case also has an exponentially decaying width profile,

$$w_z = w_0 + (w_1 - w_0)\frac{e^{z'} - 1}{e^{-1} - 1} \tag{3.4}$$

where $z' = \frac{z - z_0}{z_1 - z_0}$, $z_0 = 0$, $z_1 = 7\ mm$, $w_0 = 50\ \mu m$ and $w_1 = 5\ \mu m$. The height of the waveguide is kept constant at 50 μm to match with the modes of 50 μm multimode fiber. The width on the other hand is reduced along the z direction. Figure 3.6(a) shows the 3D model of such a tapered structure and Figure 3.6(b) illustrates the xz RI profile (top view). The RI of the core is chosen to be 1.6 and the upper clad is left to be air as in a ridge structure which is shown in Figure 3.6(c)-(d). The lower cladding layer is a thin film of SiO_2 with RI of 1.444 and the substrate is a Si wafer with RI of 3.456. While the length of the taper is chosen to be 7 mm, a 3 mm straight waveguide is added to the end of the taper section. This allows for the output modes to settle and the higher order modes resulting from the perturbation to dissipate. Therefore the output beam quality is less affected by these higher order modes. It is also easier to cleave the output facet without concerns for possible cleaving point errors.

Beam propagation method (BPM) was used to simulate the light propagation along the

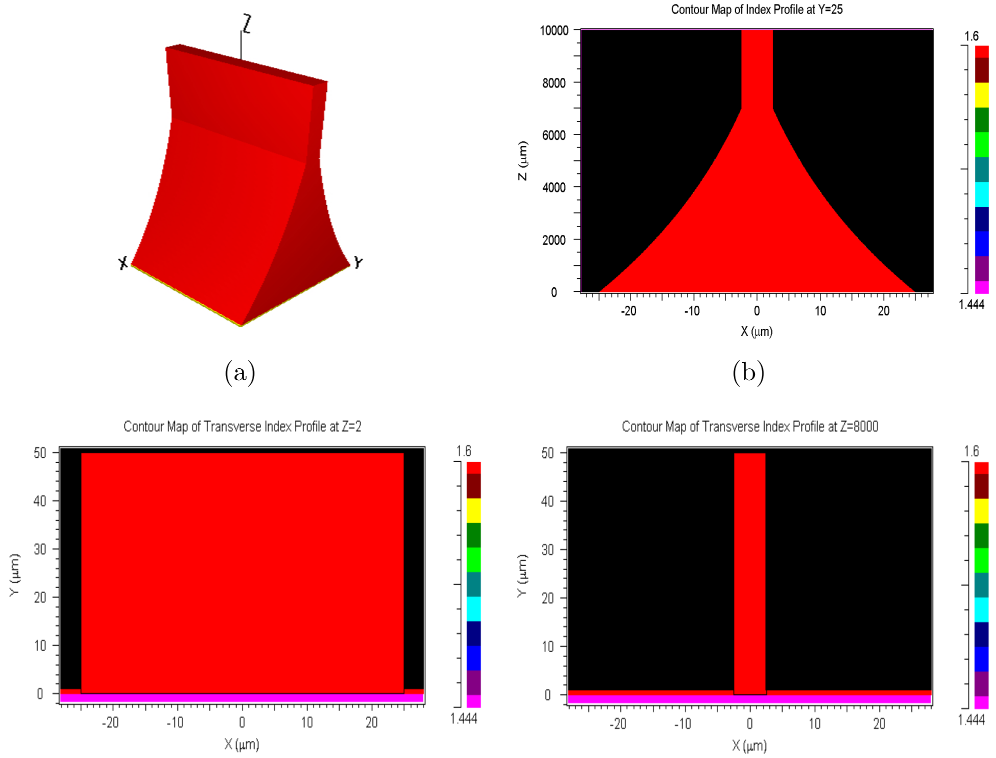

(a) (b)

(c) (d)

Figure 3.6: 3D model and refractive index profiles of the exponentially tapered waveguide (a) The 3D model of the waveguide (b) The xz RI profile from the top view (c) Input cross-section (d) Output cross-section.

taper. The excitation is a uniform rectangular field along the input facet of the waveguide at wavelength of 1 μm. This allows for excitation of all possible modes on the input side. The adiabatic transition of the waveguide width allows for minimum losses in coupling to modes of the narrowing waveguide. Figure 3.7 illustrates the propagating field profile in the tapered structure along with the normalized power profile along the propagation direction in z. As it can be seen, only about 5% of the input power couples into radiation modes in an ideal case where material losses are not considered. Figure 3.8 shows the near-field and far-field beam profiles from the output waveguide. The near-field pattern shows how the 50 × 50 μm uniform input is transformed to a 5 × 50 μm field pattern through mode coupling. The far-field pattern shows the projection in polar coordinates calculated using the two-dimensional (2D) Fourier transform. The FWHM of the output

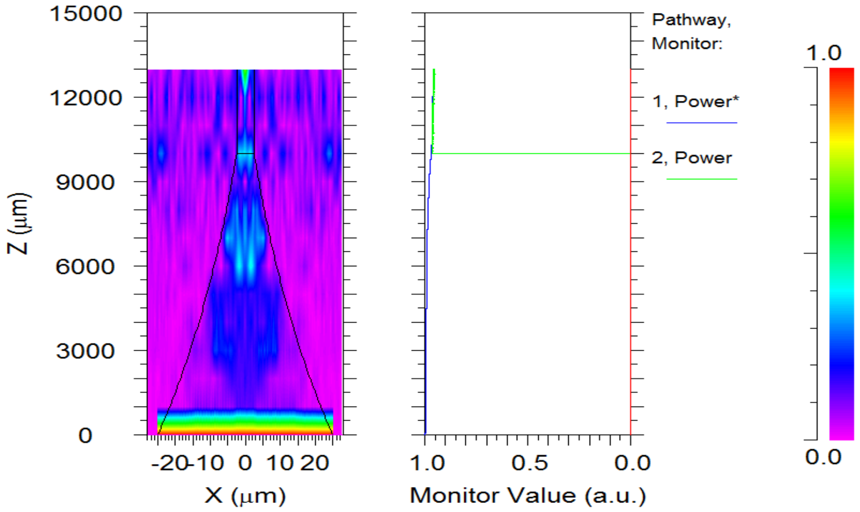

Figure 3.7: The xz propagation profile of the tapered waveguide showing the simulated intensity distribution using BPM method on the left. The power across the waveguide is calculated and monitored in the right-hand plot showing its value as the optical mode propagates in the z direction.

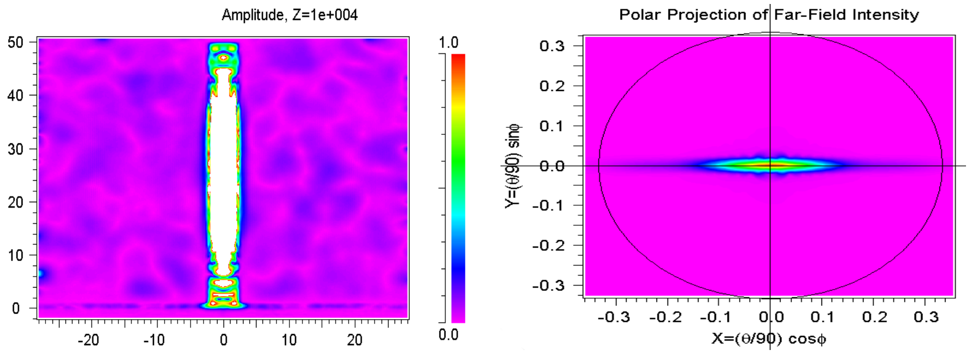

(a)

(b)

Figure 3.8: Output field intensity distribution of the tapered waveguide. (a) Near-field profile of the output facet (b) Far-field polar projection of the output waveguide field.

cut can be used to determine the divergence angle in the far-field and accordingly calculate the β value as the figure of merit. As shown in Figure 3.9, from the horizontal cut along the x axis of far-field projection, the following parameters can be calculated by considering the following; entrance cone angle: $\theta_{in} = 2°$, exit cone angle: $\theta_{out} = 15.7°$

$$< \frac{f_{out}}{f_{in}} >= (\frac{5 \times 50}{50 \times 50}).(\frac{15.27}{2}) = 0.768,$$

$$(\frac{P_{out}}{P_{in}})_{simulated} = 0.95$$

$$\Rightarrow \ \beta = \frac{0.95}{0.768} = 1.24$$

From the calculated β factor it can be concluded that in an ideal case where there are no material losses, the tapered waveguide would result in a 24% improvement compared to a physical slit. When material losses are considered, the performance of the tapered waveguide may drop below the performance of the slit making its use obsolete (i.e. $\beta < 1$). The fabrication and experimental results for the structure are described in section 4.1. In the next section, another proposed structure is explored and its performance metrics are investigated.

3.4 Inversely Tapered Multi-mode Coupler

While a simple tapered structure should theoretically change the output far-field shape through mode-coupling, implications such as choice of material, size constraints, fabrication and packaging causes the realization of the device to be difficult or impractical. In this

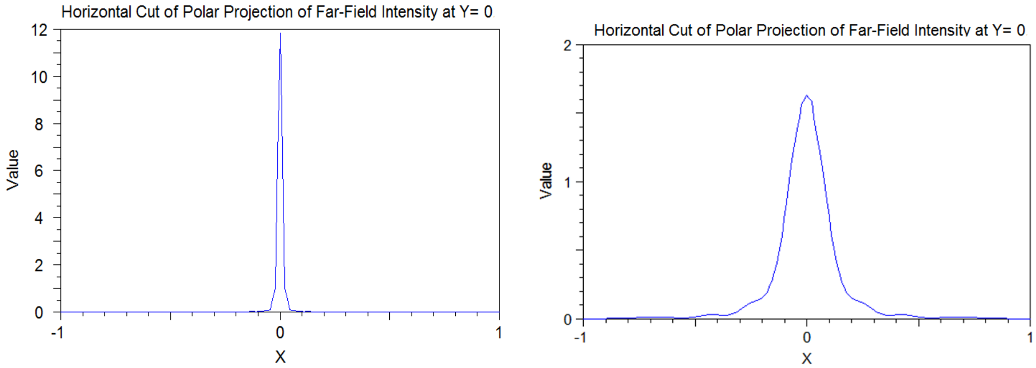

(a) (b)

Figure 3.9: Horizontal cut of polar projection through the center to determine the input-output waveguides divergences. (a) Input 50 × 50 μm waveguide divergence for a uniform input excitation. (b) Output 5 × 50 μm waveguide divergence from uniform input excitation.

section, another design methodology is explored to perform mode-coupling for certain far-field projections. Since spectrometers often operate on a fairly wide band of wavelengths, the proposed design should have the versatility to be used and optimized for different wavelength regions to remain as achromatic as possible. Therefore, the candidate solution should avoid the use of wavelength-dependent resonant-based structures. In such cases, the resonant based structure has to be designed from scratch for different wavelength regions as they are only operational in a certain narrow bandpass. Also, use of multiple modes would become cumbersome due to dispersion effects. Hence, resonant-based couplers are not scalable and practical for a high-throughput and wide-band application. Here, we will propose a multi-mode coupler that would be able to couple multiple modes of one waveguide to a waveguide of different cross section which meets the desired far-field projection constraints. While this coupler should be able to couple multiple modes efficiently, it should also work for different wavelengths as well. In the following, to illustrate the ideal scenario, first we start with coupling between similar waveguides and then progress to the case with multiple modes and dissimilar waveguides. All the simulations in the following are done in 2D where the y direction is assumed to be infinite as in a slab waveguide.

As discussed in Section 2.2.1, modes of two separated waveguides couple to one another when their modal overlap integral is non-zero. The coupling coefficient quantifies the interaction strength or alternatively the distance over which a fraction of power is exchanged between the two modes. On the other hand, the amount of power exchanged between two parallel waveguide modes is dependent on the difference between their propagation constants. Hence, coupling between parallel waveguides of arbitrary cross-section, dissimilar index and non-identical shapes can be extremely inefficient especially when multiple modes are needed to be considered. Figure 3.10 illustrates the exchange of power between two parallel slab waveguides where both waveguides have similar width and refractive indices. The blue and green monitor plots on the right side of the plots show the exchange of power between the modes of the two coupled waveguides. The waveguide width is 20 μm and it is once excited by its first mode and then using a uniform rectangular field to consider coupling of multiple modes between the two waveguides. The coupling length between the two parallel slab waveguides is about 30 mm for the fundamental mode. On the other hand when multiple modes are present, as shown, higher order modes couple much faster due to their smaller effective modal index compared with lower order modes. Therefore, there is no instance along the propagation direction where all modes are completely present in one of the waveguides.

While near ideal coupling can happen between two similar waveguides, the case is much different for dissimilar waveguides. In another example, the RI and width of the second waveguide is changed individually as shown in Figure 3.11. It is evident that the coupled

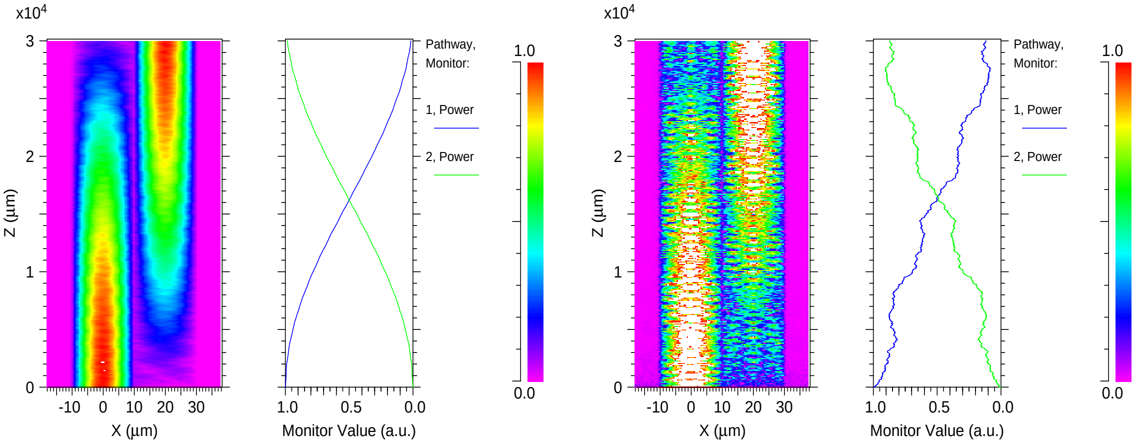

(a) (b)

Figure 3.10: Mode coupling between two similar waveguides separated by 200 *nm* gap. (a) It shows power exchange of the first mode between the two waveguides. (b) It shows power exchange between multiple modes excited by a uniform rectangular field in the first waveguide.

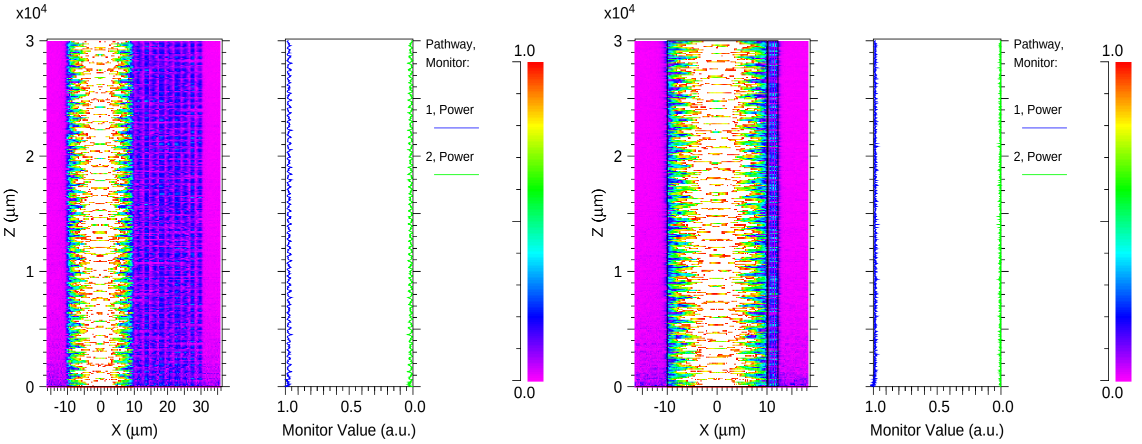

(a) (b)

Figure 3.11: Coupling of multiple modes between two dissimilar waveguides separated by 200 *nm* gap. (a) Coupling between waveguides of similar width but different refractive indices. The waveguide on the right has a higher RI. (b) Coupling between two waveguides with similar RI and different widths.

power in both cases remains well below 5%. Figure 3.11(a) illustrates the case where both waveguides have the same width but have different core refractive indices. Figure 3.11(b) on the other hand, represents the case where the second waveguide width is only a tenth of the first waveguide width. It is evident that in this case, the coupling is even lower than the previous case with different refractive indices as modal mismatch becomes greater between the two waveguides.

As explained earlier, in order to increase the proposed β factor in an optical system, one has to reduce the output aperture size in the dispersive direction while its throughput is maintained and the output beam divergence is not increased by a large factor. The proposed mechanism to achieve this goal was through mode coupling. It was shown that the coupling efficiency between two dissimilar waveguides is extremely low due to the large modal-mismatch between their corresponding eigen-modes. In order to increase this efficiency, the first waveguide can be tapered down. As the waveguide is tapered down, the existing modes are coupled to the modes of the smaller cross section and as the waveguide width reduces to the width of the second waveguide, coupling between the two waveguides would increase. When the width of the first waveguide is reduced, the effective modal index of the structure is reduced and the modes become less confined, hence it would result in a larger coupling factor between the two waveguides. As illustrated in Figure 3.12(a), the main coupling starts after 10 mm of propagation along the taper where the width of the larger waveguide tapers down to about 3.5 μm. At this point, the higher order modes would be weakly confined and hence couple to the adjacent waveguide which becomes a better guiding structure as the main waveguide tapers down. During this process only 70% of the input light couples to the narrow waveguide and the rest leaks out. Through the beginning of this coupler, only the higher order modes would couple to the narrow waveguide as they have a lower effective modal index. As the modes propagate along the z direction and the main waveguide becomes narrower, the modes in the main waveguide begin coupling to all the modes of the narrow waveguide. This can result in destructive interference between the coupling mode and the traveling mode in the narrow waveguide. Hence, some power is lost in the coupling process when the main waveguide is only tapered down.

In order to increase the coupling ratio further, an inversely-tapered coupler is proposed which is shown in Figure 3.12(c). As the first waveguide is being tapered down, the second waveguide is being tapered up. While the coupling mechanism is similar to the one taper case, the adiabatically tapered-up waveguide allows for larger coupling to its main mode. Since the narrow waveguide width is extremely small in the beginning, only one mode exists and the higher order modes of the main waveguide couple effectively into the main mode of the narrow waveguide. As the width is increased, coupling occurs between the higher-

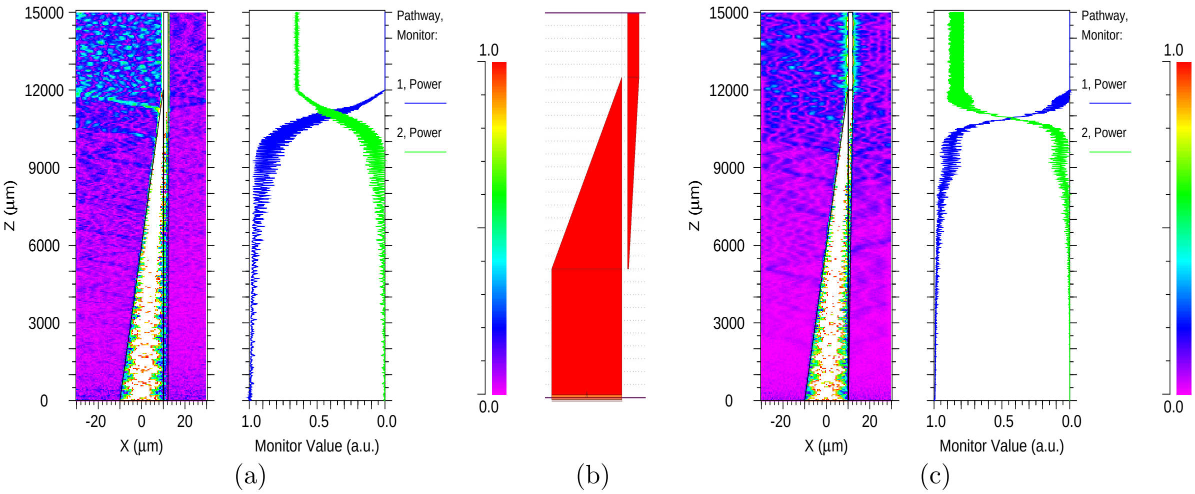

Figure 3.12: Coupling between waveguides with similar core RI. (a) The first waveguide is only tapered down while the second waveguide has constant width. (b) The top view CAD model of the inverse tapered coupler (c) Both waveguide are coupled in an inversed tapered setting.

order modes of the main waveguide and the lower-order modes of the narrow waveguide as well. In this structure, the coupling increased to 83% which is significantly higher than the previous tapered coupler system. As seen in the power profile, the coupling increases at about 9 mm into the taper when the main waveguide width becomes small enough so that its modes begin to lose confinement. This is exactly when the main waveguide couples efficiently into the adjacent waveguide. While there is a big change in coupling ratio, the modes of the initial waveguide still do not couple efficiently to the tapered up narrow waveguide in the first 9 mm of the taper. This is due to large effective modal index difference as they both have the same RI despite their different cross sectional dimensions.

In order to reduce the effective modal index difference between the two inverse tapers and potentially reduce the coupler length, the RI of the narrow waveguide can be chosen to be higher than the RI of the main waveguide. For instance as shown in Figure 3.13(a), the coupling happens between the main guide with RI of 1.5 and the narrow guide of RI 2 with the cladding of 1.444. As shown in Figure 3.13(b), with the increasing width of the narrow guide, the first few modes would branch out and hence the higher order modes of the main waveguide would couple into the first few modes of the narrow guide as they see the perturbation of the waveguides widths along the taper. In this case, the coupling starts much earlier into the taper at about 3 mm length. This is due to the fact that the higher RI of the narrow guide makes it a more suitable guide at narrower widths where the modes are more confined. From the power monitor, the dynamic of the coupling mechanism between the two guides can be explained. The maximum power coupling is further increased to 91% from the previous 83% which shows a higher efficiency by increasing the RI of the narrow guide. In addition, one of the primary goals in the coupler element design was a broad-band response in order to be efficiently deployed and used at different band passes. Here, the multi-mode coupler element has been tested with two additional wavelengths while all previous coupling simulations were done at wavelength of 1 μm. As shown in Figure 3.14, the coupling efficiency remains above 90% for both excitation wavelengths of 632 nm and 782 nm which indicates its ability to be used for a broad band-pass region.

The proposed coupler in this section was presented as a conceptual coupling mechanism in two dimensions. In reality however, 3D waveguides are used and the proposed coupling mechanism can be used to couple modes of a wide waveguide to modes of a narrower waveguide in the dispersive direction. In the remainder of this chapter, two 3D structures are proposed which are based on the inversely tapered coupling concept. These structures are evaluated and simulations have been done along with required optimizations to achieve the desired far-field output.

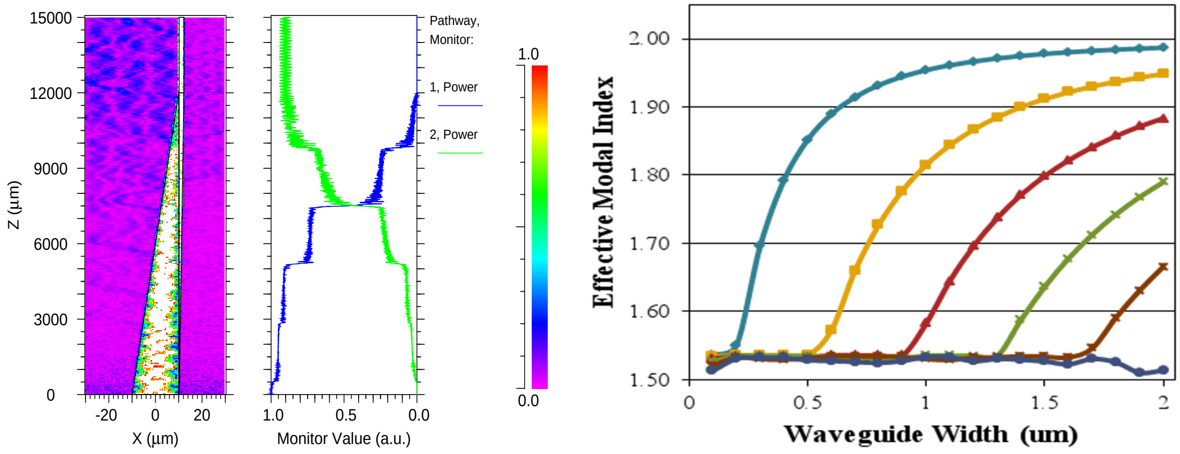

(a) (b)

Figure 3.13: Coupling between inversely tapered waveguides where the narrow waveguide has also a higher RI core. (a) Inversed tapered coupler simulation illustrating the power exchange between the waveguides. (b) Effective modal index change for the first few modes as the narrow waveguide of RI 2 is tapered up in the lateral direction.

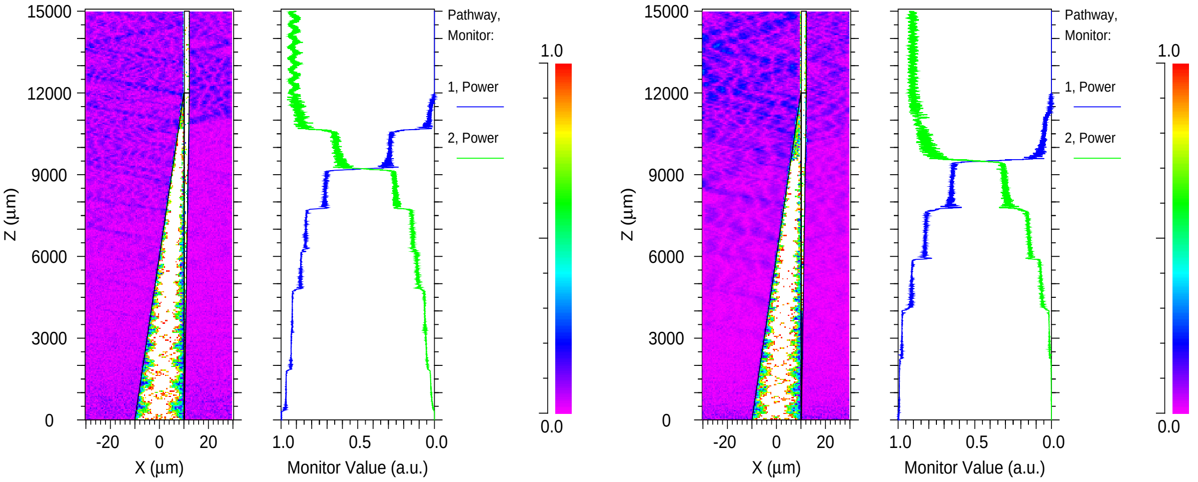

(a) (b)

Figure 3.14: Inversed taper coupler operating at two different wavelengths of (a) 632 *nm* and (b) 782 *nm*.

3.4.1 Multiple tapered channel waveguides in a ridge structure

The inverse tapered couplers proposed in the previous section were modeled in 2D. In a 3D setting however, due to the large modal miss-match between the multi-mode 2D input and a quasi-1D planar output waveguide, the coupling is not efficient. In order to achieve a better coupling and reduce the miss-match (i.e. 2D input waveguide and the slab region), a multi-core waveguide is proposed where each core is tapered individually creating a change in the effective refractive index of the slab region. As the width of these individual waveguides are increased, the slab area effective refractive index increases which would provide the required perturbation to couple the light from the tapered down 2D input waveguide to the slab region. The Bruggeman effective medium index approximation [69] can be used to calculate the effective refractive index of the slab region as the individual waveguide widths increase from zero to the desired width. Comparison of the effective mode of the slab which has smaller higher index cores with just one tapered up waveguide, shows that the former results in a larger fundamental supermode which can increase the overlap integral and hence increase the coupling ratio. In addition, having individual waveguides would allow for optimization of the desired output mode based on the required far-field pattern which would be explained further through this chapter. Thus, the proposed structure allows significant freedom in the design of the photonic slits.

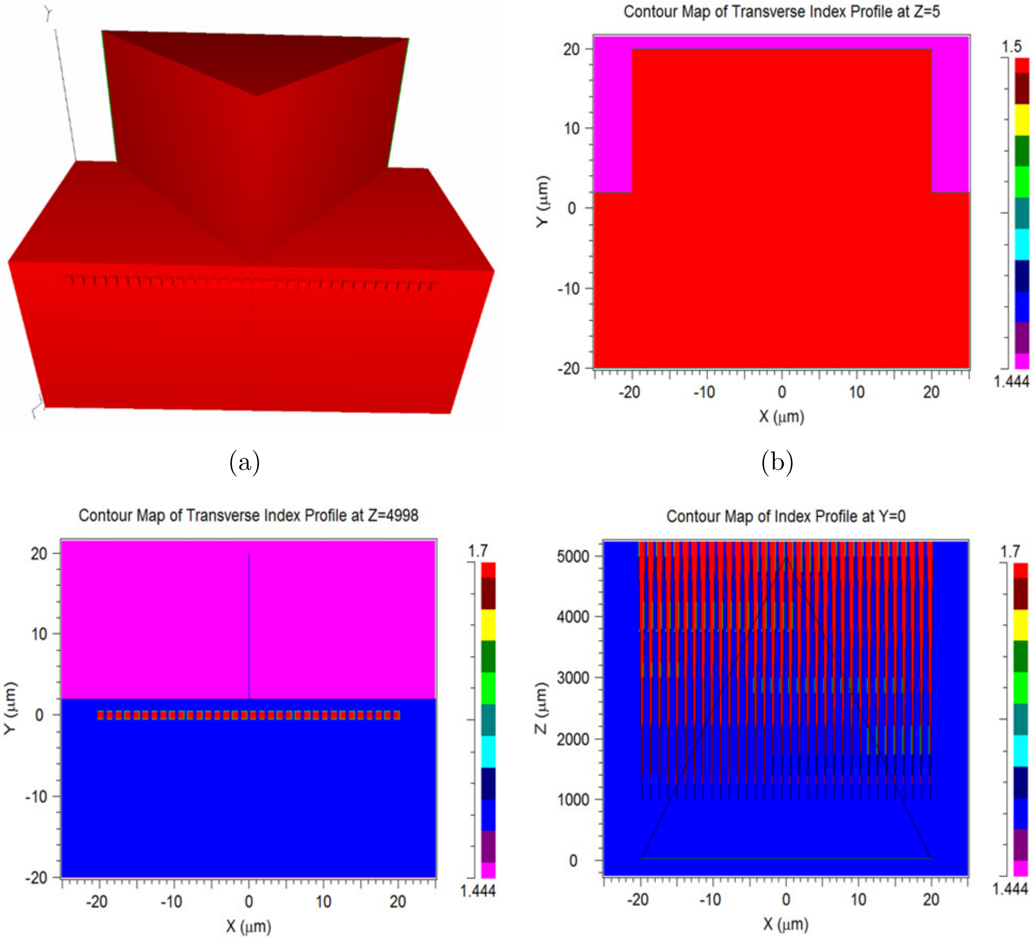

(a) (b) (c) (d)

Figure 3.15: 3D CAD model and RI profile of the tapered ridge structure with tapered up micro-channels in the middle of the ridge area. (a) 3D CAD model. (b) XY RI cross-section at the beginning of the tapers. (c) XY RI cross-section at the end of the tapers.(d) XZ RI profile in the middle of the structure.

Assuming that the input fiber is coupled into a ridge structure on the input, the proposed structure is shown in Figure 3.15 along with cross-sectional cuts showing the RI profiles of the overall structure. The input is a 40 μm × 40 μm ridge-type waveguide at $z = 0$ to which the multi-mode fiber butt-couples. The ridge structure is constructed from SiO_2 with RI of 1.55, the lower cladding has RI of 1.444 and the upper cladding is air.

As the field propagates along the z direction, the multiple high index channels are tapered up while the ridge area is tapered down as shown in Figure 3.15. At the cross section of $z = 5$ mm, the channel waveguides reach their maximum width of 0.8 μm and a gap of 0.4 μm. On the other hand, the height is kept constant throughout the structure at 1 μm which allows the use of conventional planar fabrication methods without the need for complex vertical tapering fabrication techniques. Silicon Oxy-Nitride ($SiON$) is used as the choice of material for the high index channel waveguides. In a PECVD machine, by adjusting the Oxygen factor in the deposition process one can deposit $SiON$ with refractive indices ranging from 1.6 to 2.

The inversed tapered waveguides force the modes of the ridge structure to effectively couple into the multiple channel waveguides. The high-indexed tapered up channel waveguides cause the perturbation needed for coupling of different modes of the ridge area to super modes of the multiple channel waveguides. This process is similar to the inverse tapered couplers introduced at the beginning of this section. When the ridge area width is reduced, the modes start to leak into the slab section of the waveguide. Eventually due to the RI difference between the channel waveguides and the main ridge waveguide, the tapered-up channels become more confining and the modes of the ridge are coupled to modes of these small channels. The channel waveguides are not strictly single mode but most of the optical power is within the lowest order mode. This allows for coupling of multiple input modes to a bundle of few-mode waveguides. Due to small proximity of these channel waveguides, the near field coupling between them results in the formation of supermodes. The resulting first order supermode would be very similar to a mode of a simple slab. Therefore, the proposed structure can effectively couple multiple modes of a ridge waveguide to modes of a slab-like structure which has a height much smaller than the ridge height. If the coupling mechanism is done efficiently, this would potentially produce a high β value.

Figure 3.16 illustrates the simulated field propagating through the proposed structure. The ridge area is excited by a rectangular uniform field which excites multiple modes of the ridge structure. As the modes propagate through the tapered down ridge area, they couple into the tapered up channels in the slab area. Figure 3.16(a) shows the xz view through the structure center and Figure 3.16(b) shows the yz view through the center of the waveguide, illustrating the coupling of the mode in the vertical direction to the slab region. As shown in Figure 3.16(c), the power coupling ratio is 70%. The remaining 30% of the power is not coupled and leaked to the lower part of the slab region. While this might be considered a bit low for general couplers proposed in literature, the mode-coupling proposed here is between two extremely dissimilar waveguides with dimensions of 40×40 μm and 1×50 μm. This type of coupling between uncontrolled multi-mode

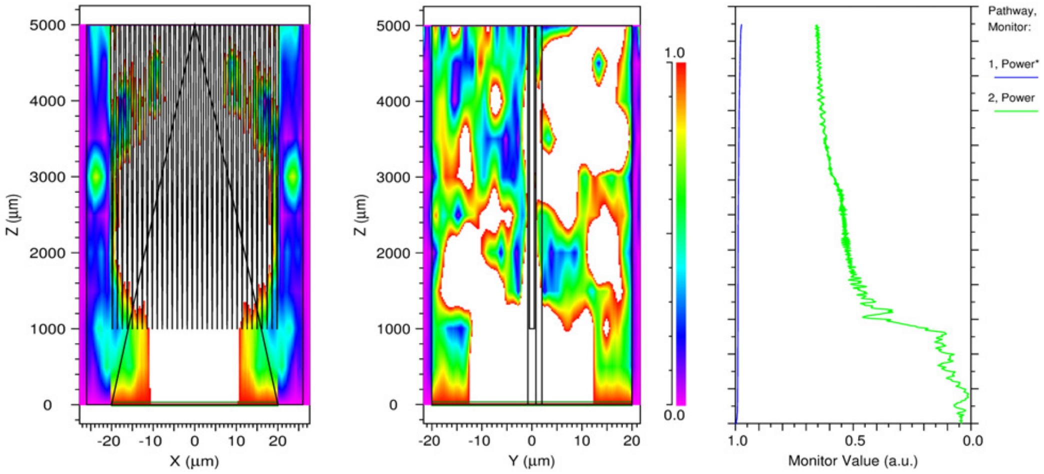

(a) (b) (c)

Figure 3.16: Beam propagation through the tapered ridge waveguide illustrating the intensity pattern in the xz and yz planes along the waveguide. (a) The xz intensity profile view from the y-cut through the center. (b) The yz intensity profile view through the center of the waveguide. (c) Power coupling to the slab area around the channels shown in green.

waveguides with a fairly broad operational wavelength range is different than conventional single mode and single wavelength couplers proposed in the literature.

Figure 3.17 illustrates the dynamics of coupling as the modes propagate in the z direction. As the ridge width decreases, the smaller channel waveguides taper up and the ridge modes start to couple into these small waveguides. The length of the taper is only 5 mm long. It is evident from this figure that after 4 mm of propagation, the majority of the power is coupled into the small channel waveguides. In order to maximize the coupled power, the center of the modes should be positioned at the same height as the channel waveguides. This would minimize the ridge area deposition needed in the fabrication step as well. In this case, if a 40 μm fiber is going to be coupled into the ridge waveguide, a ridge waveguide of 40 μm wide and 20 μm height can be used with a slab height of greater than 20 μm. Therefore, the fiber center can be positioned below the slab height where the channel waveguides are going to be placed. In this simulation, the slab region and channel waveguides are continued from 5 mm to 9 mm without any dimensional change in order to let the leaky modes dissipate. This would allow for a more accurate far-field analysis without the influence of higher order leaky modes in the calculations.

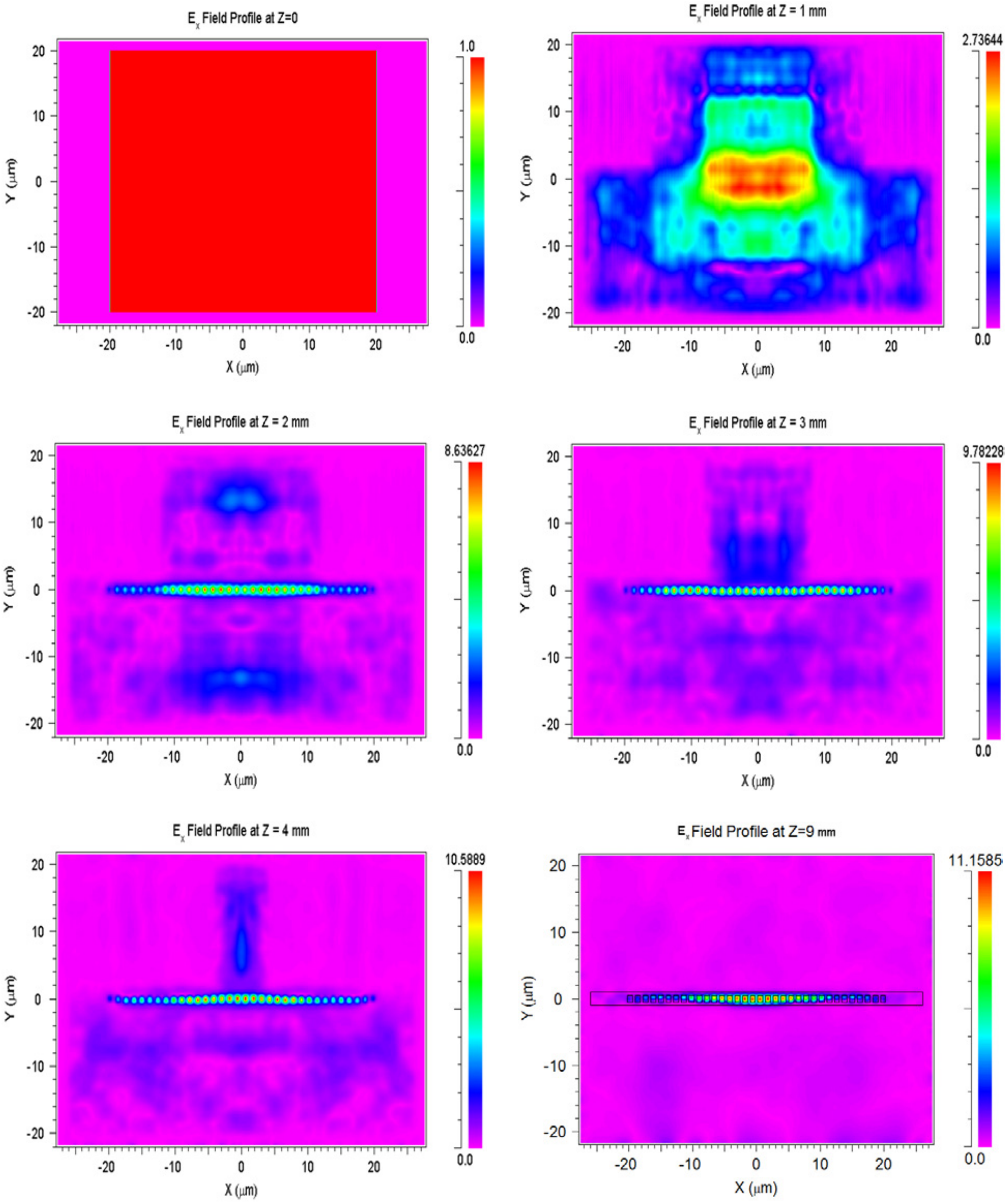

Figure 3.17: xy cross sections of the field propagating through the structure at various z distances. It starts as a uniform rectangular field and as it progresses, it will couple into the tapered up channel waveguides. The length of the taper coupler is 5 mm and after that the slab and the small waveguides are continued up to 9 mm for the modes to stabilize.

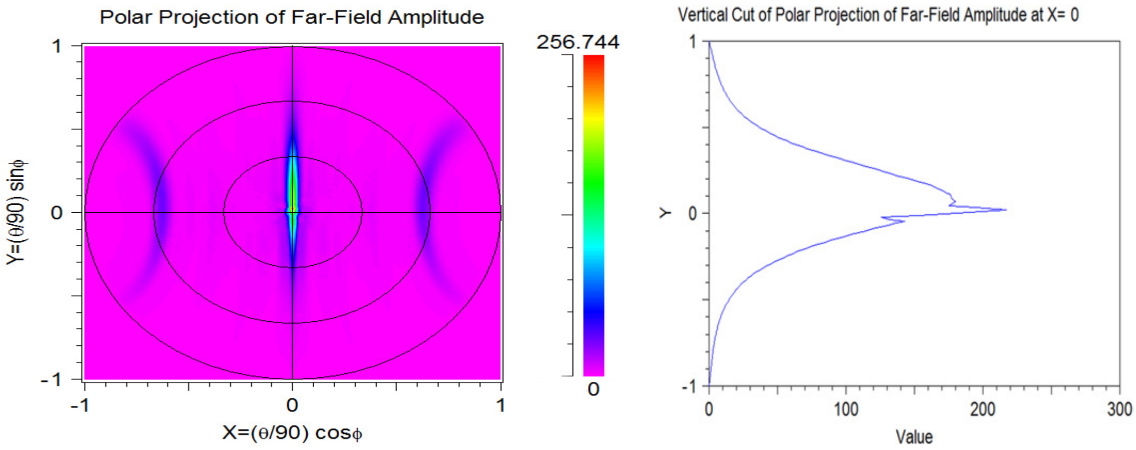

(a) (b)

Figure 3.18: (a) Far-field projection of the output field of tapered ridge waveguide. (b) The vertical cut is used to calculate the FWHM of the far-field leading to the output divergence angle.

After the BPM analysis of the tapered ridge structure, the output field and power can be used to calculate β. As shown in Figure 3.18, since the mode is coupled in the vertical direction to channel waveguides in the slab section, the output would become divergent in the y direction. Hence, by measuring FWHM of the vertical cut through the center of the projected far-field, β can be calculated as follows:

entrance cone angle: $\theta_{in} = 2°$, exit cone angle: $\theta_{out} = 17.8°$

$$< \frac{f_{out}}{f_{in}} >= (\frac{1 \times 50}{40 \times 40}).(\frac{17.8}{2}) = 0.272,$$

$$(\frac{P_{out}}{P_{in}})_{simulated} = 0.70$$

$$\Rightarrow \ \beta = \frac{0.70}{0.272} = 2.572$$

Since $\beta > 1$, the merits of using mode-coupling to achieve high throughput while maintaining the resolution of the spectra in a dispersive spectrometer are clear.

As mentioned earlier, β is dependent on the actual throughput and also the expected flux ratio. Therefore, the parameters which have an effect on β can be divided into two groups. In the first group, throughput of the device should be increased by optimizing the coupling ratio in the design. This was considered in the design phase of the selected structures during which a simple taper and also the inverse taper design were proposed. In the proposed designs, parameters such as length of the taper, waveguide dimensions, and choice of materials in use would affect the throughput power. In the second group, there are certain steps that can be taken to improve the expected flux ratio. Since the output aperture size is fixed due to resolution criteria, the output divergence angle is the only parameter that has to be adjusted. The output divergence is dependent on parameters such as RI difference between the core and cladding area and the modes present at the output facet of the structure. On the other hand, changing the index difference between the core channel waveguides and the surrounding ridge waveguide would result in different coupling ratios. Although the design optimization process is iterative, there are certain steps that can be done individually to ensure proper coupling is made to the desired supermode of the multiple channel waveguide. In the next section, the optimization procedure for achieving the desired far-field through exciting the fundamental supermode of the coupled multiple channel waveguides is explained.

3.4.2 Far-field Optimization Scheme

As shown in the beginning of this chapter, the choice of mode changes the far-field projection. In order to reduce the output divergence, it is best that the multiple modes of the ridge waveguides are coupled into the lower order modes of the channel waveguides. While it is hard to determine which modes are naturally coupled, by use of near-field coupling, a closely coupled set of channel waveguides could form the supermode resembling a low order Gaussian mode. Figure 3.19 illustrates how the number of channel waveguides, their spacing and dimensions can affect the projected far-fields. The simulations were performed on two similar ridge waveguides with different number of channel waveguides in the slab area. Both structures are based on the same inversely tapered couplers which couple the multi-mode input to the channel waveguides over a 3 mm length. It is evident from the structure with 8 channel waveguides that the input is coupled into a lower order supermode showing more resemblance to a simple Gaussian mode. This effectively resulted in a better far-field projection with smaller side lobes. The projected far-field is in fact expected to be smaller with lower order modes as they should have a lower divergence which is confirmed here as well.

As the structure becomes larger and the taper section of the coupler gets longer, it becomes impractical to simulate the whole structure and evaluate the projected far-fields. Instead, an optimization scheme was devised to achieve the closest match to a Gaussian mode for the multiple channel waveguides. Hence, the output channel waveguides cross-section was used in a finite element (FEM) mode solver to find their corresponding modes.

For instance, Figure 3.20 shows the fundamental quasi-TM (qTM) mode of the output cross-section found using the FEM mode solver. In this instance, if all the input modes are coupled into the fundamental mode of the structure in an ideal case, the output far-field would become an elliptical beam without any side lobes. This far-field is similar to the far-field of the fundamental mode of a channel waveguide which is as wide as the sum of the small channels and about the same height. A far-field pattern from the fundamental mode of a channel waveguide being 1 μm high and 16 μm wide was shown in Figure 3.1. The two figures are very similarity and an overlap integral calculation would quantify this resemblance as discussed later in the optimization procedure.

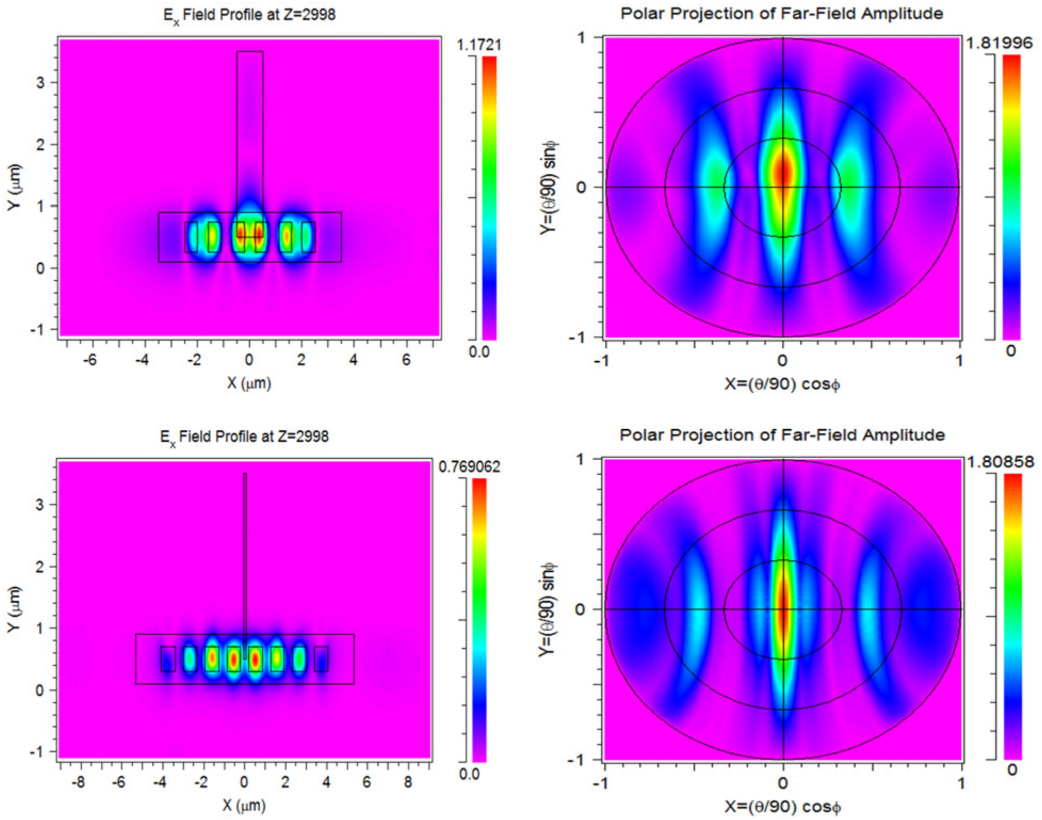

Figure 3.19: Field distribution profiles within two sample cross-sections of coupled channel waveguides shown on the left. The top-left structure has 6 core waveguides while the bottom-left structure posses 8 cores. The right hand side plots their respective far-field patterns.

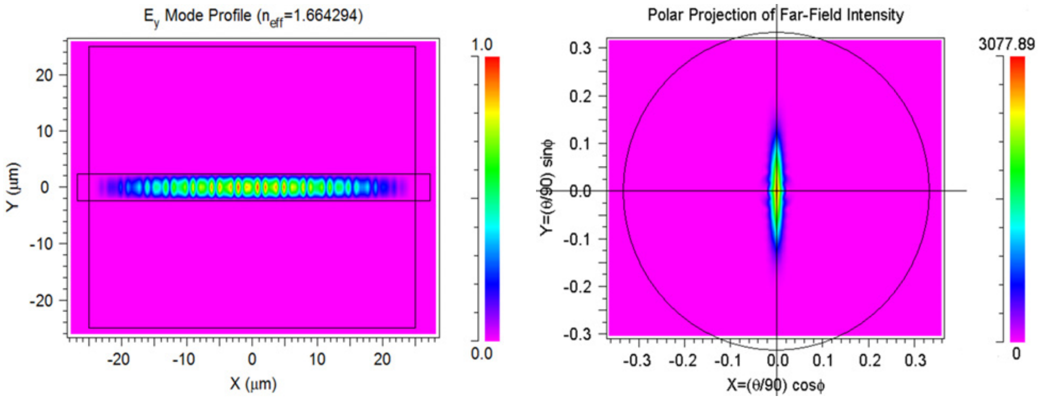

Figure 3.20: Fundamental quasi-TM mode of the output cross-section and its projected far-field.

Therefore, without the need to further calculate the far-fields of the small channel waveguides with varying parameters such as width and gap, the similarity of the calculated supermodes of a number of small channel waveguides can be compared to the modes of a simple wider slab-like waveguide. Figure 3.21 illustrates the first few supermodes of such a structure. It consists of the first quasi-TM and quasi-TE modes along with the second asymmetrical quasi-TM mode. The electric field distribution shows the corresponding field variations for these modes. The modes of a simple channel waveguide as wide as the whole multiple channel waveguides given above are shown in Figure 3.22. The modes are very similar to the modes found in Figure 3.21. In order to produce the far-field close to the far-field of a simply wide channel waveguide, the overlap integral between the two modes of the multiple channel waveguide structure and a simple wide channel waveguide can be used as a figure of merit. By changing the multiple channel waveguides width and gap and finding its resulting fundamental supermode, an overlap integral can measure the modes similarity to a simple wide channel waveguide. The overlap integral discussed in Section 2.2.2 can be used between the two calculated fields to act as a cost function in the optimization procedure.

Figure 3.23(a) plots the calculated overlap integral values between the fundamental supermode of the structure and a fundamental q-TM mode of a simple slab waveguide. Overlap integrals are calculated at discrete points where channel waveguides widths and gaps are varied separately. The highest overlap integral indicates the resemblance of the structures fundamental mode to a Gaussian TM field in a simply wide channel waveguide. As evident from the plot, the region where the channels widths are in the range of $0.8-1\ \mu m$

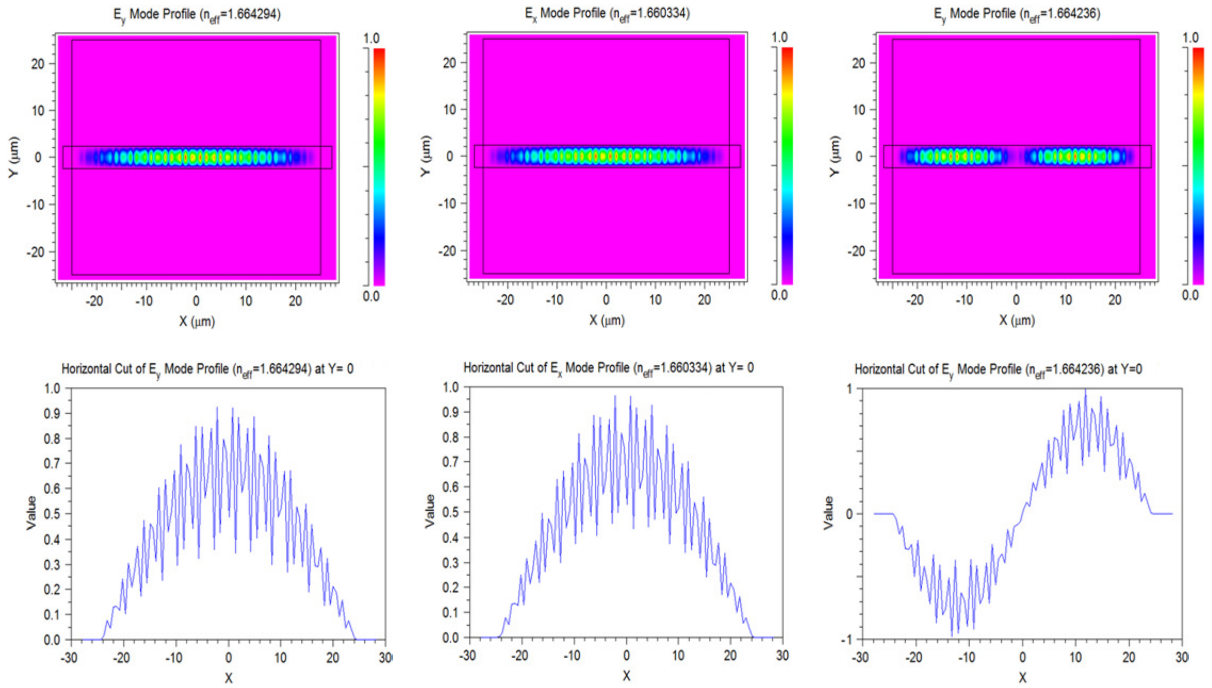

Figure 3.21: The first few supermodes of the small multiple channel waveguides with their respective horizontal cuts through their waveguides showing the varying electric fields.

while the channel gap is only 0.4 μm provides the best resemblance with overlap integral value of above 90%. On the other hand, as plotted in Figure 3.23(b), the corresponding effective modal indices are monitored to make sure porous modes are not considered in these calculations.

As a result of this optimization step, the channel width of 0.8 μm and gap of 0.4 μm was used in the simulations performed for the tapered down ridge structure as well. In fact, Figure 3.17 clearly shows how the final excited supermode of the multiple channel waveguides can be somehow controlled and expected to resemble a simple Gaussian mode. Although, looking at the result of the output far-field projection in Figure 3.18 it can be seen that despite our expectation, there are other higher order modes present as well. Hence, with the above mentioned optimization procedure, one can expect to facilitate coupling into the fundamental supermode but not entirely eliminate the role of higher order modes as the whole structure still remains multi-mode. In the following section, the third type of the proposed series of structures is explained which is also based on the inverse tapered coupling method.

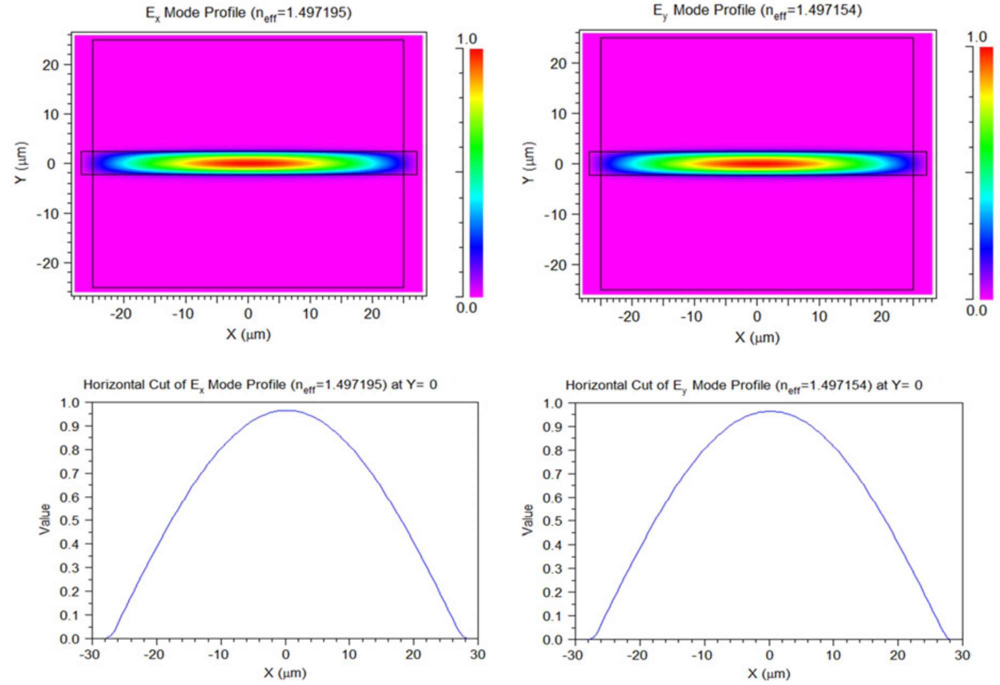

Figure 3.22: Fundamental modes of a simple wide channel waveguide which has a dimension equal to dimension of the whole multiple channel structure.

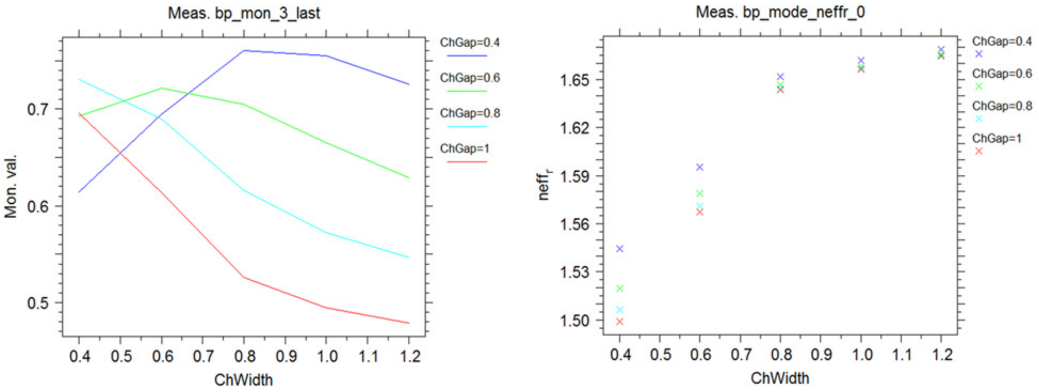

(a) (b)

Figure 3.23: Optimization of the multiple channel waveguide widths and gaps. (a) The overlap integral between the two fields is used as the cost function. (b) The effective modal index for the calculated modes of the multiple channel waveguides are monitored to avoid consideration of porous modes.

3.4.3 Multiple tapered channel waveguides with a wedged fiber

While the multiple tapered channels with the ridge structure seem to be an ideal candidate, there are inherent fabrication issues if the sizes scale up. For instance, assume that the input fiber has a 200 μm core , which has a reasonable light collecting capability in most spectroscopic applications. In order for the fiber modes to couple to the ridge with minimum loss, a 200 μm ridge waveguide should be used. Although the size can be reduced in an optimization step, this number could not be reduced to less than half which is 100 μm when the mode center is placed at the height of the micro-channels. If the height and width is chosen to be 100 μm, in order for the fiber center to be aligned, the ridge has to be 100 μm wide by 50 μm tall on a slab of at least 50 μm thick. This means that for the ridge alone, 50 μm of SiO_2 should be deposited while each micron of deposition would take an hour of equipment time. Hence, this solution does not seem to be scalable as fabrication becomes more complex and extremely costly. On the other hand, if the tapering could be done in both lateral and vertical directions, a better coupling would be achieved. As it was shown previously in Figure 3.17, some of the power is lost through the top and bottom of the channels simply because they are too far away from the center. This situation is expected to get worse when the size is increased further which is due to extreme modal mismatch between a 100 μm fiber core and modes of a 1×100 μm channel waveguide. Aside from the coupling ratio, the ridge waveguide solution still needs a butt-coupling procedure to couple light into the ridge area. Therefore, extra effort has to be taken to make sure alignment tolerances are met and extra insertion losses are avoided.

Another potential structure that can be proposed based on a similar mechanism is using a tapered wedged fiber to couple the light into a slab area with multiple small channel waveguides. As illustrated in Figure 3.24, a multi-mode fiber of chosen core size can be polished using chemical-mechanical polishing (CMP) process. This fiber can then be aligned and flip-chip bonded on top of a slab-like thin film which contains multiple tapered up small channel waveguides. The small channel waveguides operate in the same manner as the small channel waveguides work in the tapered down ridge waveguide. They are also designed and optimized on the same principals explained in previous subsection. Using a tapered fiber is expected to eliminate the need for thick depositions and also solve the problem of scaling up the size of the input fiber to the structure. Once the polished fiber is fixed on the chip the other end can be either spliced or connected to the feed in fiber or light collecting optics.

Figure 3.25 shows the RI profile of the structure cross-section is plotted at two different lengths of 500 μm and 4500 μm. The wedged fiber tapers down along the z direction till reaches a zero width. Therefore in this type of taper, both lateral and vertical directions

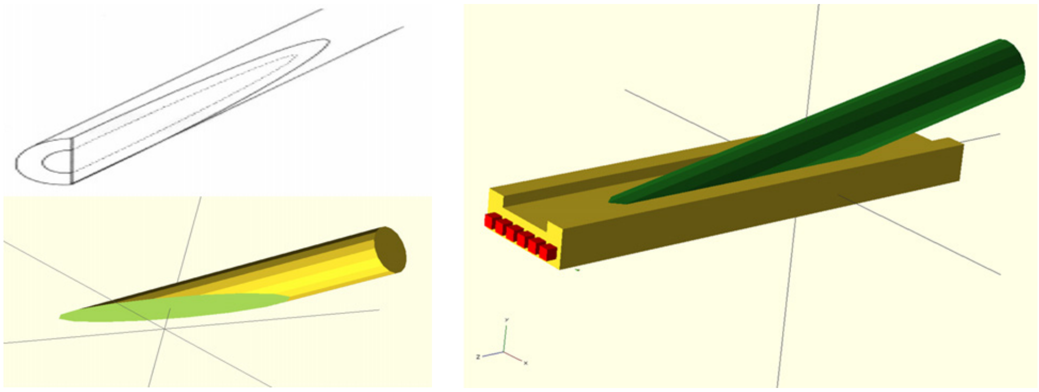

(a) (b)

Figure 3.24: Tapered wedged fiber CAD design sitting on top of tapered up multiple channel waveguides in a slab structure. (a) Polished fiber CAD design making a wedged shape through the core of the fiber (b) Wedged fiber CAD and assembly on top of the multiple channel waveguides.

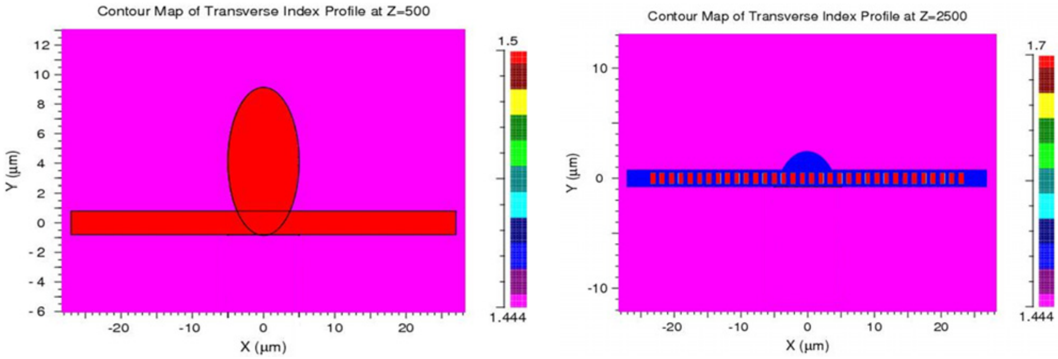

(a) (b)

Figure 3.25: Cross-sectional RI profile of the tapered fiber and the multiple channel waveguides in the slab area. (a) the xy cross-section at $z = 500\ \mu m$ into the taper (b) at $z = 4500\ \mu m$ within the taper region.

are tapered down which can increase the overlap integral of the local fiber mode and the modes of the multiple channel waveguides.This in turn translates into a larger coupling factor between the fiber and the waveguides. Figure 3.26 illustrates the propagating field though this structure. As it can be seen from the xz cut and the yz cut the initial input is

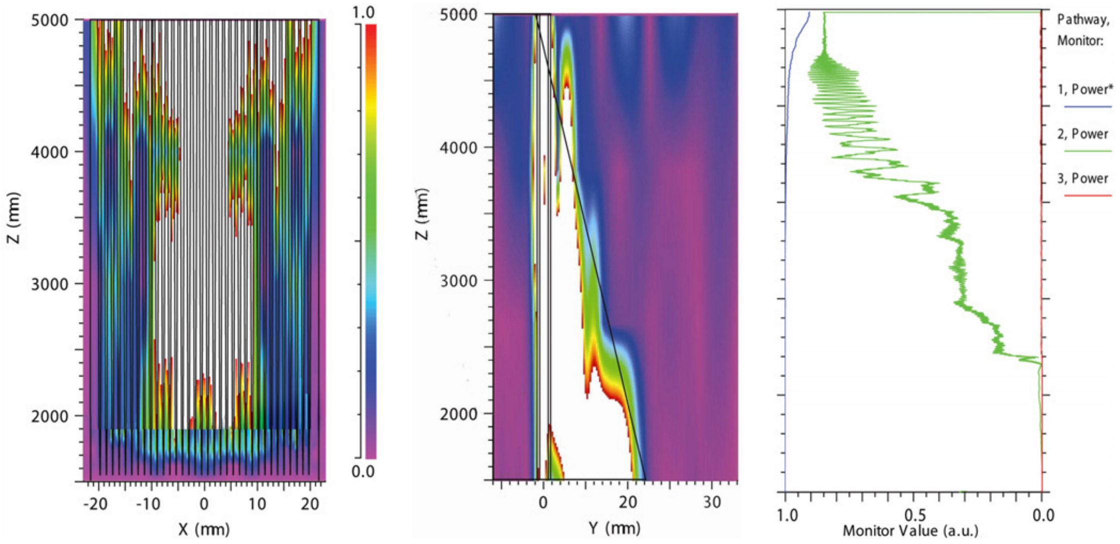

(a) (b) (c)

Figure 3.26: Beam propagation through the wedged fiber on top of tapered up channel waveguides. (a) The xz view from the y-cut through the center. (b) The yz view from the x-cut through the center. (c) Power coupling to the slab area around the channels shown in green.

a multi-mode fiber of diameter 20 μm. The yz cut shows how the vertical tapering would help with increasing the interaction of modes with the tapered up channel waveguides underneath increasing the coupling ratio between the fiber and the small channels to 85%. Figure 3.27 on the other hand illustrates the xy cross-sections of the coupler structure as the initial multi-mode field progresses through the taper. These xy cross-sections are taken at various z distances along the optical propagation path. The modes of the input fiber would couple according to the same mechanism explained for the inverse taper couplers. The small channel waveguides underneath the wedged fiber are similar in design and dimension to the channel waveguides used for the inverse taper structure.

In summary, the underlying inverse taper coupling mechanism performs similarly to the tapered ridge structure. However, it is expected that a wedged fiber would couple light more efficiently due to the simultaneous vertical and horizontal tapering. From the fabrication point of view, it is also believed to be much easier to polish a fiber than deposit few tens of microns of SiO_2 thinfilm without provoking issues such as film stress or uniformity which can lead to additional propagation losses. Therefore, there are inherent benefits in using the polished wedged fiber setting instead of the ridge structure.

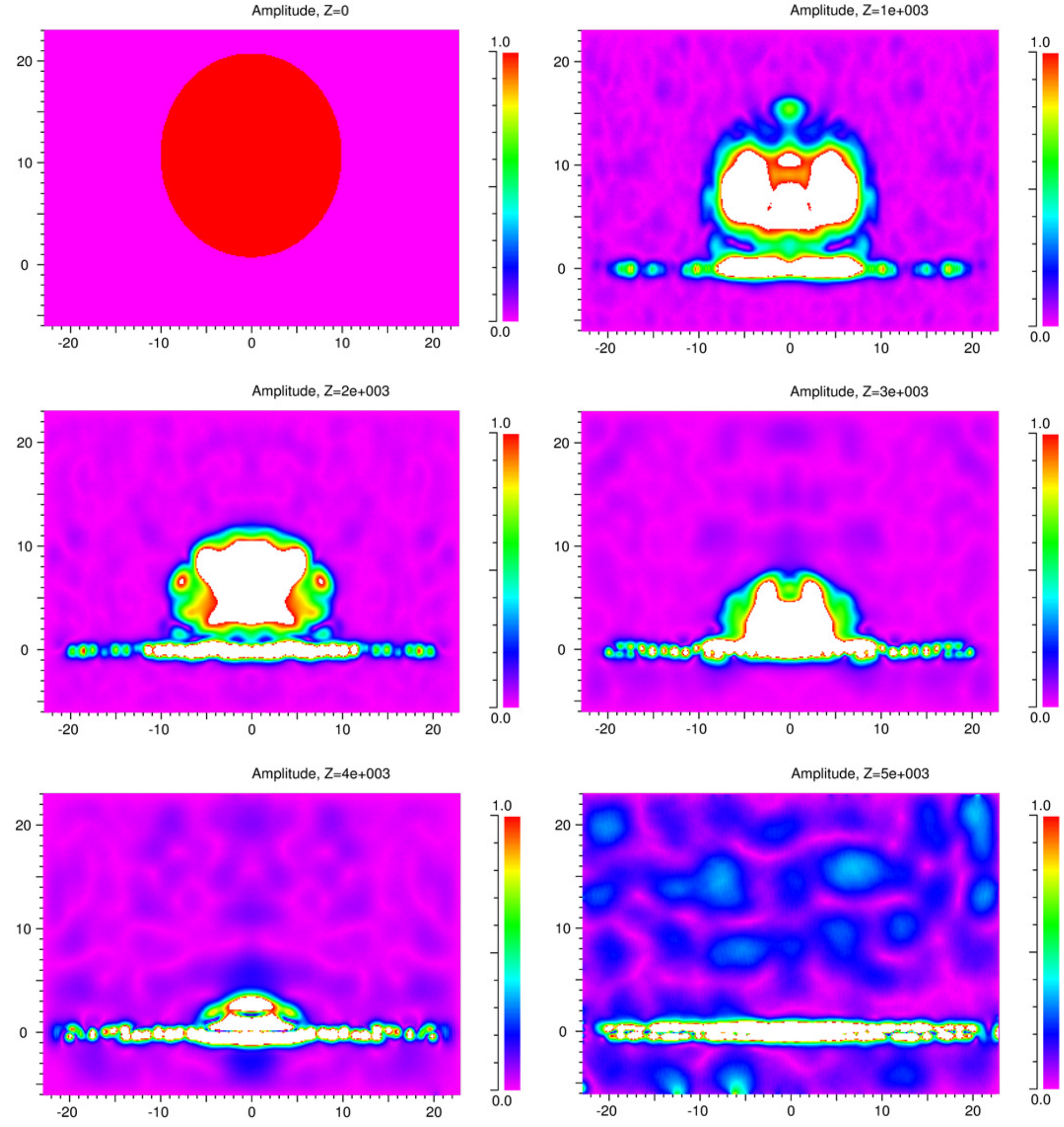

Figure 3.27: xy cross sections of the field propagating through the structure at every 1 mm of propagation in z direction. It starts as a uniform circular field and as it progresses, it will couple into the tapered up channel waveguides.

In order to make a comparison between this structure and the previously proposed designs, it is useful to calculate the β factor as well. As seen in Figure 3.28, the simulated output field from the tapered wedge fiber coupler has an elliptically projected far-field. The spikes in the far-field projection profile come from fluctuations associated with higher order modes present in the output radiation profile and the numerical errors due to BPM errors that are propagated to the far-field using Fraunhofer approximation [18].

To approximate the divergence angle, a Gaussian profile was fit to the respective far-field cross-section which would mainly represent the Gaussian far-field from the fundamental supermode of the structure. Using this approximation, the following calculations can be done:

entrance cone angle: $\theta_{in} = 2°$, exit cone angle: $\theta_{out} = 31.7°$

$$< \frac{f_{out}}{f_{in}} >= (\frac{1.40}{\pi.20^2}).(\frac{31.7}{2}) = 0.504,$$

$$(\frac{P_{out}}{P_{in}})_{simulated} = 0.85$$

$$\Rightarrow \ \beta = \frac{0.85}{0.504} = 1.68$$

Since $\beta > 1$, the performance of the tapered wedged fiber is expected to be superior to

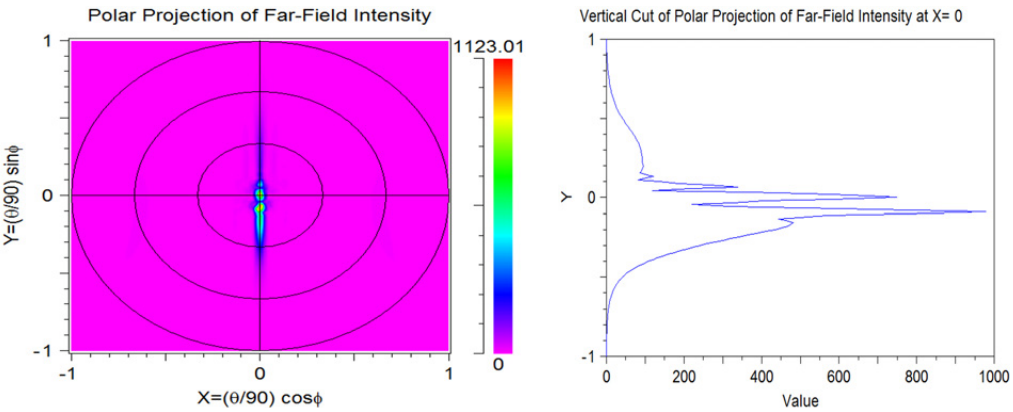

(a) (b)

Figure 3.28: (a) Far-field projection of the output field of wedged fiber coupler. (b) The vertical cut is used to calculate the FWHM of the far-field leading to the output divergence angle.

a slit. This is expected to be a result of simultaneous vertical and horizontal tapering of the wedged fiber which should potentially result in better coupling to the underneath channel waveguide area. While these results are preliminary, optimization steps based on fabrication limitations are needed to enhance the output divergence angle and coupling ratio. Using a combination of different simulation techniques, these various parameters and their influence are studied in the following section.

3.4.4 Optimization of Overall System Throughput

The overall system throughput is a function of parameters such as the coupling factor and end-to-end losses. Physical fabrication limitations such as choice of materials in various layers, design parameters such as dimensions and distances and material losses determine the coupling factor and end-to-end loss figures. In this sub-section, the coupling mechanism is investigated using basic concepts from perturbation theory and numerical 2D and 3D BPM methods, resulting in conclusions on various ways to improve the coupling factor.

Taper couplers have been previously proposed for applications such as integrated laser couplers and mode converters/couplers between the active and passive regions [64,70,71,72]. Within the earlier works, 3D-BPM simulations were used to do an optimal design of taper couplers. However, it is very difficult and time consuming to perform such simulations for the multi-mode wedged fiber setup with large diameters. Due to the round shape of the fiber, a dense grid line is also required for the BPM simulations. In a set of simulations, a 20 nm grid was used to get converging results from the 3D BPM calculations. However with such a dense grid, simulating fibers larger than 20 μm (i.e. 1000^3 grid points) is not possible due to computing memory restrictions. Simulations involving a 20 μm wedged fiber requires time scales on the order of weeks. As discussed earlier, a number of simulations are needed to identify and optimize the coupling mechanism. Some of the physical parameters should also be modified based on fabrication limitations. These parameter are the tapered up channel waveguides length, varying inter-channel gap, the vertical distance between the wedged fiber and the waveguides, the slab cladding area RI, channel waveguide core RI and etc. Performing 3D BPM simulations for such a large number of variations is impractical. Therefore, the 2D counter part model of inverse tapered couplers developed earlier in section 3.4 is used and expanded here with such variations. In order to keep the relationships simple and better understand the coupling mechanism, the 1^{st} waveguide is designed to support only 3 modes and the 2^{nd} waveguide is designed to be single mode. Figure 3.29 shows the inversely coupled waveguide setting along with its xz RI profile. The 1^{st} waveguide is a 5 μm slab waveguide with core RI of 1.45 while the 2^{nd} waveguide has a core RI of 1.46. The 2^{nd} waveguide can be buried in an intermediate cladding layer with a different RI situated on top of a buried oxide buffer layer. A gap would be present between the two guides which in this example is 200 nm. The cladding RI in this example is 1.444 and equals the lower cladding RI. Over the length of $1,000\ \mu m$ the 1^{st} waveguide is tapered down while the 2^{nd} is tapered up.

Using such simplified model of the coupling system helps with understanding of the coupling mechanism and its underlying critical components. Considering the case where the intermediate and lower claddings are the same material and RI of the upper cladding, a set of BPM simulations were performed based on a 2D parameter scan. The results of this simulation set is shown in Figure 3.30. In this set, RI difference between the two waveguide cores were varied between 0 and 0.556 which is shown by the parameter $Delta_1$. These simulations were performed across the wavelength span of $0.4 - 1\ \mu m$ for taper lengths of 1,000, 2,000, 3,000 and 5,000 μm. As the length of the taper increases, the coupled power improves to a max of 93% along a wider wavelength range. As the performance improvement becomes less substantial with increase of the taper length beyond a point, the actual material losses becomes the limiting factor in the actual experiment. Material losses are not considered in these simulations. Therefore there is an optimal zone in terms

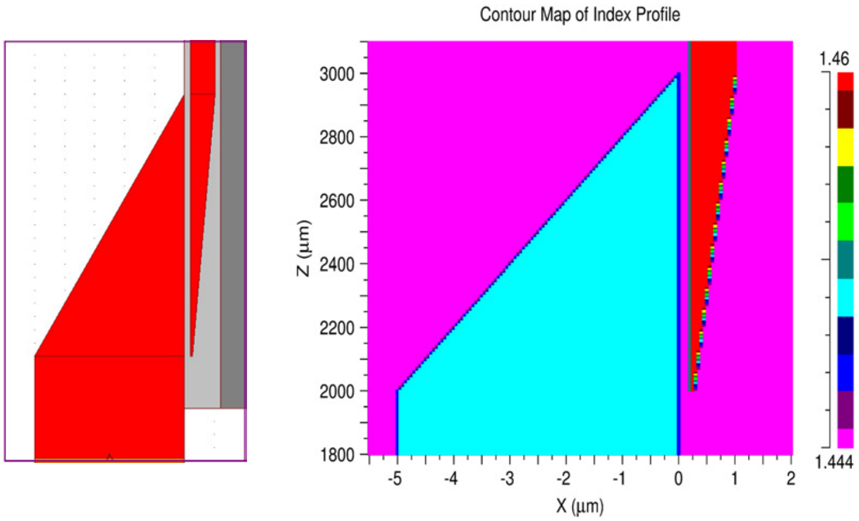

(a) (b)

Figure 3.29: Inversely tapered slab waveguides coupling from a few mode waveguide to a single mode waveguide. (a) 2D CAD model of the inversely tapered waveguides showing the xz profile.(b) xz cut of the waveguides RI profile.

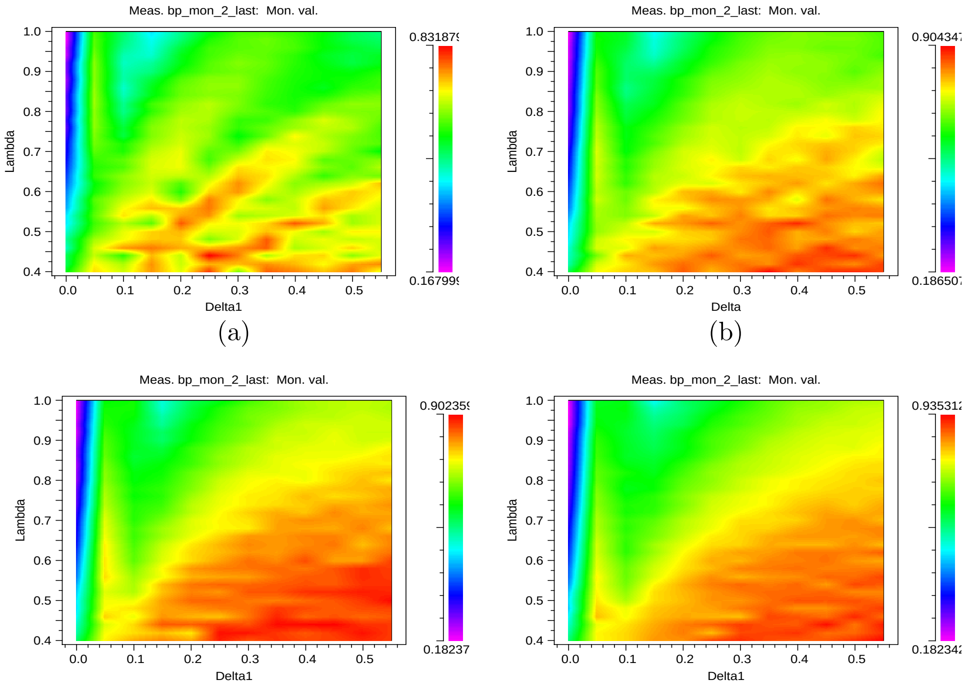

(a) (b) (c) (d)

Figure 3.30: Coupled power values for two dimensional parameter scans of inversely tapered slab waveguides at various taper lengths. (a) taper length of 1000 μm (b) taper length of 2000 μm (c) taper length of 3000 μm (d) taper length of 5000 μm.

of length and coupled power.

The above parametric scan also shows that increasing the 2^{nd} waveguide core RI can increase the coupled power. This is due to ability of the 2^{nd} waveguide to support additional modes to which the power can be coupled from the 1^{st} waveguide in earlier points along the taper. In reality we are limited by the choice of materials which are optically transparent, have high refractive index and can be fabricated. In addition, increasing the 2^{nd} waveguide core RI would make it highly multi-mode and this can affect the final far-field and divergence angles.

Another parameter of importance limiting the final coupled power is the distance between the two inversely tapered waveguides. As the gap between two coupled waveguide increases, the coupled power reduces due to decrease of modal overlap integral of one guide on the other guide. This overlap integral depends on factors such as operation wavelength, λ-dependent RI and modal confinement of each waveguide. As the core waveguides RI in-

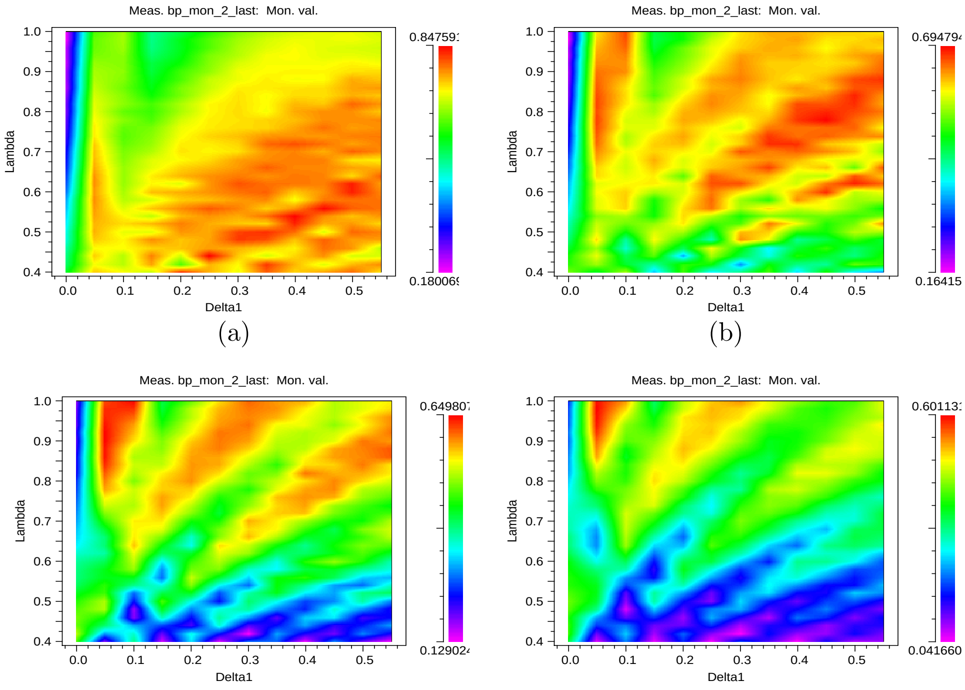

(a) (b) (c) (d)

Figure 3.31: Coupled power values for two dimensional parameter scans of inversely tapered slab waveguides at various gaps between the waveguides. (a) gap of 600 nm (b) gap of 1 μm (c) gap of 1.4 μm (d) gap of 1.8 μm.

creases, the modes become more confined and as a result the coupling becomes harder. On the other hand, larger wavelengths mean that the mode becomes less confined and hence extend further to the neighboring waveguides and increase the coupling factor. These results are illustrated in Figure 3.31 where a 2D parameter scan is done over wavelength (the vertical axes in μm unit) and RI difference between the core of the two inversely tapered waveguides (horizontal axes or δn) for increasing gap between the two. The length of taper was chosen to be $3,000$ μm which was kept constant along with other parameters across the whole experiment. As the gap is increased while other parameters are kept constant, the overall coupled power is reduced. In addition, the higher coupled power values shift towards the longer wavelengths compared with Figure 3.30(c) with similar parameters except for a gap distance of 200 nm.

One other set of target parameters to be investigated are the RI combinations between the lower and intermediate claddings. The intermediate layer is mainly necessary in the fabrication step in which it provides support and planarization for the etched channel waveguides on the chip. Since this has to be another material that is spin coated, it is necessary to consider the effect of RI changes with respect to the common cladding of 1.44 for the wedged fiber. The lower cladding on the other hand provides the necessary buffer layer between the channel waveguides and silicon substrate as the handling wafer in order to avoid leakage of power to the substrate. This layer is SiO_2 which has a RI close to 1.44 depending on the layer growth mechanism. The actual layer arrangement, used materials and details of fabrication are be discussed further in the next chapter, but it would suffice here to investigate the effect of RI changes of these two layers on the overall coupled power. As shown in Figure 3.32, the lower cladding RI changes between 1.39 up to 1.46. In general, the results show better coupling when the lower cladding RI (n_{lc}) value is less than or equal to the wedged fiber cladding RI (n_{wfcl}). In Figure 3.32(d), the overall coupling drops to below 10% when the lower RI is above the wedged fiber cladding RI. On the other hand, the variation of RI difference between the two cores (i.e. δn_1 on the horizontal axes) versus the RI difference between planarizing cladding (n_{cl}) and $n_{wfcl} = 1.44$ (i.e. δn_2). It is clear that the intermediate planarizing layer RI should also be as close as possible to the wedged fiber cladding RI. As this RI becomes lower or higher than 1.44, the optical mode cannot further penetrate into the tapered up waveguide region due to RI mismatch and hence the coupling factor decreases drastically. At the same time, this set of simulations are also following the general trend discussed previously in which the coupled power increases by increasing the core RI of the tapered up waveguide.

So far, the 2D equivalent analysis has provided us a basis to begin the design, and to understand the underlying processes involved in coupling from one waveguide to the other. However, this definition needs to be extended to the 3D case that matches the actual coupling system more closely. Apart from the 3D BPM method which is extremely time and memory consuming, there are numerical methods that involves estimation of coupling factor based on local coupled mode theory and scattering coefficient calculations. In 2005, Xia *et al.* proposed a method to perform monolithic photonic integration using asymmetric twin waveguides (ATG) [64]. The ATG structure uses vertical couplers to couple light between active and passive regions on a single chip. In this paper, the authors proposed an optimization algorithm to design optimal tapers based on local coupled mode theory. Generally two types of tapers, resonant and adiabatic, have been proposed and used in literature. However, all the taper couplers used in ATG are adiabatic. The adiabatic tapers have lower tolerances and are easier to implement. The goal here is to verify the effect of various parameters studied so far based on the 2D model and extend our understanding to 3D models. In this regard, we need to minimize the scattered power into higher order modes other than the fundamental super-mode of the multiple channel waveguides. In this section, a 2D implementation of Xia *et al.* was used to compare with 2D BPM simulation results. Then, this formulation was extended and used in the 3D model to make suggestions

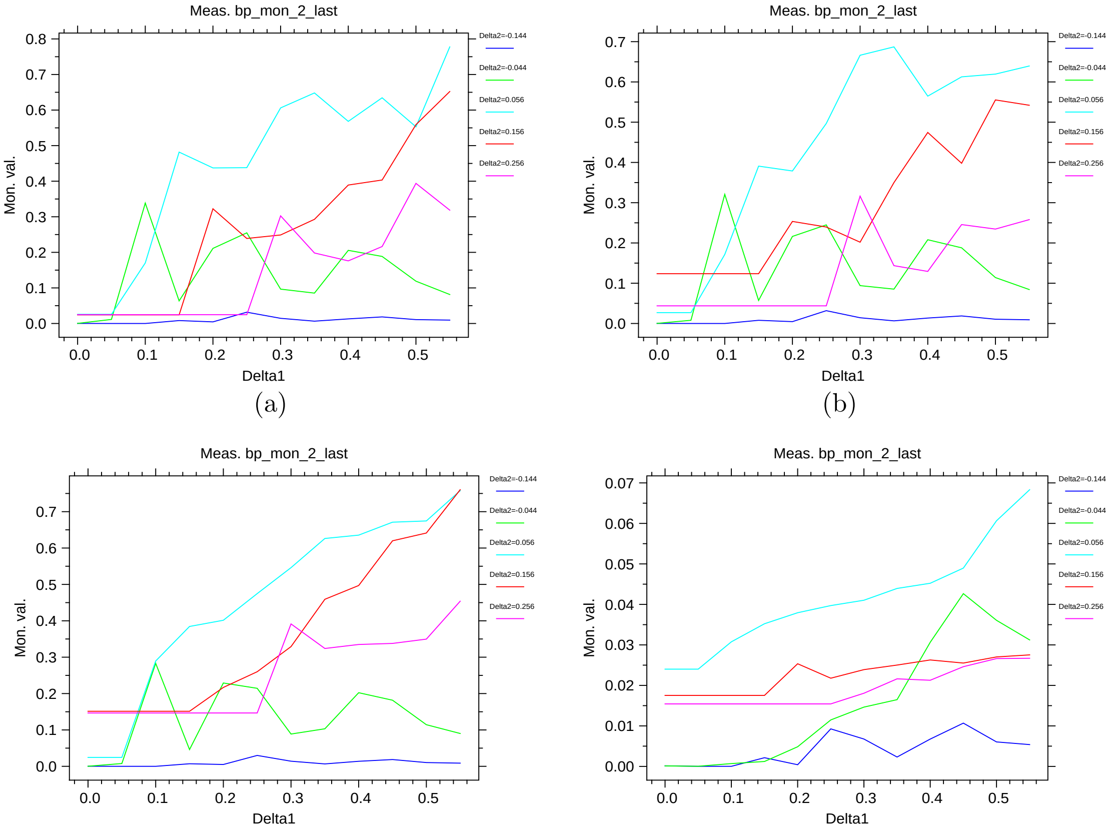

(a) (b) (c) (d)

Figure 3.32: Coupled power values for two dimensional parameter scans of inversely tapered slab waveguides at various lower cladding refractive indices (a) $n_{lowerClad}$ of 1.39 (b) $n_{lowerClad}$ of 1.42 (c) $n_{lowerClad}$ of 1.44 (d) $n_{lowerClad}$ of 1.46.

based on the calculated scattering coefficients. They start from Taylor series expansion of a wave equation for an unperturbed homogeneous medium. Using a Fourier transform to solve the wave equation and applying adiabaticity, the scattering coefficient is [64]:

$$S_{01} = \frac{|d\langle m_1|\varepsilon_r|m_0\rangle|}{dw.\Delta k_z} \tag{3.5}$$

where S represents the scattering coefficient from $|m_1\rangle$ to $|m_0\rangle$ due to perturbation of ε_r at various taper width from W_i to W_f. Therefore, simple mode calculations can be done discretely along the taper to find the effective modal index and the electric field distribution. The scattering coefficient can be calculated based on the overlap integrals. In order to verify this method, the same 2D equivalent model of the inversely tapered

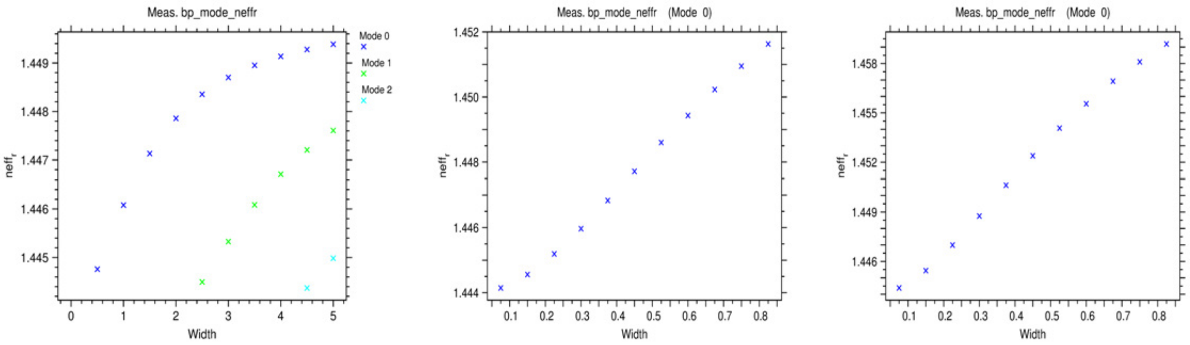

(a) (b) (c)

Figure 3.33: Effective modal indices of the slab waveguides calculated individually at various widths (a) n_{eff} for the first waveguide with core RI of 1.45 (b) n_{eff} for the second waveguide with core RI of 1.46 (c) n_{eff} for the second waveguide when its core RI is increased to 1.47.

waveguide are considered to start. Modal calculation was done and the scattering coefficient was computed from the overlap integrals. The two waveguides are similar to the ones shown in Figure 3.29(a). Using simple mode calculation techniques at each z distance along the taper, the modal effective index can be calculated at each waveguide width for both waveguides independently. Figure 3.33 shows the calculated effective modal index at various widths along the taper length for the two waveguides. The cladding RI is 1.44 and the wider 5 μm waveguide has the core RI of 1.45 that tapers down. The 2^{nd} guide has a core RI of 1.46 for which the effective modal indices are calculated and shown in Figure 3.33(b) as its width narrows down. In order to observe the effect of the 2^{nd} waveguide core RI change on the scattering coefficients and ultimately the coupled power, the effective modal indices where recalculated for the case that the 2^{nd} guide core RI is increased to 1.47. The result is shown in Figure 3.33(c) and in both cases it can be seen that the 2^{nd} guide still remains a single mode waveguide while the 1^{st} waveguide supports up to three modes.

After calculating the effective modal indices along with its corresponding electric field distribution, this data is used in Equation 3.5 to calculate the scattering coefficients. The calculated coefficients are plotted in Figure 3.34 where the horizontal axes shows the 1^{st} waveguide width as it varies from 5 μm to 0. Figure 3.34(a) shows the scattering coefficients for the case where the 2^{nd} waveguide core RI is 1.46 and Figure 3.34(b) shows the scattering coefficients when the 2^{nd} waveguide RI is increased to 1.47. In both cases, the scattering coefficient is calculated between the 3 modes of the 1^{st} waveguide and the fundamental mode of the 2^{nd} waveguide. Comparing the scattering coefficients for the first mode in both cases, it is evident that the scattering peak is broader when the core RI difference between the two waveguides is less, suggesting a slower power coupling mechanism. However, as seen in Figure 3.34(b), the scattering peak is much larger in the case where the RI of the 2^{nd} waveguide is increased to 1.47 indicating a larger power transfer over a smaller length in that case. While Xia *et. al.* propose that the coupling itself is not of resonant nature [64], given enough length it can be shown that the coupling would be resonant in nature for a specific wavelength [73]. This shows that at that width, the scattering intensity is significantly larger than other points along the taper and that the width should vary more slowly around such width to increase the coupled power. In order to verify such conclusions, a 2D BPM simulation was carried for both cases and the results are illustrated in Figure 3.35. Figure 3.35(a) shows the case where the core RI difference between the two waveguides is 0.1 and Figure 3.35(b) shows the case where the RI difference is increased to 0.2. As correctly predicted by the scattering coefficient approach, in the case of Figure 3.35(b), there is a major coupling point around 250 μm of propagation along the length of the taper which corresponds to the width of 3.5 μm. In contrast, Figure 3.35(a) shows a slower power transition to the 2^{nd} waveguide, and the total coupled power is 62% compared to the 72% in Figure 3.35(b).

Based on these simulations, the formulation can be extended and applied to the 3D based wedged fiber coupler. In one sample, to investigate the effect of the intermediate pla-

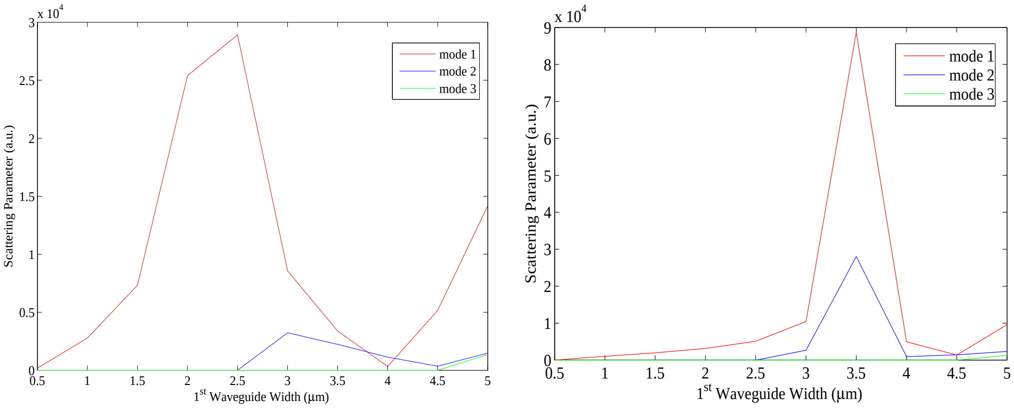

(a) (b)

Figure 3.34: Scattering coefficients between the 1^{st} and the 2^{nd} waveguide calculated along the taper length at discrete taper widths. The 2^{nd} waveguide RI is (a) $n_{core_2} = 1.46$.(b) $n_{core_2} = 1.47$.

narizing cladding, the wedged fiber based inversely coupled taper with length of $1,500\ \mu m$ was used. The modes of the wedged fiber and the tapered up channel waveguides were calculated using a 3D finite element mode solver. In this simulation, the size of the fiber was limited to core diameter of $15\ \mu m$ with core RI of 1.46 and cladding RI of 1.444. To investigate the effect of the planarizing layer RI, the channel waveguide area modes was calculated in two cases of $n_{plan} = 1.5$ and $n_{plan} = 1.7$. The calculated scattering coefficients are plotted in Figure 3.36. For the case that the planarizing layer has lower RI, the scattering coefficients are higher meaning better coupling can occur. This finding agrees with the earlier conclusion in the 2D case which is plotted in Figure 3.32(c). The lower RI of the intermediate planarizing layer and its closeness to the cladding layer of the fiber allows for better modal coupling to the tapered up channel waveguides. The same procedure can be used for optimization of the other parameters based on the limitations we face in the actual fabrication phase. It is clear that in the fabrication step, the choice of thin-film materials and the actual refractive indices vary based on deposition processes. Therefore it is important to understand the effect of such variations and limitations and correlate that to the experimental coupling factors and device performance.

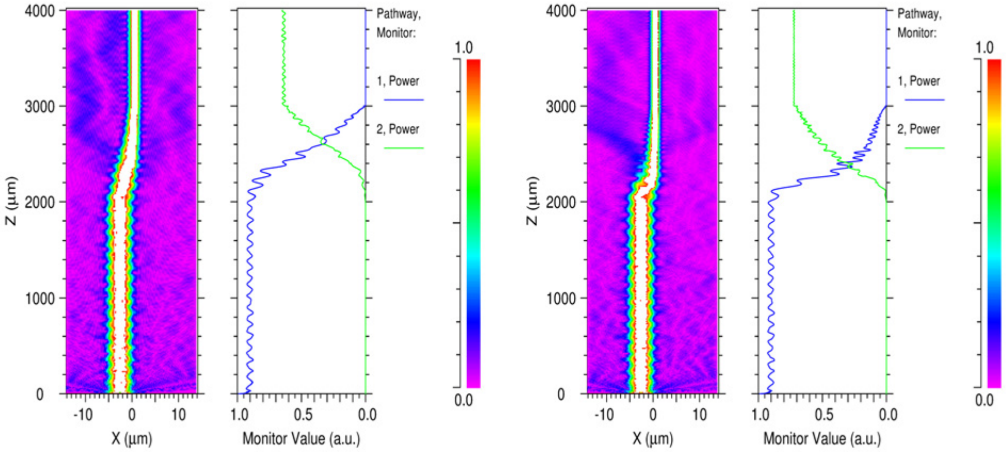

(a)

(b)

Figure 3.35: 2D BPM simulation showing the coupled power between the two waveguides when the core RI between the two waveguides is (a) $\delta n = 0.1$ (b) $\delta n = 0.2$.

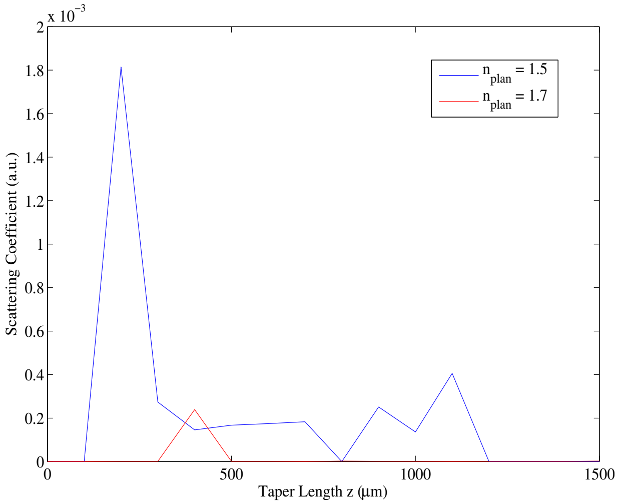

Figure 3.36: Scattering coefficients for 3D model of the inversely tapered wedged fiber coupler. The coefficients calculated for two different planarizing cladding layer RI of 1.5 and 1.7.

3.5 Conclusion

In this chapter, a number of theoretical designs were proposed that use integrated photonic elements to increase the throughput of spectrometers while maintaining their spatial resolution. A figure of merit was defined to measure the performance of design to a conventional slit within a spectrometer. These integrated photonic structures work based on mode coupling principles which are used to improve the performance and figure of merit for the device. Various BPM simulations have been provided to show the mechanism and dynamics of modal coupling within the proposed devices. A number of optimization strategies were employed to increase the output coupling based on physical limitations such as fabrication and material constraints. The fabrication procedures and physical device experiments are performed and explained in detail over the next chapter. Within the system throughput optimization topic, a number of results were obtained to improve the overall system performance for the inversely tapered wedged fiber system. It is worth summarizing those results here:

- In order to increase the coupling ratio, the core RI of the multiple tapered channel waveguides needs to increase as much as possible while maintaining the few mode operation of these waveguides.

- The planarizing cladding layer needs to have a RI as close as possible to the RI of the wedged fiber cladding.
- While the planarizing layer should cover the channel waveguides, it should not be much higher than the height of the waveguides and hence not causing extra spacing between the wedge fiber and the channel waveguides.
- The lower cladding layer that sits below the channel waveguides and the substrate should have a RI lower than the RI of the wedge fiber cladding.
- The length of the taper should be chosen such that around the peak scattering points, the width variation is minimum and hence the power coupling mechanism is as efficient as possible.

Using these summarized points, the fabrication processes can be developed and modified such that it ensures optimal device performance.

Chapter 4

Fabrication of the Proposed Photonic Structures

In this chapter, the fabrication process and experimental results for some of the devices proposed in chapter 3 are provided. To verify this theoretical exploration, the designed taper waveguide is characterized which has been fabricated through a collaboration with IIT Bombay. A similar waveguide structure with the same material platform was developed and fabricated in IIT Bombay for evanescent sensing applications [67]. The fabricated tapers were then cleaved and used in our experimental setup to measure the output beam shape and power for further characterization. Some of these characteristics with their associated shortcomings are provided and discussed. In another attempt to realize the other two proposed structures, the first section of the device, which is the tapered up channel waveguides, were fabricated at the QNC Quantum Nanofab facility at University of Waterloo. For this step, a number of new approaches were developed to produce long and stitch-free waveguides using $Raith^{TWO}$ Electron Beam Lithography (EBL) system. The rest of the developed process details such as etching recipe, cleaving method and bonding methods are discussed consecutively. The fabricated waveguides were then surface-coupled to a wedged fiber and the entire system was checked for its experimental performance.

4.1 Fabrication and characterization of the tapered waveguide

The fabricated waveguides have a taper profile which is given by Equation 3.4. In the final fabricated waveguides, the input width is 50 μm and the output width is between $7-10$ μm due to over exposure effects in the mask in some instances. The samples have a thickness of 50 μm and were built using a photolithography step. The material used for the waveguide is an organic resin solution with trade name of SU-8 [74]. SU-8 has long polymer chains which can produce thin-films with thicknesses up to 100 μm when spin coated. The refractive index of the SU-8 used here is 1.6 which allows it to act as a waveguide core when there is a lower cladding of SiO_2 with refractive index of 1.444 and upper cladding of air. The fabricated waveguides are shown in Figure 4.1. As it can be seen, a slot has been designed on the entrance side of the taper which allows the fiber to be guided towards the entrance of the tapered waveguide.

After dicing the wafer into individual waveguides and cleaving the output facet of the waveguide, the multi-mode fiber was butt-coupled to the input of the taper and the output was positioned in front of a detector (shown in Figure 4.2(a)). The fiber and the detector were located on a 3-axis stage to properly align them on the input and output of the waveguide. Using a moving stage, the fiber can be fixed on the input facet of the waveguide with the help of the overhead microscope to achieve maximum mode coupling as shown in Figure 4.2(b). The input of the taper is a multi-mode fiber field which excites many modes in the highly multi-mode waveguide. The projected far-field of the bare fiber

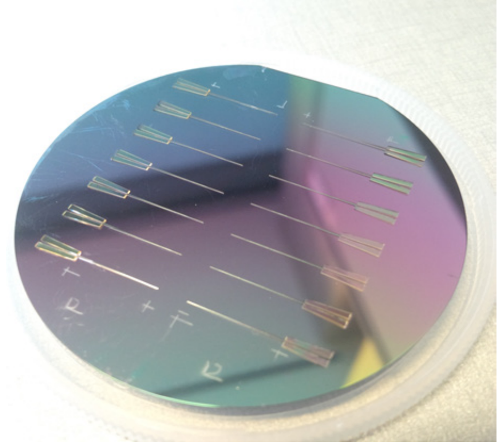

Figure 4.1: Fabricated tapered SU-8 waveguides.

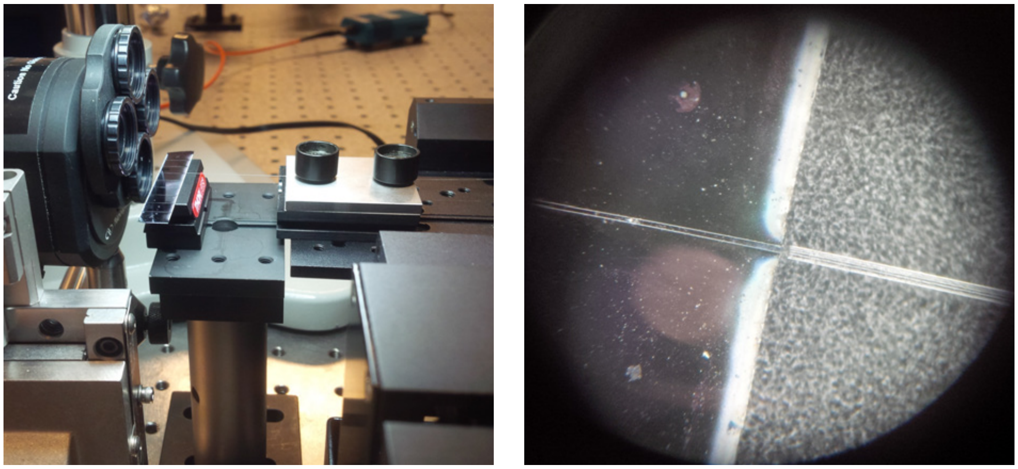

(a) (b)

Figure 4.2: The experimental setup for characterization of the tapered SU-8 waveguide. (a) Side view of the fiber setup on the 6 axis stage, the structure on a fixed stage and the beam profiler on the 3-axis stage. (b) The fiber-waveguide alignment using an overhead microscope.

is shown in Figure 4.3(a) which is used to calculate the divergence angle of the field from the fiber. According to reciprocity theorem, the output of the bare fiber can be considered to be the same as the input to the fiber-waveguide optical system ignoring effects such as losses and non-ideal coupling conditions. The far-field projection of the output facet is also shown in Figure 4.3(b). There is an unwanted reflection visible on the top of the main lobe which is related to cleaving issues. This result verifies the simulated tapered waveguide output projection that is shown in Figure 3.8(b).

One characterization method that can help with understanding output divergence angles is simple imaging of the tapered waveguide output facet. In this test, a high power He:Ne laser was used as the input with a wavelength of 632 *nm*. A 1:1 and 1:5 imagining was performed on the output of the tapered waveguide as shown in Figure 4.4. This illustrates use of a convex lens with focal length of 150 *mm* for $1X$ and $5X$ magnifications for which the resulting images are shown in Figure 4.4(b) and Figure 4.4(c) respectively. In order to better understand these images, lets consider a cross-cut through them in both horizontal and vertical directions. As shown in Figure 4.5, the x and y cuts through the center of the $1X$ image can be used to estimate the output waveguide dimensions using the FWHM measurements on these cuts. The horizontal axes in this image represents the

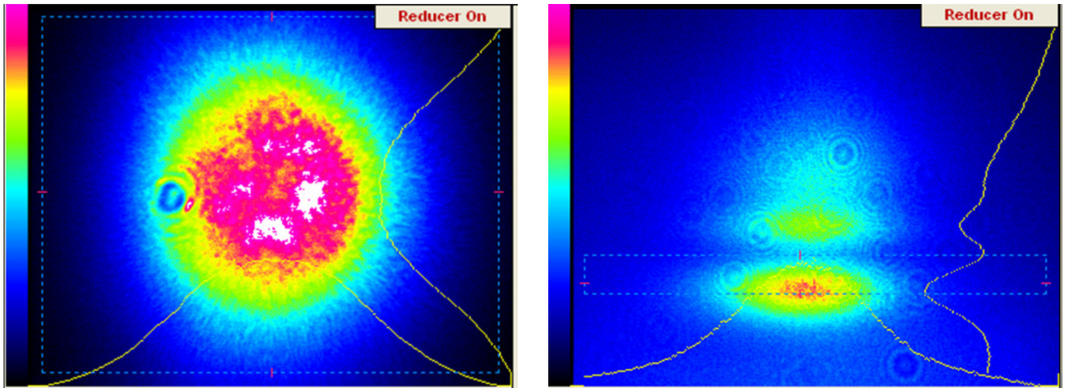

(a) (b)

Figure 4.3: The input and output field of the tapered SU-8 waveguide. (a) Multi-mode input of the waveguide. (b) Output mode of the tapered waveguide.

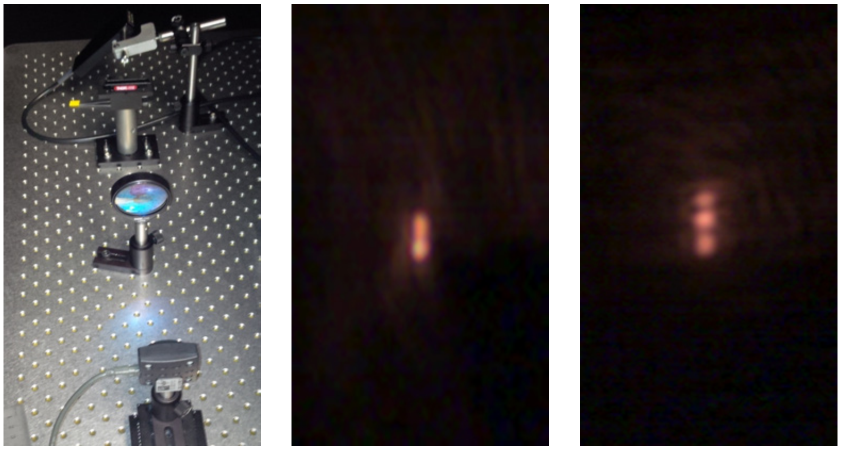

(a) (b) (c)

Figure 4.4: The optical setup for imaging of the waveguide output facet. (a) optical setup. (b) $1X$ magnified output image (c) $5X$ magnified output image.

pixel numbers across the detector and the vertical axes is the intensity in arbitrary units (a.u.). Figure 4.6 also shows similar image profiles for the $5X$ magnified image. Using the pixel counts from the FWHM of each image, and knowing the pixel dimension on the detector to be 5 μm on the detector, the output dimensions are found to be as follows for

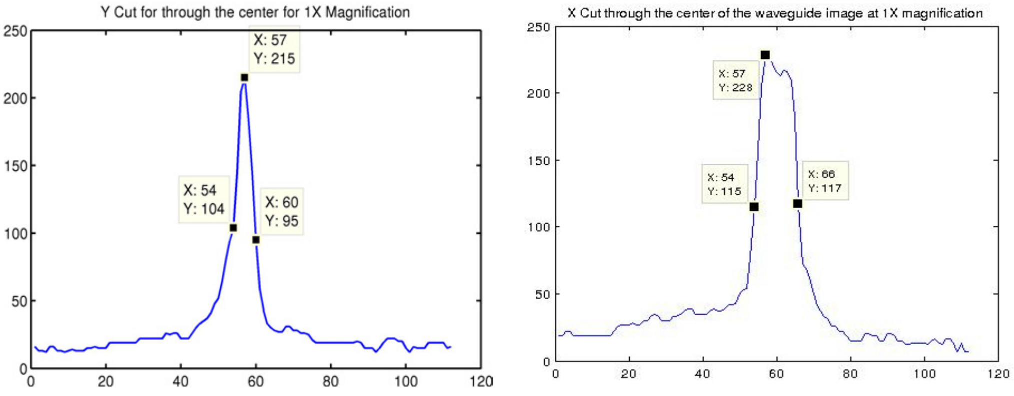

(a) (b)

Figure 4.5: The $1X$ magnified image profile measurements of the SU-8 tapered waveguide through the (a) horizontal cut (b) vertical cut. The horizontal axis is the pixel number on the detector.

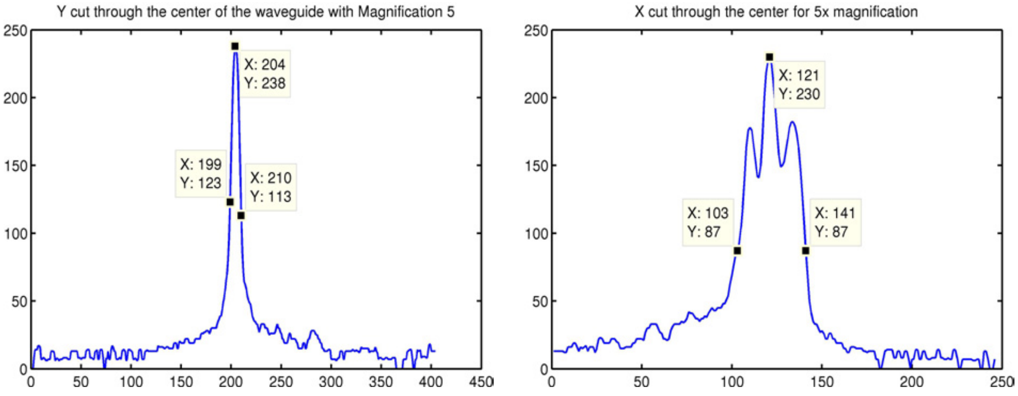

(a) (b)

Figure 4.6: The $5X$ magnified image profile measurements of the SU-8 tapered waveguide through the (a) horizontal cut (b) vertical cut. The horizontal axis is the pixel number on the detector.

each magnification ratio:

- $1X$ magnification: $f = 150\ mm \Rightarrow$ measured magnification: $M = 1.44$
- $5X$ magnification: $f = 150\ mm \Rightarrow$ measured magnification: $M = 5.3$

In the above measured values for the output waveguide dimensions, the $1X$ magnified image shows 180% error in the dispersive direction (i.e. horizontal) and 20% measurement error in the vertical direction. The high error in the horizontal direction is basically due to the limitation of our imaging system in not being able to resolve such a narrow width waveguide. The $5X$ image shows about 47% error in the dispersive direction and 30% measurement error in the vertical direction. Imaging aberrations, the output waveguide small dimensions and the output waveguide high NA are root causes of such imaging errors. In order to do a more accurate measurement, a much faster lens is needed which also does not introduce further aberrations. Despite the apparent errors in the current imaging system, it becomes clear that if the throughput of the system is high enough (i.e. waveguide losses are minimized); the proposed mechanism could prove to be much more efficient than a slit while maintaining a certain resolution. In the above experiment for instance, the dispersive width of the output image still remains below 20 μm which would result in a sufficient resolution in most spectroscopy applications. Due to coupling losses and material absorption in SU-8 waveguide, the output power measured on the waveguide output facet is much less than the anticipated power output from the simulations. Therefore, proper investigation of the β value is not feasible.

4.2 Limitations of tapered SU-8 fabrication and characterization

There are a number of factors which result in high losses in SU-8 based waveguides which are discussed further in this section. The initially fabricated taper waveguides included a V-groove guide which was embedded to assist with coupling of fiber end to the taper. However, since the input fiber had core and cladding diameter of 125 μm, there was inherent vertical misalignment when the fiber was inserted in the V-groove. Therefore in one attempt, the fiber cladding was etched in a buffered Hydrofluoric acid (HF) with 5:1 ratio for approximately 7 hours to reduce the cladding radius to 55 μm. While this attempt resolved the vertical misalignment issue to a great extent, the fiber became extremely brittle, hence handling and cleaving issues became a major drawback. From two sets of etched fibers in groups of 6, only one survived through the cleaving and initial alignment procedure but was eventually damaged during the actual experiment. To overcome this misalignment issue in another attempt, the start of the tapered waveguide was cleaved instead along with the output of the waveguide to produce a uniform input and output facet for modal coupling.

The traditional cleaving mechanism using the OEG MR 200 diamond scriber did not

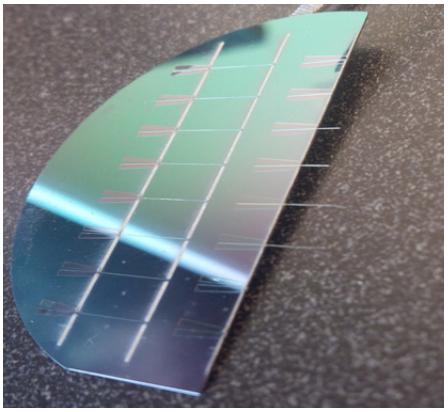

Figure 4.7: Cleaving the fabricated SU-8 tapered waveguides and demonstration of peeling issues of high aspect ratio SU-8 structures.

prove useful since the SU-8 waveguides peeled off and had rough end faces. This was mainly due to the force exerted on the waveguides by the diamond tip as well as lack of adhesion to the substrate due to high aspect ratio structure of the waveguide. Therefore, a laser cleave method was chosen instead. Cleaving was done using an LPKF laser prototyping system at University of Waterloo Rapid Prototyping Lab [75]. Due to the heat generated by the laser system, the SU-8 polymer melted during the cleave process; therefore a dashed line method was used to avoid direct contact of laser beam with the waveguide itself. As a result, when trying to break the silicon wafer, the waveguides broke rather randomly at different locations. Figure 4.7 illustrates this issue in one of the processed samples which indicates the low yield of these types of waveguides. In another attempt, the cleaving was done using a DISCO dicing saw DAD3240 [76]. In order to minimize adverse effects of the dicing blade on the SU-8 layer, the dicing was done from the back of the wafer leaving about $50 - 100$ μm of substrate material behind just underneath the SU-8 film. While this improved the cleaving to an extent, the SU-8 waveguides still showed mechanical instability especially on the narrow side of the taper due to the higher aspect ratio.

Other issues causing high material losses in SU-8 waveguides are defects and non-uniformities of the SU-8 thin-film itself. Since SU-8 is a polymer solution which is spin-coated on the wafer, there are more defects present in the thin-film compared to plasma enhanced chemical vapor deposition (PECVD) methods. Figure 4.8 shows typical defects on different sets of 50 μm thick fabricated waveguides. As the thickness of the waveguides is increased, these non-uniformities and defects become more severe. Figure 4.9 illustrates how the defects become more severe when the waveguide thickness is increased to 200 μm.

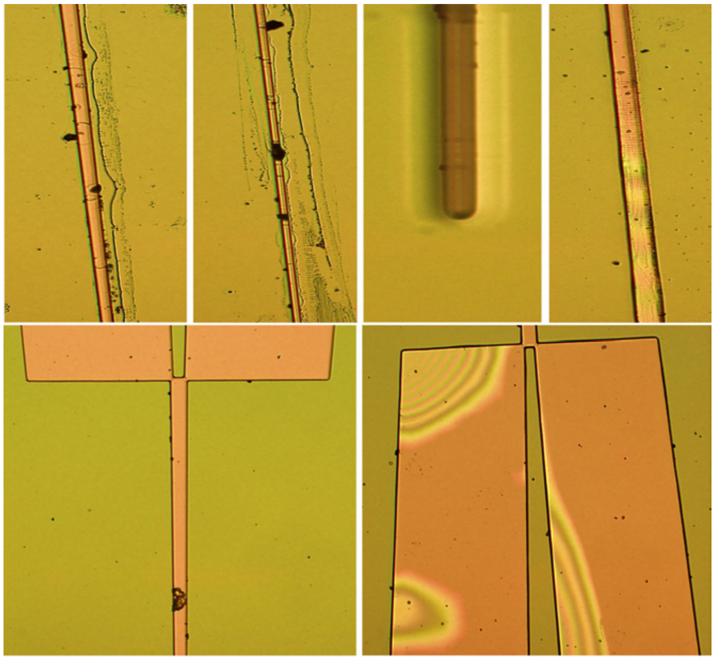

Figure 4.8: Illustration of material defects in a number of different fabricated waveguides with thickness of 50 μm.

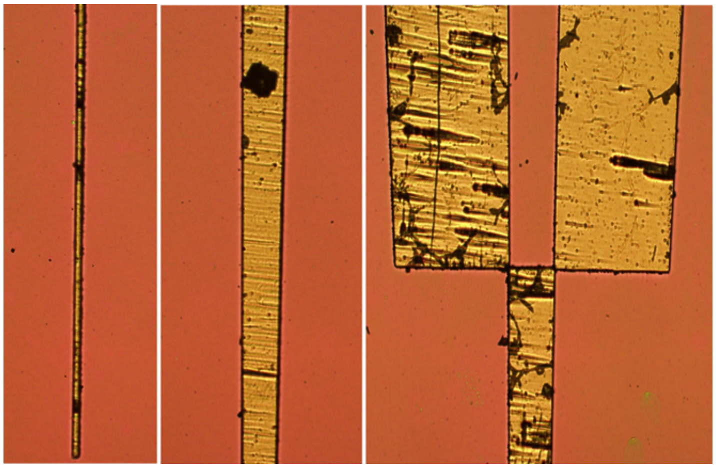

Figure 4.9: Illustration of material defects in a number of different fabricated waveguides with thickness of 200 μm. The dark spots in the waveguides determine non-uniformities in the SU-8 thin-film.

4.3 Fabrication of Tapered Channel Waveguides

The second set of proposed devices use an inversely tapered waveguide design. This design and the fabrication procedures are discussed further in the remainder of the chapter. The inverse tapered coupler system consists of two parts: the multiple channel waveguide section which is a number of coupled smaller channel waveguides that are tapered up and have a higher refractive index and the tapered down section which could be either a tapered down ridge waveguide or a wedged fiber. The first step to constructing the coupler system is to fabricate the tapered up channel waveguides. Tapers are very common in photonic integrated circuits (PICs). They are long aspect ratio patterns where the width is changed adiabatically along the length to reduce mode shape conversion losses. Most of the fabrication processes were developed and modified for construction of such a coupler system. Figure 4.10 shows a flowchart of the fabrication and coupling system preparation steps needed to construct a functional chip for further testing and characterization.

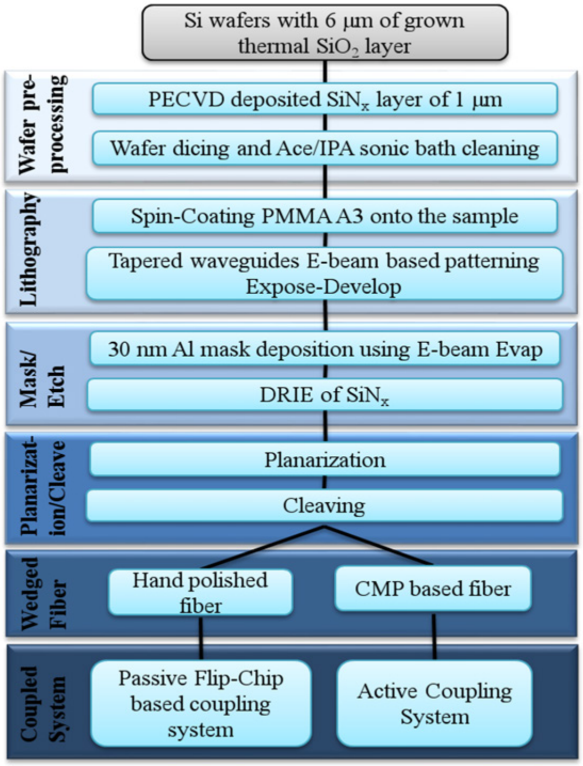

Figure 4.10: Coupler system fabrication and sample preparation stages.

In the first step, 1 μm of Silicon Nitride (SiN_x) film was deposited on a Si wafer that contained 6 μm of wet thermal SiO_2 as the lower cladding layer. The SiN_x was deposited using an Oxford Instruments PECVD tool. First, the wafer table was pre-heated to $330°C$ degrees and the chamber was pumped down to 10^{-6} $Torr$. Then the deposition was done using 30 standard cubic centimeters per minute (sccm) units of SiH_4 and 900 sccm of N_2 at high frequency plasma generation power of 40 $Watts$. At the deposition rate of about 19 nm/min, it took about 52 minutes to deposit 1 μm of SiN_x.

Then, using EBL and an experimental writing scheme called the fixed beam moving stage method (FBMS), the small tapered waveguides were written on top of a photoresist.

Due to the small widths and narrow features of the tapers, conventional optical lithography methods are not suitable for fabrication of such structures. On the other hand, due to the long length of the tapers, conventional EBL writing methods would not be cost-effective either. Using conventional beam deflection methods with a fixed stage, writing fields of a few hundred microns would result in extremely long writing times as well as large stitching errors. Therefore, a new all-FBMS method scheme was developed to write such large number of waveguides effectively and efficiently. The proposed writing method is discussed further in the following subsection.

4.3.1 Electron Beam Lithography using Fixed Beam Moving Stage

Electron beam lithography is a widely-used machine in research, nanofabrication and small volume prototyping. Writing large area patterns with sizes of a few millimeters and submicron features is a challenging task. Especially with smaller EBL machines where acceleration voltage is less than 30 kV, the field of view is limited and the pattern generators are slow. Directly writing such patterns requires write times on the order of several hours, during which the pattern is split into many different write fields. The final pattern is written through a combination of beam deflections within a write field and stage movements between different write fields. One major concern is stitching error which is the error introduced into the patterned structure due to random stage movement errors between various write fields. In order to increase the precision of positioning, a settling time is needed every time the stage moves from one write field to the other which results in longer writing times [77].

Four types of stitching error have been observed; shift error, field distortion, field rotation and deflector scale error [77,78]. These errors can either be stochastic or systematic in nature. The scaling error and field rotation errors are due to column settings and misalignment. They would be replicated along the different write field borders and hence they are systematic. Field distortion error is also a systematic error that is negligible if the gun column is well-maintained. Shift error on the other hand is stochastic and is due to stage movement errors. Therefore, it varies between different write fields. Shift error is dependent on the stage laser interferometer accuracy and is prone to thermal drifts and etc on top of mechanical jitter. In order to increase the precision of positioning, a settling time is needed every time the stage moves from one write field to the other. Within this time, vibrations in the displaced stage dampen, and the stages location can be checked through the feedback mechanisms within the stage controller. While the additional time for stage settlement adds to the overall writing time, there is no guarantee that the movement error is minimized due to its stochastic nature. Certain optimization procedures are needed to speed up the writing while maintaining high resolution high and few patterning errors [77, 78, 79].

For small 100 μm writing fields, the random stage movement error can be as high as 40 nm for Raith 150^{TWO} tool. In writing long structures, this error can propagate through the structure resulting in even greater errors in some cases. Such errors can completely misplace the output waveguide and cause misalignment issues. In addition, the errors between different write fields would contribute to propagation loss as optical modes within the waveguides perceive such misplacement as additional surface roughness. Gnan *et al.* performed a more detailed study of losses due to stitching imperfections using a numerical method to compute optical throughput [80]. Vivien *et al.* estimated the losses to be as high as 0.1 dB/cm for stitching error of 1 nm in optical waveguides [81]. Therefore, stitch-free structures are essential to realizing low-loss optical waveguides. Various methods have been proposed in literature to reduce the stitching errors:

- Multiple exposures at reduced doses with shifted boundaries [82]
- Using different writing field sizes
- Using adjusted zoom factors (based on Raith recommendations)
- Using fixed-beam moving stage (FBMS) mode [82, 83]

Amongst the proposed methods, FBMS method is an interesting way to overcome the issues related to stage settling time and stitching errors. In FBMS mode, the beam spot is deflected with high frequency in a circular fashion while the stage is moved. This would result in a fixed width circular pattern to be swept through the sample. This mechanism was first introduced by Kahl in 2005 [83]. Use of such a method is explained in a series of articles by Raith for various integrated optical waveguide applications [83, 84, 85].

FBMS is mostly effective for long and fixed width patterns such as long waveguides. FBMS has been proposed for a number of applications such as long X-Ray channel waveguides [86], optical waveguide couplers [87] and large area zone plates [88]. One other widely used photonic structure after fixed length waveguides is a taper. In photonic integrated circuits, tapers help with mode shape and size conversion, coupling into and out of the photonic circuits. In addition, tapers can be used for evanescent field sensing applications and atom trapping [83].

Since tapers cause perturbations in the propagating modes due to their width variations, additional losses occur from surface roughness due to stitching errors especially when the waveguide becomes narrow. Therefore, it is increasingly important to minimize stitching and roughness artifacts on their sidewalls especially on their narrower side where the evanescent field is larger. Piaszenski *et al.* proposed a combination of bulk stitching mode with FBMS borders to create long and smooth tapered waveguides [85]. While this is an interesting method to produce smooth tapers, it does not provide any writing time advantage compared to bulk stitching mode. In addition, in cases where the other end of the taper is extremely narrow (about $50 - 200$ nm), fixing stitching errors with the FBMS border path is not trivial.

In the following sections, three different methods of writing long tapers are proposed and investigated using only FBMS mode. These methods were implemented and tested to the degree that Raith hardware allowed. The results show the advantages and challenges of a full FBMS mode implementation for such large structures. Here, first we discuss the differences of FBMS mode patterning compared with the bulk stitching mode. Then an all FBMS writing mode is proposed and discussed with three different methods.

FBMS Mode versus Stitch-Field Method

When writing in FBMS mode, an area is described by a series of circles along a designated path. While the stage moves along a defined path at a calculated speed, the beam is deflected in a circular fashion to apply a constant dose over the designed line width (illustrated in Figure 4.11). Since the stage is moved in a continuous fashion, there is no stage settling time overhead while writing such long patterns. A patterning time simulation was done using Raith software for a single 200 nm fixed width waveguide where the conventional stitch field mode and FBMS modes were compared. The length of this waveguide was varied between 100 nm up to 3 mm. Table 4.1 shows the patterning time break out for these various lengths. It is evident from the table that as the number of stitch fields increases, the stage movement jitter and settling times scale linearly and become compatible

Length (mm)	**Number of Stitch Fields**	**Dwell Times (S)**	**Settling Time (S)**	**Stage Move Time (S)**	**Stage Settling Time (S)**
0.10	0.00	0.56	0.50	0.60	0.00
0.20	1.00	1.11	1.00	1.20	0.50
0.30	2.00	1.67	1.50	1.80	1.00
0.40	3.00	2.22	2.00	2.40	1.50
0.60	5.00	3.33	2.99	3.60	2.50
0.80	7.00	4.45	3.99	4.80	3.50
1.00	9.00	5.56	5.00	6.00	4.50
1.25	11.50	6.95	6.25	7.80	6.00
1.50	14.00	8.34	7.50	9.00	7.00
1.75	16.50	9.37	8.74	10.80	8.50
2.00	19.00	11.11	9.99	12.00	9.50
2.25	21.50	12.50	11.25	13.80	11.00
2.50	24.00	13.89	12.49	15.00	12.00
2.75	26.50	15.28	13.74	16.80	13.50
3.00	29.00	16.67	14.98	18.00	14.50

Table 4.1: Simulated dwell and settling times associated with regular stitched patterning method when width of waveguide is 200 *nm*.

to the actual beam dwell times. The settling time itself is an additional time needed to allow for the beam to become stationary at a new location, stabilizing the column deflection unit. Also, the total amount of settling time for a given pattern consists of the number of stops needed per write-field times the settling time per stop. The optimum settling time varies according to the movement. The longer the movement, the longer the settling time. A small movement, within a structure, will require a shorter settling time than a movement over a longer distance between structures or stitch fields. While the settling time and stage settling time are needed to ensure accuracy of beam movement, they are a great overhead to the actual beam dwell time which results in writing the pattern. A comparison of the total patterning time for the bulk stitching mode and FBMS mode are plotted in Figure 4.12. It is clear that in FBMS mode, the total patterning time at very long lengths becomes almost 1/3 of the time needed to write the same pattern using regular stitch field mode. This is mainly due to elimination of the overhead wait time for stage movement and settling. Therefore, FBMS mode not only removes the stitching error artifact from a long straight pattern, it also speeds up the patterning procedure by eliminating the stage settling time requirements.

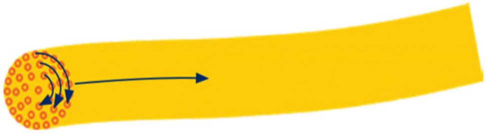

Figure 4.11: FBMS beam construction for lines of fixed width [85].

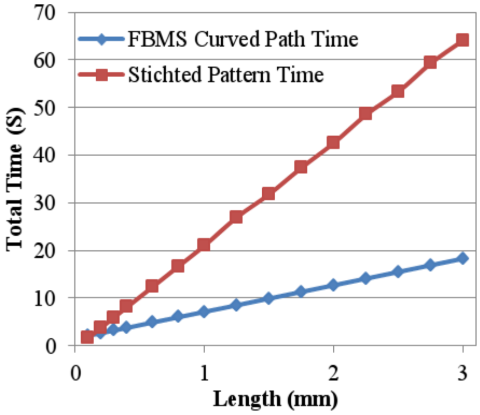

Figure 4.12: Comparison of total patterning time for the regular stitch-field patterning and FBMS mode patterning.

While FBMS patterning mode is quite advantageous for very long fixed width waveguides, the fixed beam width becomes a limitation for long variable width structures such as tapers. The combined bulk stitching and FBMS mode method proposed by Piaszenski *et al.* would minimize the stitching error losses by smoothing the rough edges of the taper through two FBMS trace-retrace paths [85]. However, the proposed solution does not provide any advantage from the patterning time standpoint. In fact, the total time is more than the bulk stitch mode due to having additional FBMS-based patterns. In the following section, an all-FBMS mode is used to write such long tapers in an efficient manner.

Novel FBMS Modes of Writing

FBMS is one way to lithographically taper structures by writing the edges of the tapers with a smaller beam spot and the interior with standard stitch-field method with a larger write field. While this reduces the stitching errors, it actually adds to the time required for patterning. This method was unsuitable for long tapered waveguides. In order to address this problem, new methods for FBMS writing were developed and investigated which do not use stitch field patterns. These new methods are described below and are being currently considered for commercialization by Raith.

All these methods use some unique features of FBMS mode. As discussed previously, an FBMS area mode consists of a path over which the stage and sample are moved and the beam is deflected to make a uniform exposure over an area. The beam deflection pattern can either be defined individually by the operator, or it can be set automatically by the system in circle generator mode. The circle generator mode generates a circle-symmetric pattern with an outer diameter that corresponds to the width of the FBMS area element. The inner part of the pattern is written using a series of smaller concentric circle-symmetric patterns, giving a constant dose profile perpendicular to the stage movement (as shown in Figure 4.11). Since the pattern is circle-symmetric, FBMS path elements with a constant width can be written in any writing direction of the FBMS path with this mode.

The line width can be specified directly in the GDSII design by the curved path parameter Width. If the parameter "*max. structure width*" (w_{max}) has a non-zero value, the pattern generator creates a high speed circulating beam, while the stage is moving along a path. Due to the high speed of the beam in its circular movement, (single pixel addressing is typically done in the 0.5 to 1 MHz regime) the resulting beam dose profile is almost stationary relative to the moving stage. The "*calculation width*" (w_{cal}) is entered by the user and corresponds to the minimum (narrowest) possible expected width of the FBMS path. The w_{cal} is used to calculate the area dosage or stage speed (v_{stage}) based on the beam current (I_{beam}) according to the following relationship:

$$Area\ Dose = \frac{I_{beam}}{v_{stage} \times w_{cal}} \tag{4.1}$$

As the formula shows, to have a constant area dose, the thinnest lines are written at the highest stage speeds. The w_{cal} is simply a reference value, which relates width, stage speed and dose. Stage speed will be automatically adjusted by the software depending on the pattern being written. For example, if the user has entered a calculation width of 1 μm, but the current waveguide width is 2 μm, the stage speed used for the 2 μm pattern will be half the reference stage speed [89]. Now depending on the fracturing mechanism used and the minimum calculation width set, one can achieve various long patterns completely in FBMS mode.

Method A: Sleeving FBMS Mode

Similar to the way painters adjust their pen size with their minimum feathers, this methods simply changes the pen size for different feature widths. This is achieved by dynamically changing the w_{cal} to produce larger circular patterns along the length of the waveguide as the stage is moving. This concept can be visualized in Figure 4.11. However, this type of beam width variation cannot be currently implemented in Raith systems due to hardware limitation in the Raith controller cards. In order to overcome the variable width limitations, a number of fracturing methods were developed and used. The methods fracture a long taper structure into a number of FBMS paths with different widths. One approach is to use a sleeving mechanism where different widths represent different pen types. This fracturing method is illustrated in Figure 4.13 for different widths along the taper. A coarse pen is used for the majority of bulk area and smaller width features are patterned using fine pens. For better flexibility in performing the patterning, these different pen sizes are broken down into 4 different layers. As it can be seen in Figure 4.13 (a), the taper is broken into discrete stair like steps of 100 nm and 150 nm. Figure 4.13 (b) and (c) show the incremental 50 nm step like change from $150-250$ nm respectively. Figure 4.13 (d) shows how 100 of these tapers that are 1.6 mm long each are broken down into 4 different layers where there are four pen sized of $25, 50, 100$ and 200 nm. The dosage is selected to be higher for the narrower pens.

This type of fracturing was done automatically through a program developed using RAITH-GDS II Matlab toolbox written by NanoFab facility at University of Alberta [90]. As the number of steps are increased and finer pen sizes are chosen, we would have a better chance to fabricate a smoother tapered waveguide. The choice of minimum pen size is dependent on a number of factors such as the acceleration voltage, beam current (consequently depends on aperture size), dosage as well as the stage speed. According to Equation 4.1 for a constant dose, as the width decreases, the stage has to speed up in order to avoid over exposure. However, accurate deflection of the beam in FBMS mode is only possible for stage speeds up to 1 mm/sec. Therefore, the minimum waveguide width or pen size is limited. In case of acceleration voltage of 25 kV and aperture size of 10 μm, the minimum w_{cal} is 25 nm for area doses of 330 $\mu C/cm^2$ in order for the stage speed to be less than 1 mm/sec. While this method was thought to enhance the writing time and accuracy using all FBMS paths, the actual patterning tests did not show much improvements in terms of accuracy. The patterning was done by grouping different pen types into separate layers and writing each layer based on a specific pen size width with certain stage speed. Going back and forth over such large number of discrete FBMS paths and separate layers, causes the same stage drift errors as writing in the conventional stitch field method. In a test fabrication run, 180 nm layer of *PMMA A3* photoresist was exposed and developed using the above mentioned FBMS mode of writing. Figure 4.14 shows the patterned taper after the lift-off process. It is evident that the fracturing method using different pen sizes introduces random offset errors in the sleeve locations on the sample due to thermal drifts

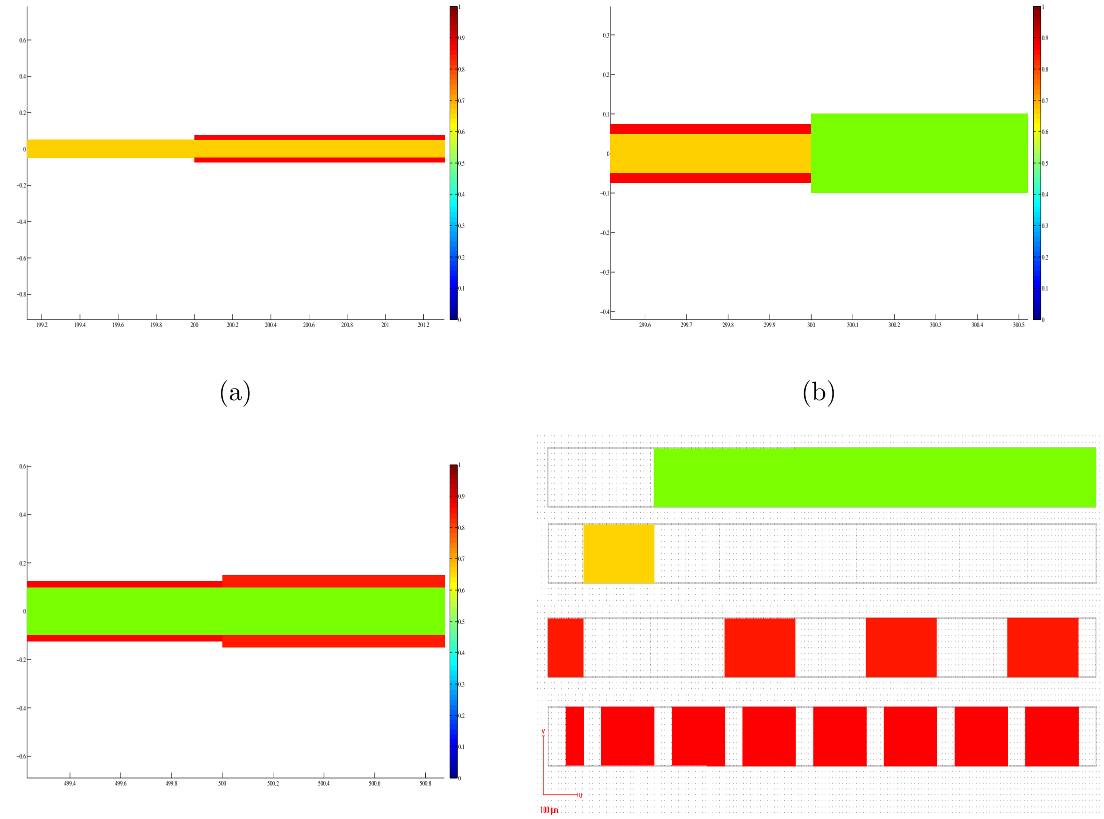

(a) (b) (c) (d)

Figure 4.13: The sleeve type fracturing method where the junction between discrete waveguide widths are steps between (a) $100 - 150\ nm$ (b) $150 - 200\ nm$ (c) $200 - 250\ nm$ (d) associating layers with various pens and fracturing along the $1.6\ mm$ long taper pattern.

in the stage controller. Therefore, the number of discrete FBMS paths should be minimized in general.

Method B: Longitudinal FBMS-Path Fracturing Mode

The second method developed and tested is based on longitudinal fracturing of an FBMS pattern based on a predefined FBMS path width. In this method, a taper is broken down to finite width increments and the width of the FBMS path is kept the same in that subsection. The w_{cal} is chosen to be equal to these increments and each subsection can

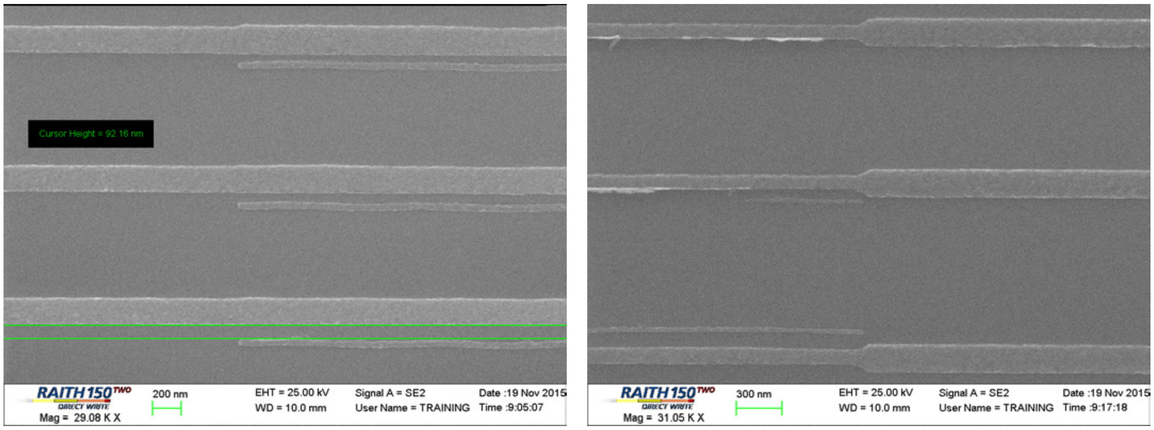

(a) (b)

Figure 4.14: Exposed and developed patterns using the sleeve method with different pre-defined FBMS pattern widths.

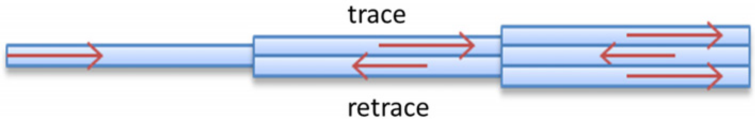

Figure 4.15: Longitudinal fracturing of FBMS paths.

be written by an integer multiple of these smaller FBMS paths. This way the number of discrete FBMS paths can be minimized as compared to the previous approach. Figure 4.15 illustrates a fracturing mechanism where the different widths of the taper are divided into a series of trace and re-trace FBMS paths along the stage movement direction. The tests showed that due to the limited circular pattern generator frequency, a FBMS path with a width of 100 nm and w_{cal} of 50 nm would be patterned for the same time as a FBMS path of width 100 nm and w_{cal} of 100 nm. While in the former case trace and retrace has to be done to pattern a 100 nm width waveguide with fixed widths of 50 nm, in the latter case, the 100 nm width waveguide has to be written at half the stage speed for the same area dosage. A sample taper waveguide was patterned, exposed and developed using the same procedure. Figure 4.16 shows the scanning electron microscopy (SEM) images of this patterning procedure for widths from 50 nm to 100 nm. The additional roughness seen in the SEM is due to the lift-off process similar to the previous fabrication steps performed for the sleeve method. As it can be seen, the stage is moving in a more predictable manner in this case and the resolution at the step junctions is somewhat limited to the

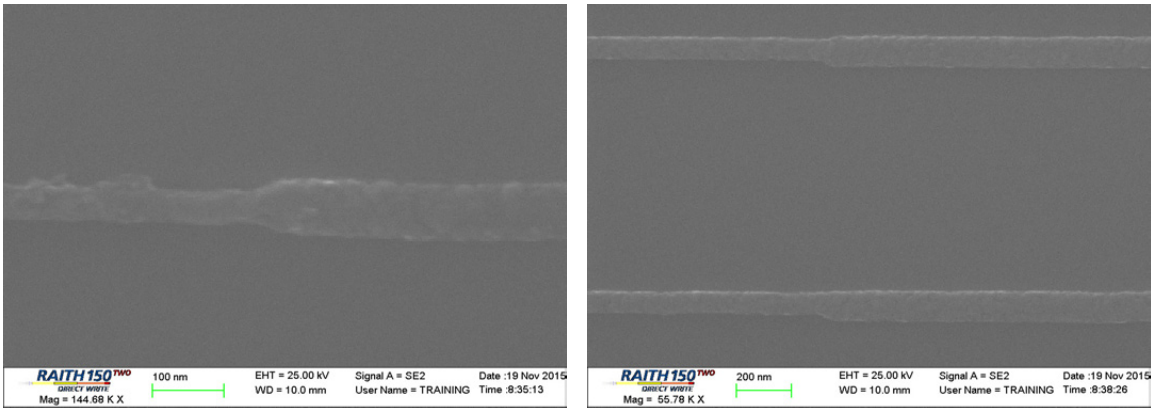

(a)

(b)

Figure 4.16: SEM images of the fabricated waveguides using the longitudinal fracturing method. The SEMs show the junction of going from 50 nm to 100 nm and the fixed width trace and re-trace writing mechanism.

minimum w_{cal} chosen. In this case, if the minimum w_{cal}, aperture size and acceleration voltage are chosen in a manner that the stage can run at its maximum peak velocity of 1 mm/sec, the FBMS patterning can be performed at the maximum optimized speed for the desired resolution. While the proposed method provides better accuracy and faster write times, due to the discrete nature of the FBMS paths the structure is still prone to stage shift errors. Depending on the number of steps, finite automatic alignments in between each FBMS path can be implemented to correct for stage movement errors. For example, in a series of the tapered structures that were fabricated and tested, there are about 15 steps with widths varying between $0 - 800$ nm in steps of 50 nm. Performing 3-point automatic alignments is quite manageable by using the alignment scripts as defined through Raith operation manuals for each of the 15 steps. Thus, this method can be a promising fabrication mechanism for a wide number of photonic structures.

Method C: Custom Beam Deflection Using FBMS Modes

In order to further increase the accuracy and speed of writing, a third method was used to implement an all-FBMS patterning method using principles of modulated beam moving stage (MBMS) technology developed by Raith. Custom beam deflection patterns are used along with stage movement to create the tapered structure. In this case also, the taper is broken into a piecewise step function with various widths. Then for each section of the

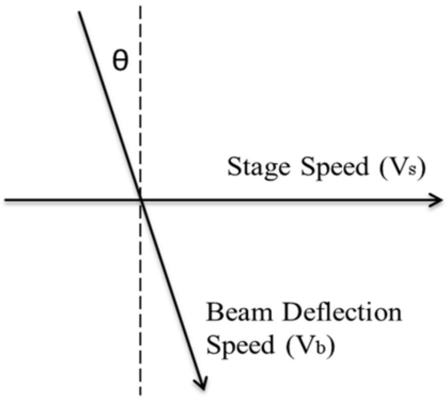

Figure 4.17: The relationship between the stage speed and beam speed vectors.

step, a custom beam deflection pattern is calculated and the beam movement is dictated to the beam column controller by means of an ASCII file. Having the stage speed calculated for each of these step functions, the patterning is done by moving the stage while the beam is deflected in a certain pattern. Consider the case where the desired pattern is a series of straight lines that need to be written over a long distance. If these lines are perpendicular to the stage path, Riath is capable of writing these lines while the stage is moving. Raith software can use a "user-defined" pattern with an FBMS path to control how the beam is deflected. The user-defined pattern consists of a series of single pixel dots with a specific order. To expose a line perpendicular to stage movement, the beam can be deflected with an angle as shown in Figure 4.17. As the stage moves from the left to right, the beam also deflects with an angle such that the horizontal element of beam deflection speed vector (v_b) stays equal to the stage movement speed (v_s). This way it would appear as if the beam is following a straight perpendicular line with respect to the stage movement.

Based on the beam current, step size of the custom deflection pattern and the single pixel line dose for a predetermined line width, one can use the patterning calculator to calculate the beam speed. The beam speed determines the line cycle times based on the line height. From the line cycle time, the FBMS dwell time can be calculated as the ratio of the line cycle time divided by the number of dots within a predefined pattern width. The stage speed can be calculated by dividing the value of line pitch distance by line cycle time. To achieve a uniform waveguide pattern, the line pitch should be chosen such that the area is uniformly exposed. This can be achieved by performing standard dose tests which are a common practice. In essence the patterns are written as a series of periodic lines in which the pitch is very small. Figure 4.18 illustrates this concept where the beam

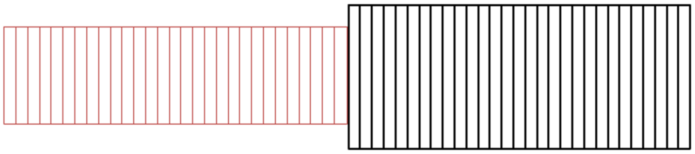

Figure 4.18: Writing FBMS structure by means of customized beam deflections while the stage moves.

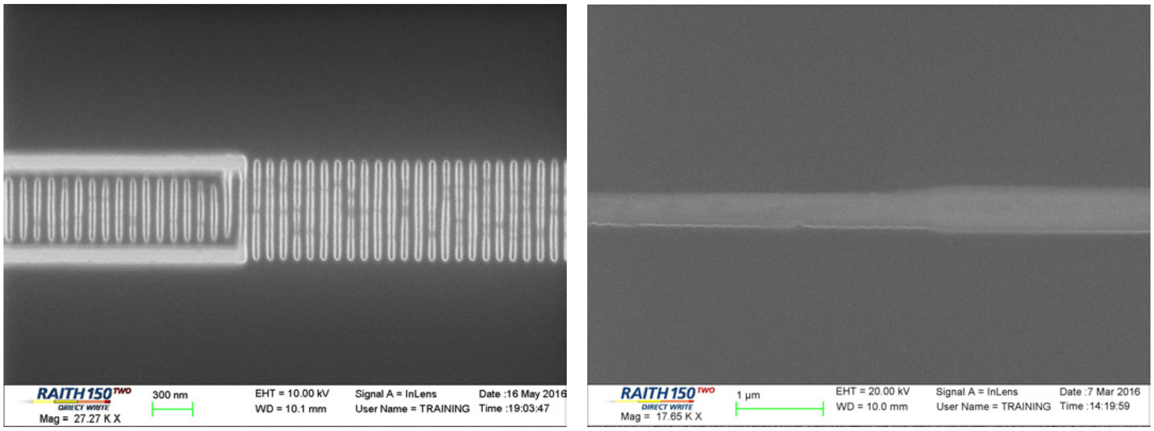

(a)

(b)

Figure 4.19: SEM images of the fabricated waveguides using the custom deflection pattern method. (a) Microscope image shows how lines can be patterned using custom beam movement. (b) The SEMs show the junction of two variable steps patterned using the custom beam deflection.

is deflected up and down along discrete lines as the stage moves. In order to achieve such patterning, the dosing, beam speed and stage speeds need to be accurately calculated and controlled. In order to pattern a complete taper in step wise fashion, each group of the lines with certain widths need to be deflected with an angle based on the beam deflection speed and stage speed respectively. The deflection angle can be written as:

$$\theta = sin^{-1}(v_s/v_b) \tag{4.2}$$

and the deflection points can be rotated around their center based on the calculated θ value. Then, each of the taper sections can be written with its respective deflection pattern and the column parameters can be adjusted through user scripts in real-time. In order to make the taper walls smoother, two FBMS paths can be written on both sides of the taper to remove the step like artifact of this writing procedure. Hence, not only the write time is optimized in this manner and an all-FBMS patterning is done, the side walls are also smoothed out by means of the two additional FBMS paths added to the taper in form of a trace and re-trace. Figure 4.19(a) illustrates a fabricated sample which was patterned using single pixel lines of 100 nm and pitch of 100 nm. The step is between lines of 600 nm and 800 nm wide from left to right of the figure. Two FBMS paths are also surrounding the 600 nm section which would smooth the step transition to reduce optical losses. If the pitch of the lines is reduced and proper dosing is done, a smooth and uniform exposure can be done which is shown in Figure 4.19(b). This is a completely new method of writing tapers that was develop during the course of this project. While these three FBMS patterning modes were proposed and tested, method B was used in the majority of the experiments due to its easy implementation scheme and relative taper reproduction accuracy. In the following sub-sections, other aspects of the fabrication steps are explored and explained in detail along with final post fabrication steps to prepare the device for in lab testing and characterization.

4.3.2 SiN_x Etching

The waveguide cores in the proposed structure consist of 1 μm deep SiN_x structures which are placed close to each other with gaps in the order of 200 nm. The smallest feature size for each waveguide is width of 50 nm requiring an aspect ratio of 10:1. To our best knowledge, such aspect ratios and packing densities have not been achieved in SiN_x. Hence, a new etching recipe had to be developed to realize the proposed structures.

After the initial exposure and development of the *PMMA A3* photoresist, a 30 nm Aluminum mask layer was deposited on the sample using an IntelVac E-beam evaporator at high vacuum levels of about 10^{-6} *Torr*. Then, the photoresist was removed in a lift-off process using PG-remover, leaving behind the tapered Aluminum ridges as mask layer to be used for the etching step. An etching recipe was developed for the SiN_x using an inductively coupled plasma (ICP) ion etching machine, which provides stable and uniform etching with good vertical sidewalls. The etching tool used is an Oxford Plasmalab ICP380 III-V and metal etcher. Table 4.2 show a few tests that were done to characterize and fine tune the etch recipe. The wafer was back cooled to $15°C$ and the chamber was pumped down to 10 $mTorr$.

A precursor mixture of SF_6/C_4F_8 was used in the high density ICP reactor to perform a deep reactive ion etching (DRIE) of SiN_x film. Based on a modified Bosch process, continuous passivation procedure was used instead of pulses of individual etching and passivation

Etch	SF_6 **(sccm)**	C_4F_8 **(sccm)**	**ICP Power (W)**	**Forward Bias Power (W)**	**Etch Rate (nm/min)**
A	22	38	1200	50	14.5
B	37	23	1200	50	35.3
C	32	28	1200	20	18.2

Table 4.2: Optimizing etching parameters and settings for the developed SiN_x etch recipe.

cycles. The SF_6 contributes to the plasma fluorine radicals that perform the etching step and C_4F_8 contributes to the fluorocarbon passivation layers [91]. Ion-assisted anisotropy is a result of physical and chemical removal processes. The presence of molecules with unsaturated species causes polymerization, which tends to adhere to the material being etched. Ion bombardment causes these polymers to desorb, and exposes the horizontal surfaces to the etchant radicals while the vertical surfaces face less or no bombardment and therefore the horizontal etching can be minimized or completely blocked.

Figure 4.20 shows microscope and SEM images associated with the different etching parameters given above. Etch recipe A has a larger passivating gas flow and further inspection of the waveguides showed signs of notching and significant lateral etching. The etching rate is also very low and as evident from Figure 4.20(a), there are signs of pitting on the substrate. In order to reduce the lateral etching and improve on the etch rate, the etching gas (SF_6) flow rate was increased and the other parameters kept the same. Figure 4.20(b) shows that the pitted substrate has worsen and this is mainly due to excessive etchant radicals and high forward bias power. Therefore, the etching gas flow rate and the forward bias was decreased. Performing a few test resulted in an optimal ratio between the forward bias power, SF_6 flow rate and the C_4F_8 passivation gas flow rate as outlined in Table 4.2.Figure 4.20(c) shows the top view SEM of a sample etched using the 3^{rd} etching parameters. In a test procedure to measure the lateral etching and its effect of various widths along the taper, a series of waveguides with discrete widths were patterned and etched. Figure 4.21 shows a top view and an angled SEM image of these waveguides for waveguides of widths 800, 600, 400, 200, 100 and 50 nm.

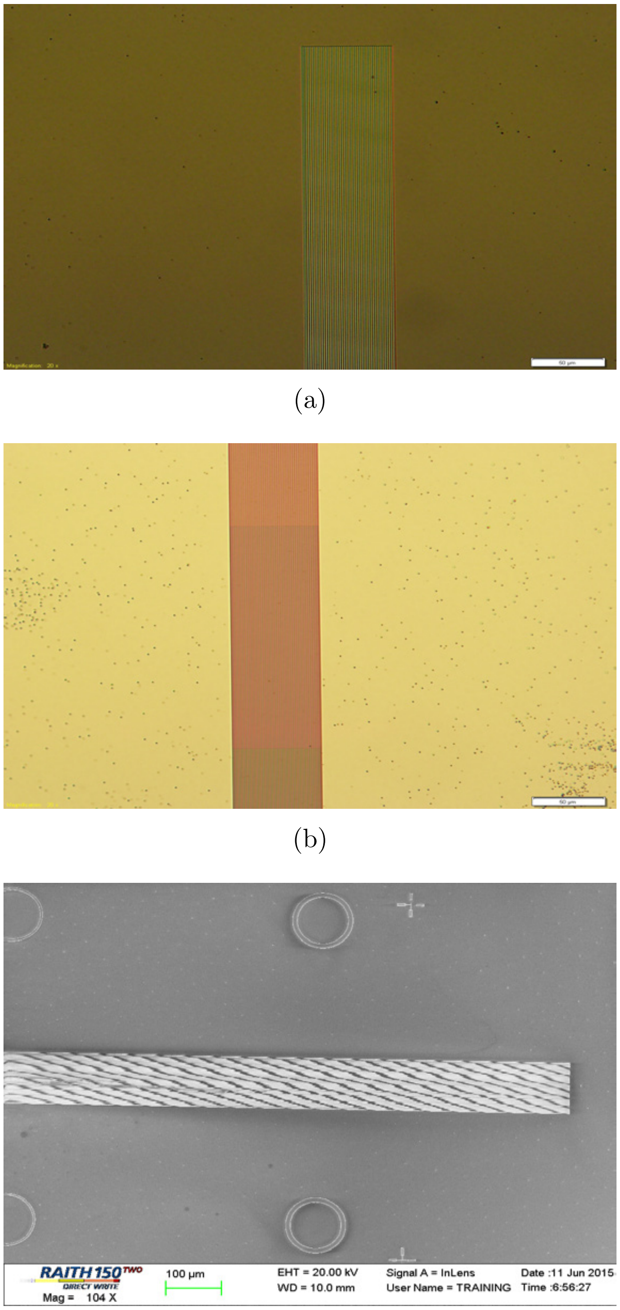

(a)

(b)

(c)

Figure 4.20: Microscope and SEM images of the etched waveguide associated with various etching parameters as outlined in Table 4.2 (a) Etch recipe A (b) Etch recipe B (c) Etch recipe C.

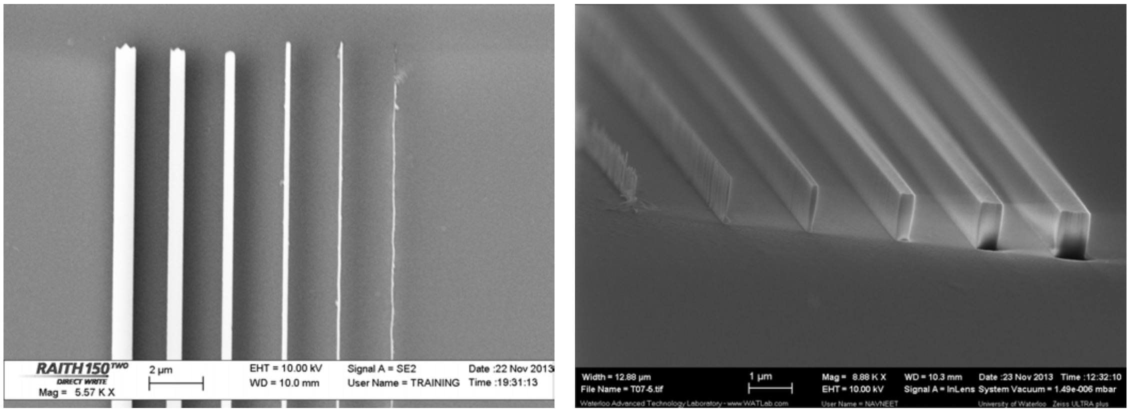

(a)

(b)

Figure 4.21: SEM images of the etched waveguides with various widths of 50, 100, 200, 400, 600 and 800 nm. (a) Top view (b) Side view showing side walls.

Lateral or horizontal etching is still present and the 50 nm waveguide is barely standing. Side view measurements show that the 50 nm waveguide is thinned to $20-30$ nm and at some points collapses due to lack of mechanical stability. The 100 nm waveguide is thinned down to about 60 nm and so are the larger widths. While there is side-wall roughness present for these two thinner waveguides, it is almost invisible to the operational wavelengths of 450 nm or higher. Therefore, propagation losses should not be high for these thinner waveguides.

Figure 4.22 shows the SEMs taken from an etched sample using the recipe C etch parameters. The SEMs are taken from the tapered waveguide's narrowest and widest points along with an angled SEM from its far end which has the maximum width. About 60 - 100 of these tapered waveguides are packed together to test the etching recipe for the waveguides roughness and aspect ratio parameters. Figure 4.22(b) shows the final width of the waveguides at their narrowest point. Due to high aspect ratio and very thin profile, the waveguides lack mechanical stability and have a wavy pattern in some regions. Figure 4.22(d) shows side wall roughness when there is only 200 nm gap between the waveguides at their widest point at the end of the tapers. The roughness varied between $15-25$ nm at some points along the taper. Based on these images, it was concluded that the developed high aspect ratio etch recipe successfully generated suitable tapered waveguide patterns in SiN_x. After the waveguides were etched, the sample needed to be planarized for further processing and testing purposes.

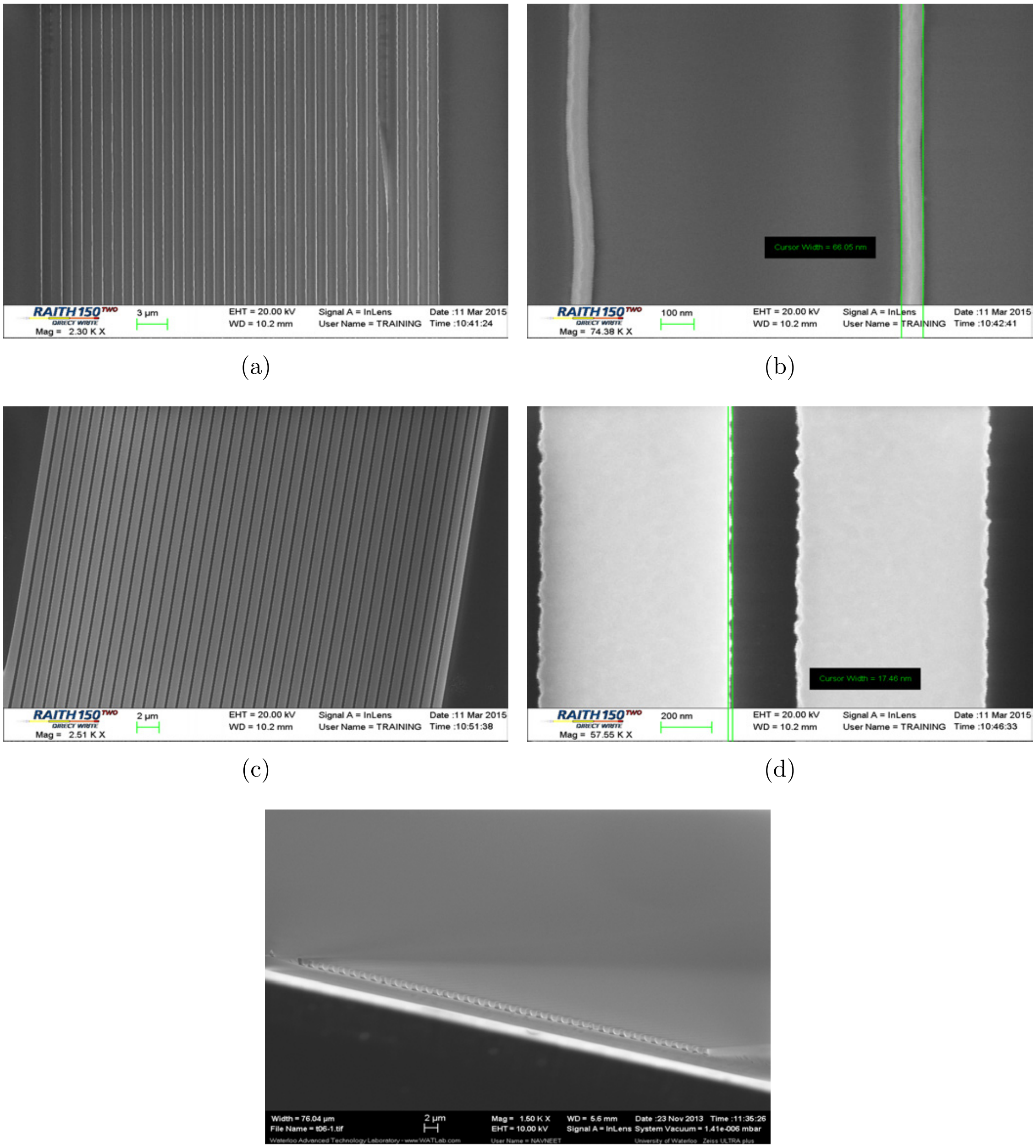

(a) (b) (c) (d) (e)

Figure 4.22: SEM images of the etched waveguides (a) Top view showing etched 100 *nm* waveguides (b) Top view 100 *nm* waveguides that show 17 *nm* of lateral etching on each side (c) Top view at the widest end of tapers (c) Top view showing the surface roughness at widest end (e) Side view at the widest point of the tapers.

4.3.3 Planarization and Cleaving

After the etching step, the aluminum mask was removed using an Alkaline based solution called Microposit MF-319 [92]. Unlike metal etchers, the developer etches Al but does not etch SiN_x or SiO_2, keeping the waveguides intact. In order to get a uniform mode at the output facet, planarization is needed for the waveguide cores. The planarization layer acts as an intermediary cladding between the waveguides and the wedged fiber. Cyclotene BCB polymer is one of the most common materials used in planarizing photonic structures. However, according to simulation and optimization results in the previous chapter, its higher refractive index of 1.6 would result in low coupling efficiencies between the wedge fiber and the channel waveguides [93]. Another common planarization material being used is spin-on-glass (SOG) and should sarisfy the required fabrication demands. However, for this material, special furnaces with accurate heat ramp-up and ramp-down capability are needed. Unfortunately due to lack of such furnaces at QNC NanoFab, SOG could not be used. As a fallback, PMMA resist was used for the planarization step. The MichroChem's 950k PMMA A3 has a refractive index of 1.482 at wavelength of 800 nm [94]. This type of resist was chosen due to its lower refractive index and abundance in NanoFab lab. However, it should be noted that its absorption is high at the lower end of the visible spectrum and thus, the structures will not work well at blue wavelengths. This problem can be removed by using SOG. The resist layer would have a thickness of about 180 nm when spin coated onto the sample at 3000 RPM for 60 seconds and then hard baked for 20 minutes at $180°C$. In order to completely cover the height of the SiN_x waveguides, multiple layers of resist are needed consecutively with soft bake steps in between. A characterization test was done to make sure adhesion and hardness of the planarizing layer is acceptable. During the test, a complete 20 minute hard bake hardened each layer of the resist. This in turn lowered the adhesion of multiple layers on top of each other causing flaking issues. On the other hand, shorter soft bake times caused improper evaporation of the solvent, resulting in a final layer that was hard on the top and bottom but softer on the inside. This would create problems during cleaving. While cleaving the facet, the softer center of the PMMA would randomly fracture creating stress on the facet, ultimately manifest as roughness and causing scattering losses. Figure 4.23 illustrates these various soft bake times from shorter to the longer times. As it can be seen in Figure 4.23(b), a suitable soft bake time would result in a uniform planar layer of resist which would have a thickness of about 1200 nm.

Figure 4.24 shows the optical microscope image of a planarized waveguide with PMMA. Good uniform coverage over the complete waveguide is achieved and the waveguide is now suitable for flip chip bonding on the wedge fiber. A good quality facet is also achieved after cleaving the device. After the planarization step, the waveguides needed to be properly

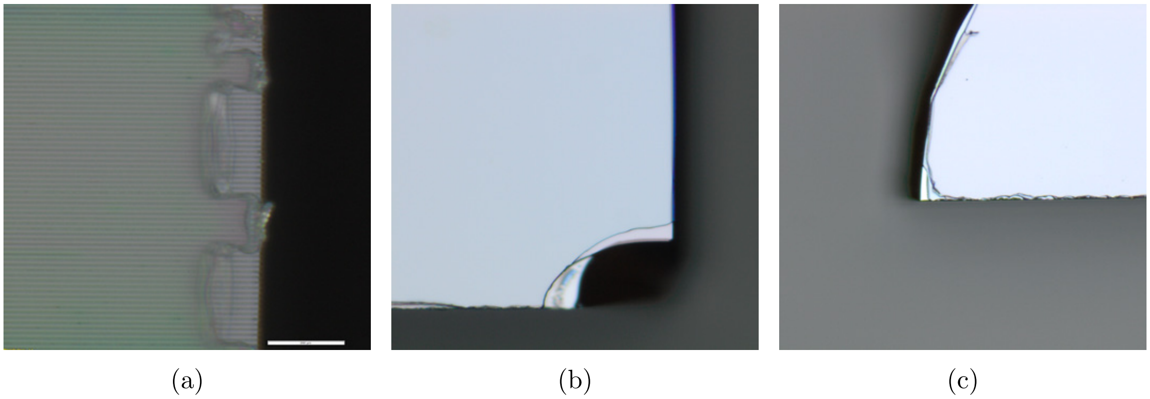

Figure 4.23: Microscope images of test wafer and resist layer cleaved facet (a) 5 minutes of soft bake (b) 10 minute soft bake (b) 15 minute soft bake.

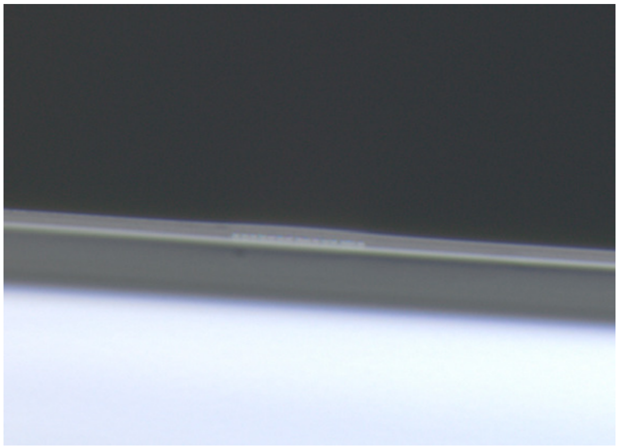

Figure 4.24: Planarized facet of the waveguides.

cleaved towards the end of the taper. Facet quality is preeminent to further characterization steps within this device as any imperfections would change the power output and also the output mode divergence angles due to unwanted scattering. Both of these parameters were key components in the β-factor calculation which was developed and suggested as a performance metrics for this device in Equation 3.3.

A number of cleaving methods were used and tested to achieve the best results. One of such methods was using the DISCO saw machine as explained earlier. In this attempt, the diamond blade was used to cut up to $70 - 80$ nm from the back of the wafer. Then,

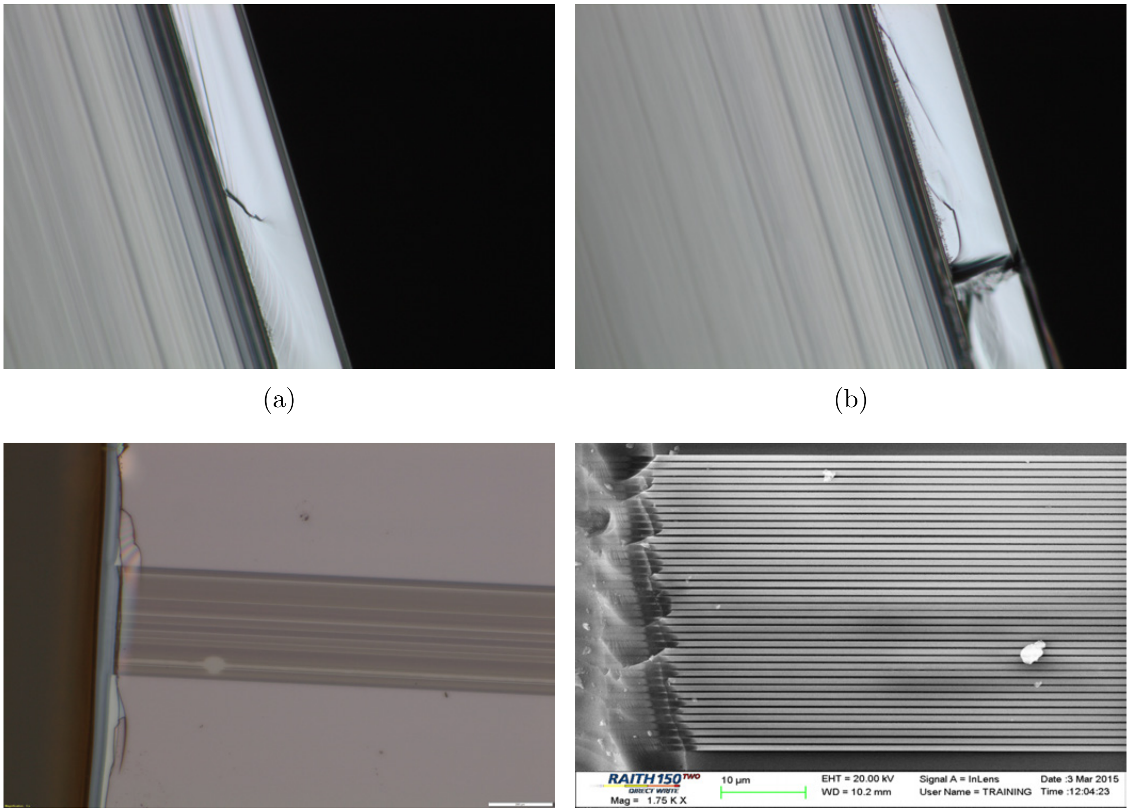

(a) (b) (c) (d)

Figure 4.25: Microscope and SEM images of the cleaved samples and some of the issues (a) a small kink showing the stress points when the saw cuts through the back side of the wafer (b) another sample showing a crack in the facet at the stressed point (c) planarization layer being peeled off at the facet (d) cleaving a sample without planarization.

the wafer is forced to break which can potentially leave us with a clean facet. While this approach was used a number of times to find the optimum thickness, breaking pressure and force direction, the results were not consistent each time. Figure 4.25 shows some of these issues. Figure 4.25(a)-(b) shows the cracks and kinks in the facet due to stress points present when the wafer was thinned and then cleaved. Figure 4.25(c) shows the issue of planarized layer peeling during the cleave when the dicing saw was used and the cleave was forced from the back side of the wafer. In general, cleaving of dielectric waveguide is challenging since there is no defined crystal lattice and hence the facet can be randomly cut depending on the stress or uniformity of layers. Figure 4.25(d) shows this issue for a

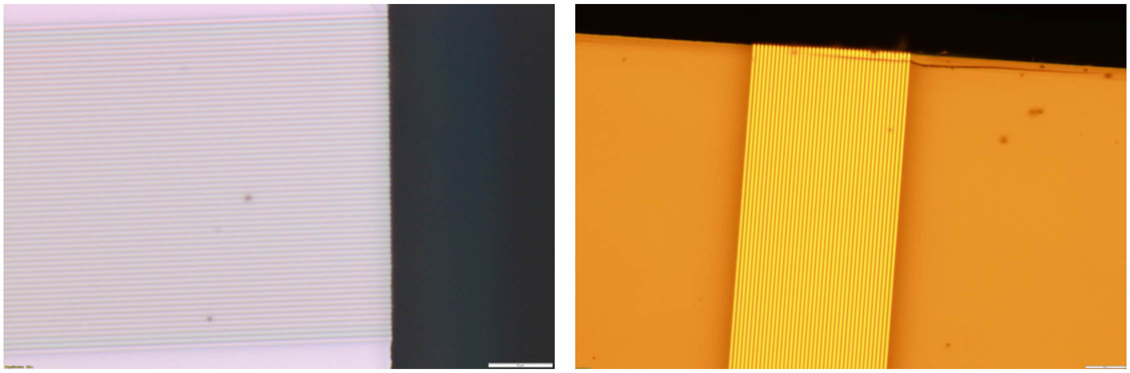

(a) (b)

Figure 4.26: Microscope images of the cleaved samples showing two of the acceptable cleaves for the SiN_x waveguides.

non-planarized sample and how this can increase scattering losses at the facet. Another cleaving mechanism tested was using an OEG diamond scriber unit. The wafer was scribed up to the vicinity of the waveguide and then was simply broken along the scratch line by applying pressure. Figure 4.26 shows two samples that were cleaved with this method and it was found that this type of cleave would give the best possible results in terms of facet quality. Another part of the system apart from the waveguides is the wedged fiber which is discussed in the following section.

4.3.4 Wedge Fiber

After the fabrication steps and planarizing the sample wafer, the wedged fiber needs to be coupled to these tapered waveguides from the top of the wafer. The wedged fibers need to be smoothly polished at shallow angles and the surface of the wedge needs to be free of particles to minimize scattering losses within the coupler setup. In order to achieve an adiabatic taper, the wedge angle needs to be 8° or less which is extremely hard to achieve [53]. Two versions of the wedged fiber were developed and tested with the chip. One was a hand polished version which was designed and polished in-house in Waterloo and the other version was ordered through a fiber customization shop which used chemical and mechanical polishing (CMP) to manufacture the wedged fibers. In the following section, each of these wedged fibers are discussed.

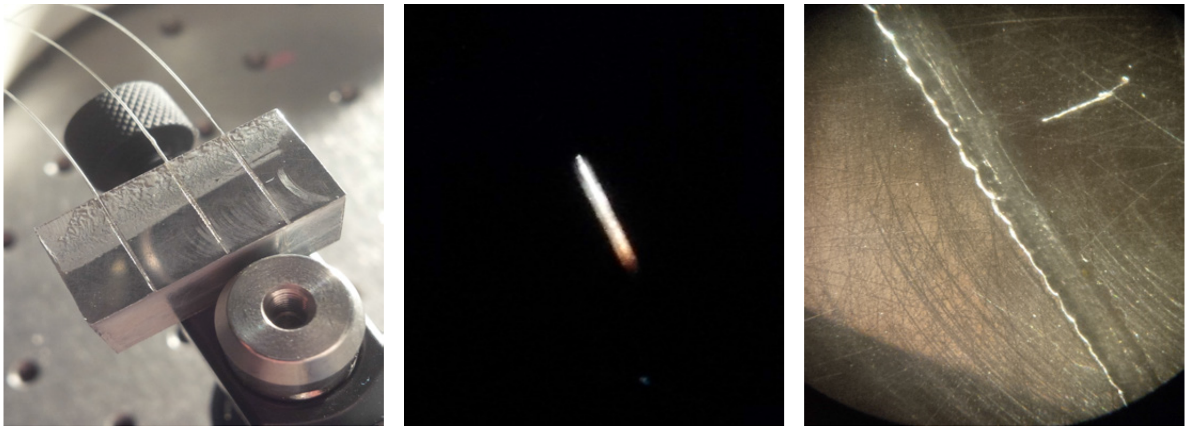

(a) (b) (c)

Figure 4.27: Hand polished wedged fiber on a custom machined block (a) The designed angled block housing 3 test fibers (b) Dark field image of a wedged fiber coupled onto a Halogen-Tungsten light source (c) Magnified image of one of the polished wedged fiber.

Hand-Polished Wedged Fiber

An Aluminum block holder was designed and machined to hold the fibers in place during the polishing process. The top part of the block had a 4 mm long angled section of less than 5°. There were grooves of about 150 μm deep for positioning the fibers. The fibers were epoxied in place using optically transparent epoxies, and then hand polished using specialized lapping films with very fine grit sizes. Figure 4.27 illustrates the hand-polished fibers on the machined holding block. Figure 4.27(a) shows that if polished to really fine levels, the block surface can become shiny and reflective. The epoxied fibers used here were step index 50 μm multi-mode fibers and care was taken when polishing the fiber close to its core. If the polishing is done perfectly, one should end up with a trail of light emitting the fiber tip evenly as shown in Figure 4.27(b). The dark field image shows the emission of light from the fiber. However, this is an extremely divergent light and measurement of the emitted light either through an integrating sphere power meter or an imaging mechanism is not a trivial task. On the other hand. Figure 4.27(c) shows the magnified image and the imperfections present on the fiber surface. Due to being a hand polished fiber, any extra pressure can cause uneven polish, resulting in potential damage to the fiber core.

In order to characterize the emission profile, near-field coupling to a fiber was used. The input of the wedged fiber was coupled to a 1050 nm super-luminescent diode (SLED). Then, another 50 μm step index multi-mode fiber was cleaved and held on top of the

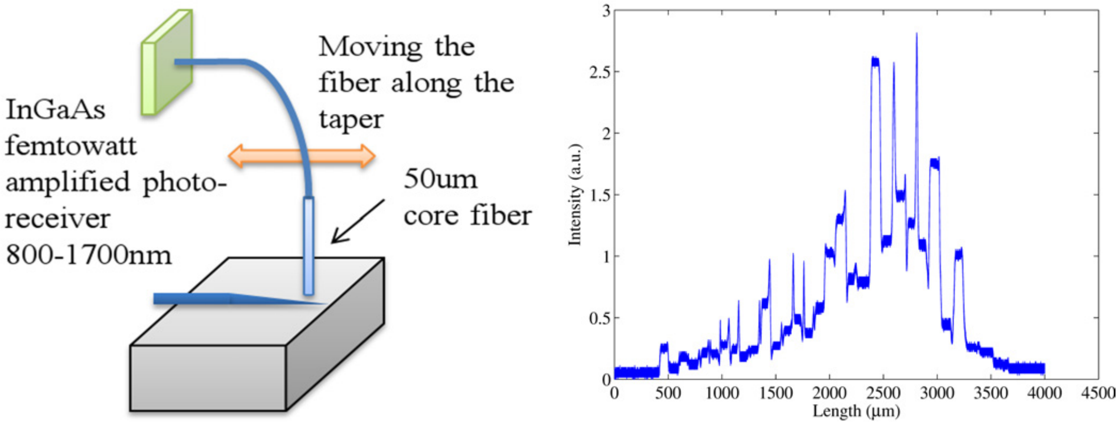

(a) (b)

Figure 4.28: Hand polished wedged fiber radiation pattern measurement (a) The radiation pattern measurement setup (b) Measured signal on the photo-receiver.

wedged fiber block using a 3-axis stage. Also using the stage, the fiber probe tip can be traced as close as possible to the wedged fiber where the leaked light from the taper would couple into the probe tip by means of near-field coupling. The fiber probe was connected to a very sensitive and low noise Femtowatt photoreceiver, and the signal was output to an oscilloscope to measure the wedged fiber light emission level as the fiber probe is moved along the wedged fiber. This setup is shown in Figure 4.28 and the measured signal from the photoreceiver is plotted in Figure 4.28(b). The modes start to leak out towards the end of the wedge where the fiber core becomes narrower. The leaked power increases towards the fiber end until most of the power is leaked out and the fiber core cannot longer preserve the optical power within itself. While the measurements are done at intervals along the wedged fiber length, the presence of scatterers due to polishing residue can cause the fluctuations seen on the voltage level. As the surface roughness of the polished fiber decreases, it is expected that the radiation pattern becomes smoother with less intensity fluctuations. The best trails of the hand polished fiber still show indications of significant surface roughness which can be circumvented if chemical etching is also done with the mechanical polishing. Due to lack of necessary equipment this avenue was not pursued at that time.

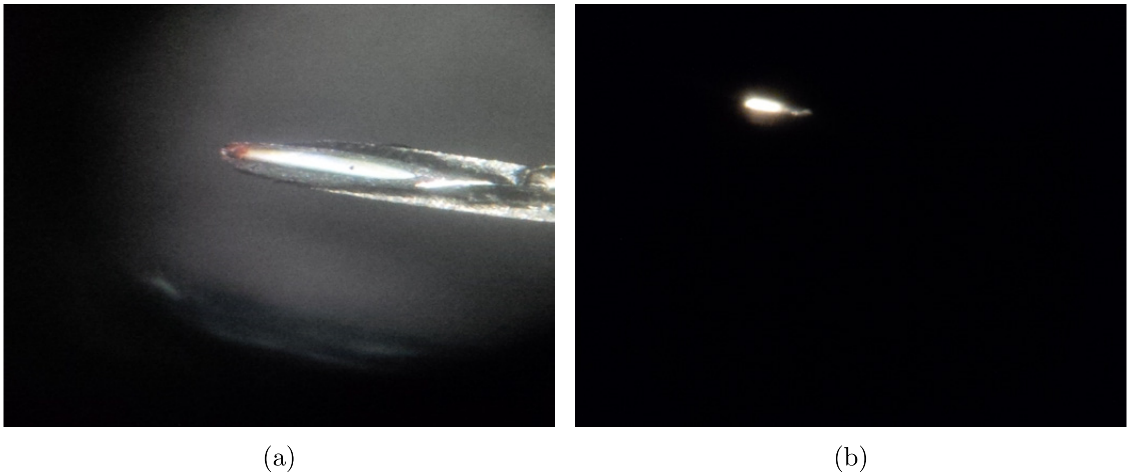
(a) (b)

Figure 4.29: CMP based wedged fiber tip (a) Bright-field image (b) Dark-filed image.

CMP Polished Wedged Fiber

A chemical and mechanically polished fiber tip was ordered through WT Technology Inc. which provides commercially polished fiber probes and fiber tip lenses based on customer designs and specifications [95]. Two sample fibers were procured and ordered, one with core diameter of 50 μm and the other one with core diameter of 100 μm with polishing angle of $75 - 80°$. Both fibers were placed in a 10 mm metal tubing for protection and handling but the wedge angle could not be reduced further due to manufacturing process limitations. Figure 4.29 shows bright-field and dark-field images of the fiber tip. As it can be seen in the bright-field image, the bright surface reflection from the tip shows the mirror like surface quality of the fiber tip. Such high quality surface is essential in reducing the optical losses within the wedge fiber. Figure 4.29(b) shows the dark-field image where the fiber tip emission profile can be observed. Due to high quality optical finish of the fiber tip, the modes do not leak out or scatter from the tip until reaching the narrower end of the wedged tip.

The CMP-polished fiber tip was only used towards the end of the project and is discussed further in the next chapter. Both the hand-polished tip and the CMP-based tip were used at different stages and provided some insight towards the system dynamics and physics of the coupling between the wedged fiber and the inversely tapered multiple channel waveguides.

4.3.5 Chip to Wedged Fiber Coupling System

After having the waveguides planarized and cleaved and also manufacturing the wedged fiber, it is necessary to couple the input light from the wedged fiber onto the waveguide system. Here, two flip-chipped coupling systems were tested. A passive-coupled system was built using a FineTech FinePlacer Lambda machine from the Rapid ProtoTyping Lab (RPL) at University of Waterloo. In addition, another-active coupling system was designed, built and used along with the CMP-based wedged fiber. In the following, each of these systems are briefly discussed.

Passively Aligned Flip-Chipped System

In this system, a flip-chip setup was used to align the waveguides to the wedged fiber and place them on top of each other without any real-time feedback from waveguides output. The FinePlacer system is shown in Figure 4.29(a). It consists of two imaging cameras; one on top and the other on the side. The top camera has a beam splitter in its optical path where it can collect and overlay two images from the chip and the wedged fiber. The chip was supported from its backside in a vertical position by means of a vacuum tip. Then after the alignment was done using the overlay image, the moving arm flipped the chip and positioned it on top of the wedged fiber.

Figure 4.29(b) shows the wedged fiber dark field image when coupled to a UV laser diode source. After the chip alignment and placement on the fiber block, UV-cured epoxy was deposited around the chip on the block in order to preserve the alignment. The epoxy naturally flowed into the gap between the chip and the wedge fiber. As an extra measure to cure the epoxy, the UV light was coupled into the wedged fiber to cure the epoxy in between the block and chip in the wedge area. In addition, the dark field image showed how surface imperfections and roughness result in bright scattering spots along the wedged fiber length. Figure 4.29(c) shows the waveguides image on the chip while the chip is held in the vertical position using the vacuum tip. Figure 4.29(d) on the other hand shows the overlay image of the waveguides on top of the wedged fiber that was coupled to the UV laser source. Injecting a narrow-band source into the fiber helped with the alignment procedure. After the position and angle of the lines were completely aligned, the chip was placed on top of the wedged fiber while applying a pressure of about 5 *lbs*. Then the UV curable epoxy is used around the edges of the chip to fix it in place.

While this method of alignment worked in some of the test instances, it did not guarantee optimal coupling in all cases. In fact due to variations in the hand polishing process, the fiber emission profile was not uniform across all the lab tests. Hence, the location to

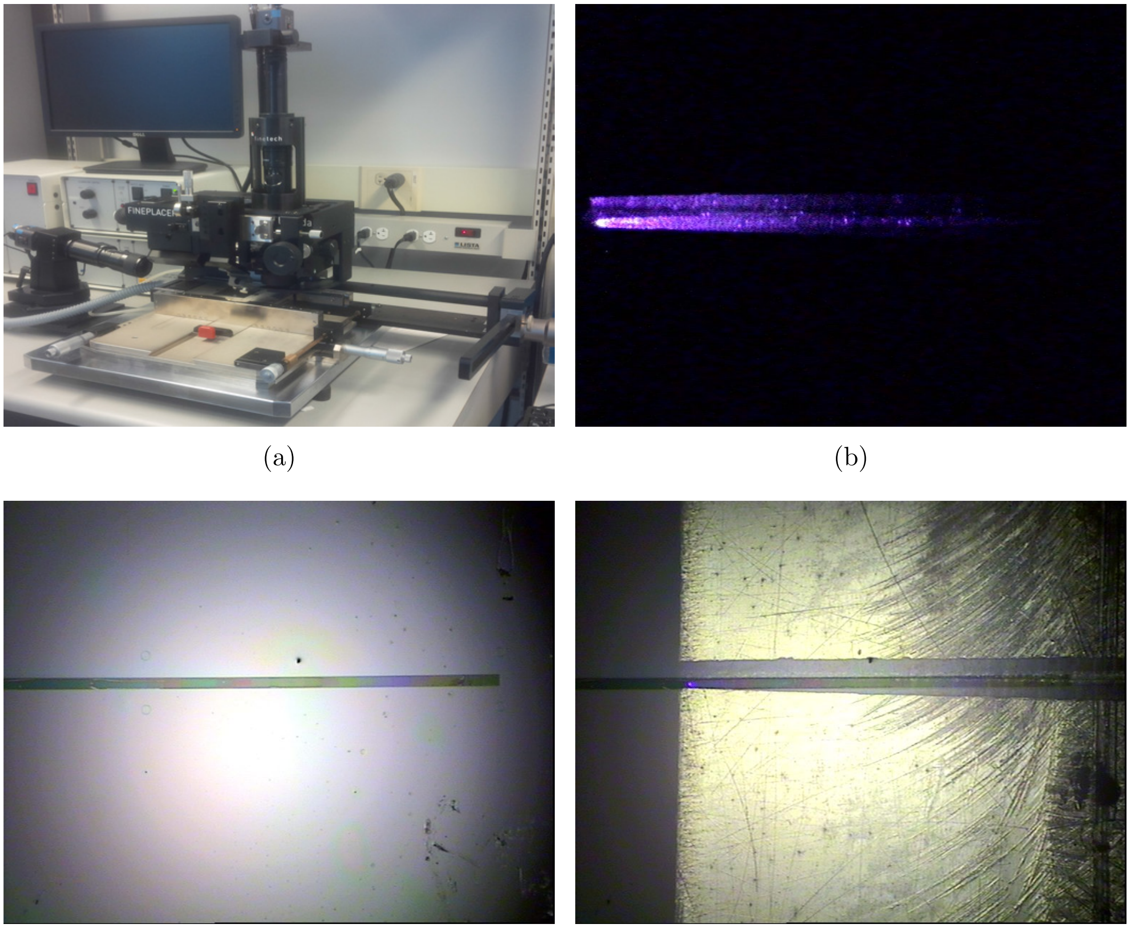

(a)

(b)

(c)

(d)

Figure 4.30: Passive coupling system using flip-chip bonding mechanism (a) The Fineplacer flip-chip bonding setup (b) Wedged-fiber dark field image from the top camera without overlay when coupled to a UV laser diode (c) Chip image showing the waveguides from the top camera with wedged fiber without overlay (d) Overlay image of the waveguides on top of the light coupled wedged fiber.

achieve the best coupling condition varied greatly and an active coupling mechanism was needed to ensure maximum output at the waveguides output facet. The active coupling mechanism was however only possible on the CMP polished fiber due to smaller size of the fiber tubing and smoother finished surface. The active coupling setup is discussed in the following section.

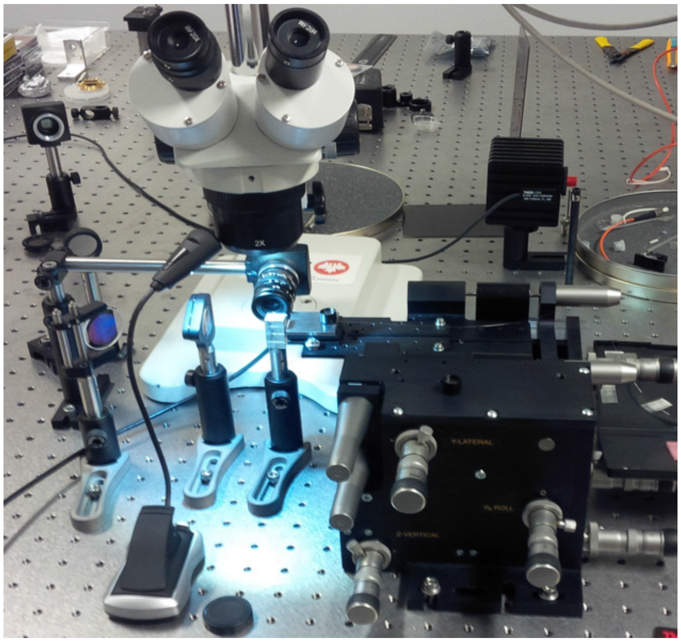

Figure 4.31: Optical setup of the actively aligned coupling system.

Actively Aligned Coupling System

In order to address some of the shortcomings of the passive flip-chip coupling setup, an active coupling system was constructed in which the wedged fiber tip was placed on the chip using a two camera setup. As shown in Figure 4.31, the fiber tip was fixed on a 6-axis stage providing 3-dimensions of sheer and tilt. The chip was fixed on a block holder on a post. Then the alignment was optimized using two images from top and the side. The side image was collected on a camera while the top image was collected using a long focal length microscope. The output of the chip was monitored using an imaging system to measure the waveguide output intensity. In case of this setup, the output was directly used within a custom designed high-resolution spectrometer setup which is explained further in the next chapter.

Figure 4.32(a) shows the top view of the system where the chip is vertically held on the post-mounted block by an epoxy drop. The fiber tip is aligned and angled such that it sits flat on the chip. The fiber tubing shows the shallow angle of the tip and care was taken when placing the fiber on top of the chip. This top view provides a suitable image of the coupling distance between the fiber and the chip. Figure 4.32(b) shows the side view through the camera which imaging the chip from top. This view would

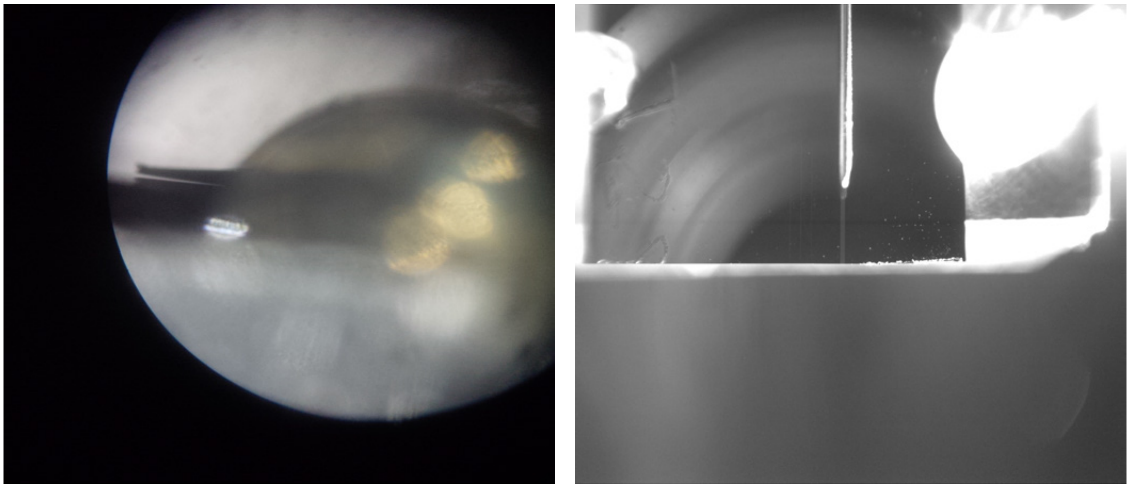
(a) (b)

Figure 4.32: Active alignment system camera views (a) Top camera image showing the distance between the wedge fiber and the chip from the side (b) Side camera image showing the lateral alignment of the system.

provide the lateral placement position of the fiber. While these two views would provide approximate placement position between the wedged fiber tubing and the waveguides on the chip, the more accurate alignment is done by means of monitoring the waveguide outputs and maximizing the output power. In the following chapter, details of this setup and the results from the spectrometer are discussed.

4.4 Conclusion

In this chapter, details of fabrication and system design were discussed. As mentioned at the beginning of the chapter, many of these processes and designs were developed and implemented for the first time based on the requirements of the system, and modified on an on-going basis with respect to improvements seen at various stages. While the discussed procedures are not an exhaustive list of all tested methods and developed procedures, it is representative of the systematic approaches taken to ensure the samples are made with highest possible design accuracy replicating the theoretical design constraints and criteria discussed in Chapter 3. The following list summarizes some of these practical considerations as discussed in this chapter and the developed methods and procedures to address them to the best of our ability:

- The tapered multiple channel waveguides should closely follow the ideally designed tapered structures for optimal implementation of the inversely tapered coupled waveguide concept. This requires the development of nano-fabrication processes to the extent that the patterning, lithography, lift-off and etching steps are done reliably and efficiently.

- New e-beam writing methods needed to be developed to be able to pattern large area samples with accuracy of e-beam writing and placement and minimum stitching errors.

- The etching processes had to be developed to ensure optimal mask replication capability through the SiN_x film and providing smooth side walls. This would reduce the propagation-related optical losses through the design. The tapered waveguide etching was a challenging task, especially it involves high aspect ratio regions especially towards the narrow end of the tapers where the waveguide could have widths of about 50 nm and height of about 1 μm.

- Planarization and cleaving steps are essential to achieve the optical mode output. The output facet quality determines the output optical mode shape and power. Any additional surface roughness or imperfections would result in additional scattering losses and hence lower quality device performance. The planarizing layer needs to be optimally chosen in terms of refractive index and tensile strength such that it would not affect the cleaving process. As discussed in Chapter 3, the refractive index of this intermediate layer also plays an important role in the coupling ratio between the wedged fiber and the inversely tapered waveguides.

- The wedged fiber also needs to be polished at very shallow angle and the adiabaticity condition minimizes the further optical losses along the coupler in form of stray light. Such shallow polishing angles are hard to achieve using CMP-based machine so a hand polishing procedure and mount was developed and tested. However, surface imperfections and polishing variations caused additional losses within the wedged fiber system. Therefore, a CMP polished fiber was procured and tested with a polishing angle as small as physically possible considering manufacturing limitations.

- The hand-polished and CMP-based fibers were each used within their respective setups. In case of the hand polished wedge fiber, the flip-chip procedures were developed using a FinePlacer system to passively align the wedged fiber to the inversely tapered waveguides. For the CMP-based wedge fiber, an active coupling setup was designed and built to test the output of the coupled system.

While these fabrication and sample post processing techniques were developed along with actual sample tests at various stages, in this chapter a list of the most important procedures were given. In the next chapter, the test results from a few generations of these samples are given and discussed outlining the key performance metrics and their improvement methods.

Chapter 5

Experimental results and Characterization of the Photonic Slicer

In the previous chapter, a number of developed fabrication techniques and procedures were discussed with the goal of achieving a viable and operational coupled system consisting of a wedged fiber and the integrated photonic chip. While the fabrication techniques were developed and enhanced along with various characterization techniques, the characterization results and discussion are provided individually in this chapter for better understanding. The results for various generations of fabricated structures are given in a chronological order and while the core fabrication and sample preparation steps remain unchanged, the smaller variations were used to provide better results at each respective stage. In the following, first the measurement and characterization methods are discussed in general terms. These characterization methods were specifically developed to help with understanding and quantifying the performance of each chip. Then the results from various generations of these devices are discussed.

It is worthwhile to review some of the objectives from Chapter 3. The goal of a photonic slicer design is to re-shape the beam from a multi-mode input fiber in an efficient manner with minimum losses in power. This reshaping can be done by means of the inversely tapered coupling structures for which a few different geometries were suggested. Out of those, the inversely tapered wedged fiber structure seemed to be the most promising and practically viable solution to fabricate and further characterize. Using the optimization criteria discussed in Chapter 3 and considering the fabrication limitations seen in Chapter

4, a few generations of the inversed coupling systems were tested. The results are discussed and evaluated with respect to the theoretically calculated values at the end of this chapter.

5.1 Measurement and Characterization Methods for the Photonic Slicer

A number of measurement techniques were used and developed to characterize the performance of the photonic slicer coupling system. One of the key applications of the photonic slicer was in spectrometers such that miniaturization could be achieved while having high resolution and high throughput. As discussed earlier, achieving all three goals is not feasible at the same time. In Chapter 3, a performance variable called the β factor was introduced that gauges the performance with respect to a slit in a spectrometer setup. To calculate the β factor, the input and output beam divergence angles and optical power should be measured and compared with that of a slit setup. While these measurements provide an initial prediction for the system performance, it can often be an overestimate. The measured power at the output facet can include stray light from the imperfect fiber tip or higher order modes from the waveguides having larger divergence angles. Therefore, the imaged line would be broadened due to higher NA of the waveguides output. In order to perform a more accurate comparison between the slit and the photonic slicer, a more comprehensive approach should be taken which considers the losses due to imaging as well. For this purpose, a very high resolution spectrometer setup was designed and built to further analyze the results. This spectrometer setup is discussed at the end of this section.

5.1.1 Far-field Radiation Pattern and Near-field Imaging of the Output Facet

Near field imaging and far field radiation pattern of the chip output facet and also the imaging of a bare fiber can provide valuable information about the coupling system's output and input beam characteristics. Near field imaging can be done using a lens system while the far field pattern can be studied using a lens-less detector. Here, details of each imaging method is provided.

Far-Field Radiation Pattern

Far-field radiation pattern is studied by simply aligning a lens-less detector in close proximity from the output facet. Then using a translational stage, the detector can be moved away from the output facet in small increments to measure the divergence angle of the beam in different axises. Figure 5.1 illustrates the lensless images at close proximity of about z_0 from the output facet as the beam diverges from z_0 to $z_0 + 450\ \mu m$ points. Using the horizontal and vertical cuts through the far-field profile of the beam, one can calculate the point-point divergence angles by measuring the beam FWHM values.

Figure 5.2(a) shows the vertical cut through the center of the far-field radiation pattern at $z_0 + 450\ \mu m$. There is a main lobe along with a secondary lobe that has a tail above it. As the detector is moved far away, the far-field pattern diverges and the radiation pattern would have two distinct lobes. At this point the working hypothesis is that one lobe is the actual output of the waveguides and the other is the remainder optical mode from the fiber area. In order to verify this hypothesis, the vertical profile was fitted with two Gaussian functions and the overall fit was optimized using non-linear least squares method. The fit function used is as follows where the coefficients of (a_1, b_1, c_1) and (a_2, b_2, c_2) are calculated such that the MSE is minimized between the fit function and the actual data points and

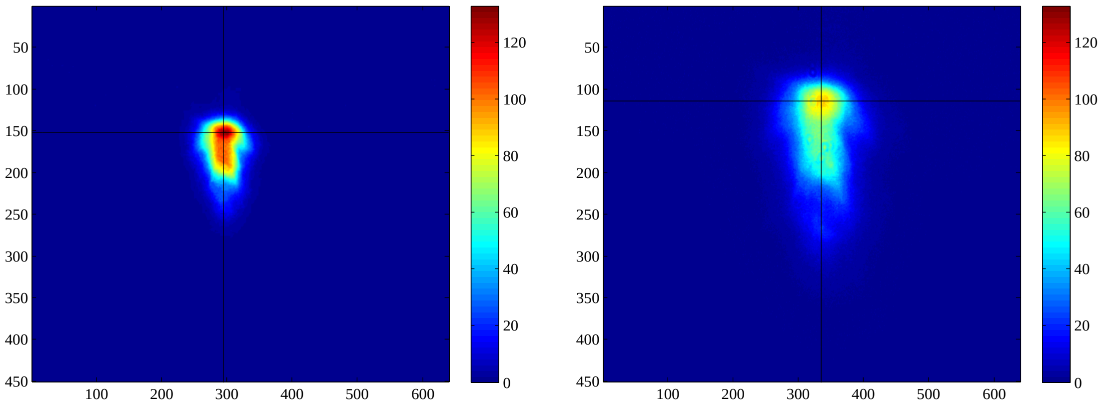

(a)

(b)

Figure 5.1: Far-field images of the chip output facet with the axises determining the pixel numbers (a) The lensless image at close proximity of z_0 (b) The lensless image at close proximity of $z_0 + 450\ \mu m$.

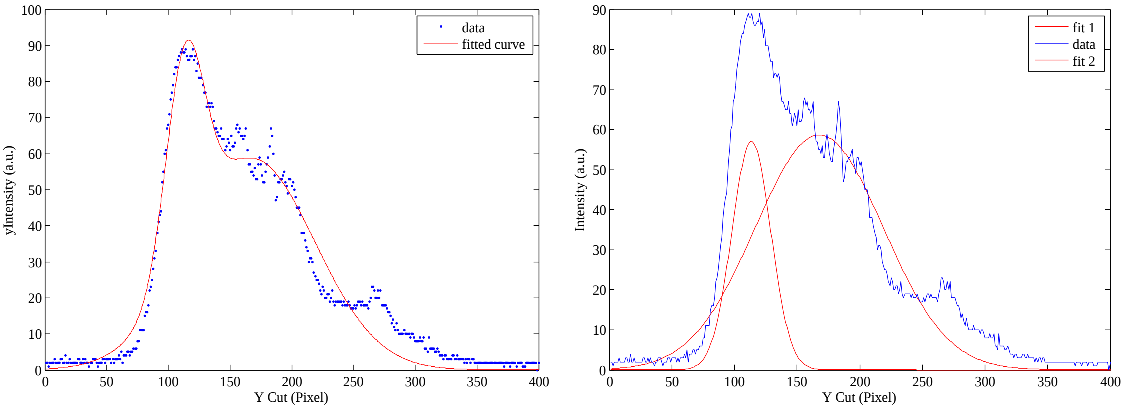

(a) (b)

Figure 5.2: Vertical cut through the center of the far-field pattern at $z_0 + 450\ \mu m$ (a) The vertical cut profile and the fitted data (b) The vertical cut profile and the fitted Gaussian functions to the far-field radiation pattern.

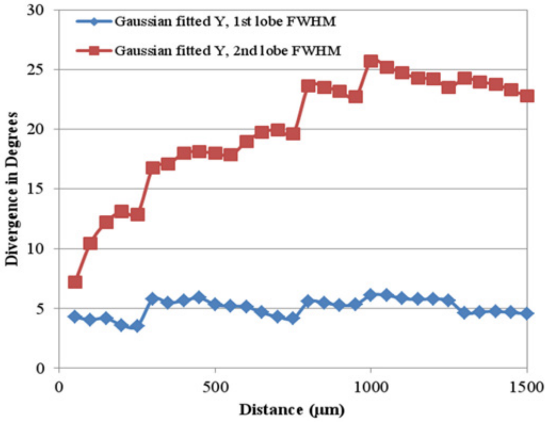

Figure 5.3: Gaussian fit FWHM values for both lobe of the vertical profile as the distance between the detector and output facet increases.

the resulting R^2 value is above 0.9.

$$f(x) = a_1.e^{-(\frac{x-b_1}{c_1})^2} + a_2.e^{-(\frac{x-b_2}{c_2})^2} \tag{5.1}$$

As evident from Figure 5.2(b), the vertical beam profile can be effectively modeled with two Gaussian beams with different beam waists. Analyzing this data further and having the Gaussian fits calculated as the detector is moved away from the facet output, further information can be gathered on the output beam characteristics. For instance, Figure 5.3 plots the output beam divergence angles for each of these fits as the distance is increased. The main lobe FWHM values do not vary much with the distance which shows that it represents a well defined Gaussian beam with an asymptotic divergence angle. The 2^{nd} lobe however, shows much larger divergence angles as the distance is increased. The difference between the main and the 2^{nd} lobe divergence values shows that the output beam consists of two separate Gaussian beams likely from two different sources. In addition, the increase in the divergence angle of the 2^{nd} lobe shows that the beam is not purely Gaussian and stray light or higher order deflection beams are possible explanations for the data. Characterizing the far-field radiation pattern using this technique would help with calculation of the β-factor from the estimated divergence angles as well as understanding the modal field distribution pattern between the chip and the fiber. While the far-field method provides valuable information, it is not sufficiently conclusive by its own and therefore a near-field imaging would be a complementary characterization step which is discussed in the next section.

Near-Field Imaging

A number of different lens systems can be used for the near-field imaging purposes. A trivial imaging method is to use microscope objectives to identify the waveguides output from stray light and other coupling imperfections. This is a qualitative analysis rather than a quantitative measurement. Figure 5.4 illustrates a number of these near-field images where the individual waveguides are visible using high magnification microscope objective lenses. In Figure 5.4(b) the input is a broadband white light source and the red/yellow output color indicates the high losses at the smaller wavelengths. The output shown in Figure 5.4(c)-(d) is with a band-pass filter centered near 780 nm. Using the near-field imaging along with high magnification objective lenses, the output facet of the waveguide can be inspected for coupling quality.

Another method for imaging the output waveguides is to use individual lenses. However, since the divergence angle in x and y direction is different, cylindrical lenses with different focal lengths should be used to collimate the waveguide output. Figure 5.5 shows a such setup where the chip block is positioned on an controlled stage to fine tune its position with respect to the 1^{st} cylindrical lens. The 1^{st} cylindrical lens has a focal length of 10 mm and the 2^{nd} cylindrical lens focal length is 75 mm and is mounted on a second linear moving stage to fine tune to collimation. An achromatic lens was used to image the beam onto a detector which had a focal length of 75 mm. Hence, the imaging in the x direction is 1:1

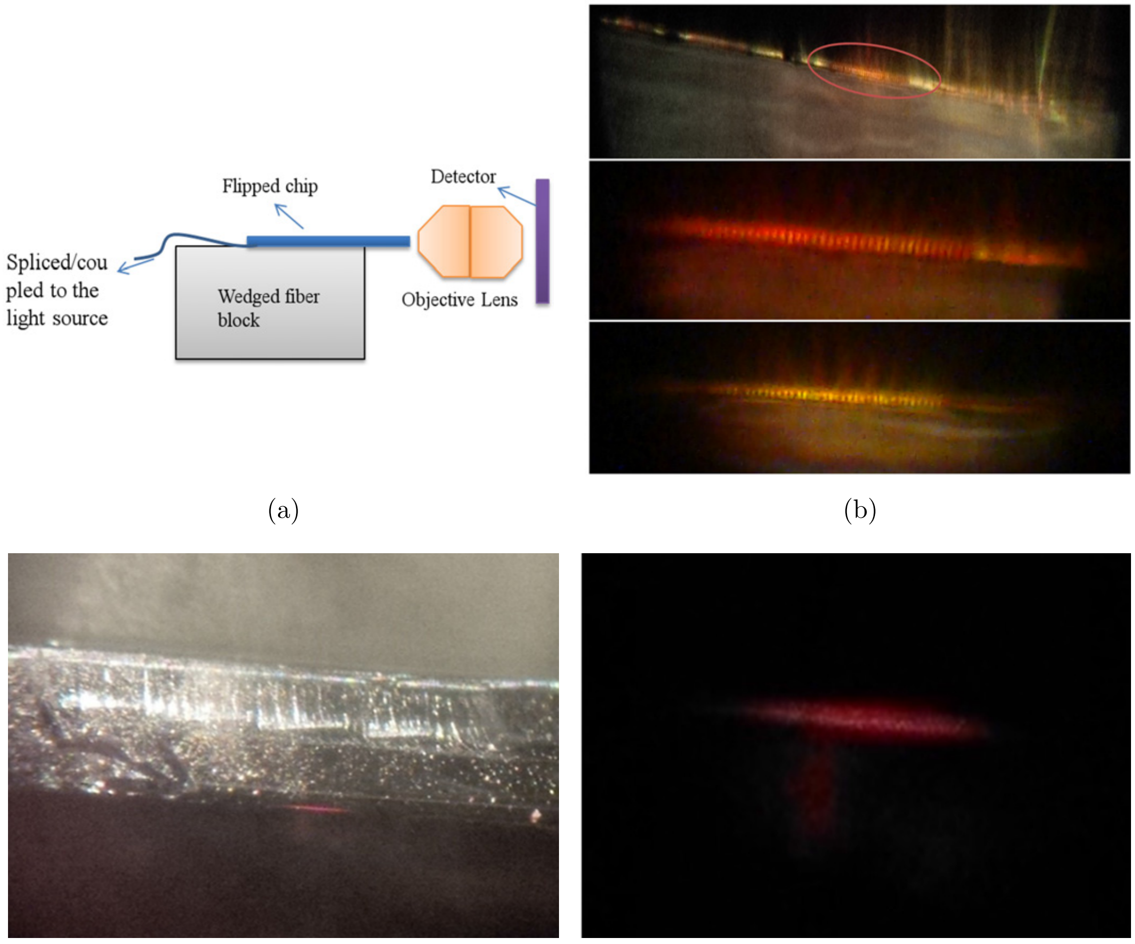

(a)

(b)

(c)

(d)

Figure 5.4: Near-field images of the couplers output facet (a) The imaging setup using objective lenses (b) Near-field images of the output facet with a broadband Tungsten-Halogen lamp as the input (c) Near-field images of the chip with a 780 *nm* band-pass filter after the light source (c) Dark-field image of the chip with a 780 *nm* band-pass filter.

while it is 1:7.5 in the y direction. While this method was thought to reduce the aberrations and reproduce a slit-like spot on the detector, the additional degree of freedom in selection of the x and y magnifications independently did not provide improvements. Due to the high NA output beam, the size of the radiating waveguide and the different divergence angles in x and y axis, imaging using a simple singlet or achromat lens is not optimal. To

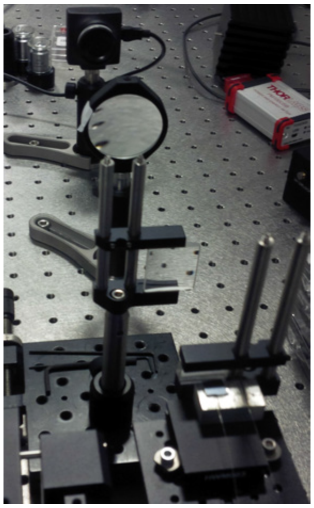

Figure 5.5: The crossed cylindrical imaging setup for the waveguides output facet.

reduce the aberrations seen in the output, an equivalent optical system was modeled and simulated in Zemax Optics Studio, which is a commercial ray tracing based software [96]. The non-sequential ray-tracing method was used for simulation in which the source was modeled as an array of diode lasers with different x and y divergence angles. This source type and configuration was used to resemble the array of waveguides output facet and their corresponding divergence angles. The source rays are emitted based on a Super-Gaussian profile with the ability to adjust the source parameters to become a Gaussian point type source. Figure 5.6 illustrates the difference between the source types that can be used and shows how it can be adjusted to produce Gaussian to flat-top intensity profiles. If ideal thin lenses are used, the sources can be imaged as shown in Figure 5.6(b). In case of a Super-Gaussian source, the image resembles a multi-mode facet similar to the fabricated waveguides whereas the Gaussian source would resemble a point source with a smooth Gaussian distribution as in a single mode waveguide.

The whole system was modeled in Zemax where the sources were modeled to be Super-Gaussian. The crossed cylindrical lenses were chosen from Thorlabs lens catalog as shown in Figure 5.7(a). Figure 5.7(b) depicts the imaged spots on the detectors. The top image is on a detector with pixel pitch of 100 nm showing the fact that to correctly image the diode sources, a very fine detector is needed which is not implementable in reality. The bottom image however, shows the imaged spot considering a realistic detector pixel pitch of 5 μm. While this model predicts an ideal response for the imaging system, the lab experiments showed images with large aberrations and larger dimensions. Further alignment tolerancing studies where done to evaluate the system performance and imaging spot quality. Studies showed that the most sensitive alignment variable is the lens clock difference between the

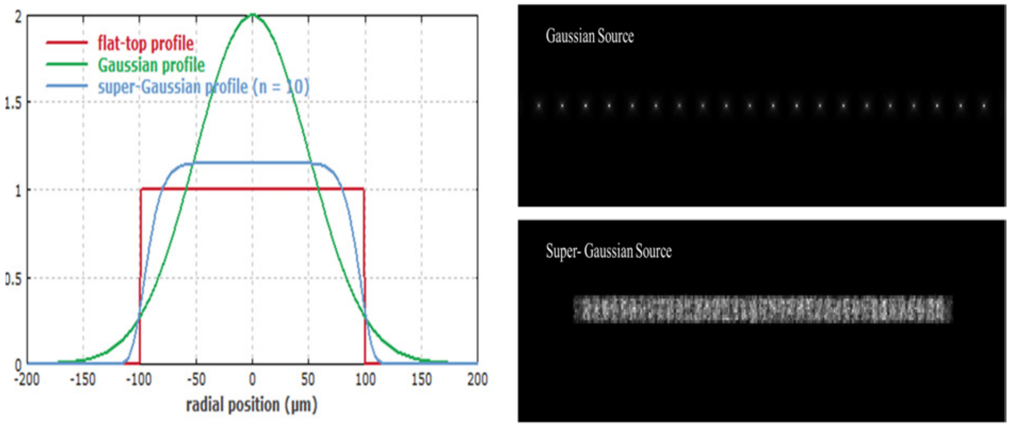

(a) (b)

Figure 5.6: Various source types in Zemax software (a) The sources intensity profiles for various Super-Gaussian based sources. (b) Imaged sources using ideal thin lenses.

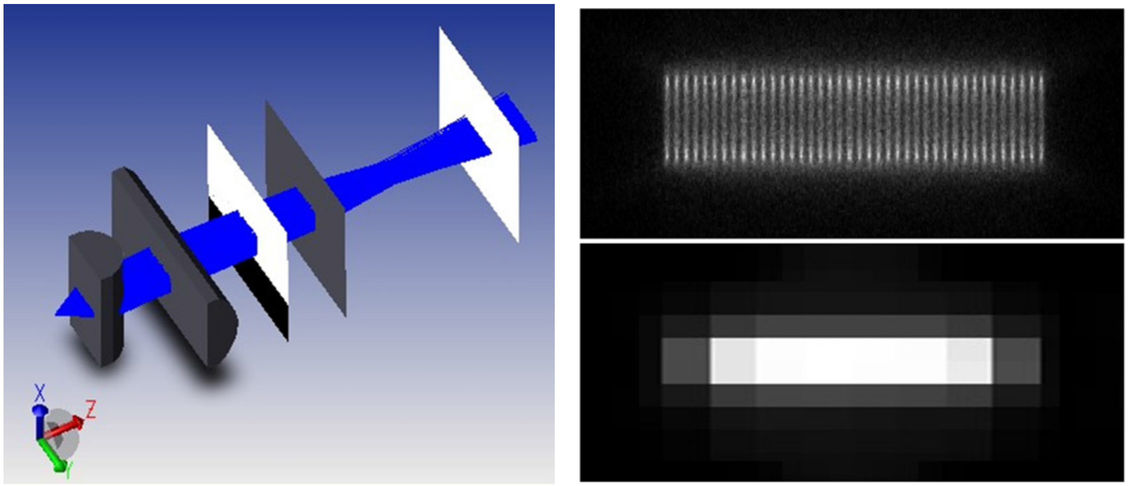

(a) (b)

Figure 5.7: Modeled imaging system in Zemax (a) The crossed cylindrical system setup (b) The imaged spots on the detector; the top image is on a very small pixel detector and the bottom image is the imaged spot on regular lab-based detectors.

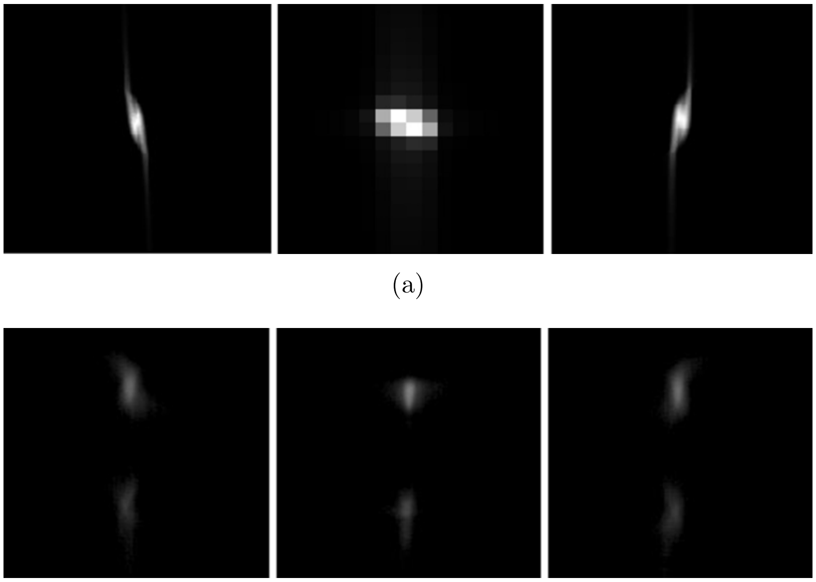

(a)

(b)

Figure 5.8: The effect of cylindrical lens clock with respect to each other where the columns show the lens clock angle differences of -2, 0 and 2 degrees from left to right (a) Zemax simulated results (b) Experimental results from the chip output.

two crossed cylindrical lenses. Figure 5.8 illustrates the effect of lens clock differences of -2, 0 and 2 degrees from the left column to the right. Figure 5.8(a) shows the Zemax simulation results while Figure 5.8(b) shows the experiments conducted in the lab with the chip output as the imaged object. The second cylindrical lens was mounted on a goniometer where the clock angle could be precisely controlled using the micrometer. The second cylindrical lens angle was varied till the minimum aberration image was observed on the detector. This experiment showed the tight clocking angle tolerancing needed with the two cylindrical lens imaging system. While it provided valuable information about the suitable imaging system for such a setup, it does not provide further information and comparison grounds to evaluate the β factor or throughput compared with a slit. Therefore, further measurement and tests are needed to estimate the β factor.

5.1.2 Coupling Efficiency and Beta estimations

After initial measurements of the chip output divergence angles, the output optical power values are needed for β value calculations. In order to measure the output power, an integrated sphere based power meter was used. This would help with output power measurement as the output of the waveguide is a divergent beam. Then using the measured power value and the measured divergence angles, the estimated β can be calculated by means of Equation 3.3.

5.1.3 Hardware Setup

The β value calculated using divergence angle and power measurement provides a good initial quantitative estimate to the photonic slit performance. However, due to the complex nature of the problem which involves multi-mode wedge fiber and near field coupling to the waveguides, the measured divergence angles and output power are not good estimates. When the photonic slit is used within a spectrometer, the imaging optics would have limited capability in capturing the highly divergent output beam of the photonic slit. In other words, building a high resolution spectrometer with a fast input beam to collect as much light as possible is not a feasible task. Therefore in the β estimates, using only the divergence angle and power measurements would result in over-estimation of β. Having an imaging optics with lower NA would result in drop of throughput and therefore a lower β estimate.

In order to properly quantify the performance of the photonic slit with respect to a free space slit counter-part, a high-resolution spectrometer was designed, built and used. Figure 5.9 shows the proposed spectrometer setup in which the schematic is given for both a free space slit and a photonic slit case. Figure 5.10 illustrates the bench-top optical setup of the designed spectrometer. In order to make a quantitative performance comparison between the free space slit and the photonic slit, a fiber coupling setup is added to the entrance of the usual spectrometer setup. In Figure 5.9, the extended light source is focused onto a 50 μm core stepped-index multi-mode fiber using a condenser lens. Then for the free space slit case (i.e. Figure 5.9(a)), the output of the fiber is placed on the slit entrance to restrict the input width based on the designed resolution. In the photonic slit case (i.e. Figure 5.9(b)), the chip replaces the entrance slit and the wedge fiber input is placed at the focal point of the condenser lens. Both fiber ends are terminated with FC/APC connectors and therefore the input coupling system remains the same in both cases. With the same input power and the same spectrometer design, the intensity and FWHM profile of the output spectrum can be used to compare the performance between the free space slit-based and photonic-slit based systems.

The spectral resolution is dictated by the output dimension of the chip which has a thickness of about 1 μm. Therefore the slit in the slit-based setup should also have a

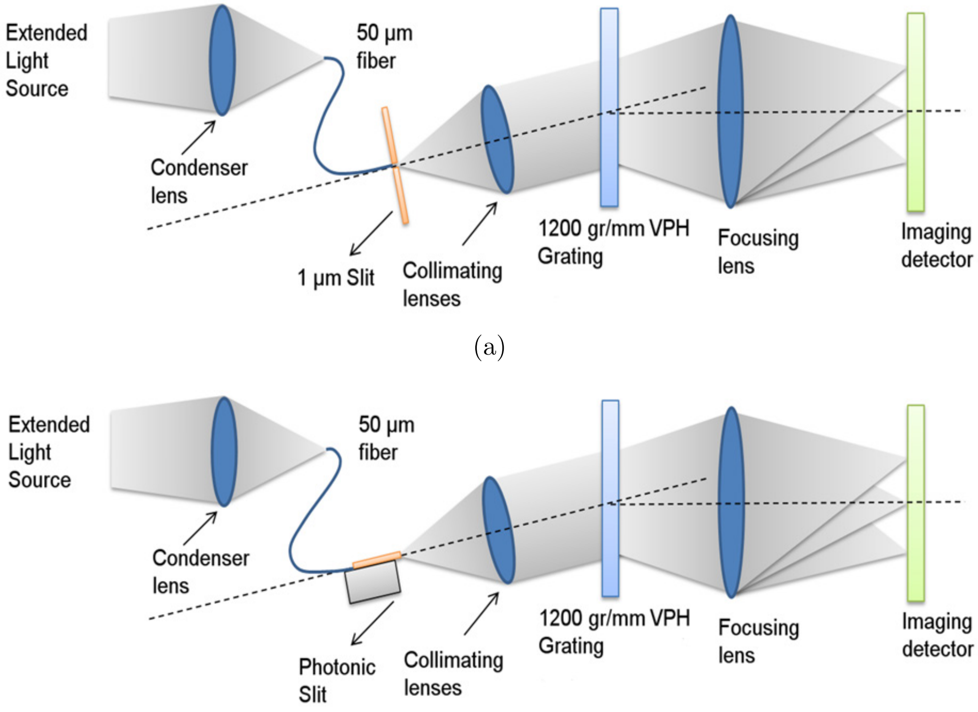

(a)

(b)

Figure 5.9: The high resolution spectrometer design used for performance testing of slit versus the photonic slit (a) proposed setup for the spectrometer with an entrance slit (b) proposed setup for the spectrometer with the photonic chip as entrance slit.

similar width to achieve the same spectral resolution. By using a 1 μm entrance slit, the imaging optics should be selected such that the imaged spot is in the order of the detector pixel size or larger. In this case, an imaging magnification of 8 was chosen such that the 1 μm slit width would become an 8 μm spot on the detector. This results in at least a pixel wide imaged spot in most of the visible range detectors with pixel sizes of 6 μm or less. The imaging optics diameter was chosen according to the grating size which is $1''$. The entrance collimating lens was chosen to be an $f/2$ lens with a focal length of 50 mm. To get a magnification ratio of 8, the focusing lens needs to have a focal length of 400 mm. The detector used is a μEye UI-1225-LE model with a pixel pitch of 6 μm.

The VPH grating was manufactured by Wasatch Photonics with 1,200 lines per millimeter and Bragg diffraction angle of 35° at the wavelength of 912 nm. The calculated linear dispersion on the detector is calculated to be 1.1565 nm/mm at the operation wave-

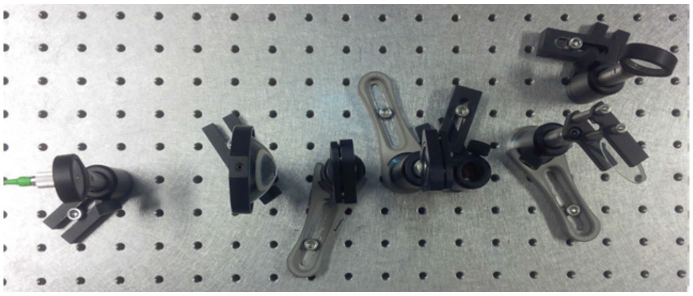

Figure 5.10: The bench-top setup of the designed spectrometer.

length which yields a spectral resolution of 0.0069 nm/pix and the resolving power of $R = \frac{\lambda}{d\lambda} \approx 130,000$. Using Avantes Mercury-Argon calibrated light source and Argon emission lines at 912.30 nm and 922.45 nm, the constructed spectrometer was calibrated and the spectral resolution and resolving power was determined. The measured spectral resolution was 0.0084 nm/pix and therefore the resolving power was about $110,000$. In the next section, a number of fabricated chips are tested and characterized using some of the above mentioned characterization methods. The results are discussed in each case as the shortcomings of each method is addressed in a chronological order in each of the cases.

5.2 Results and Discussion for the Photonic Slicer

In this section, four types of the fabricated wedged fiber coupler system are reported and characterized. As the progression shows, the characterization methods used are advanced and the fabricated chips are refined to improve the results.

5.2.1 *Type A*: Flipped-chipped Tapered Waveguides on Top of the Polished Wedge Fiber

These series of chips only have one millimeter of straight waveguide at the end of the taper for modal stabilization. In addition, this would reduce the tolerances on the cleaving location at the end of the waveguide. In order to reduce the propagation losses, in the first series of fabricated chips, this straight waveguide region length was kept to a minimum. As it was illustrated in Figure 5.4, the output mode can be imaged using a high numerical aperture objective lens system. However, due to wedged fiber imperfections and additional space present between the fiber and the chip, a percentage of the input light is not coupled

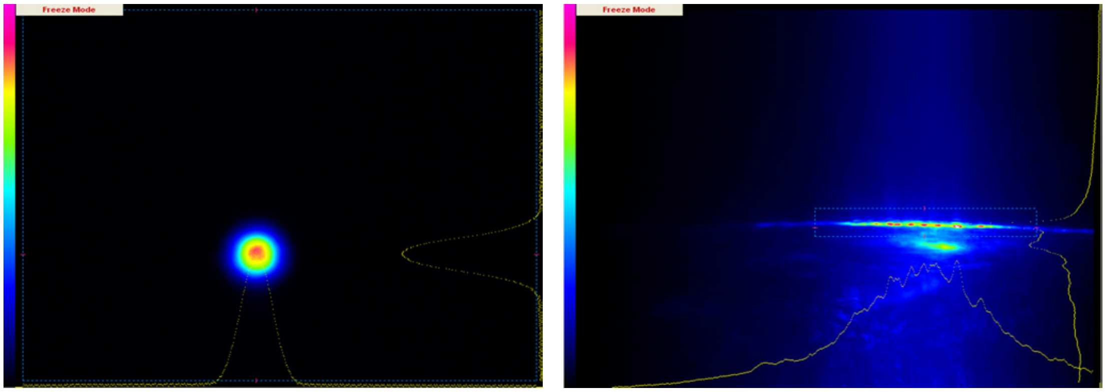

(a) (b)

Figure 5.11: Imaging of the input and output of the *type A* photonic slit system (a) Imaged input multi-mode fiber tip. (b) Imaged output facet of the photonic slit demonstrating the stray light issue.

into the waveguides. Therefore, the stray light would be present at the output which results in difficulties when the waveguide facet is imaged. This effect was shown in Figure 5.1 when introducing the far-field imaging concept. Due to the small dimension of the waveguides group (i.e. rectangles of $\sim 1 \times 100$ μm), any attempt to spatially filter the stray light out and alignment of such spatial filters proves to be very difficult. Figure 5.11 shows the imaged input fiber tip as well as the output facet image where the stray light is present under the main waveguides. This would cause additional broadening of the spectral line and hence loss of resolution. In addition, any further measurements of output optical power and output divergence angles would become inaccurate due to overlap between the stray light and the actual output mode from the chip facet. Therefore, in the following sections, the two device types of B and C are fabricated and tested to address this issue.

5.2.2 ***Type B***: S-Bend Based Photonic Slit

In order to spatially filter out the stray light from the residual wedged fiber tip and separate the modes, an S-bend waveguide was added to the output of the tapered up channel waveguides. Figure 5.12 shows the fabricated S-bend as it extends out from the coupling region between the polished wedge fiber and the tapered up channel waveguides. The S-bend laterally displaces the output mode for 200 μm while it would also extend the optical mode radiation point along the optical axis. The change in the focus point of the imaging

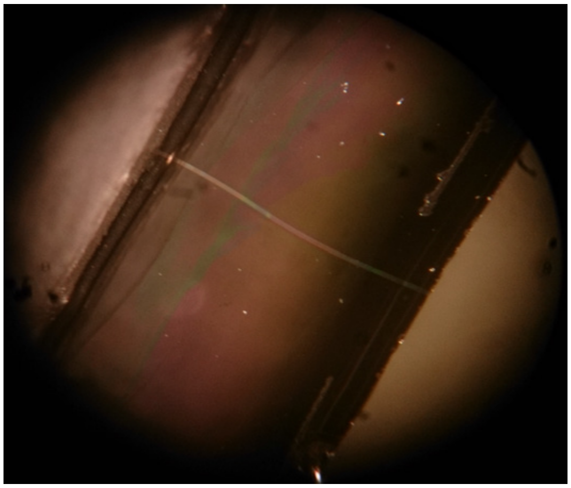

Figure 5.12: The extended S-bend section of the waveguides to spatially filter the waveguide modes from the stray light.

optics (based on the S-bend length) would also help with filtering the stray light out due to the fact that the stray light and the waveguide modes have different divergence properties. Figure 5.12 also shows the effect of chip extension from the edge of the fiber block. The epoxy used to bond and fix the chip to the polished wedge fiber block would form thin layers on the chip extending from the fiber block. This thin-film effect is noticeable within the figure as different colors reflect due to Fabry-Perot effects of thin-films. The existence of an additional epoxy layer on top of the planarization layer changes the propagation medium and modal confinement factor for the coupled multiple channel waveguides.

While the output mode of the S-bend structure had improved due to separation from stray light, the optical losses through the S-bend section was higher than expected. Therefore, this was investigated further by using the same fiber tip sensing mechanism used for inspection and characterization of the polished wedged fiber. Figure 5.13 shows the optical setup and a top view marking the regions around which the measurement was done. In Figure 5.13(b), the voltage readout from the photodiode is plotted for the cases when the light source is off and then turned on as progressing along the S-bend. Towards the facet of the chip in region I, there is some light coupled to the fiber tip. As the tip is moved back towards the fiber block, first the photodiode voltage readout is reduced but then there is a noticeable increase at the very end in region IV which is an indication of stray light from the wedged fiber end. In another attempt to verify this measurement, the S-bend section of the waveguide was imaged using an objective lens at an angle. Figure 5.14 shows the light leakage out of the waveguide region at steps through the S-bend. By changing the

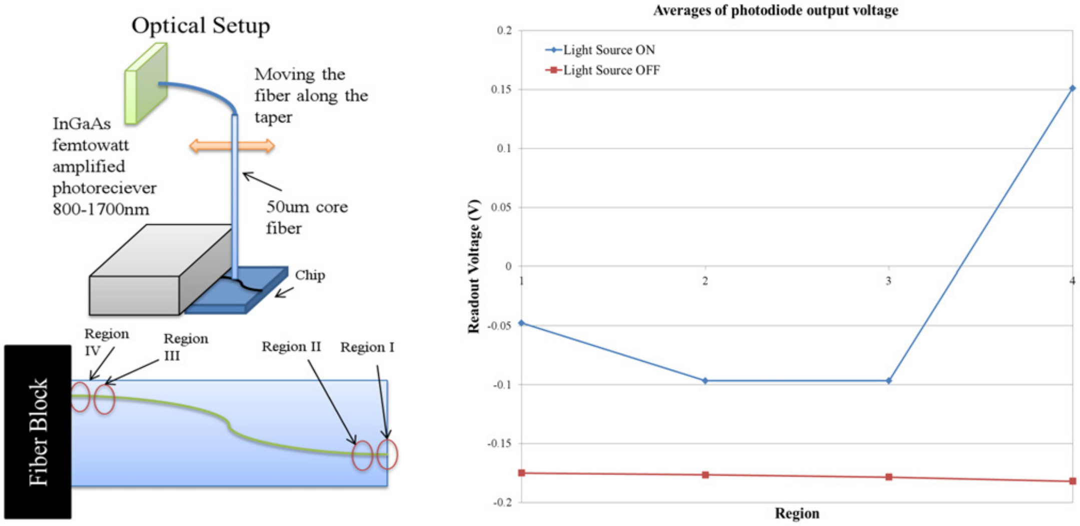

(a) (b)

Figure 5.13: Fiber tip measurement system to determine optical losses along the S-bend structure (a) The optical setup on the top shows the measurement system and the top-view image at the bottom shows the measurement region designations. (b) Plotted voltage readout from the photodiode as progressing from region I to region IV along the S-bend.

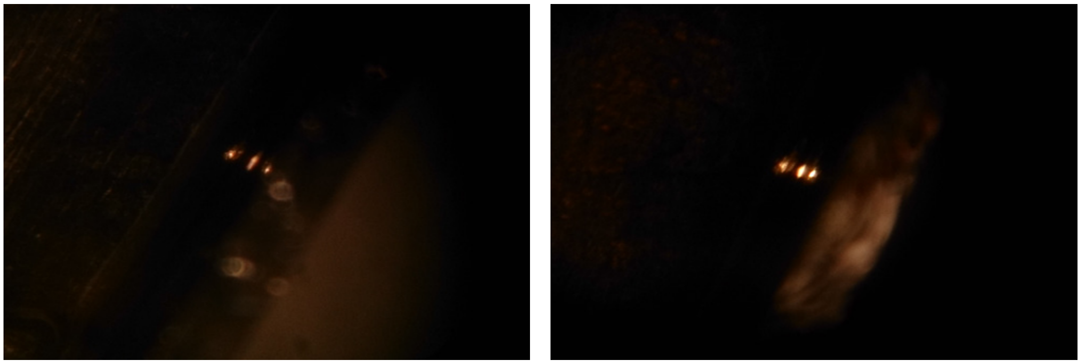

(a) (b)

Figure 5.14: Imaging showing light leakage from the S-bend at multiple sections along the structure (a) The objective lens focus is at the very begging of the S-bend (b) The objective lens is focused on the end facet of the S-bend.

distance between the objective lens and the leaking spots, the images can be focused at various points along the S-bend. At the starting point, the stray light output from the wedged fiber area is evident (i.e. Figure 5.14(a)) while at the end, the waveguide facet is emitting the remaining optical power (i.e. Figure 5.14(b)). The combination of epoxy layers extended on the S-bend as well as the low modal confinement through the curved sections of the S-bend has contributed to high optical losses in this chip. While the optical losses where high, the optical output mode shape was found to be closer to the fundamental super-mode of the multiple channel waveguides due to the fact that higher order modes would naturally leak out of an S-bend because of the lower confinement factor. Since the S-bend design is not optimal in terms of propagation losses, in another attempt, the next generation of the chips were built using a straight and longer stabilizing waveguide. This new type is explained in more detail in the following sub-section.

5.2.3 *Type C*: Stabilizing Waveguide Based Photonic Slit With Passive Coupling

By extending the output waveguide further in a straight line, the stray light can be simply filtered out due to being emitted at a different focal plane. Therefore, similar to the S-bend case, the facet is imaged with minimum stray light and without additional modal losses due to the S-bend curved paths. This improves the throughput of the system. Figure 5.15 shows the output facet of this longer stabilizing waveguide. The dark-field image shows the stray light present under the chip which can broaden the line width when the chip is used as a pseudo-slit in a spectrometer. Therefore, minimizing the stray light output is essential to the spectrometer performance.

Since the stray light and the light leakage was minimized in this type of fabricated chip, further characterization was performed on this chip. In the first step, the divergence angle was measured in the x and y directions using the techniques discussed in the far-field measurement section at the beginning of this chapter. The far-field images of this chip is shown in Figure 5.16 where the images are taken at 100 μm apart showing the diverging output mode. Figure 5.16(a) shows the main waveguide output in the middle with a small tail around it from the optical power coupled into the thin-film area around the waveguides. While the facet dimensions are 125 μm wide by 1 μm tall, the ellipse-like far-field image with a larger vertical semi-major axis shows a larger vertical divergence angle compared to the horizontal direction divergence angle. Taking the cross-cut through this central area and using FWHM of the intensity profile, the divergence angles can be calculated. Several images were taken at 50 μm intervals up to 1 mm away from the closest possible distance

(a) (b)

Figure 5.15: Imaging the facet of the long stabilizing waveguide (a) The bright-field image showing the facet of the chip (b) The dark-field image showing the waveguide output and the stray light underneath it.

to the output facet. These images were used to determine the output divergence angles. When the input wavelength is 1050 nm, the output divergence angle was measured to be $\theta_x = 0.57$ and $\theta_y = 5.42$ degrees. The x direction divergence is expected to be very small due to the fact that the coupled waveguides have a width of about 125 μm and the optical

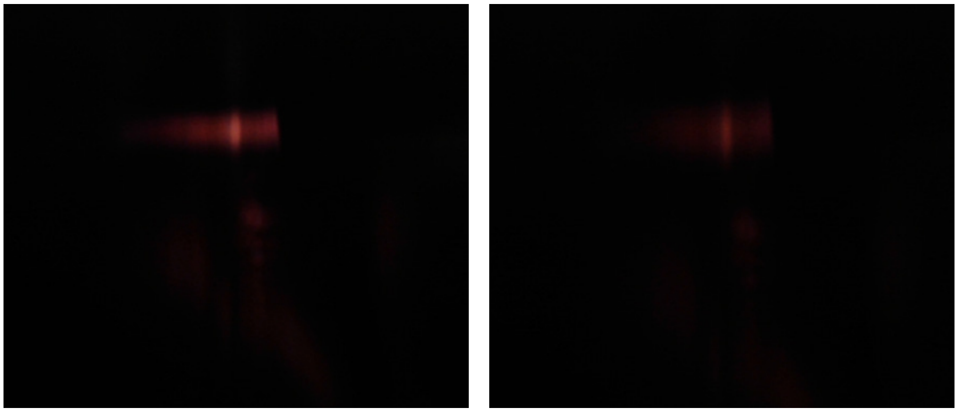

(a) (b)

Figure 5.16: Far-field images of the waveguide outputs at two different distances that are 100 μm apart. (a) z_0 (b) $z_0 + 100$ μm.

mode is a pseudo-Gaussian super-mode. In the y direction, however, the thickness of the waveguide is about 1 μm and therefore the output mode has a larger divergence angle. In the next step, the output and input power is measured using an integrating sphere power meter. At the input wavelength of 1050 nm, the input power in the input fiber is 2.14 mW and the output power measured at the output facet is 125 μW from which 94% of power lies within the fundamental super-mode of the multiple channel waveguides.

Using Equation 3.3, the β metric of the system can be calculated which compares the photonic slit performance to a slit. One of the assumptions made during the β calculation phase is that the output super-mode is approximated by a Gaussian beam carrying all the optical power. In essence, this is not true as the effect of higher modes with larger divergence angles are completely ignored. While this would result in a lower β factor in practice, measurement of the divergence angle at longer distances from the waveguide would be more accurate for β estimation. In a spectrometer setting, the slit needs to be imaged and the collimating lens is usually not a fast lens. Therefore, some of the optical power is lost due to the imaging optics limitations. In addition, one other assumption is the dimensions of the output multiple channel waveguides. Depending on the modal coupling dynamics and fabrication and flip-chip variations, the actual dimensions of the facet can differ from one chip to another. Therefore, one mechanism to overcome such output dimensions uncertainty is to back-calculate the output facet width from a range of assumed β values using the β formulation. The output width can be written as follows:

$$w_{out} = \frac{\left({}^{P_{out}}/_{P_{in}}\right)}{\left({}^{\beta}/_{w_{in}}\right).\left({}^{\theta_{out}}/_{\theta_{in}}\right)} \tag{5.2}$$

Assuming a Gaussian beam radiated from the waveguide output facet of width w_{out}, the projected beam width can be calculated at the initial distance of z_0 from the facet. Then using different β values, various far-field beam widths can be calculated and overlaid on top of the actual beam at z_0. In this manner, the range of β value for the chip under test can be found. Figure 5.17 shows the range of β estimates with different color codes overlaid on top of the experimental data. In order to find the experimental β value by means of overlaying on top of the estimated values, the average baseline of the experimental data is deducted from the plotted data. This explains the negative intensity values at some points on the graph which would be on no interest in the *beta* value estimation. The plot shows that the experimental β value observed is within the range of 1.25 - 1.5. This is much less than the theoretically predicted values of β and is mainly due to optical losses present in the experimental coupling system. In addition, within the calculation of β values, it was observed that the β of $1.25 - 1.5$ corresponds to effective output modal width of about $5 - 6$ μm assuming a pure Gaussian output beam. While the waveguides are only 1 μm

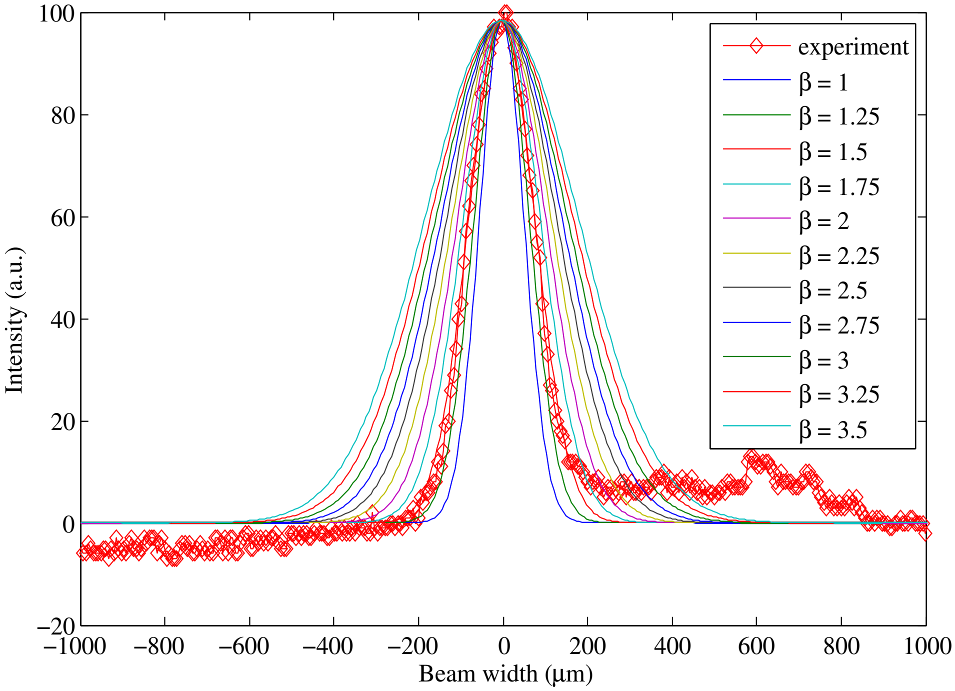

Figure 5.17: Output mode width calculated from different β estimates. The experimental output width shows the device would have a respective β value between 1.25 and 1.5.

thick, there is no hard aperture effect and a percentage of the optical power extends to the cladding area around the waveguides. In addition, due to the fact that the output beam is not a pure Gaussian mode, the beam diverges at a larger angle and therefore it appears as if it is emitted from a larger aperture. This can be characterized using the beam quality factor or $\mathcal{M}^2$ for lasers [97]. However, it was not investigated further here due to the variations between different wedged fiber setups and therefore the modal content of the output beam. The calculations done in this section are based on the assumption that all of the measured optical power reaches the detector in a spectrometer setup. In other words, the output mode that is being imaged is very close to a Gaussian beam and there is no losses associated with diverging higher order modes in the output. Additionally, the uncertainty around the effective modal width of the output adds to measurement error in calculation of the β value as outlined here. In practice, the higher order modes add to the optical losses and the imaging of micron level facets and measuring the effective mode area would be very challenging. Therefore, in the next section, the photonic slit is placed within a spectrometer setup and compared directly with a slit of similar size.

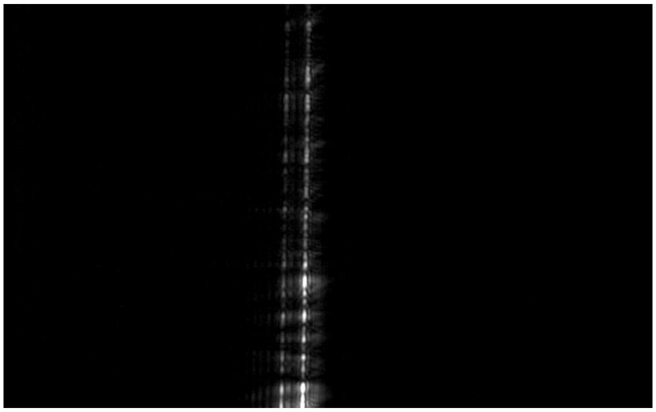

Figure 5.18: Imaged slit on the detector when the input is coupled to a 632 nm laser diode source. The lines show mode hoping of the laser diode.

5.2.4 *Type D*: Active Coupling System using CMP Wedged Fiber

The most accurate way to compare a photonic slit to a physical slit is using them in a spectrometer setup. As mentioned earlier in the hardware setup section, the light collection part as well as the dispersing, focusing and detector part of the setup remains the same to allow for accurate throughput and line width comparison between the two. The details of the setup and its configuration for both cases were discussed in Section 5.1.3. In this section, the results are provided and discussed.

In the first step, the spectrometer was built and aligned at 632 nm to test for coupling and system setup procedures. A laser diode was used as the input which was coupled into a 50 μm core fiber. Then the fiber was taken to the slit using a 3-axis stage. Figure 5.18 shows the imaged slit on the detector side. The two distinct lines are laser lines that showed constant switching with time in a discontinuous manner. This phenomena is known as mode hoping which is in general related to the case temperature and injection current fluctuations. The larger discrete wavelength jumps happen when the laser jumps from one longitudinal mode to the other. Due to the extremely high resolution of this custom spectrometer, the mode hops are clearly visible (i.e. Figure 5.18). According the the experimental resolution observed and described in Section 5.1.3, these distinct wavelength shifts are apart by approximately 0.21 nm.

After the initial test at a visible wavelength, the setup was rearranged for the central wavelength of 908 nm. By increasing the operating wavelength, the propagation losses along the coupling system are expected to decrease and therefore a better β value should be observed. In this setup, first the 1 μm slit was used and the fiber was placed as


(a) (b)

Figure 5.19: Imaged 908 nm line by the spectrometer setup with (a) 1 μm Slit (b) Photonic slicer.

close as possible to the slit without any lens system. Figure 5.19(a) shows the imaged slit on the detector. Since the fiber is used without any lens before the slit, the vertical extent of the image correlates to the divergence of the beam from the fiber tip to the collimating lens. The width of the image, however, depends on the width of the slit and the resulting diffraction. To control the input light power to the spectrometer, the laser diode is stabilized via a laser current driver and a thermo-electric cooler (TEC) from Thorlabs (i.e. LDC205C and TED200c respectively). The input is kept the same and the slit is swapped with the photonic slicer in the same setup. The wedged fiber is also terminated with an FC/APC connector which would be plugged to the input coupler. Then the chip is placed at the focal plane of the collimating lens and the active coupling is done. Figure 5.19(b) shows the imaged chip in the spectrometer setup. The imaged line is not as narrow as the slit and stray light is still present which can be due to imperfections in the fiber tip. While the aberrations present could ultimately result in line broadening and lower resolution, they can be removed using additional spatial filtering and aperture stops.

In order to better study the line profile, the 2D array of spectral data were vertically binned and plotted together. Figure 5.20 shows the two line profiles. The slit profile also shows a slight broadening of about 1 nm which can be due to mis-alignments. The photonic slicer profile shows similar broadening as mentioned earlier which can be corrected by use of additional spatial filters. It is important to note that despite the imperfections in the achieved experimental data, the main lobe intensity for the photonic slicer is 33% higher

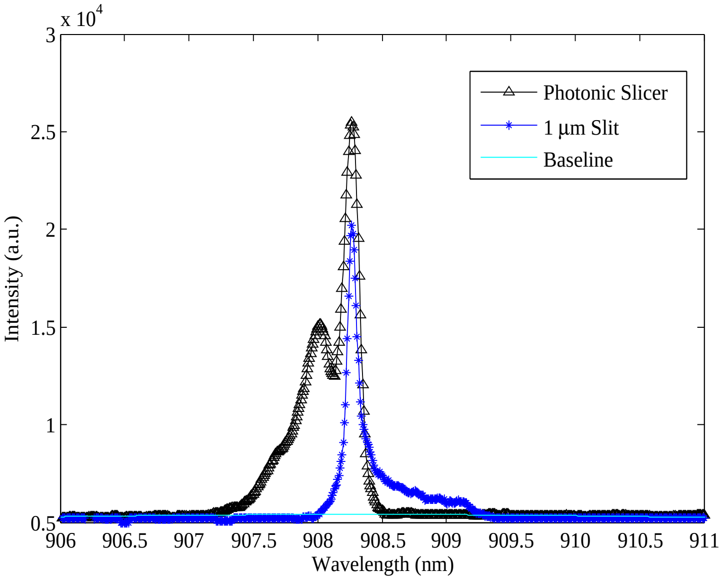

Figure 5.20: Vertically binned spectra of the 908 *nm* laser diode using the slit and photonic slicer.

than the slit counterpart. In order to determine the line broadening, Gaussian fits were used similar to the examples given in section 5.1.1 for measuring the characteristics of the main lobe. The FWHM of the photonic slicer was increased by 26% from 0.101 *nm* in the physical slit to 0.126 *nm* in the photonic slicer case. This result demonstrates the experimental feasibility of using modal coupling to perform optical slicing in an integrated photonic chip.

5.3 Conclusion

In this chapter, a number of characterization techniques were proposed and developed to experimentally test and validate the concept of an integrated photonic slicer. A suite of measurement techniques and optical setup were used including near-field and far-field imaging, coupling efficiency measurements, β value estimation and also a high resolution near infra-red spectrometer setup to measure the efficiency of the photonic slicer against a conventional slit. A number of these techniques have been used to characterize four generations of these devices. These devices were designed, fabricated and tested in the chronological order that has been provided here. Each device is meant to be an improved

Device Type	**Input Aperture**	**Output Aperture**	**Estimated β**	**Measured β**
A	50 μm Fiber	$1 \times 100\ \mu m$	not measured - strong stray light	N/A
B	50 μm Fiber	$1 \times 100\ \mu m$	not measured - high optical losses	N/A
C	50 μm Fiber	$1 \times 125\ \mu m$	$1.25 - 1.5$	N/A
D	50 μm Fiber	$1 \times 125\ \mu m$	N/A	1.33

Table 5.1: Estimated and measured β values from different fabricated samples.

version of its predecessor based on the results and feedback achieved from the previous generation experiments. The details of the experimental results are discussed in length through the second half of the chapter using the experimental methodologies explained in the first half. Table 5.1 summarizes these results further. The β estimate using Equation 3.3 could not be calculated for the first two devices. Having strong stray light on the output prevented accurate estimation of divergence angle and actual output aperture dimensions. In addition, high optical losses would result in a inferior device compared with an actual slit. Device C showed better throughput and performance which resulted in an estimated β in the range of $1.25 - 1.5$. Device D however, is the one that was actually used in a spectrometer setup to measure the β value instead of making an estimated guess. This was done by direct comparison of a slit throughput versus the photonic slit throughput in a similar setup.

In order to compare these results with other slicer technologies, the features and results of the proposed structure are compared and summarized in Table 5.2. It should be noted that the implementation technology of each device is different and each device offers its unique advantages. For instance, the free space implementation of HTVS [27] with a spectrometer is the most versatile in terms of wavelength operation range and throughput although it lacks the smaller footprint and robustness of integrated photonic based spectrometers. The photonic lantern on the other hand, is an interesting design tested in the infrared region reporting low losses in a much smaller footprint. However, use of the coupler for larger core multimode fiber is not feasible due to large number of transitions needed between the multiple input modes and single mode output fibers. In addition, the estimated β value is low due to the fact that the cladding of individual single mode fibers increases the output aperture area.

The photonic dicer on the other hand addresses some of the shortcomings of the photonic lanterns such as fiber assembly complexities and low β estimates due to individual fiber claddings. In terms of operation wavelength, the photonic dicer has also been tested in the 1550 nm region and it is not clear how it would perform in the near infrared or visible range. While the best throughput reported in [62] is about 57% at 1550 nm, the actual measured throughput varies between $9 - 44\%$ based on the adaptive optic coupling system conditions and performance. Hence, achieving a high throughput and therefore a high β value requires a complicated coupling system. In addition, fabrication of 3D waveguides in glass slabs is a complex and lengthy procedure. This becomes more prominent as the input fiber size increases from 50 μm and the number of individual waveguide routings increases. As a result, there would be larger transitions in all three dimensions and the length of the device would also increase. The estimated β value based on the parameters reported/envisioned for the photonic dicer in [62] is about 1.66.

While the end-to-end throughput in the proposed device is estimated to be around 3% from the experimental results, the coupling will improve at longer wavelengths since the material absorption due to fabrication imperfections is decreased. The simulations indicate that the coupled power can be increased to above 50% if the following improvements are made: the distance between the wedged fiber to the waveguides is minimized, the wedged fiber profile is better controlled for adiabaticity, and refractive index differences between the fiber clad and the planarizing layer is minimized. Therefore there is room for further performance improvements in the proposed device by refining the fabrication processes. It should be noted that the device performance cannot be compared directly with other devices reported in literature due to the smaller operation wavelength and higher output spectral resolution (i.e dispersive direction width of 1 μm instead of 9 μm).

Device	**Input Aperture**	**Output Aperture**	**Implementation**	**Throughput**	**Operating Range**	**Estimated β value**
HTVS [27]	200 μm fiber	14×500 μm	free-space	$< 95\%$	visible	2.24
Photonic Lantern [11]	80 μm fiber	125×875 μm	fiber based	$< 89\%$	$1000 - 1800$ nm	0.184
Photonic Dicer [62]	50 μm fiber	9×300 μm	3D waveguides	$9\% - 44\%$	1550 nm	1.65
Proposed Device	50 μm fiber	1×125 μm	planar integrated photonic chip	$\sim 3\% <$	$900 - 1000$ nm	1.33

Table 5.2: Comparison of the experimental results with other competing platforms and technologies for increasing optical throughput in a spectrometer.

Chapter 6

Optimization of Multiple-Slot Waveguides for Biochemical Sensing

In the previous chapters, a novel photonic slicer chip has been proposed and demonstrated for applications in spectroscopy. While, conducting this research, other applications for the photonic slicer were also thought of and one very promising area is their use in optical bio-chemical sensors. Optical bio-chemical sensors have been the subject of numerous studies over the past decade due to their inherent advantages in various fields such as medical diagnostics, environmental monitoring, drug development, process-quality control and homeland security [98,99]. Some of these advantages compared to conventional electro-mechanical transducers includes small size, immunity to electromagnetic interferences, ease of multiplexing using wavelength encoding and their effectiveness in remote sensing [100]. Optical sensors can be categorized into two major groups; fluorescence based detectors and label-free detectors. In fluorescence based detectors, target molecules are labeled with fluorescence tags where they fluoresce during the detection process. This type of sensor is extremely sensitive providing detection sensitivity down to a single molecule [101]. However, the measurements are extremely cumbersome while being invasive to the monitored process. In addition, since the number of flourophores attached to the target cannot be controlled, quantitative measurements are difficult to be performed [102]. On the other hand, in label-free detectors, targeted molecules are detected in their natural form. The targeted molecules are surface attached to the optical sensor using probe molecules which change the optical properties of the sensor. Among different optical sensors, sensors based on silicon-on-insulator (SOI) photonics are favorable due to their compatibility with CMOS fabrication and the possibility of integrating detection and processing units on the same chip [100]. Furthermore, integrated sensors allow for integration of multiple sensors in a single chip. Therefore, different sensors based on directional couplers [103], Mach-Zehnder interferometers [104], Bragg grating based Fabry-Perot resonators [105], microdisks [106], microtoroids [107], photonic crystal cavities [108], microring resonators [109], and slot waveguides [110] have been proposed in literature. Generally in such sensors, except for photonic crystal cavities, a targeted molecule is probed by the evanescent field of the guided wave. The surrounding medium acts as the cladding for the waveguide which typically has a refractive index of about 1.325 at wavelength of 1550 nm for water based solutions. The surrounding refractive index is perturbed by attachment of higher index ($n \sim 1.45 - 1.6$) organic molecules to the sensor surface which results in a spectral shift in the resonant cavity response. Mach-Zehnder interferometers [104], Fabry-Perot resonators [105], microdisks [106], photonic crystal cavities [108] and ring resonators [109] have been demonstrated using silicon photonics. Mach-Zehnder interferometers suffer from low Q-factor and long device lengths for higher sensitivities. Bragg-reflectors and Fabry-Perot based resonators both have a drawback of high insertion losses. Photonic crystal devices also have high propagation losses with the additional difficulty of coupling light in and out of the chips reproducibly. Microdisks suffer from large number of excited whispering gallery modes that make detection difficult due to interferences. Ring resonators on the other hand, offer the most promising solution as they have low insertion loss, single mode cavities and high quality factors [111]. By simply changing the diameter of the ring in the resonator, one can multiplex different sensors on a single chip for different wavelengths.

One problem in all integrated photonics based bio-sensors is the coupling of light into the waveguides. Typically the waveguides are few hundred nanometers wide requiring high numerical aperture optics with stringent alignment tolerances to achieve coupling from a single mode fiber. Coupling from multi-mode fibers into these sensors has not been achieved or even tried yet. The proposed photonic slicer architecture could allow for low cost multi-mode fiber coupled sensors in future. One interesting platform for photonic sensors is the SOI photonic waveguide. Biochemical sensors based on SOI photonic waveguides have been studied extensively by researchers. In 2007, Vos *et al.* reported a sensitivity of of 70 nm/RIU for bulk refractive index changes, while a 625 pm shift was detected when label free proteins were present [109]. In a previous work [112], we proposed a new kind of biochemical sensor using silicon nanowire (SNOW) based ring resonators. It consisted of 9 rows of 40 nm diameter vertical nanowires with a pitch of 100 nm. It was shown that if the diameter is significantly smaller than the wavelength, the arrays of nanowires start to behave as an effective-index medium. Using SNOW, a five fold increase was achieved with a sensitivity of 350 nm/RIU. The fundamental mode in such structures is primarily a quasi-TM mode in which the electric field is polarized along the nanowire length. Therefore, the effective modal index in the structure is higher than the refractive index of the target sensing solution. If the effective modal index is reduced to the approximate refractive index value of the target solution, the sensitivity of the device can be increased with respect to refractive index changes. While reducing the diameter of the nanowires would help, the confinement of the propagating mode becomes an issue and hence the maximum sensitivity becomes limited. Although introducing transverse electric modes across the nanowires would help in increasing the sensitivity, but due to the nature of the nanowires, scattering increases the waveguide loss appreciably especially over waveguide bends.

Slot waveguides have been proposed in literature [110, 113, 114, 115] to increase the sensitivity even further. In slot-waveguides, the transverse electric field is enhanced in the low refractive index region sandwiched between two high index waveguides [116]. The low refractive index region can act as a channel for biological solutions therefore allowing the field to interact with the target medium. Since the field is enhanced in the slot region, the sensitivity of the structure is increased with respect to refractive index changes in the target medium. In one design, a sensitivity of 298 nm/RIU was achieved in a footprint of 13×10 μm [110]. In addition, multiple-slot structures have been proposed to further enhance the optical confinement in the low index slot regions and increase the sensitivity of the structure. Vivien *et. al* proposed a triple slot structure of silicon nitride waveguides on silicon oxide [114]. In a comparison, the reported modal power flux for TE mode of a single slot waveguide is 11% while this figure for a triple slot structure is estimated to be 18%. For a triple slot configuration, it is also reported that an improved normalized modal index variation of 20% and 60% is achievable in comparison with single slot and strip waveguide. This improvement shows how multiple-slot structures can be used to increase the sensitivity of such sensors. Sun *et. al* proposed and fabricated a polymer based multiple slot structure as a bio-sensor [115]. The structure consisted of four strips of SU-8 resist waveguides of 2 μm tall by 500 nm wide and three slots of 200 nm in between. They also reported a maximum bulk sensitivity of 244 nm/RIU. The achieved performance of these multiple slot waveguides is less than a single slot waveguide mentioned previously in [110] which is mainly due to the fact that in the multiple slot structure proposed, low contrast refractive index dielectric structures were used rather than high refractive index silicon.

The multi-slot waveguide is naturally compatible with the photonic slicer which consists of multi-core waveguide structure at the output. However, before we can design a structure, we need to optimize the multi-core waveguides for sensing purposes. Although multiple-slot structures have been proposed by various research groups, there is no detailed study of how different parameters influence the sensitivity of such devices and the maximum achievable sensitivity using high refractive index contrast materials. In this Chapter, a multiple slot waveguide in SOI is proposed and a systematic approach to optimize a bio-chemical sensor for maximum sensitivity is developed. The sensitivity can be numerically estimated by varying the cladding medium refractive index ,n_c, in a narrow range and finding the relevant change of modal index, n_{eff}. To determine modal index ,n_{eff}, a rigorous numerical approach based on vectorial finite element method (FEM) is used. According to the FEM modeling, a theoretical improvement of at least 3× can be expected in our proposed multiple-slot configuration. In addition, the effect of bends on the modal analysis and the resulting perturbation in multiple-slot modes in a ring resonator setup is studied. Even if we do not integrate the Photonic Slicer, this chapter provides systematic guidelines for designing multi-slot waveguide sensors and achieves the highest sensitivity reported in the integrated photonics bio-sensors.

6.1 Sensor Structure and design

The schematic diagram of a multiple-slot waveguide cross section is shown in Figure 6.1. The channels are silicon with refractive index of 3.476 at a center wavelength of 1550 nm. The lower cladding is chosen as SiO_2 with refractive index of 1.5 and the upper cladding is the solution containing the targeted molecules to be detected. In the simulation, the SiO_2 layer is considered to be semi-infinite and the upper cladding of water based solution has a refractive index of 1.325 which will change due to environmental factors [117]. Structure modes are calculated using a vectorial FEM in which the fundamental quasi-TE mode (henceforth simply called TE mode) is considered. While the structure supports multiple modes, higher order modes would not survive waveguide bends due to higher propagation losses. The sub-domains in the structure cross section were partitioned into triangular mesh elements with quadratic Lagrange functions. A non-uniform meshing method is used

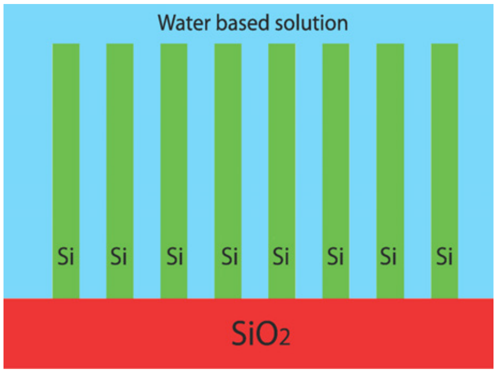

Figure 6.1: Multiple-slot waveguide shown with 8 ridges of Si constructing a 7-slot waveguide.

which has a higher density near the index variation boundaries. The nonuniform meshing allows for more accurate simulation of surface attachments. The maximum mesh size in the bulk region was chosen to be 400 *nm* while the minimum was 0.1 *nm* along the material boundaries. Further, the change from the minimum to maximum was weighted more towards the smallest grid size ensuring a minimum of 10 grid points in any layer of the structure. This also ensured that there was at least 10 grid points within the 1 *nm* thick surface layer with an uniform grid. The mode was converged till the error in the effective modal index was less than 10^{-7}. This would also improve the graded index approximation of FEM solvers by considering much finer grid points at the boundaries.

The lower effective modal index of the TE mode and its high intensity in the slot region makes the sensor more sensitive to refractive index changes of the solution and surface agents. Figure 6.2 shows the cross-sectional profile of the TE mode in the structure in which each channel has a width and height of 80 *nm* and 1 *μm*, respectively. The slot width within the waveguides is 40 *nm* and the whole waveguide consists of 17 ridges and 16 slots. At this step, these parameters are chosen for illustrative purposes and they are optimized quantitatively later in the following section.

In a qualitative manner, parameters such as width of the channels, number of slots, pitch and surrounding medium index determine effective modal index of the overall structure and cut-off conditions. Figure 6.3 illustrates how the effective modal index of the TE mode

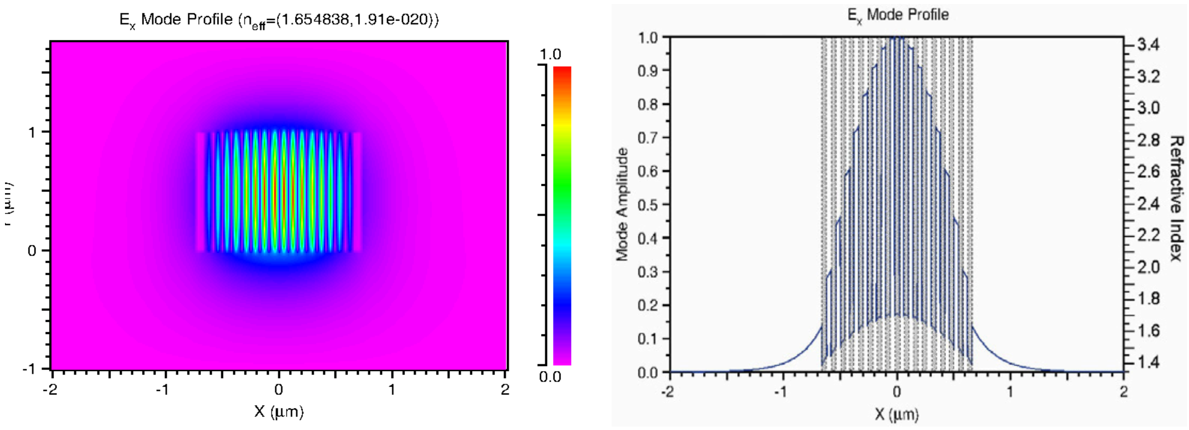

(a)

(b)

Figure 6.2: TE mode profile of a multiple-slot structure with 16 slots, 1 *μm* height, 80 *nm* ridge width and slot width of 40 *nm*. (a) the 2D z-cut of the field profile. (b) The corresponding lateral cut of the field at $y = 0.5$ *μm*.

changes by changing such parameters. In Figure 6.3(a), the width (w) of the channels is varied between 15 nm to 170 nm while the pitch used for the structure is $w + 90$ nm. This assumption keeps the slots width constant at 90 nm. The effective modal index is calculated for cases in which the sensor is primarily used in the basic water-based analyte with a refractive index of 1.325. Change of effective modal index versus the number of slots is shown in Figure 6.3(b) where $w = 80$ nm and $slotwidth = 90$ nm. It is seen that

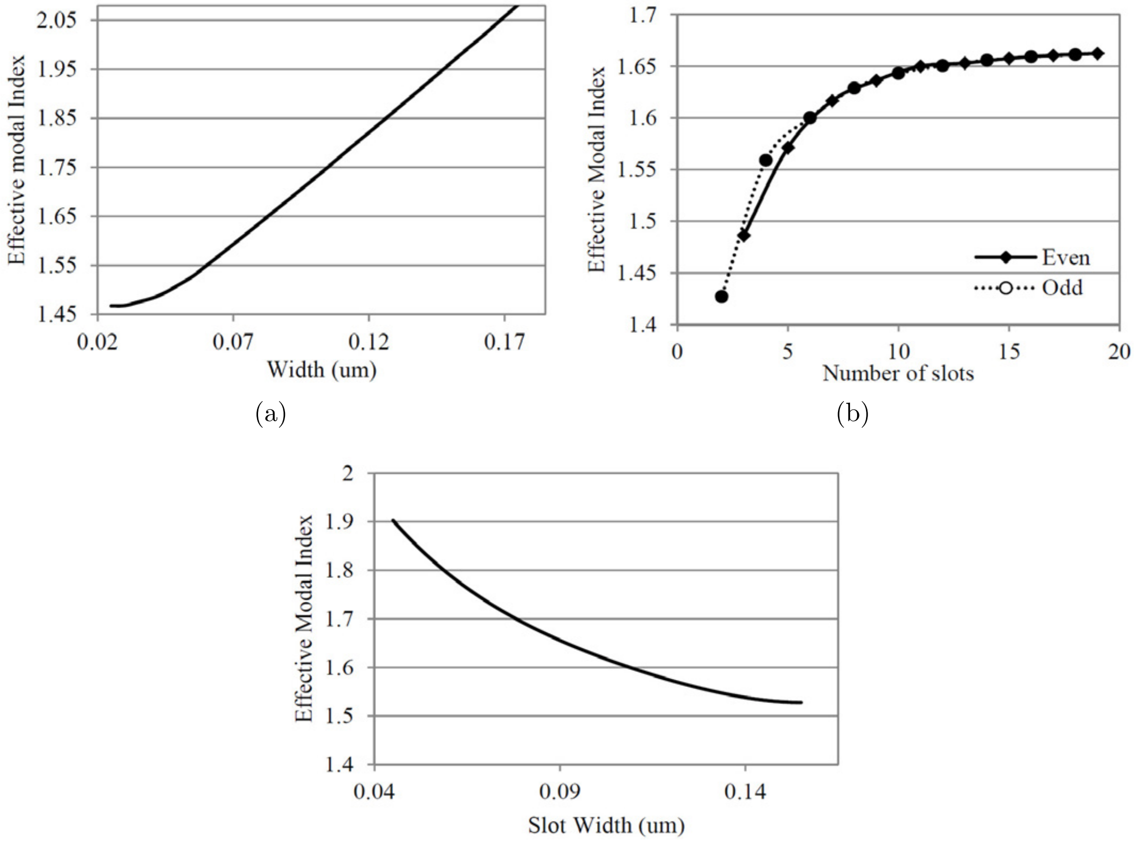

(a) (b)

(c)

Figure 6.3: Change of effective modal index with different parameters. (a) Change of n_{eff} versus width where there are 16 slots and the slot width is kept constant at 90 nm. (b) Change of n_{eff} versus different number of slots in even and odd numbered cases where the ridge width and slot width are kept constant at 80 nm and 90 nm respectively. (c) change of n_{eff} versus different slot widths when the number of slots is 16 and the ridge width is constant at 80 nm.

as the number of slots is lowered in one end, the effective modal index reduces to a value below the refractive index of the lower cladding (i.e. SiO_2). Figure 6.3(b) demonstrates this cut-off region in which there is no propagating mode for the structure with only $N = 1$ or 2 slots. On the other hand, as the number of slots increases the effective modal index of the structure flattens out and there is not much change in the effective propagation index of the fundamental mode. This trend shows that increasing the number of slots would not change the sensitivity of the structure beyond a certain point as commonly suggested in literature [115, 118]. Therefore, sensitivity tends to be more dependent on the channels width and pitch. In the next section, sensitivity parameter is introduced and the relative sensitivity values are calculated for bulk and surface sensing in different scenarios.

6.2 Bulk and Surface Sensing

The response of the sensor to bulk and surface refractive index changes can be quantified by considering the following sensitivity formula as a figure of merit for optimization [114].

$$S = \frac{\partial n_{eff}}{n_{eff}} \tag{6.1}$$

In order to find bulk sensitivity changes, the refractive index of the surrounding medium was changed and the effective modal index of the resulting optical mode was calculated. By calculating the above mentioned figure of merit, one can optimize the waveguide for maximum sensitivity to bulk changes. Surface sensing also plays an important role in a wide range of biochemical applications including DNA hybridization, antigen-antibody reactions and protein attachments [119]. A layer of receptor molecules that are surface attached to the sensor can be used to perform selective attachment to targeted molecules. Since the refractive index of the molecule is different from the surrounding medium, a change of refractive index happens at the surface of the sensor which is measured for detecting the presence of the molecule. A molecule layer with test thickness of 1 nm is assumed to be attached to the surface of the multiple-slot sensor. Water is considered as the surrounding medium with refractive index of 1.325 at a wavelength of 1550 nm [117]. The refractive index of the layer attached is considered to be 1.6, similar to 3-aminopropyltriethoxysilane (APTES) which we have measured previously [120] and controllably attached different thicknesses on the surface.

Different parameters of a multiple-slot waveguiding structure are changed to optimize its sensitivity for bulk and surface sensing settings. It is clear that the effective modal index of the whole structure depends on all the aforementioned parameters at the same time, hence in some cases, a recursive optimization method is needed to find the local optimum sensitivity point. Additional constraints should also be considered when optimizing the structural parameters. For instance, in case of surface sensing, the minimum slot width is suggested to be around 100 *nm*. It should be noted that external particles or molecules cannot be introduced in much narrower slot regions due to size constraints, capillary forces or other limiting criteria in certain liquids [121]. In this work, slot width of 90 *nm* was considered as a starting point for optimization.

Figure 6.4 illustrates the effective refractive index change versus different silicon channel widths for a structure with 16 slots. The two cases of bulk sensitivity and surface sensitivity are considered and they both show that refractive index change is highest when the ridge width is around 80 *nm* while the width of the slot is kept constant at 90 *nm*. As can be seen from the plot, the width of the silicon waveguides can be chosen to be in the range of $70 - 110$ *nm* for maximum bulk and surface sensitivities. Below 70 nm, the mode is not guided well enough by the silicon waveguides and above 120 nm, the sensitivity starts to decrease as the confinement within the silicon waveguide starts to increase. Another set of simulations were done for variant slot widths while the waveguide widths were kept constant. This would illustrate how the effective modal index changes with various slot widths for the cases of bulk and surface sensing. Figure 6.5 shows the n_{eff} change for slot widths ranging from $50 - 150$ *nm*. As illustrated, increasing the slot width would slightly increase the bulk sensitivity. On the other hand, as the slot width is increased, the surface sensitivity decreases due to lower field intensity in the slot region. Therefore, surface sensitivity is affected drastically by the slot width and one can conclude that it

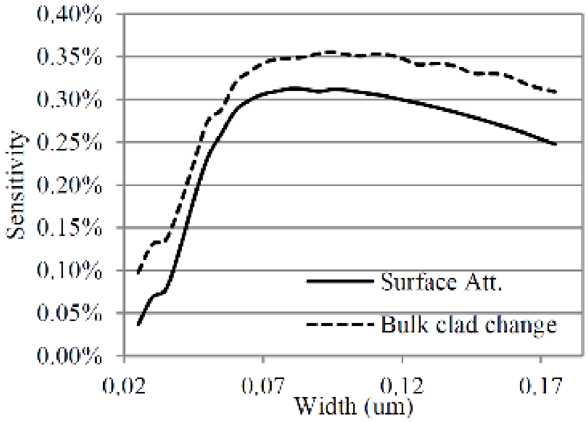

Figure 6.4: Change of effective modal index versus waveguides width for 16 slots with constant slot width of 90 *nm*.

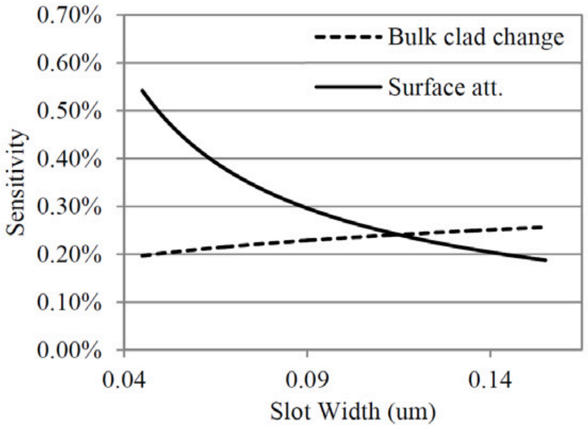

Figure 6.5: Change of effective modal index versus slot width for 16 slots as the ridge width is kept constant at 80 nm.

should be kept as small as possible for surface sensing applications. Therefore in this work, the slot width is fixed at 90 nm which is suitable for DNA surface attachments (typically in thicknesses of $2-3$ nm) in water based solutions while avoiding complications due to capillary forces for narrower slots [121]. It is notable that slot width plays an important role in modal confinement in the slot region that adjusts sensitivity of the structure to surface attachments or bulk refractive index changes. By decreasing the slot width, one can achieve even higher sensitivities. However, there is the cost of lower interaction between the sensing material and the sensor due to capillary and molecular forces. Hence, the minimum slot width should mainly be determined by fluidic flow through the slots.

While the slot width of 90 nm and the ridge width of 80 nm seems to show quite high sensitivities, the number of slots would also play an important role. In order to optimize that figure and achieve the best combination of parameters, a 2D parameter sweep was performed on ridge widths and the number of slots while the slot width is kept at its minimum allowable value to ensure maximum field intensity in the slot region. As illustrated in Figure 6.6(a)-(b), there is a sweet spot in designing multiple slot sensors for bulk and surface sensing purposes. As opposed to what has been suggested in literature [115,118] where increase of surface area increases the surface sensitivity, the current results show that increasing the number of slots does not increase the sensitivity indefinitely. After utilizing a certain number of slots, the modal index change would flatten out and there would be no sign of significant improvement in sensitivity of the sensor. In case of surface sensing, the minimum number of slots needed for maximum sensitivity is shown to be 16 (Figure 6.6(b)). Having more than 16 slots would have minimal effect on sensitivity of the sensor while increasing design complexity and reducing the efficiency of the overall system. Considering the even and odd number of slots, it can be seen that the even number of slots (odd number of silicon waveguides) shows a slightly higher sensitivity which can be related to better structural symmetry where one ridge is present at the center of the multiple-slot waveguide. On the other hand, bulk sensitivity would hardly change as the number of slots increase. This is evident from Figure 6.6(a) where the sensitivity looks mostly dependent on ridge width as opposed to the number of slots. Bulk sensitivity is a function of mode confinement and hence ridge width is the major parameter affecting the sensitivity in slot waveguides. Therefore, in order to achieve both bulk and surface sensitivities at the same time, one should consider regions of interest from both Figure 6.6(a)-(b) and balance the design to accommodate both cases. Since bulk sensitivity is mostly dependent on ridge widths while surface sensitivity is mostly dependent on number of slots, ridge width can be chosen to be 80 nm from Figure 6.6(a). On the other hand, Figure 6.6(b) shows that surface sensitivity is mostly dependent on the number of slots and almost constant for a wide range of ridge widths between $70 - 150$ nm. Hence to achieve high bulk and surface sensitivity at the same time, one can chose the number of slots to be 16 with ridge width of 80 nm and slot width of 90 nm.

Fabrication tolerance is a major factor that should be taken into consideration within all photonic sensor designs. One important factor is the sensitivity of the device in case there is residual silicon left at the bottom layer of the multiple-slot structure after the etching

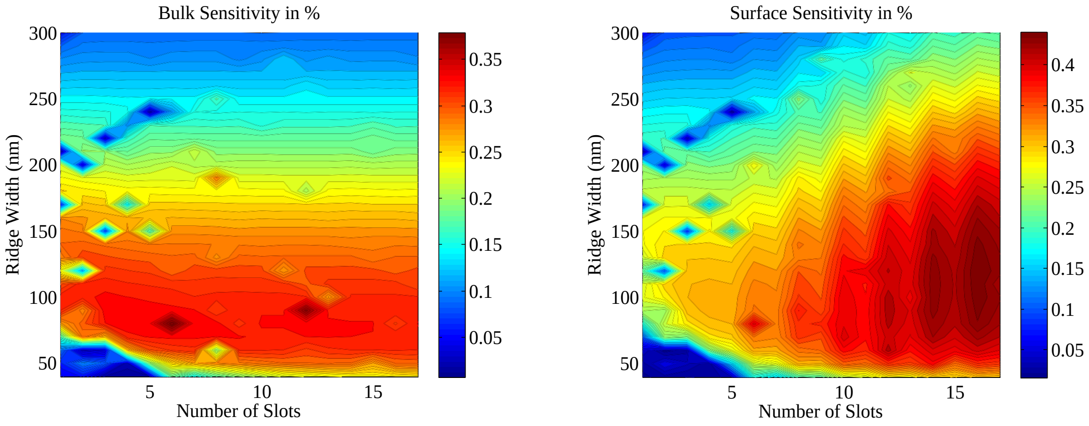

(a) (b)

Figure 6.6: Sensitivity figure for various number of slots versus variations in ridge widths while the slot width is kept constant at 90 nm (a) Bulk sensing (b) Surface sensing.

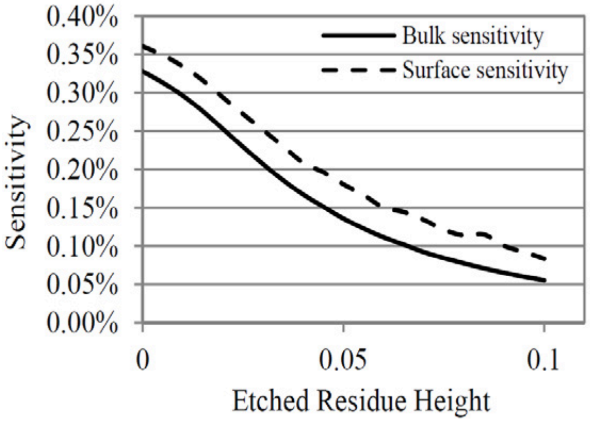

Figure 6.7: Change of effective modal index in case of residual slab from etching when the other waveguide parameters are kept constant.

step. This thin layer of silicon would act as a slab waveguide, hence forcing the mode to shift downwards from the upper clad layer. As a result, the interrogation capacity of the mode from the upper cladding layer (i.e. the medium to be sensed) is reduced. In order to take this effect into consideration, a silicon layer with various thicknesses between 0 to 100 nm was added at the bottom of the waveguide between the etched slots and the SiO_2 lower cladding. Other parameters of the multiple-slot structure are kept at the optimal point (i.e. ridge width of 80 nm, slot width of 90 nm and height of 1 μm) to evaluate the effect of residual silicon. Figure 6.7 illustrates this effect and shows how the sensitivity is decreased drastically with increasing residual layer thickness. This suggests that etching has to be strictly controlled during the fabrication process and one might have to etch into the oxide layer beneath to achieve the highest sensitivity.

6.3 Bend losses and Ring Resonator Design

As mentioned earlier, ring resonators are attractive structures for biochemical sensors as they provide high quality factors along with multiplexing features for different sensors in a chip. In this section, a multiple slot ring resonator solution is proposed for biochemical sensing applications based on the optimization performed in previous section. It is also important to understand whether these multiple-slot waveguides show low bending losses.One main concern is whether the introduction of multiple slots would create excess radiation. The second concern is whether the effective waveguide is strong enough to guide light through bends.

In order to address the first concern, a series of two dimensional (2D) finite difference time domain (FDTD) simulations were performed to measure the bending losses of the proposed multiple-slot waveguides. Other waveguide parameters including the width, slot width and height were kept at the optimum point. In any bent waveguide, the amount of radiation losses is directly proportional to how strong or weak the waveguide is while it is inversely proportional to the bending radius. The set of parameters such as number of slots, ridge and slot widths in the multiple slot waveguide design determines the guidance ability of the structure especially in waveguide bends. In this section, in order to investigate the effect of adding multiple slots in the bend, 2D FDTD simulations were done to find the losses in the lateral direction. Figure 6.8(a) shows the TE mode of a 16 slot waveguide traveling through a 360° bend. To measure the losses in the lateral direction due to addition of slot waveguides, the fundamental TE mode of the structure is launched and the modal power is measured at 15° points through out the bend. It can be seen from the figure that close to the launching plane there is a higher loss due to small modal mismatch between the calculated mode (considering the straight structure) and the actual propagating mode of the structure. As the mode progresses through the bend, the measured loss becomes more accurate and resembles the actual bending loss of the waveguide in the lateral direction. Figure 6.8(b) also shows the fundamental TE mode of the ring resonator excited using a

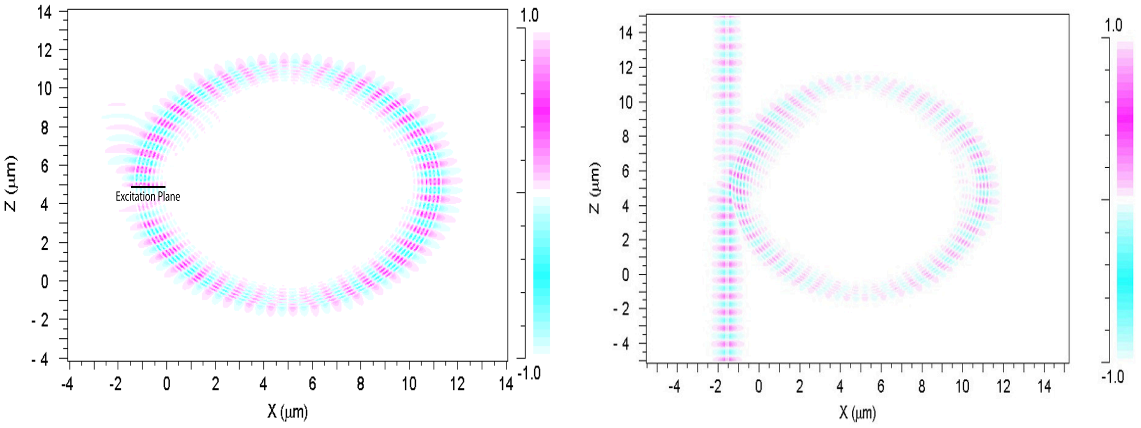

(a)

(b)

Figure 6.8: TE mode field distribution of a 16 slot ring resonator with radius of 5 μm. (a) E_x field distribution of in-circle excitation for bending loss measurement. (b) E_x field distribution excited through a bus waveguide in a ring resonator setup.

bus waveguide in a 2D FDTD simulation. In order to construct the ring resonator, the bus and ring resonator distance should be designed for critical coupling conditions. While the 2D FDTD simulation provides valuable information regarding coupling and excitation of such modes using a bus waveguide, it can be used to evaluate excessive losses due to slot structure. The calculated bending losses for this model shows that the proposed multiple-slot structure would cause radiation losses of 0.02 $dB/turn$ or lower for bend radii larger than 10 μm. These results suggest that the addition of slots do not fundamentally increase the radiation appreciably.

Although the slot waveguides cause minimal radiation in the lateral direction, due to the modal effective index close to that of the substrate, there is a larger possibility of radiation into substrate modes. This is not addressed by 2D FDTD simulations and 3D simulations in FDTD are prohibitive. In order, to investigate the radiation into substrate modes, an effective index model was developed. In the effective index model, the slot waveguide was replaced by a rectangular dielectric waveguide with same dimensions as the multi-slot waveguide. The refractive index of the effective dielectric waveguide was adjusted till the effective modal indices were the same for both the waveguides. This was done for the straight waveguide. However, it was found that the modal shapes remained the same even over the bends as illustrated in Fig. 10 for a multi-slot waveguide with 16 slots and a bend radii of 12 μm. The effective index model becomes quite useful as conventional integrated optics calculations can be readily used in designing bends and other devices. In the case of straight waveguides, the 16-slot guide with ridge width of 80 nm and slot width of 90 nm was modeled with a similar dimension ridge waveguide with core index of 1.768 and the same lower and upper cladding conditions. This effective waveguide model is able to predict the real part of the propagation constant with only 0.01% error compared with the FE mode solving method for the straight 16 slot case. The effective index model was used to calculate the radiation losses into the substrate over different bend radii and the results are plotted in Figure 6.9 for a 360° bend. The losses are less than 0.1 dB per turn for bend radii greater than 12μm. Thus, small diameter ring resonators can be fabricated using the 16 slot multi slot waveguide with 80 nm ridge and 90 nm gap. It needs to be mentioned here that if the number of slots or ridge width is changed, the loss through the bend will also change. For example, for ridge width of 40 nm and slot width of 90 nm, the radiation loss was calculated to be 33 dB per turn for a radius 10μm. In multi-slot waveguides, larger ridge width improves the surface sensitivity and thus, one can optimize the structure for sensitivity and bend radius without constraints.

However, it is apparent that in a bent waveguide, the mode travels through the outer side of the waveguide and this may change the sensitivity of the sensor in a bend. So the next question which arises is whether a smaller or a larger radii will give better sensitivity.

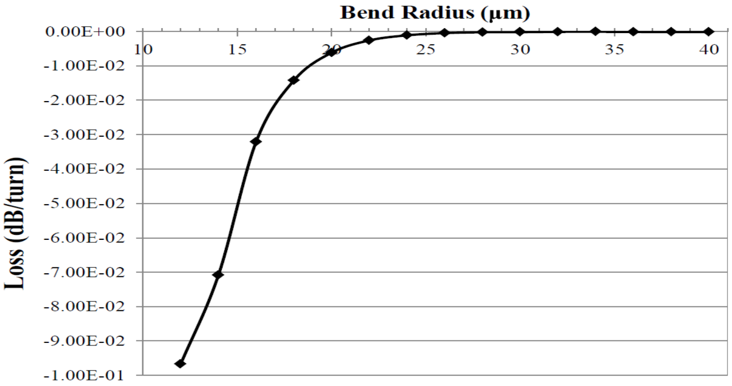

Figure 6.9: Bend losses versus the radius of a 16 slot ring resonator design modeled using the effective index method.

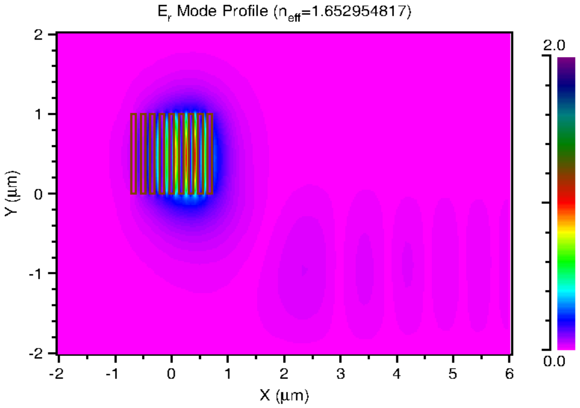

Figure 6.10: TE fundamental mode of a bent 8 slot waveguide with radius of 12 μm.

Clearly in SOI ring resonators, smaller radius improves the sensitivity as it pushes the mode to the outside of the ring increasing the evanescent field. However, this may not be the case for multi-slot waveguide as the interaction of the mode with the inner slots decrease. To investigate this phenomena further, full vectorial finite element mode solving method was used in cylindrical coordinates to find the fundamental TE mode of the multiple-slot bent waveguide structure. In order to illustrate the difference, Figure 6.10 shows the fundamental TE mode for 8 slot bend waveguide as opposed to the 16 slot waveguide shown in Figure 6.11(a) with similar bend radius of 12 μm. Although the fundamental supermodes of the two structure are extremely similar in shape, the effective modal index of these two structures are completely different. The fundamental TE mode of the 16 slot

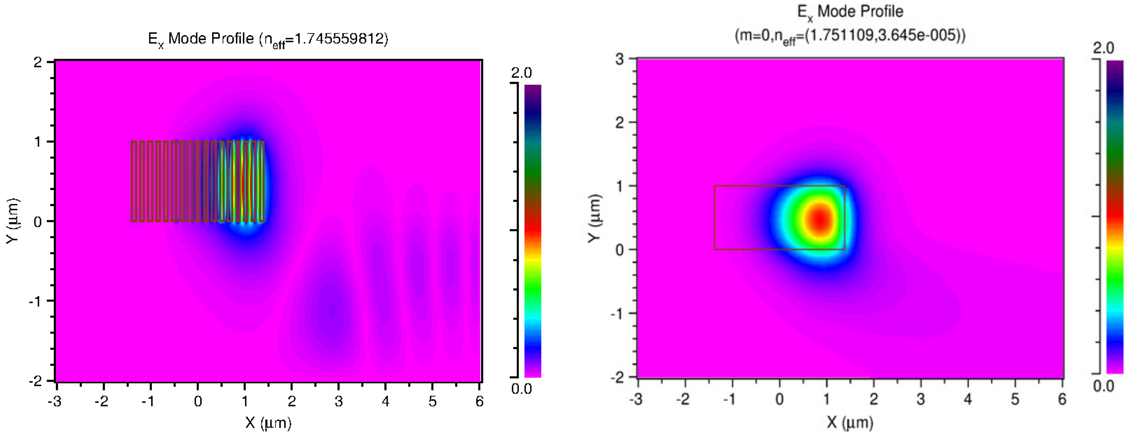

(a)

(b)

Figure 6.11: TE fundamental mode of bent waveguides with radius of 12 μm. (a) E_x field distribution of 16 slot waveguide. (b) E_x field distribution of the effective index modeled rectangular waveguide

waveguide has an effective modal index of 1.745 while the 8 slot waveguide has an effective modal index of 1.652. By calculating the bent structure sensitivity for bulk and surface sensing, it was found that the 16 slot waveguide shows a modal index change of 0.66% for surface attachments while the 8 slot waveguide shows a modal index change of 0.36% for the same surface attachment. Therefore, it is clear that while the supermode travels through the outer slots in a bend, the number of slots still plays an important role in determining the sensitivity to the bulk and surface changes. It should also be noted that when bend modes are considered for ring resonator based sensors, the sensitivity values are changed due to the fact that modes would travel through the outer side of the structure and hence showing different confinement factors. While one might consider the inner slots not useful, the simulations done in the later part of this section shows that they do have an effect on modal properties and hence the sensitivity of the whole structure.

To quantify the sensitivity improvement of the proposed multiple-slot structure, the response of a ring resonator based multiple-slot sensor to the bulk and surface changes were calculated and compared with the SOI ring resonator design which is excited with TE mode. The SOI waveguide has a width and height of 0.3 μm and 0.2 μm, respectively, and its sensitivity was calculated in a similar scenario to our multiple-slot structure with the same bulk and surface refractive index changes in the surrounding medium. In the first set of simulations, the change in resonant wavelength of the SOI waveguide is calculated by [110],

$$\Delta\lambda = \frac{\Delta n_{eff}\lambda}{n_g} \tag{6.2}$$

where Δn_{eff} is the change of the effective index due to the change of the refractive index of the surrounding medium, λ is the initial resonance wavelength and n_g is the group index.

Over the bend of a ring resonator, the sensitivity would be a function of the radius and number of slots. As the radius is decreased, the bend losses would increase due to radiation effect. On the other hand, as the number of slots decreases, it would help with spreading the mode through the guides by making a weaker waveguide while it would result in increase of radiation losses over bends. Straight waveguides are the limit of rings when the radius is large enough for the mode not to be significantly perturbed in a bend. In the following, SOI based ring resonator is compared with 20 μm and 12 μm radius multiple-slot waveguides. With the radius of 20 μm, the straight waveguide effective modal index was used to calculate the resonance wavelength. However, for the radius of 12 μm the bend mode of the multiple-slot was calculated using conformal mapping and the resulting wavelength shift was found.

In order to investigate sensitivity changes in rings, the resonance wavelength shift of the SOI based ring resonator is calculated for the cases of bulk and surface sensing scenarios. In case of surface sensing, a shift of 1.12 nm is achieved while this shift is 0.74 nm for bulk sensing (as shown in Figure 6.12). For bulk sensing, as the surrounding index is changed only 0.005, the calculated bulk sensitivity becomes 148 nm/RIU. The free spectral range in this case is calculated to be 7.48 nm for cladding of 1.325. On the other hand, Figure 6.13

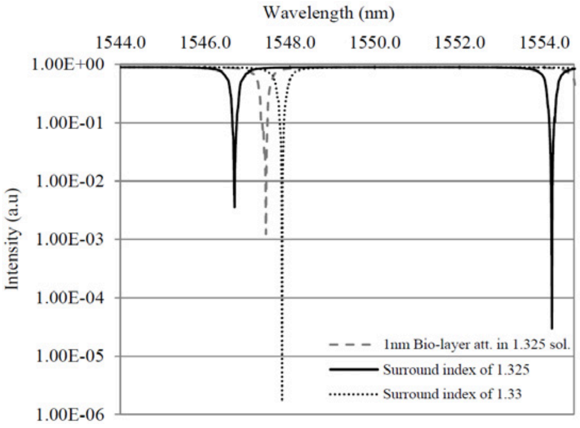

Figure 6.12: Wavelength shift of a 300 nm wide Si waveguide based ring resonator in cases of bulk and surface changes of refractive index due to environmental changes.

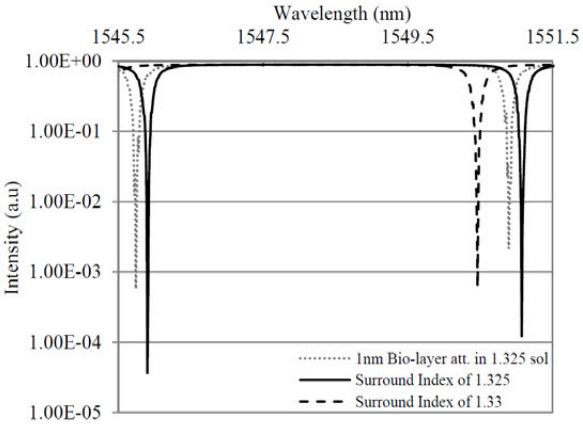

Figure 6.13: Wavelength shift of a 16 slot based ring resonator in cases of bulk and surface changes of refractive index due to environmental changes with a radius of $20\mu m$.

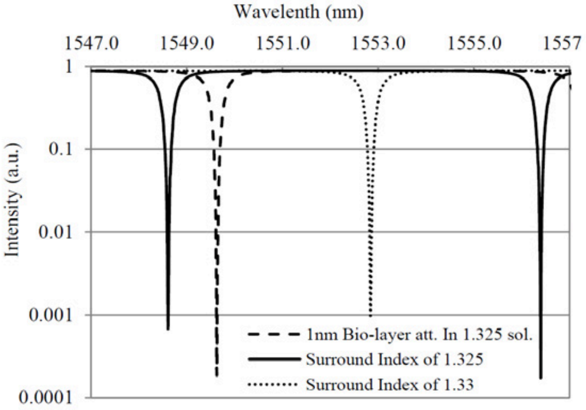

Figure 6.14: Wavelength shift of a 16 slot based ring resonator in cases of bulk and surface changes of refractive index due to environmental changes with a radius of 12 μm using the perturbed bent waveguide mode.

illustrates the calculated resonance wavelength shift of the multi-slot based ring resonator for the similar cases of bulk and surface refractive index changes of SOI setup in the limiting case of straight effective modal index. In this case, the calculated wavelength shift for the surface sensing is 4.99 nm and the shift for bulk sensing is 4.56 nm. Hence, the bulk sensitivity of the 16-slot ring resonator sensor is 912 nm/RIU which is an improvement of at least 6 times over the sensitivity of a single SOI based ring resonator. The FSR in this case is calculated as 5.17 nm for cladding of 1.325. Figure 6.14 shows the wavelength shift for a ring resonator of 12 μm radius. It is notable that the modal shift for the bulk changes is almost similar to the straight case. However, the shift due to the surface change is degraded significantly. This result is due to the fact that the fundamental TE mode is coupled to the outer slots of the structure where there is limited surface attachments as compared to the straight case with the slot modes spread through the waveguide width. According to this figure, the shift due to the bulk changes is 4.23 nm where as the shift due to the surface attachments is only 1.02 nm and the calculated FSR is 7.79 nm for cladding of 1.325. This shows the significance of bend mode consideration when designing small radius multiple-slot based ring resonators for surface sensing applications. In fact as suggested by the simulations, smaller bend radii degrade the surface sensitivity, a behavior in direct contrast to SOI ring resonators.

As mentioned earlier, the perturbed mode shows different characteristics with respect to the nearly straight rings (i.e. large radius ring resonators). As shown in the simulations, with increase in the number of slots the effective modal index changes in bends as well. Figure 6.11(a) shows the increase in effective modal index from a 16 slot waveguide structure when the ring radius is reduced to 12 μm. This would effectively change the sensitivity value for bulk and surface refractive index changes. Figure 6.15 utilizes the change in effective modal index of a bent mode in a ring resonator with radius of 12 μm and different number of slots. It illustrates the relative shift in resonance wavelength for the cases of bulk refractive index change and surface attachment. While bulk sensitivity remains relatively constant for different number of slots, there is a sweet spot in designing such ring resonators with multiple-slot waveguides for surface sensing applications. In

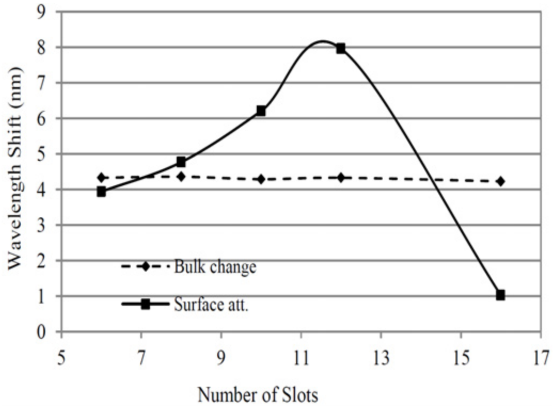

Figure 6.15: Wavelength shift of a multiple-slot ring resonator with varying number of slots in cases of bulk and surface changes. In all cases the radius is fixed to 12 μm and the perturbed bent waveguide mode was used for calculations.

order to improve upon surface sensitivity, the modes need to be spread out over multiple slots, hence reducing the number of slots would help to the point where the ratio of surface attachments area to the modal area is not significant. A higher effective modal index means that the confinement factor increases and as a result, the interrogation power of the sensor in the sensing medium decreases. This would lead to smaller resonance shifts for higher number of slots. As shown in this plot, when the number of slots is reduced to 12, the resonant wavelength shift peaks to 7.96 nm and then it reduces again as the number of slots are lowered. Therefore, the design of the sensor for surface sensing applications should incorporate these findings while for bulk sensing applications the number of slots does not impose much critical change in sensitivity levels.

6.4 Conclusion

We have proposed and optimized a multiple-slot based ring resonator design for highly sensitive optical sensing applications. An investigation of the waveguide modal properties along with rigorous optimization were performed to find the optimum structure parameters. Parameters such as ridge widths, slot width, the number of slots and their symmetry in terms of odd and even numbered were investigated in detail. The mentioned parameters were adjusted to find the highest bulk and surface sensitivities. The bend properties of the investigated multiple-slot structure were studied in order to construct ring resonators. The proposed ring resonator based sensor is able to achieve sensitivity values of 912 nm/RIU which is at least 2 times higher than the multiple-slot structures proposed in literature.

Chapter 7

Spectral Sensing Using High Order Diffraction Spots from Ordered Vertical Silicon Nanowire Arrays

In this chapter, use of high order diffraction spots from two dimensional silicon nanowire (2D SiNW) arrays is proposed for refractive index sensing based on spatial changes in the diffractive spots position. The nanowire arrays act both as a refractive index sensor and as dispersive elements eliminating the need for external spectrometers for the measurement of refractive index changes. The setup uses a simple laser diode source and a low-cost camera and results in higher sensitivity to environmental refractive index changes as compared to previously demonstrated colorimetric sensors. The sensitivity is greater for higher order diffraction spots as compared to the lower order ones due to a larger dispersion angle change at higher orders. It is also demonstrated that the observed diffraction angle and efficiency of the diffractive orders depend upon a number of factors such as excitation wavelength, nanowire diameters, pitch and surrounding medium index. The simple solution of using diffraction spot displacements on a 2D detector array would provide a novel means of sensing refractive index changes in the surrounding medium of nanowires without the burden of complicated spectral analysis.

Structural features in the order of visible light wavelengths create many interesting light interactions with materials like thin-film and multilayer interferences [122, 123], light scattering due to diffraction gratings [124, 125, 126], light trapping in photonic crystals [127], plasmonic resonances [128,129,130] and spectrally selective absorption which generates colors in transmission or reflection [131]. These enhanced light-material interactions have been utilized in a variety of optical sensors. In such sensors, various modalities can be used to detect physical changes in the environment based on changes in the optical resonances. In one instance, the one/two dimensional (1D/2D) diffraction patterns have been used to study field-induced liquid crystal phase changes in a periodic manner for applications in areas such as multiplexing and processing optical signals in optical interconnects, beam steerers, and sensor array interrogation devices [125,126]. Pan et al. have proposed use of thermally grown ordered ZnO nanowire arrays as diffraction gratings for spectroscopy applications. While they propose such diffraction gratings for applications such as miniaturized integrated optical chips or simple beam dividers in CD players, they did not performed much analysis on the diffraction behavior of such periodic nanowire structures [132]. In other simple cases, diffraction based structural color generation is used to detect environmental changes around the sensor. Change of surrounding medium refractive index imposes different phase conditions and hence, generates a different color based on the amount of index change [133,134,135]. While this color change can be detected in RGB mode using a simple imaging sensor [136], higher sensitivities can be reached by adding spectroscopic measurements [135]. Kumawat and Varma proposed a design which permits a differential, ratiometric measurement of the reflectance intensity change from 2D diffraction patterns of periodic SiO_2 structures [137]. In that method, by looking solely at the intensity of the 0^{th} and 1^{st} order diffraction patterns, one can eliminate signal drifts from the sample flow cell. While the proposed method can create relatively accurate predictions in terms of refractive index change, the dynamic range of the detector offers a great limitation to this type of sensor especially where the 0^{th} order tends to include the larger percentage of the reflected power. In a recent paper, we showed how simple colorimetric measurements on a two dimensional silicon nanowire (2D SiNW) array can yield refractive index resolution of 10^{-4} for refractive index sensing using colorimetric measurements while with spectral analysis one can increase the index resolution up to 10^{-6} [135]. Similar to many other periodic structures, SiNWs arranged in 2D periodic lattices act as 2D diffraction gratings. As shown by Walia et al. [135], the diffracted light from SiNW arrays would follow Bragg diffraction rules. The angular dispersion of these spots at a specific wavelength would depend on diameter and pitch of the NW as well as the refractive index of the medium surrounding them.

In this chapter, we propose to image the higher order diffractive modes from 2D arrays of SiNWs and increase the refractive index sensitivity while using simple cameras and no additional optical components. This would increase the refractive index sensing resolution of such sensors to the order of 10^{-5} without the need of any additional spectral analysis. Higher diffraction orders are more sensitive to refractive index changes and result in larger dispersion angles. Hence, they are suitable candidates to use in sensing applications. Due to the high index contrast between SiNWs and the surrounding medium, the modulation depth of such an array is high, which results in highly diffractive orders that can span to about 80 degrees angle from the normal to the substrate surface. Using a single wavelength source along with diffractive characteristics of the 2D periodic structure, one can achieve high sensitivities without the need for complicated and expensive spectroscopic approaches. In fact, the 2D grating acts as a standalone self-referenced dispersive spectrometer that performs refractive index sensing on its dispersive element in a simple and elegant manner. In order to optimize the proposed sensor, we also do experimental studies to first understand the diffraction patterns and efficiencies of the periodic nanowire arrays and its dependence on the various geometrical parameters like pitch, diameter and length. Then a sensor is proposed based on the studied characteristics. To our knowledge, such studies have not been performed for semiconductor nanowire arrays and this novel approach for combined sensing and spectroscopic measurements have been proposed for the first time. In the following, first the fabrication steps and sample details are discussed. Then, the diffraction patterns and efficiencies are calculated and measured for a fabricated sample. From these initial studies, a sensor design is proposed and discussed. The experiments confirm and validate the proposed sensor concept.

7.1 Fabrication and Sample Details

In order to perform diffraction pattern studies and compare with theoretical predictions, 2D SiNW arrays, each 100×100 μm in cross-sectional area, were fabricated on a (100) silicon wafer using e-beam lithography and pseudo-Bosch inductively coupled plasma reactive ion dry etching (ICP-RIE). The fabrication steps have been previously described in detail [134]. The diameter and the length of the nanowires were 135 nm and 1 μm respectively. Different values of pitch ranging from 600 nm to 1300 nm were fabricated. The arrays were separated by a distance of 1 mm so that each array could be individually measured. A 30 nm thick Aluminum mask was used for etching and was kept intact after the etching as it increases the reflectance from the top of the nanowires and hence it improves the diffraction efficiency. Figure 7.1 shows the top down and side views of the fabricated nanowire arrays showing good uniformity in diameter and pitch and vertical nature of the fabricated nanowires.

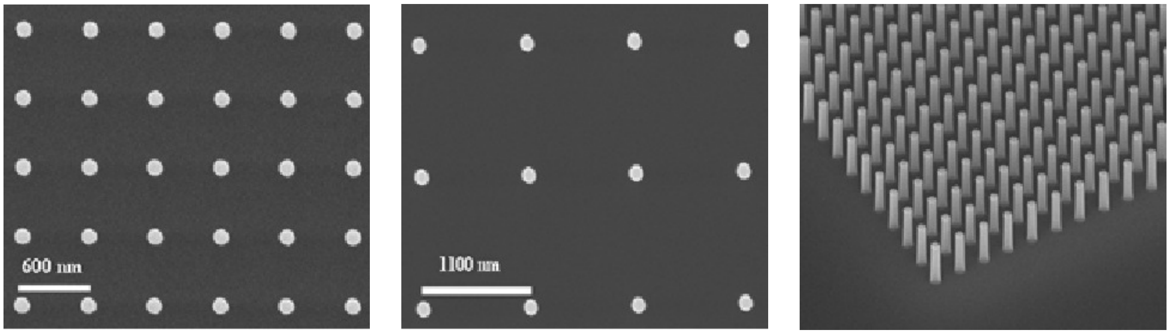

(a) (b) (c)

Figure 7.1: SEM images of the SiNW arrays. (a) Top view of a square lattice with pitch of 600 *nm*. (b) Top view of a square lattice with pitch of 1100 *nm* (c) Side view SEM at the array with pitch of 600 *nm* which shows the perfect vertical nanowires. Scale bars are shown in the figures.

7.2 Diffraction Patterns and Efficiency Studies

As discussed earlier, 2D periodic arrays of nanowires act as diffraction gratings based on the generalized Bragg diffraction formula given by the condition [138]:

$$(nsin\theta_i \pm nsin\theta_{r,ml}) = \frac{m\lambda}{d_x} + \frac{l\lambda}{d_y} \tag{7.1}$$

where n is the refractive index of the surrounding medium, θ_i and θ_r are the incident and diffracted angles, m and l are the order of diffraction, λ is the free space wavelength of the incident beam, and d_x and d_y are the spacing between the nanowires in the lateral direction. As can be seen from the equation, an m^{th} order Bragg diffraction spot will exist if the spacing is larger than the wavelength. Assuming that the incoming beam hits the sample perpendicularly such that θ_i is 0°, then the sensitivity of diffraction angle in one direction, S_{θ_x}, due to the change in surrounding medium refractive index would be given by:

$$S_{\theta_x} = \frac{d\theta_{r,m}}{dn} = \frac{d}{dn} sin^{-1}(\frac{m\lambda}{nd_x}) = \frac{-m\lambda}{n\sqrt{(nd_x)^2 - (m\lambda)^2}} \tag{7.2}$$

It is evident from the equation that sensitivity is increased by the order m. The negative sign indicates that as the surrounding medium refractive index increases, the diffraction angle decreases while allowing for higher diffraction orders to exist. Thus, higher order diffraction modes are of interest for increased sensitivity but they need to be excited at high efficiency to keep signal to noise ratio (SNR) at an acceptable level. To our knowledge, no studies for diffraction efficiencies have been done for 2D SiNW arrays.

In order to measure the diffraction pattern and the efficiency of the various modes, the measurements were done using a setup for which the schematic is shown in Figure 7.2(a). Light from a 633 nm laser diode is focused with a lens at normal incidence on a nanowire array. The beam spot of the lens is about 150 μm in diameter completely covering a 100 μm square array of SiNWs while not coinciding with the neighboring arrays. If the nanowire arrays are fabricated in a manner that they are far away from each other, there is no need for an external lens to focus down the beam. The various diffraction spots are imaged on a registration surface which has a hole in the center for the incidence beam to pass through. As the nanowires are on an opaque substrate, the reflected diffraction patterns are captured on this registration plane. The hole can be as small as two times the incident beam waste at which the power drops to $1/e^2$ in order for it not to further diffract the incoming beam. The images on the registration surface are illustrated in Figure 7.2(b)-(c) for different values of pitch. In Figure 7.2(b), the four 1^{st} order diffraction spots can be seen for the pitch of 650 nm while the excitation wavelength is at 633 nm. Also in Figure 7.27.2(c), 2^{nd} and 3^{rd} order spots appear for the pitch of 1300 nm at the same excitation wavelength. The curvature on the diffraction spots is due to the fact that the incoming field has a spherical wavefront from the focusing lens. The spherical wavefront causes a portion of the incident beam to be non-perpendicular on the sample and hence some of the diffracted power would be due to the oblique incident light. As a result, the reconstructed diffraction spots appear with spherical aberration and the spots would show a larger diffraction angle with larger beam size. This effect is clearly noticeable in 2^{nd} and 3^{rd} orders within Figure 7.2(c).

Diffraction patterns were simulated using a commercial rigorous coupled wave analysis (RCWA) module from Rsoft [139]. First, the reflection field from a single unit cell of the nanowire was calculated considering periodic boundary conditions on the arrays lateral plane. The bi-directional scattering distribution function (BSDF) of the structure was then calculated from the reflected electric fields. A finite Gaussian beam was passed through the BSDF database to produce the reflected and transmitted near-field information. The near-field data was used to calculate the far-field diffraction patterns of the 2D SiNW structures which are plotted in Figure 7.3. As shown in this figure, the diffraction patterns match the experimental patterns. However, the diffraction spot intensity has a 2D Sinc function pattern in the experimental case which is due to the fact that we are dealing with a limited rectangular periodic array instead of an infinite periodic array which was considered in the simulation.

Using a 633 nm collimated beam from a laser diode, we measured the diffracted beam

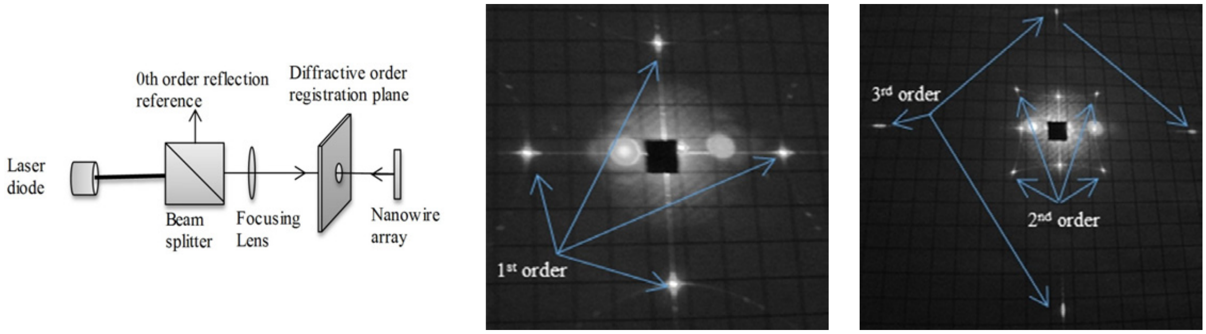

(a) (b) (c)

Figure 7.2: Experimental diffraction pattern from a SiNW array of 135 *nm* diameter (a) The measurement apparatus for the diffraction pattern from the SiNW array (b) Diffraction pattern from SiNW array with pitch of 650 *nm* (c) Diffraction pattern from SiNW array with pitch of 1300 *nm*.

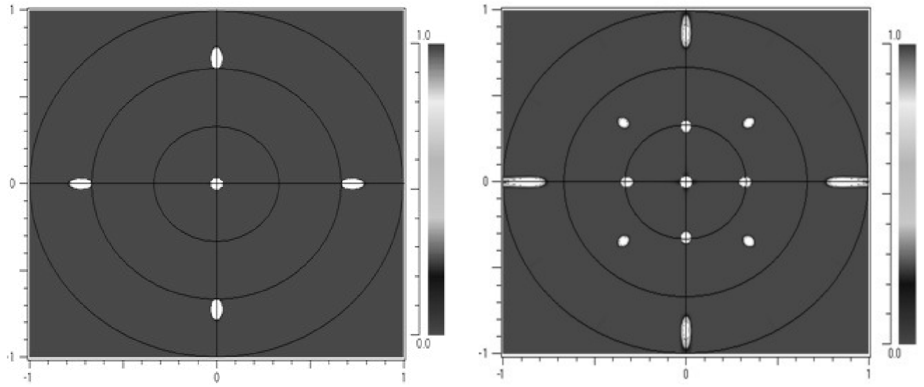

(a) (b)

Figure 7.3: Simulated diffraction pattern from a SiNW array of 135 *nm* diameter using bidirectional scattering distribution function (a) pitch of 650 *nm* (b) pitch of 1300 *nm*.

efficiencies using a setup similar to the one shown in Figure 7.4(a). The nanowire sample was placed on a manual 3-axis stage where we could laterally move through different nanowire arrays. Instead of the registration plane, an integrated sphere photo-diode power sensor from *Thorlabs Inc.* (SC140) was used to measure the diffracted power at each of the diffraction points coming off from the sample. In order to reduce the experimental error due to tilt of the sample, the power of all diffraction spots in each order was measured and then the average value was taken. To calculate the diffraction efficiency for each of the arrays, the ratio of averaged diffracted power in each order was taken with respect to the incident power. Figure 7.4 plots the measured and calculated first and second order diffraction efficiencies for different pitches of the nanowire. Experimental results have smaller values as compared to the simulations due to the finite size of the arrays and the incident beam being slightly larger than the arrays. In addition, surface roughness on the structures which can be from the lift-off and etching processes contribute to further scattering and reduced diffraction efficiency. It should also be noted that there is a difference between the exact n and k values of SiNW in the experiments and the estimated n and k values in the simulations which can result in further discrepancies between the calculated and actual diffraction efficiencies. However in general, the variations in efficiency versus the pitch can be reproduced with the simulations. For the first order, the peak diffraction efficiency is achieved at a pitch of 650 nm and reduces with increasing pitch till a pitch of 1050 nm and then starts to increase again for another local maxima at a pitch of 1200 nm. The trends are also confirmed by the simulations. A peak diffraction efficiency of 3% per 1^{st} order diffraction spot was achieved experimentally for such design parameters. As it is evident from Figure 7.3(b) at the wavelength of 633 nm, the second order diffraction does not exist for arrays with pitch less than 850 nm. Maximum 2^{nd} order diffraction efficiency of 2.7% per diffraction spot is achieved experimentally for a pitch of 1100 nm. As it can be seen from the diffraction efficiency figures, the diffracted power is maximized in the 2^{nd} order while the 1^{st} order power is at its lower range. Simulations also confirmed that the aluminum mask remaining on top of the nanowires after the lift-off process, substantially increased the diffraction efficiency due to increased reflectivity from nanowire-air interface. Using the above mentioned considerations, one can optimize the diffraction efficiency for certain sensing medium at a given wavelength.

The above measurements were done when the nanowires were surrounded by air. In sensing applications, the nanowires will normally be surrounded by water based solutions. Thus, it is essential to see how the efficiency changes when the refractive index of the surrounding medium is changed from air. The diffraction efficiency for different values of pitch is plotted in Figure 7.5 for refractive index of 1.33, close to that of water. As the refractive index of the surrounding medium is changed, higher diffraction orders start to appear at a lower pitch. In this case, the 2^{nd} order starts to appear at a pitch of 700 nm and higher. Further, highest efficiency is now achieved for a shorter value of spacing. This is quite useful for our sensing applications where we intend to maximize the SNR on higher diffraction orders to achieve greater sensitivities. In addition, theses studies show how one can optimize further the diffraction efficiency for a given sensing medium using the combination of the pitch and diameter of the NW arrays.

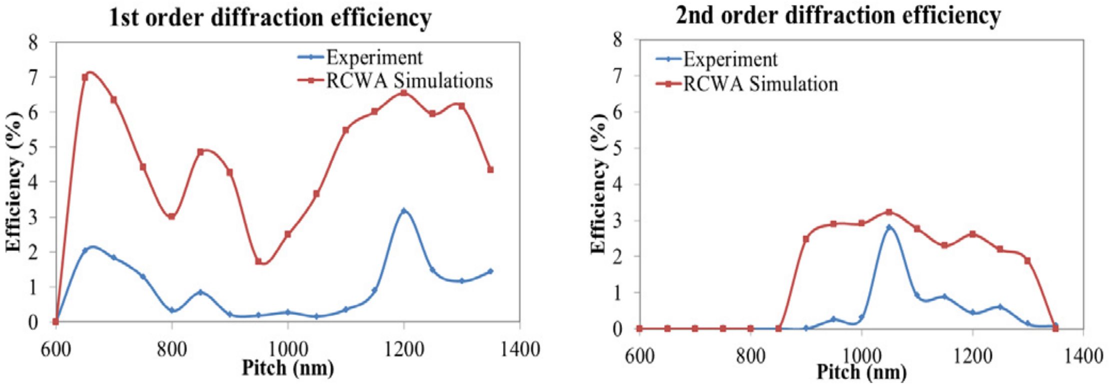

(a) (b)

Figure 7.4: Diffraction efficiency measurements and simulations from different pitches of nanowire arrays (a) 1^{st} order diffraction efficiency (b) 2^{nd} order diffraction efficiency.

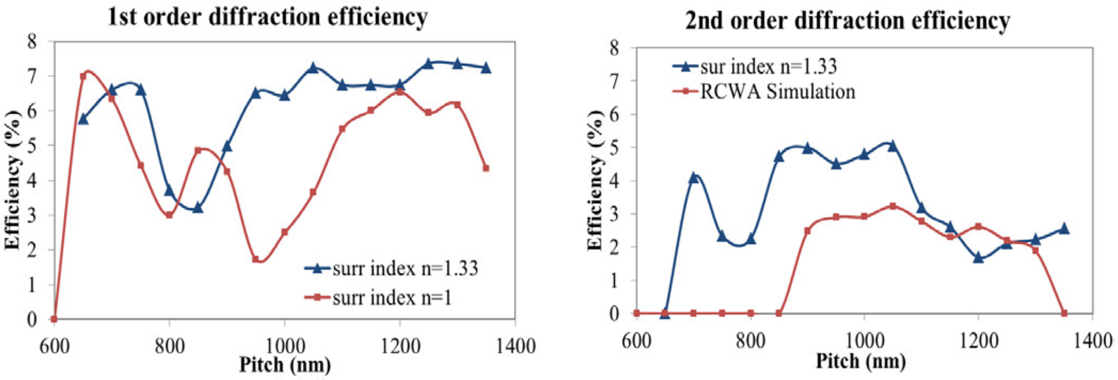

(a) (b)

Figure 7.5: Diffraction efficiency simulations for different pitches of nanowire arrays at two different surrounding medium indices of 1 and 1.33 (a) 1^{st} order diffraction efficiency (b) 2^{nd} order diffraction efficiency.

7.3 Sensor Design Results and Discussions

The proposed setup which uses the 2D SiNW array as a refractive index based sensor is given in Figure 7.6(a). As the collimated single wavelength input beam hits the structure, it gets diffracted. For different surrounding media which have different refractive indices,

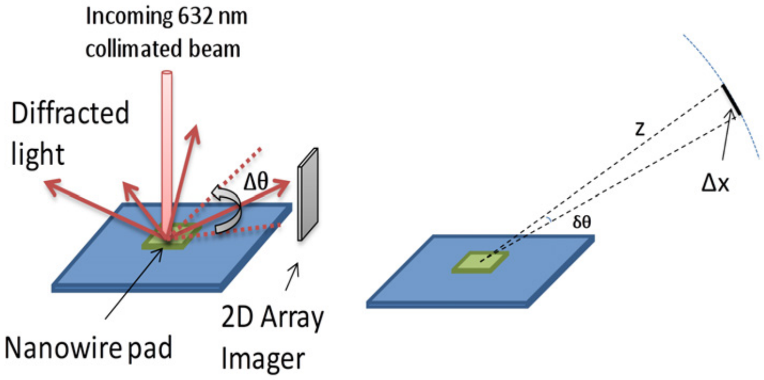

(a) (b)

Figure 7.6: Proposed sensor structure (a) Diffraction based sensor structure and measurement method (b) measurement parameters and variables for the diffraction spot.

the position of this spot would change on the detector. The change of position which correlates to the refractive index change is registered on the camera. Hence, one can associate parameters such as concentration and presence of biological agents to the changes in the diffracted spot position. In Figure 7.6(b), the change in the diffraction spot position is dependent on both the divergence angle and the distance of the detector from the SiNW array (i.e. $\Delta x \approx z\delta\theta$). Similar to a spectrometer, as we move away from the grating structure and go higher in diffraction order, the resolution or sensitivity of the system improves while its efficiency drops. For example, an off the shelf web camera was tested which could detect up to 5 μW of incident light at the highest exposure; considering the input laser to be eye safe (i.e. it's power being less than 1 mW), the diffraction efficiency per spot needs to be greater than 0.5% which is easily achievable.

Figure 7.7 shows the simulated diffraction patterns for the 700 nm pitch array at two different values of surrounding medium refractive indices of 1 and 1.33. It is evident that higher diffraction orders appear as the surrounding medium index is increased. When the surrounding medium is air, only the 1^{st} order diffraction is observed for the pitches less than 900 nm. However when the refractive index of the surrounding medium is increased, 2^{nd} order diffraction modes appear for pitches 750 nm and larger. The 3^{rd} order spots come to existence at pitches 1000 nm and larger. When the surrounding refractive index is increased, the diffraction spots start to converge inwards with respect to the 0^{th} order. Sensing of refractive index can be achieved by measuring this change in position.

As an example, consider an array of SiNW with pitch of 1050 nm where up to 3^{rd}

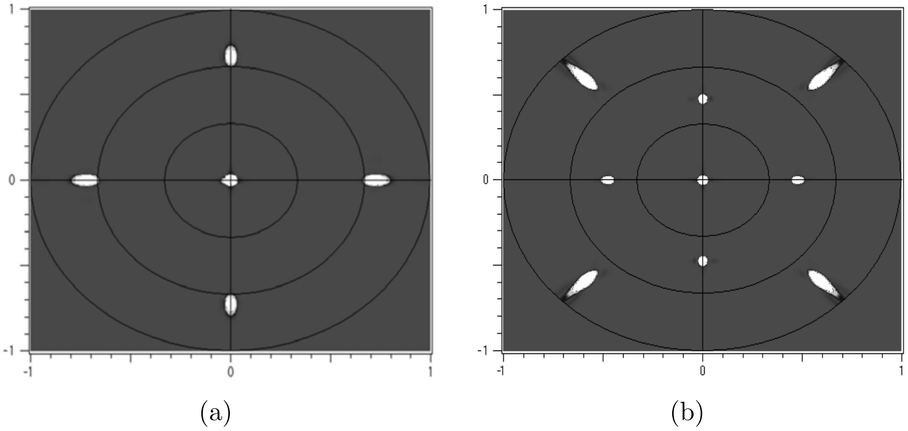

(a) (b)

Figure 7.7: Diffraction from 750 *nm* pitch SiNW array, with surrounding medium refractive index of. (a) 1 (b) 1.33

order diffraction orders exist with surrounding medium refractive index of 1.33. Taking a horizontal cut through the center, one can get the intensity of the diffraction orders versus their respective normalized diffraction angle varying within the range of $(-90, 90)$ degrees as shown in Figure 7.8 for the 1^{st} and 3^{rd} diffraction orders with two different refractive indices. For the 2^{nd} diffraction order, the spot change was measured along a line that goes through the center at 45°. By measuring the divergence angle in each respective case, one can find the respective divergence angle change, $\delta\theta$, for the case the refractive index of the surrounding medium changes from 1.33 to 1.34. The results are summarized in Table Table 7.1 for the 1^{st} and 3^{rd} order diffraction modes at pitch of 1050 *nm*.

In Table Table 7.1, the divergence angle change is given for the 2^{nd} and 3^{rd} order which is about two and five times larger than the divergence angle change for the 1^{st} order respectively. In most cases such as spectrometer designs, the grating structures are used up to their ±1 diffraction orders and the higher orders are always rejected or unwanted. Here, unlike spectrometers, we anticipate a greater sensitivity in these higher orders. Hence we propose to use the higher order diffraction orders as a means to achieve highly sensitive sensors as much as the efficiency and aberrations allow to achieve a reliable detection. In this study, we have only focused up to the 2^{nd} order due to high aberrations observed at larger diffraction orders arising due to the spherical nature of phase front at the higher diffraction angles and the fact that they are detected on a flat detector.

Another means of increasing the sensitivity of the proposed sensor is through the distance of the detector from the SiNW arrays. Instead of measuring the change in angle, it is simpler to measure the change in the position of the spot on the camera. Accord-

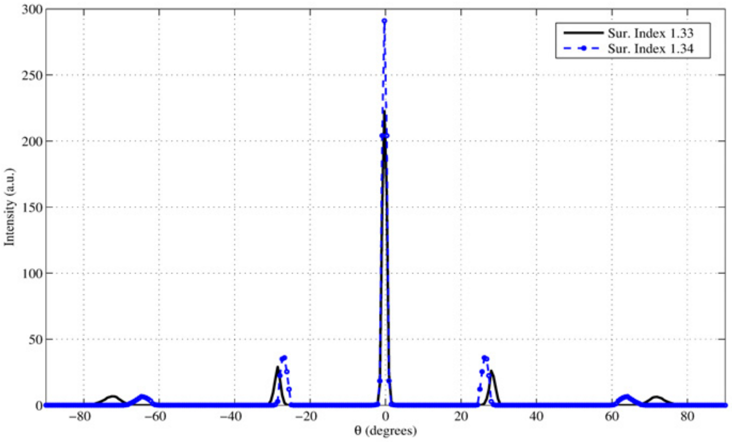

Figure 7.8: Superimposed horizontal cut through the simulated diffraction patterns in cases of surrounding media of 1.33 and 1.34 for pitch of 1050 nm.

Diffraction Order	$n = 1.33$	$n = 1.34$	$\Delta\theta$ **(degrees)**
1^{st}	27.2°	26.7°	0.5°
2^{nd}	40.3°	39.4°	0.9°
3^{rd}	66.3°	64°	2.3°

Table 7.1: Divergence angles of various diffraction orders for SiNW array of pitch 1050 nm

ing to Figure 7.6(b), sensitivity S, is dependent on the position change of the diffraction spot and can be calculated as $S = \partial n/\partial x$ $(RIU/\mu m)$. In this formula, ∂n is the change of refractive index and ∂x is the change in position of the mode defined in microns. It should be noted that in the simplest case, the minimum refractive index change that can be resolved is limited to the single pixel change in position registered on the detector. The refractive index resolution will then be the pixel size (in microns) multiplied by S. With the pixel size in the modern HD cameras approaching 1 μm, S gives a good indication of the refractive index resolution. The value can be further improved as determined through pixel size by using image processing techniques. Table Table 7.2 summarizes the simulated sensitivity values for the first and second diffraction orders from a SiNW array of pitch 750 nm at two different distances between the detector and the chip when the surrounding refractive index changes between 1.33 and 1.34. As mentioned earlier, only up to 2^{nd} order diffraction exists at the pitch of 750 nm. These values would be tested experimentally on the 750 nm pitch array for verification purposes. As it can be seen from the calculations,

Diffraction Order	$\delta\theta$	$\Delta x(\mu m)$ at $Z = 2\ cm$	$\Delta x(\mu m)$ at $Z = 4\ cm$	Sensitivity at $Z = 2\ cm$ $(RIU/\mu m)$	Sensitivity at $Z = 4\ cm$ $(RIU/\mu m)$
1^{st}	0.4°	140	279	7.16×10^{-5}	3.58×10^{-5}
2^{nd}	1.5°	524	1047	1.91×10^{-5}	9.55×10^{-6}

Table 7.2: Diffraction spot changes for two different distances between the detector and the SiNW array of pitch 750 *nm* with surrounding refractive index changing between 1.33 and 1.34

sensitivities up to 10^{-5} can be achieved using the proposed simple setup without the need for additional complex and expensive spectroscopic tools.

While the theoretical prediction of the sensitivity provides a promising basis for highly sensitive sensor design, there are limitations to the level of sensitivities one can achieve experimentally. The *SNR* is an important factor to begin with. As the detector moves away from the SiNW array, the signal intensity drops and the beam would diverge as we are not using any collimating optics to keep the design simple. In addition, the efficiency of the diffracted patterns at higher orders drops drastically which makes further image processing on the detected image to be nontrivial. An alternative means of achieving high *SNR* value for a specific diffraction order at a smaller angle is to move the incident beam to an oblique angle that corresponds to the desired diffraction angle. In such case, a similar approach outlined here can be taken to ensure that the sensitivity of the proposed sensor is maximized.

We tested one of the SiNW arrays with pitch of 750 *nm* for its sensitivity. Cargille fluids with specific refractive indices of 1.33 and 1.34 were used to verify the diffraction pattern divergence change that is registered on a detector screen. The experimental setup is the same as the one shown in Figure 7.6(a). The diffraction pattern is registered on a web-camera without the lens. Figure 7.9(a) shows the 1^{st} order diffraction pattern from the 750 *nm* pitch SiNW array when the surrounding medium refractive index is 1.33. Using image processing algorithms, one can register the center of the diffraction spot and find the relative center and radius of the spot on the detector screen. For demonstration and measurement purposes, in Figure 7.9(b), a cut through the center of the diffraction spot is used. As it can be seen, the center of the spot changes by 684 μm, when the refractive index of the surrounding medium is increased by 0.01 as compared to the theoretical value of 1047 μm. According to the experiments, for the sample at 4 *cm* distance, the sensitivity can be calculated to be $S = 0.01/684 = 1.5 \times 10^{-5}$ $(RIU/\mu m)$.

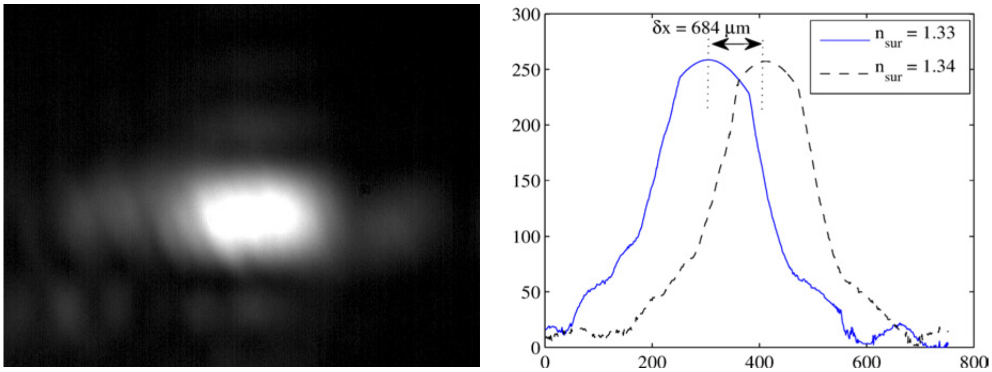

(a) (b)

Figure 7.9: Diffraction pattern registered on the detector in the measurement setup with nanowire array of pitch 750 *nm*. (a) the surrounding medium of 1.33 (b) the horizontal cut through the diffraction pattern with the cases of surrounding medium of 1.33 and 1.34.

The resultant sensitivity compares well with theory. The measurement error is due to the fact that the liquid sits as a droplet on top of the nanowire array resulting in a lensing effect which, depending on the hydrophobicity or hydrophilicity of the sample, can refract the diffraction spot further or less. Hence, this can result in smaller or larger divergence angles and change the final sensitivity from theory. Nevertheless, the achieved sensitivity compares well with spectroscopic measurements [134] in a setup which is much simpler and lower cost.

Similar sensors may also be built with conventional 1D transmission or reflective gratings. However, according to Bloch's theorem, the 2D periodic array causes 2D diffraction pattern which can act as a stand-alone and highly sensitive refractive index sensor without the need to use a spectrometer or complicated optical setups. In addition, the 2D nature of the grating, allows for polarization independent operation. With a single wavelength source, the sensing system acts similar to a spectrometer that has its grating immersed into the sensing medium. However, the 2D grating structures allows for various multivariate analyses such as ratio metric intensity measurements between the different orders as well as ratio metric and standalone divergence angle measurements registered on a 2D imaging array. In addition, by use of different wavelength sources and pulsating through them, one can achieve fast multispectral analysis of a sample medium by use of simple imaging techniques. Such multivariate analysis of a test medium can reveal valuable information such as liquid compositions, presence of biological agents in a host medium and etc.

7.4 Conclusion

We have proposed and demonstrated use of highly ordered two dimensional silicon nanowire arrays as simple and low cost but highly sensitive refractive index sensors. Diffraction spots are registered on a camera and sensing is achieved by measuring the change in position of the diffraction spot. Thus, the nanowires act both as the sensing media with a built-in wavelength specific analysis capability. Refractive index sensitivity of better than 1×10^{-5} is achieved using the proposed simple setup. We also measured the diffraction efficiency and achieved higher efficiency with increase in the refractive index of the surrounding medium. Ordered two dimensional nanowires would allow for realization of low-cost sensors without the need for external spectroscopic measurements.

Chapter 8

Conclusion

As mentioned in the beginning, the stated goal of this dissertation is to develop high performance and low cost spectral sensing solutions. Integrated photonics offer modular, robust and low cost solutions for many applications. In the first part of this thesis, an integrated photonic slicer concept is designed, fabricated and characterized (i.e. Chapters 3, 4 and 5). In the second part of this thesis, two refractive index based photonic sensor designs are proposed (i.e Chapters 6 and 7) based on the fabrication methods developed in the first section.

In Chapter 2, the general background information was provided along with the theoretical formulations used through the thesis. An extension of the coupled mode theory was done to a multi-mode case based on Hardy and Streifer work [21]. The extended formula are derived in Appendix A and the formulations are used as in Equation 2.13. This shows the directional coupling effect between dissimilar waveguides and how it can be used for mode conversion and reformatting in the following chapters.

Chapter 3 proposes designs of the photonic slit structure using a number of mode coupling methods. In order to benchmark the designs, a metric called the β factor (i.e. Equation 3.3) is derived and proposed to estimate the performance of the design compared with a free-space slit. First, a simple SU-8 based taper design is proposed and simulated. Then, two other designs are considered based on the non-resonant inverse taper couplers proposed in section 3.4. While the proposed designs were complex 3D structures, a simple optimization method is proposed which avoided complex and lengthy BPM simulations. In this optimization, discrete modal calculations are done and far-field radiation pattern is matched with fundamental mode of a slab-like equivalent (seen in Figure 3.23). This provides the channel waveguide width and gap parameters. Between the two proposed structures for the photonic slicer design, the wedged fiber system was chosen for implementation due to practical feasibility. In addition to the far-field mode shape optimization, based on the wedged fiber design, another 2D model of the system is also proposed and developed (Figure 3.29) to optimize the system throughput. While this model is in 2D, its result is validated by a 3D extension of the scattering parameters method (shown in Figure 3.36) which was originally proposed to optimize adiabatic taper designs in 2D [64]. Based on the optimization results, in the end it is concluded that which parameters would be critical to the systems throughput. In the next chapter, these would determine the choice of material and fabrication processes.

In Chapter 4, the fabrication methods developed for realization of the photonic slicer is proposed. While the SU-8 based tapered waveguide was fabricated through a collaborating team [67], the cleaving and testing was done in out lab at University of Waterloo. Due to difficulties in cleaving the SU-8 waveguides and thinfilm defects (see Figure 4.7 and Figure 4.8), the throughput was low and the simple taper waveguide did not show any advantage over a free-space slit. In order to fabricate the coupler system, the fabrication processes proposed and developed are summarized in Figure 4.10. Figure 4.12 clearly demonstrates the merits of writing using only the FBMS mode for the long tapered structures. Three FBMS writing methods are proposed which can be extended to fabrication of large area patterns in other applications. A novel way of writing large area patterns is provided in section 4.3.1 which can be extended to periodic structures as well. A SiN_x etch recipe is proposed and developed which is capable of etching high aspect ratio structures with highly vertical side walls (shown in Figure 4.21). Planarization step is done based on the inputs from the optimization steps discussed in Chapter 3 and the chip is cleaved at the end of the waveguide to be able to couple light out of the waveguide efficiently. Two coupling setups are proposed and used from which the active setup seems to achieve better alignment based on the coupled output signal intensity (as in Figure 4.32).

Chapter 5 provides the details on the characterization methods used as well as the experimental results for some of the fabricated chips. One of the major variables needed for calculation of the β factor is the output divergence angle. It is shown in Figure 5.2 how the output divergence angles can be estimated from far-filed radiation pattern and the waveguide mode becomes isolated from stray light. The divergence estimate with the throughput value based on either near field imaging or a power meter measurement, provides a first estimate of the device performance. While the near-field imaging is a better way of recording the throughput, the issues with stray light, the small size of the waveguides facet as well as the high NA output beam makes such measurements very hard. In order to make a fair comparison to a slit, a high resolution spectrometer is designed and built in the lab. The schematic and details are provided in Figure 5.9. Four main types of chips were fabricated and tested, the result of each are discussed in section 5.2. From these chips, Type C and D with a long and straight stabilizing waveguide at the end performed the best. Type C is a passively coupled with a hand polished wedge fiber and the β measurement technique is used to estimate its performance against a slit. Figure 5.17 shows the far-field projection for a range of calculated β values from which the experimental data shows a corresponding β value in the range of 1.25-1.5. In the Type D device, active coupling is used and the chip is incorporated in the high resolution spectrometer design for direct performance comparison to an equivalent 1 μm wide slit. Figure 5.20 plots the final spectrum recorded in both cases of a free space slit and a photonic slit showing a 33% increase in peak intensity of the main laser line.

The fabrication techniques developed in Chapter 4, especially the FBMS mode of writing long waveguide patterns (i.e. section 4.3.1), can easily be extended to other photonic sensors and structures. In Chapter 6, an optimization method is proposed for a bio-sensor based on a multiple-slot silicon waveguide. To increase light-matter interaction, the TE mode of the waveguides is considered and a series of optimization is done on the number of slots, waveguide and slot widths to increase the sensitivity of the proposed sensor to bulk and surface refractive index changes. Then the possibility of constructing ring resonators based on this design is considered. Equivalent 2D and channel waveguide models were used to simulate the propagation losses around the bends and also excitation of TE modes to the ring resonators. Based on the simulation results provided in Figure 6.14, the bulk sensitivity of the 16-slot ring resonator sensor is found to be 912 nm/RIU which is an improvement of at least 6 times over the sensitivity of a single SOI based ring resonator.

One of the goals of this dissertation is to achieve a low cost and highly sensitive spectral sensing solution for environmental sensing applications. While a portable spectrometer would be the ideal case, it is often not needed for most everyday applications. Specific refractive index based sensing can be done by using surface functionalized photonic sensors such as the multiple-slot based chip. However, detection of resonant wavelengths of the ring resonator often needs expensive spectrometers and tunable lasers. In Chapter 7, a new highly sensitive spectral sensing solution is proposed based on SiNWs where there is no need for external spectrometers. The 2D periodic nanowire arrays act as both sensing and diffractive elements shown in Figure 7.6. With multiple wavelength excitations, the ratio-metric change of the diffractive spot positions at each wavelength can be used to detect refractive index changes with high sensitivities. Figure 7.9 shows the experimental results for such a sensor where the sensitivity is in the order of 10^{-5} without using any external spectrometers.

8.1 List of Contributions

A list summerizing the unique contributions of this dissertation are as follows:

- Presents 3 designs for implementation of a photonic slicer (see section 3.3, Section 3.4.1 and Section 3.4.3)
- Presents a first approximation metric to measure the performance of a designed structure against a free space slit, both in simulations and experiments (i.e. Equation 3.3).
- Provides two methods of modeling besides the regular BPM simulations to optimize for the output far field pattern of choice as well as increasing the throughput of the system (see Section 3.4.2 and Section 3.4.4).
- Presents unique electron beam lithography methods to speed up long pattern direct writes. The manual column control method presented in section 4.3.1 is applicable to many large area patterning themes especially periodic structures and custom pattern shapes.
- Presents a unique etching process for SiN_x with high aspect ratio and vertical sidewalls (see Figure 4.21).
- Provides a number of characterization and measurement methods to quantify the performance of the proposed and fabricated devices. As presented in Figure 5.17 and Figure 5.20, the performance of the fabricated chips are estimated and also measured in a custom built spectrometer in two separate instances.
- Presents a new optimization procedure for a multiple slot silicon waveguide based biosensor. As a result of this design optimization, the bulk refractive index sensitivity is estimated to increase at least 6 time over a single SOI ring resonator.
- Proposes a novel refractive index sensor with high sensitivity without the need of an external spectrometer. This novel sensor uses the position change of the diffraction spots from a 2D periodic array of SiNWs. This design provides sensitivities that are conventionally achieved using a separate spectrometer.

8.2 Relevance to Other Fields

Historically spectrometers have been on the verge of miniaturization since their advent. While they where initially used in astronomy and chemistry, they have found many applications in various branches of science and technology. With their miniaturization and increasing performance, the vision is to have portable spectrometers within the “Internet of Things“ (IoT) remotely monitoring our surroundings for contaminants and anomalies. Currently, their use is envisioned for many applications such as food and water safety, allergens detection, air quality and safety, pathogens detection and many more.

While spectrometers are great comprehensive tools for many of these applications, in some cases, a multi-spectral approach would suffice where the target is very specific. In those applications, the types of sensors proposed in the last two chapters of this dissertation would be great lower cost alternatives to spectrometers. These specific refractive index based sensors can be surface functionalized with specific antibodies or chemical bonds to attach to specific biological agents or target molecules. Thus, a specific refractive index change would happen upon attachment with the target. This would render such spectrally selective photonic sensors as a low cost and highly sensitive solution for a number of everyday applications.

8.3 Future Work

As mentioned earlier, the subject of low cost spectral sensor is very attractive in many fields and applications. This work is not in any way conclusive of all such applications. It rather paves the way and shows what can be developed in many of these applications. The photonic slicer concept presented here is a proof of principle that tends to miniaturize and expand the use of spectrometers while maintaining its performance and resolution. There are many improvements that can be done to increase the coupling level, efficiency of the device and even extend this concept to a full integrated spectrometer design by incorporating dispersive elements on the same chip. The integrated dispersive element can be a released surface grating or an arrayed waveguide grating (AWG) which could be added at the end of the photonic slicer directly. One of the hurdles of the work presented in this thesis was to accurately measure and detect the waveguides output beam power and characteristics going from the chip to free space. Given the inherent imperfections in the fabrication steps followed by planarization, cleaving and also measurements, the output power detected is expected to be less than the actual power within the waveguides. Therefore, moving towards a fully integrated approach in the future would be very beneficial.

The highly sensitive biochemical sensor proposed in Chapter 6 based on a multiple-slot platform was not fabricated and verified experimentally. While care was taken to model the device as accurately as possible, it would need experimental verification in the future. In addition, the device itself can be surface functionalized with various antibodies after the fabrication step. Increasing its sensitivity by 6 times over conventional SOI ring resonators makes it a great candidate for very low concentration measurements.

One of the key components in designing photonic integrated chips is how to couple light in and out of these devices. Depending on the operation wavelength and the device design, this can be cumbersome or expensive at times. In addition, using external light sources and spectrometers to detect absorption, dispersion and/or wavelength shifts would add to the complexity of the system. In Chapter 7, the proposed simple system for RI sensing can be extended to other periodic structures as well. Looking at diffraction spots position changes with respect to various excitation wavelength can provide valuable information about the target medium being sensed. In addition to that, by using surface functionalization, specificity can be added to the sensor which would be an interesting to explore in the future.

References

[1] D. W. Ball. *Field Guide to Spectroscopy.* SPIE Press, Bellingham, WA, 2006.

[2] V. Saptari. *Fourier-Transform Spectroscopy Instrumentation Engineering.* SPIE Press, Bellingham, WA, 2003.

[3] J. M. Lerner and A. Thevenon. The optics of spectroscopy: A tutorial.

[4] R. F. Wolffenbuttel. State-of-the-art in integrated optical microspectrometers. *IEEE Transactions on Instrumentation and Measurement*, 53(1):197–202, February 2004.

[5] I. S. Bowen. The image-slicer a device for reducing loss of light at slit of stellar spectrograph. *ApJ*, 88:113, September 1938.

[6] W. G. Fastie. Illuminator for astronomical photoelectric spectroscopy. *JOSA*, 51:1472, 1961.

[7] Jr. F. H. Chaffee and D. W. Latham. An image stacker for high-resolution spectroscopy on the multiple mirror telescope. *PASP*, 94:386–389, April 1982.

[8] J. M. Beckers, T. E. Andersen, and M. Owner-Petersen. Very high-resolution spectroscopy for extremely large telescopes using pupil slicing and adaptive optics. *Opt. Express*, 15(5):1983–1994, Mar 2007.

[9] J. T. Meade, B. B. Behr, A. T. Cenko, P. Christensen, A. R. Hajian, J. Hendrikse, and F. D. Sweeney. Fundamental performance improvement to dispersive spectrograph based imaging technologies. *Proc. SPIE*, 7890:789013–789013–9, 2011.

[10] J. Bland-Hawthorn and A. Horton. Instruments without optics: an integrated photonic spectrograph. *SPIE*, 6269(21), 2006.

[11] D. Noordegraaf, P. M. Skovgaard, M. D. Nielsen, and J. Bland-Hawthorn. Efficient multi-mode to single-mode coupling in a photonic lantern. *Opt. Express*, 17(3):1988–1994, Feb 2009.

[12] J. Lawrence, J. Bland-Hawthorn, N. Cvetojevic, R. Haynes, and N. Jovanovic. Miniature astronomical spectrographs using arrayed-waveguide gratings: capabilities and limitations. *Proc. SPIE*, 7739:77394I–77394I–8, 2010.

[13] Ocean optics - jaz spectrometer.

[14] Rsoft - optical solutions.

[15] M. Born and E. Wolf. *Principles of Optics*. Cambridge University Press, seventh edition edition, 1999.

[16] J. E. Greivenkamp. *Field Guide to Geometrical Optics*, volume FG01. SPIE, 2004.

[17] J. M. Palmer and B. G. Grant. *The art of radiometry*. SPIE press, Bellingham, WA., 2010.

[18] B. E. A. Saleh and M. C. Teich. *Fundamentals of Photonics*. Wiley, 2nd edition, 2007.

[19] Katsunari Okamoto. Chapter 2 - planar optical waveguides. In K. Okamoto, editor, *Fundamentals of Optical Waveguides (Second Edition)*, pages 13 – 55. Academic Press, Burlington, second edition edition, 2006.

[20] H. F. Taylor and A. Yariv. Guided wave optics. *Proceedings of the IEEE*, 62(8):1044–1060, 1974.

[21] A. Hardy and W. Streifer. Coupled mode theory of parallel waveguides. *Journal of Lightwave Technology*, 3(5):1135–1146, 1985.

[22] Y. Shama, A. A. Hardy, and E. Marom. Multimode coupling of unidentical waveguides. *Lightwave Technology, Journal of*, 7(2):420–425, 1989.

[23] H. Kogelnik. 2. theory of dielectric waveguides. In *Integrated Optics*, volume 7 of *Topics in Applied Physics*, pages 13–81. Springer Berlin Heidelberg, 1975.

[24] H. A. Haus, W. P. Huang, S. Kawakami, and N. Whitaker. Coupled-mode theory of optical waveguides. *Journal of Lightwave Technology*, 5(1):16–23, 1987.

[25] W. P. Huang and H. A. Haus. Self-consistent vector coupled-mode theory for tapered optical waveguides. *Journal of Lightwave Technology*, 8(6):922–926, June 1990.

[26] J. W. Goodman. *Introduction to Fourier Optics*. Roberts & Company Publishers, third edition, 2004.

[27] J. T. Meade, B. B. Behr, and A. R. Hajian. A new high-resolution, high-throughput spectrometer: first experience as applied to raman spectroscopy. *Proc. SPIE*, 8374:83740V–83740V–8, 2012.

[28] A. T. Cenko, J. T. Meade, A. R. Hajian, and B. B. Behr. Optical slicer for improving the spectral resolution of a dispersive spectrograph, April 7 2011. WO Patent App. PCT/CA2010/001,606.

[29] D. S. Goldman, P. L. White, and N. C. Anheier. Miniaturized spectrometer employing planar waveguides and grating couplers for chemical analysis. *Appl. Opt.*, 29(31):4583–4589, Nov 1990.

[30] J. Mohr, B. Anderer, and W. Ehrfeld. Fabrication of a planar grating spectrograph by deep-etch lithography with synchrotron radiation. *Sensors and Actuators A: Physical*, 27(13):571 – 575, 1991.

[31] D. Sander and J. Muller. Selffocussing phase transmission grating for an integrated optical microspectrometer. *Sensors and Actuators A: Physical*, 88(1):1 – 9, 2001.

[32] T. A. Kwa and R. F. Wolffenbuttel. Proceedings of eurosensors v integrated grating/detector array fabricated in silicon using micromachining techniques. *Sensors and Actuators A: Physical*, 31(1):259 – 266, 1992.

[33] K. Chaganti, I. Salakhutdinov, I. Avrutsky, and G. W. Auner. A simple miniature optical spectrometer with a planar waveguide grating coupler in combination with a plano-convex lens. *Opt. Express*, 14(9):4064–4072, May 2006.

[34] S. Grabarnik, A. Emadi, E. Sokolova, G. Vdovin, and R. F. Wolffenbuttel. Optimal implementation of a microspectrometer based on a single flat diffraction grating. *Appl. Opt.*, 47(12):2082–2090, Apr 2008.

[35] S. Grabarnik, A. Emadi, H. Wu, G. de Graaf, and R. F. Wolffenbuttel. Microspectrometer with a concave grating fabricated in a {MEMS} technology. *Procedia Chemistry*, 1(1):401 – 404, 2009.

[36] P. Kumar, B. Bergner, D. Cook, and I. Avrutsky. Light focusing by chirped waveguide grating coupler. *Proc. SPIE*, 8032:803203–803203–8, 2011.

[37] C. H. Ko and M. R. Lee. Design and fabrication of a microspectrometer based on silicon concave micrograting. *Optical Engineering*, 50(8):084401–084401–10, 2011.

[38] O. Manzardo, H. P. Herzig, C. R. Marxer, and N. F. de Rooij. Miniaturized time-scanning fourier transform spectrometer based on silicon technology. *Opt. Lett.*, 24(23):1705–1707, Dec 1999.

[39] H. L. Kung, S. R. Bhalotra, J. D. Mansell, and D. A. B. Miller. Compact fourier transform spectrometer based on sampling a standing wave. In *Optical MEMS, 2000 IEEE/LEOS International Conference on*, pages 19–20. IEEE, 2000.

[40] H. Stiebig, H. J. Buchner, E. Bunte, V. Mandryka, D. Knipp, and G. Jager. Standing wave detection by thin transparent n-i-p diodes of amorphous silicon. *Thin Solid Films*, 427(1-2):152–156, 2003.

[41] H. Stiebig, D. Knipp, S. R. Bhalotra, H. L. Kung, and D. A. B. Miller. Interferometric sensors for spectral imaging. *Sensors and Actuators A: Physical*, 120(1):110 – 114, 2005.

[42] G. Lammel, S. Schweizer, and Ph. Renaud. Microspectrometer based on a tunable optical filter of porous silicon. *Sensors and Actuators A: Physical*, 92(13):52 – 59, 2001. Selected Papers for Eurosensors {XIV}.

[43] A. Rissanen, A. Akujarvi, J. Antila, M. Blomberg, and H. Saari. Moems miniature spectrometers using tuneable fabry-perot interferometers. *Journal of Micro/Nanolithography, MEMS, and MOEMS*, 11(2):023003–1, 2012.

[44] S. Kurth, K. Hiller, N. Neumann, M. Seifert, M. Ebermann, J. Zajadacz, and T. Gessner. Subwavelength structures for infrared filtering. *Proc. SPIE*, 7713:77131S–77131S–11, 2010.

[45] J. H.Correia, G. de Graaf, S. H. Kong, M. Bartek, and R. F. Wolffenbuttel. Single-chip cmos optical microspectrometer. *Sensors and Actuators A: Physical*, 82(1):191–197, 2000.

[46] Z. Xia, A. A. Eftekhar, M. Soltani, B. Momeni, Q. Li, M. Chamanzar, S. Yegnanarayanan, and A. Adibi. High resolution on-chip spectroscopy based on miniaturized microdonut resonators. *Opt. Express*, 19(13):12356–12364, Jun 2011.

[47] F. G. Watson. Multifiber waveguide spectrograph for astronomy. *Proc. SPIE*, 2476:68–74, 1995.

[48] F. G. Watson. Waveguide spectrographs for astronomy. *Proc. SPIE*, 2871:1373–1378, 1997.

[49] M. K. Smit. New focusing and dispersive planar component based on an optical phased array. *Electronics Letters*, 24:385–386(1), March 1988.

[50] M. K. Smit and C. V. Dam. Phasar-based wdm-devices: Principles, design and applications. *Selected Topics in Quantum Electronics, IEEE Journal of*, 2(2):236–250, 1996.

[51] H. Takahashi, S. Suzuki, K. Kato, and I. Nishi. Arrayed-waveguide grating for wavelength division multi/demultiplexer with nanometre resolution. *Electronics Letters*, 26(2):87–88, 1990.

[52] S. G. Leon-Saval, T. A. Birks, J. Bland-Hawthorn, and M. Englund. Multimode fiber devices with single-mode performance. *Opt. Lett.*, 30(19):2545–2547, Oct 2005.

[53] J. D. Love, W. H. Henry, W. J. Stewart, R. J. Black, S. Lacroix, and F. Gonthier. Tapered single-mode fibres and devices. i. adiabaticity criteria. *Optoelectronics, IEE Proceedings J*, 138(5):343–354, 1991.

[54] R. J. Black, S. Lacroix, F. Gonthier, and J. D. Love. Tapered single-mode fibres and devices. ii. experimental and theoretical quantification. *Optoelectronics, IEE Proceedings J*, 138(5):355–364, 1991.

[55] S. G. Leon-Saval, A. Argyros, and J. Bland-Hawthorn. Photonic lanterns: a study of light propagation in multimode to single-mode converters. *Opt. Express*, 18(8):8430–8439, Apr 2010.

[56] D. Noordegraaf, P. M. W. Skovgaard, M. D. Maack, J. Bland-Hawthorn, R. Haynes, and J. Lægsgaard. Multi-mode to single-mode conversion in a 61 port photonic lantern. *Opt. Express*, 18(5):4673–4678, Mar 2010.

[57] J. Bland-Hawthorn, S. C. Ellis, S. G. Leon-Saval, R. Haynes, M. M. Roth, H. G. Lohmannsroben, A. J. Horton, J. G. Cuby, T. A. Birks, J. S. Lawrence, P. Gillingham, S. D. Ryder, and C. Trinh. A complex multi-notch astronomical filter to suppress the bright infrared sky. *Nat Commun*, 2:581, December 2011.

[58] J. Bland-Hawthorn, J. Lawrence, G. Robertson, S. Campbell, B. Pope, C. Betters, S. Leon-Saval, T. Birks, R. Haynes, N. Cvetojevic, and N. Jovanovic. Pimms: photonic integrated multimode microspectrograph. *Proc. SPIE*, 7735:77350N–77350N–9, 2010.

[59] N. Cvetojevic, N. Jovanovic, J. Lawrence, M. Withford, and J. Bland-Hawthorn. Developing arrayed waveguide grating spectrographs for multi-object astronomical spectroscopy. *Opt.Express*, 20:2062–2072, 2012.

[60] R. R. Thomson, T. A. Birks, S. G. Leon-Saval, A. K. Kar, and J. Bland-Hawthorn. Ultrafast laser inscription of an integrated photonic lantern. *Opt. Express*, 19(6):5698–5705, Mar 2011.

[61] M. Ams, G. D. Marshall, and M. J. Withford. Study of the influence of femtosecond laser polarisation on direct writing of waveguides. *Opt. Express*, 14(26):13158–13163, Dec 2006.

[62] D. G. MacLachlan, R. J. Harris, D. Choudhury, R. D. Simmonds, P. S. Salter, M. J. Booth, J. R. Allington-Smith, and R. R. Thomson. Development of integrated mode reformatting components for diffraction-limited spectroscopy. *Opt. Lett.*, 41(1):76–79, Jan 2016.

[63] J. W. Goodman. *Statistical Optics.* John Wiley & Sons, second edition, 2015.

[64] F. Xia, V. M. Menon, and S. R. Forrest. Photonic integration using asymmetric twin-waveguide (atg) technology: part i-concepts and theory. *Selected Topics in Quantum Electronics, IEEE Journal of*, 11(1):17–29, 2005.

[65] D. Dai, Y. Tang, and J. E. Bowers. Mode conversion in tapered submicron silicon ridge optical waveguides. *Optics express*, 20(12):13425–13439, Jun 4 2012. id: 946; JID: 101137103; ppublish.

[66] S. Park, R. S. Ryong, and O. Beom-Hoan. Novel design concept of waveguide mode adapter for low-loss mode conversion. *IEEE Photonics Technology Letters*, 13(7):675–677, 2001. id: 1; issn: print 1041-1135; issn: electronic 1941-0174.

[67] A. Prabhakar and S. Mukherji. Microfabricated polymer chip with integrated u-bend waveguides for evanescent field absorption based detection. *Lab Chip*, 10:748–754, 2010.

[68] Y. Fu, T. Ye, W. Tang, and T. Chu. Efficient adiabatic silicon-on-insulator waveguide taper. *Photon. Res.*, 2(3):A41–A44, Jun 2014.

[69] R. E. Smith, M. E. Warren, J. R. Wendt, and G. A. Vawter. Polarization-sensitive subwavelength antireflection surfaces on a semiconductor for 975 nm. *Opt. Lett.*, 21(15):1201–1203, Aug 1996.

[70] V. Vusirikala, S. S. Saini, R. E. Bartolo, S. Agarwala, R. D. Whaley, F. G. Johnson, D. R. Stone, and M. Dagenais. 1.55-μm ingaasp-inp laser arrays with integrated-mode expanders fabricated using a single epitaxial growth. *Selected Topics in Quantum Electronics, IEEE Journal of*, 3(6):1332–1343, 1998.

[71] S. S. Saini, V. Vusirikala, R. Whaley, F. G. Johnson, D. Stone, and M. Dagenais. Compact mode expanded lasers using resonant coupling between a 1.55-μm ingaasp tapered active region and an underlying coupling waveguide. *Photonics Technology Letters, IEEE*, 10(9):1232–1234, 1998.

[72] K. Kawano, M. Kohtoku, M. Wada, H. Okamoto, Y. Itaya, and M. Naganuma. Design of a spotsize-converter-integrated laser diode (ss-ld) with a lateral taper, thin-film core and ridge in the 1.3-μm-wavelength region based on the 3-d bpm. *Selected Topics in Quantum Electronics, IEEE Journal of*, 2(2):348–354, 1996.

[73] M. Galarza, D. V. Thourhout, R. Baets, and M. Lopez-Amo. Compact and highly-efficient polarization independent vertical resonant couplers for active-passive monolithic integration. *Opt. Express*, 16(12):8350–8358, Jun 2008.

[74] Su-8/2000 datasheet 2025-2075, ver4. available at `http://microchem.com/pdf/SU-82000DataSheet2025thru2075Ver4.pdf`.

[75] Center for intelligent antenna and radio systems (ciars) - rapid prototyping lab (rpl), university of waterloo.

[76] Disco dicing saw - dad 3240.

[77] A. L. Bogdanov, J. Lapointe, and J. H. Schmid. Electron-beam lithography for photonic waveguide fabrication: Measurement of the effect of field stitching errors on optical performance and evaluation of a new compensation method. *Journal of Vacuum Science and Technology B*, 30(3), 2012.

[78] R. K. Dey and B. Cui. Stitching error reduction in electron beam lithography with in-situ feedback using self-developing resist. *Journal of Vacuum Science and Technology B*, 31(6), 2013.

[79] M. M. Greve and B. Holst. Optimization of an electron beam lithography instrument for fast, large area writing at 10 kv acceleration voltage. *Journal of Vacuum Science and Technology B*, 31(4), 2013.

[80] M. Gnan, D. S. Macintyre, M. Sorel, R. M. De La Rue, and S. Thoms. Enhanced stitching for the fabrication of photonic structures by electron beam lithography. *Journal of Vacuum Science & Technology B*, 25(6):2034–2037, 2007.

[81] L. Vivien and L. Pavesi. *Handbook of silicon photonics.* Taylor & Francis, 2013.

[82] R. Steingrueber, H. Engel, and W. Lessle. Essential reduction of stitching errors in electron-beam lithography using a multiple-exposure technique. In *26th Annual International Symposium on Microlithography*, pages 317–322. International Society for Optics and Photonics, 2001.

[83] M. Kahl. Zero stitching error using fixed beam moving stage (fbms) mode. Raith application note, Raith GmbH, 2005.

[84] M. Kirchner and M. Kahl. Raith-electron beam lithography for research. *Acta Physica Polonica A*, 116(s):s198–s200, 2009.

[85] G. Piaszenski, J. Sanabia, R. Schmits, P. Bodis, and F. Nouvertne. Continuous electron beam lithography writing modes for optical waveguide nanofabrication. Raith application note, Raith GmbH.

[86] H. Neubauer, S. Hoffmann, M. Kanbach, J. Haber, S. Kalbfleisch, S. P. Krüger, and T. Salditt. High aspect ratio x-ray waveguide channels fabricated by e-beam lithography and wafer bonding. *Journal of applied physics*, 115(21):214305, 2014.

[87] J. E. Sanabia, K. E. Burcham, J. Klingfus, G. Piaszenski, M. Kahl, and R. Jede. Fixed beam moving stage electron beam lithography of waveguide coupling device structures. In *Lasers and Electro-Optics (CLEO), 2012 Conference on*, pages 1–2, May 2012.

[88] J. Meszaros. Large area zone plate exposure by fixed beam moving stage lithography. 2011.

[89] Patterning parameter subdialogs. Raith NanoSuite Software Reference Manual V6.0, Raith GmbH.

[90] A. Hryciw. Raith-gds ii matlab toolbox user guide v1.2. University of Alberta NanoFab Facility, September 2014.

[91] T. Tut, Y. Dan, P. Duane, W. N. Ye, F. Degirmenci, Y. Yu, M. Wober, and K. B. Crozier. Silicon photodetectors integrated with vertical silicon nitride waveguides as image sensor pixels: Fabrication and characterization. *Journal of Vacuum Science & Technology B*, 32(3), 2014.

[92] Microposit mf-319 developer. available at `http://www.espchemicals.com/Downloads/MSDS/MF-319Developer_MSDS.pdf`.

[93] Cyclotene advanced electronics resins - refractive index vs. wavelength. available at `http://www.dow.com/cyclotene/solution/refwave.htm`.

[94] G. Beadie, M. Brindza, R. A. Flynn, A. Rosenberg, and J. S. Shirk. Refractive index measurements of poly(methyl methacrylate) (pmma) from $0.4 - 1.6\ \mu m$. *Appl. Opt.*, 54(31):F139–F143, Nov 2015.

[95] Fiber probes and lensed fibers, wt technology inc. `http://www.wttechnology.com/`.

[96] Zemax optics studio. `http://www.zemax.com/`.

[97] M. W. Sasnett and T. J. Johnston. Beam characterization and measurement of propagation attributes. volume 1414, pages 21–32, 1991.

[98] X. Fan, I. M. White, S. I. Shopova, H. Zhu, J. D. Suter, and Y. Sun. Sensitive optical biosensors for unlabeled targets: A review. *Analytica Chimica Acta*, 620(12):8 – 26, 2008.

[99] B. Marta, H. Martin, V. Janos, and G. H. Michelle. Optical microarray biosensing techniques. *Surface and Interface Analysis*, 38(11):1442–1458, 2006.

[100] S. Balslev, A. M. Jorgensen, B. Bilenberg, K. B. Mogensen, D. Snakenborg, O. Geschke, J. P. Kutter., and A. Kristensen. Lab-on-a-chip with integrated optical transducers. *Lab Chip*, 6:213–217, 2006.

[101] W. E. Moerner. New directions in single-molecule imaging and analysis. *Proceedings of the National Academy of Sciences*, 104(31):12596–12602, 2007.

[102] W. G. Cox and V. L. Singer. Fluorescent dna hybridization probe preparation using amine modification and reactive dye coupling. *BioTechniques*, 36(1):114–122, 2004.

[103] B. J. Luff, R. Wilson, D. J. Schiffrin, R. D. Harris, and J. S. Wilkinson. Integrated-optical directional coupler biosensor. *Opt. Lett.*, 21(8):618–620, Apr 1996.

[104] F. Prieto, B. Sepulveda, A. Calle, A. Llobera, C. Dominguez, A. Abad, A. Montoya, and L. M. Lechuga. An integrated optical interferometric nanodevice based on silicon technology for biosensor applications. *Nanotechnology*, 14(8):907, 2003.

[105] W. C. L. Hopman, P. Pottier, D. Yudistira, J. van Lith, P. V. Lambeck, R. M. De La Rue, A. Driessen, H. J. W. M. Hoekstra, and R. M. de Ridder. Quasi-one-dimensional photonic crystal as a compact building-block for refractometric optical sensors. *Selected Topics in Quantum Electronics, IEEE Journal of*, 11(1):11–16, Jan 2005.

[106] E. Shah Hosseini, S. Yegnanarayanan, A. H. Atabaki, M. Soltani, and A. Adibi. High quality planar silicon nitride microdisk resonators for integrated photonics in the visiblewavelength range. *Opt. Express*, 17(17):14543–14551, Aug 2009.

[107] A. M. Armani and K. J. Vahala. Heavy water detection using ultra-high-q microcavities. *Opt. Lett.*, 31(12):1896–1898, Jun 2006.

[108] L. Rindorf, J. B. Jensen, M. Dufva, L. H. Pedersen, P. E. Hoiby, and O. Bang. Photonic crystal fiber long-period gratings for biochemical sensing. *Opt. Express*, 14(18):8224–8231, Sep 2006.

[109] K. De Vos, I. Bartolozzi, E. Schacht, P. Bienstman, and R. Baets. Silicon-on-insulator microring resonator for sensitive and label-free biosensing. *Opt. Express*, 15(12):7610–7615, Jun 2007.

[110] T. Claes, J. G. Molera, K. De Vos, E. Schachtb, R. Baets, and P. Bienstman. Label-free biosensing with a slot-waveguide-based ring resonator in silicon on insulator. *Photonics Journal, IEEE*, 1(3):197–204, Sept 2009.

[111] M. Iqbal, M. A. Gleeson, B. Spaugh, F. Tybor, W. G. Gunn, M. Hochberg, T. Baehr-Jones, R. C. Bailey, and L. C. Gunn. Label-free biosensor arrays based on silicon ring resonators and high-speed optical scanning instrumentation. *Selected Topics in Quantum Electronics, IEEE Journal of*, 16(3):654–661, May 2010.

[112] M. Khorasaninejad, N. Clarke, M. P. Anantram, and S. S. Saini. Optical bio-chemical sensors on snow ring resonators. *Opt. Express*, 19(18):17575–17584, Aug 2011.

[113] F. Dell'Olio and V. M. N. Passaro. Optical sensing by optimized silicon slot waveguides. *Opt. Express*, 15(8):4977–4993, Apr 2007.

[114] L. Vivien, D. Marris-Morini, A. Griol, K. B. Gylfason, D. Hill, J. Alvarez, H. Sohlstrom, J. Hurtado, D. Bouville, and E. Cassan. Vertical multiple-slot waveguide ring resonators in silicon nitride. *Opt. Express*, 16(22):17237–17242, Oct 2008.

[115] H. Sun, A. Chen, and L. R. Dalton. Enhanced evanescent confinement in multiple-slot waveguides and its application in biochemical sensing. *Photonics Journal, IEEE*, 1(1):48–57, June 2009.

[116] P. A. Anderson, B. S. Schmidt, and M. Lipson. High confinement in silicon slot waveguides with sharp bends. *Opt. Express*, 14(20):9197–9202, Oct 2006.

[117] E. S. Larsen Jr, R. Meyrowitz, and A. J. C. Wilson. Measurement of refractive index. In *International Tables for Crystallography Volume C: Mathematical, physical and chemical tables*, pages 160–161. Springer, 2006.

[118] V. M. N. Passaro, M. La Notte, B. Troia, L. Passaquindici, F. De Leonardis, and G. Giannoccaro. Photonic structures based on slot waveguides for nanosensors: State of the art and future developments. *Int. J. Res. Rev. Appl. Sci*, 11(3):402–418, 2012.

[119] K. Schmitt, B. Schirmer, C. Hoffmann, A. Brandenburg, and P. Meyrueis. Interferometric biosensor based on planar optical waveguide sensor chips for label-free detection of surface bound bioreactions. *Biosensors and Bioelectronics*, 22(11):2591 – 2597, 2007.

[120] S. S. Saini, C. Stanford, S. M. Lee, J. Park, P. DeShong, W. E. Bentley, and M. Dagenais. Monolayer detection of biochemical agents using etched-core fiber bragg grating sensors. *Photonics Technology Letters, IEEE*, 19(18):1341–1343, Sept 2007.

[121] C. A. Barrios. Optical slot-waveguide based biochemical sensors. *Sensors*, 9(6):4751, 2009.

[122] E. Merritt. A spectrophotometric study of certain cases of structural color. *J. Opt. Soc. Am.*, 11(2):93–98, Aug 1925.

[123] S. V. Raj, L. Sang-Shin, K. Eun-Soo, and C. Duk-Yong. Non-iridescent transmissive structural color filter featuring highly efficient transmission and high excitation purity. *Scientific Reports*, 4:4921, may 2014.

[124] M. A. Steindorfer, V. Schmidt, M. Belegratis, B. Stadlober, and J. R. Krenn. Detailed simulation of structural color generation inspired by the morpho butterfly. *Opt. Express*, 20(19):21485–21494, Sep 2012.

[125] S. W. Kang and L. C. Chien. Field-induced and polymer-stabilized two-dimensional cholesteric liquid crystal gratings. *Applied Physics Letters*, 90(22), 2007.

[126] J. L. Zhu, J. G. Lu, J. Qiang, E. W. Zhong, Z. C. Ye, Z. He, X. Guo, C. Y. Dong, Y. Su, and H. P. D. Shieh. 1d/2d switchable grating based on field-induced polymer stabilized blue phase liquid crystal. *Journal of Applied Physics*, 111(3), 2012.

[127] H. Lochbihler. Colored images generated by metallic sub-wavelength gratings. *Opt. Express*, 17(14):12189–12196, Jul 2009.

[128] X. Ting, W. Yi-Kuei, L. Xiangang, and G. L. Jay. Plasmonic nanoresonators for high-resolution colour filtering and spectral imaging. *Nat Commun*, 1:59, aug 2010.

[129] M. A. Vincenti, M. Grande, D. de Ceglia, T. Stomeo, V. Petruzzelli, M. De Vittorio, M. Scalora, and A. DaeOrazio. Color control through plasmonic metal gratings. *Applied Physics Letters*, 100(20), 2012.

[130] B. Zhang, H. Wang, L. Lu, K. Ai, G. Zhang, and X. Cheng. Large area silver coated silicon nanowire arrays for molecular sensing using surface enhanced raman spectroscopy. *Adv. Func. Mat.*, 18(16):2348–2355, 2008.

[131] K. Seo, M. Wober, P. Steinvurzel, E. Schonbrun, Y. Dan, T. Ellenbogen, and K. B. Crozier. Multicolored vertical silicon nanowires. *Nano Letters*, 11(4):1851–1856, 2011. PMID: 21413684.

[132] Z. W. Pan, S. M. Mahurin, S. Dai, and D. H. Lowndes. Nanowire array gratings with zno combs. *Nano Letters*, 5(4):723–727, 2005. PMID: 15826116.

[133] S. Y. Lee, J. J. Amsden, S. V. Boriskina, A. Gopinath, A. Mitropolous, D. L. Kaplan, F. G. Omenetto, and L. D. Negro. Spatial and spectral detection of protein monolayers with deterministic aperiodic arrays of metal nanoparticles. *Proceedings of the National Academy of Sciences*, 107(27):12086–12090, 2010.

[134] M. Khorasaninejad, N. Abedzadeh, A. S. Jawanda, O. Nixon, M. P. Anantram, and S. S. Saini. Bunching characteristics of silicon nanowire arrays. *Journal of Applied Physics*, 111(4), 2012.

[135] J. Walia, N. Dhindsa, M. Khorasaninejad, and S. S. Saini. Nanowire arrays: Color generation and refractive index sensing using diffraction from 2d silicon nanowire arrays (small 1/2014). *Small*, 10(1):143–143, 2014.

[136] M. Khorasaninejad, N. Abedzadeh, J. Walia, S. Patchett, and S.S.Saini. Color matrix refractive index sensors using coupled vertical silicon nanowire arrays. *Nano Letters*, 12(8):4228–4234, 2012.

[137] N. Kumawat and M. M. Varma. Differential reflectance modulation sensing with diffractive microstructures. *Applied Physics Letters*, 101(19), 2012.

[138] M. C. Gupta and S. T. Peng. Diffraction of a light beam by doubly periodic structures. *Opt. Lett.*, 16(17):1301–1303, Sep 1991.

[139] RSoft. Diffractmod module.

[140] X. Ma, M. Li, and J. J. He. Cmos-compatible integrated spectrometer based on echelle diffraction grating and msm photodetector array. *Photonics Journal, IEEE*, 5(2):6600807–6600807, 2013.

[141] Tornado spectral systems inc.

APPENDICES

Appendix A

Expansion of Coupled Mode Theory to Parallel Multi-mode Waveguides Using H-S Theory

In this appendix we intend to find the coupled wave equations governing $U(z)$ and $V(z)$. In this derivation which is an extension to H-S theory for single mode waveguides [21], the overall field $\mathbf{E}_t$ is expanded in terms of the complete modal set of the individual waveguides. The individual waveguide field (i.e. $\mathbf{E}_t^{(p)}$, $p = a, b,$) can also be expanded in terms of the guided and radiation modes of the other guides. Lets consider having two parallel waveguides are shown in Figure A.1. Each of the waveguides a and b can support up to m

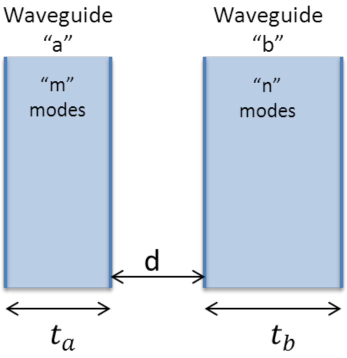

Figure A.1: Two parallel multi-mode waveguides a and b each supporting m and n number of modes respectively.

and n modes correspondingly. The total transverse field of the system can be expressed in terms of the complete sets of individual waveguide modes which can be decomposed to a set of guided and radiation modes. The guided modes whose transverse fields are $\{\mathbf{E}_t^{(a)}, \mathbf{H}_t^{(a)}\}$ and $\{\mathbf{E}_t^{(b)}, \mathbf{H}_t^{(b)}\}$ are individual waveguide modes and $\mathbf{E}_r$ and $\mathbf{H}_r$ are the residual fields. Since the system modes are not exactly linear combinations of the individual waveguide modes, the residual fields are needed in the equations. In addition, since these residual fields are neglected within most coupled mode formulations, the waveguides should not be strongly coupled. Considering these assumptions, the total transverse field of the system can be written as:

$$\begin{aligned}\mathbf{E}_t(x,y,z) &= \sum_{\nu=1}^{m} a_\nu(z)\mathbf{E}_{t\nu}^{(a)}(x,y) + \int_0^{+\infty} A_{(r)}\mathbf{E}_{tr}^{(a)}(k,x,y)dk \\ &= \begin{bmatrix} A_{(m)} & | & A_{(r)} \end{bmatrix} \begin{bmatrix} \mathbf{E}_{tm}^{(a)} \\ - \\ \mathbf{E}_{tr}^{(a)} \end{bmatrix} = A\mathbf{E}_t^{(a)}\end{aligned} \tag{A.1a}$$

$$\begin{aligned}\mathbf{E}_t(x,y,z) &= \sum_{\nu=1}^{m} b_\nu(z)\mathbf{E}_{t\nu}^{(b)}(x,y) + \int_0^{+\infty} B_{(r)}\mathbf{E}_{tr}^{(b)}(k,x,y)dk \\ &= \begin{bmatrix} B_{(m)} & | & B_{(r)} \end{bmatrix} \begin{bmatrix} \mathbf{E}_{tm}^{(b)} \\ - \\ \mathbf{E}_{tr}^{(b)} \end{bmatrix} = B\mathbf{E}_t^{(b)}\end{aligned} \tag{A.1b}$$

$$\begin{aligned}\mathbf{H}_t(x,y,z) &= \sum_{\nu=1}^{m} a_\nu(z)\mathbf{H}_{t\nu}^{(a)}(x,y) + \int_0^{+\infty} A_{(r)}\mathbf{H}_{tr}^{(a)}(k,x,y)dk \\ &= \begin{bmatrix} A_{(m)} & | & A_{(r)} \end{bmatrix} \begin{bmatrix} \mathbf{H}_{tm}^{(a)} \\ - \\ \mathbf{H}_{tr}^{(a)} \end{bmatrix} = A\mathbf{H}_t^{(a)}\end{aligned} \tag{A.1c}$$

$$\begin{aligned}\mathbf{H}_t(x,y,z) &= \sum_{\nu=1}^{m} b_\nu(z)\mathbf{H}_{t\nu}^{(b)}(x,y) + \int_0^{+\infty} B_{(r)}\mathbf{H}_{tr}^{(b)}(k,x,y)dk \\ &= \begin{bmatrix} B_{(m)} & | & B_{(r)} \end{bmatrix} \begin{bmatrix} \mathbf{H}_{tm}^{(b)} \\ - \\ \mathbf{H}_{tr}^{(b)} \end{bmatrix} = B\mathbf{H}_t^{(b)}\end{aligned} \tag{A.1d}$$

where the summations are over the guided modes while the integrations are over the radiation modes. The coefficients in the expansions for the $\mathbf{E}_t$ and $\mathbf{H}_t$ fields are identical if we consider only fields propagating in the $+z$ direction. This can be done considering the fact that neglecting backward propagating fields introduces very small errors while simplifying the derivation. The coefficients and fields can be considered as vectors catenated from the set of guided and radiation modes. On the other hand, the guided modes of each waveguide can be expanded as a complete set of waveguide modes of the other guide. By decomposing the guided modes from the radiation modes we can write,

$$\mathbf{E}_t^{(b)} = C\mathbf{E}_t^{(a)} = \begin{bmatrix} c_{11} & \cdots & c_{1m} \\ \vdots & \ddots & \vdots \\ c_{n1} & \cdots & c_{nm} \end{bmatrix} \begin{bmatrix} \mathbf{E}_{t1}^{(a)} \\ \vdots \\ \mathbf{E}_{tm}^{(a)} \end{bmatrix} + C_{(r)}\mathbf{E}_{tr}^{(a)} \tag{A.2a}$$

$$\mathbf{E}_t^{(a)} = D\mathbf{E}_t^{(b)} = \begin{bmatrix} d_{11} & \cdots & d_{1n} \\ \vdots & \ddots & \vdots \\ d_{m1} & \cdots & d_{mn} \end{bmatrix} \begin{bmatrix} \mathbf{E}_{t1}^{(b)} \\ \vdots \\ \mathbf{E}_{tn}^{(b)} \end{bmatrix} + D_{(r)}\mathbf{E}_{tr}^{(b)} \tag{A.2b}$$

where,

$$c_{ij} = 2\hat{z}.\iint_{-\infty}^{+\infty} [\mathbf{E}_{ti}^{(b)} \times \mathbf{H}_{tj}^{(a)}]dxdy \tag{A.3}$$

additionally, d_{ij} can be defined similarly when superscripts a and b are interchanged in Equation A.3. Identical expansions can be written for $\mathbf{H}_t^{(a)}$ and $\mathbf{H}_t^{(b)}$ as well. By re-writing Equation 2.11 in matrix format and substituting Equation A.1-Equation A.2, one can solve for $\mathbf{E}_r$ to find that,

$$\mathbf{E}_t = U\mathbf{E}_t^{(a)} + V\mathbf{E}_t^{(b)} + \mathbf{E}_r \tag{A.4}$$

$$\begin{aligned} \mathbf{E}_r &= \mathbf{E}_t - U\mathbf{E}_t^{(a)} - V\mathbf{E}_t^{(b)} = A\mathbf{E}_t^{(a)} - U\mathbf{E}_t^{(a)} - VC\mathbf{E}_t^{(a)} \\ \mathbf{E}_r &= (A_{(m)} - U_{(m)} - V_{(n)}C_{(m)})\mathbf{E}_{tm}^{(a)} + (A_{(r)} - V_{(r)}C_{(r)})\mathbf{E}_{tr}^{(a)} \\ &= (B_{(n)} - V_{(n)} - U_{(m)}D_{(n)})\mathbf{E}_{tn}^{(b)} + (B_{(r)} - U_{(r)}D_{(r)})\mathbf{E}_{tr}^{(b)} \end{aligned} \tag{A.5}$$

And the same equation applies for $\mathbf{H}$ replacing $\mathbf{E}$ in the above equations. Now by requiring that $\mathbf{E}_r$ and $\mathbf{H}_r$ be orthogonal to the guided modes for all z,

$$A_{(m)} = U_{(m)} - V_{(n)}C_{(m)} \tag{A.6}$$

$$B_{(n)} = V_{(n)} - U_{(m)}D_{(n)} \tag{A.7}$$

As shown for single mode waveguides with perturbations in [21], the coefficients A and B would also satisfy the following differential equations for a system of multiple modes,

$$\frac{d}{dz}A_{(m)} = iA_{(m)}\beta^{(a)}_{(m)} + i\left[A_{(m)} \quad | \quad A_{(r)}\right]\begin{bmatrix}\hat{\kappa}^{(a)}_{(m)} \\ - \\ \hat{\kappa}^{(a)}_{(r)}\end{bmatrix} \tag{A.8a}$$

$$\frac{d}{dz}B_{(n)} = iB_{(n)}\beta^{(b)}_{(n)} + i\left[B_{(n)} \quad | \quad B_{(r)}\right]\begin{bmatrix}\hat{\kappa}^{(b)}_{(n)} \\ - \\ \hat{\kappa}^{(b)}_{(r)}\end{bmatrix} \tag{A.8b}$$

where, $\beta^{(p)}_{(m)} = \begin{bmatrix}\beta_1 & \cdots & 0 \\ \vdots & \ddots & \vdots \\ 0 & \cdots & \beta_l\end{bmatrix}$ is a diagonal matrix of the propagation constants of waveguide p and $\hat{\kappa}^{(p)}$ is a matrix of the self-coupling coefficients with elements defined as,

$$\hat{\kappa}^{(p)}_{ij} = \omega\iint\limits_{-\infty}^{+\infty}\Delta\epsilon^{(p)}\mathbf{E}^{(p)}_{ti}\cdot\mathbf{E}^{(p)}_{tj}\,dxdy - \iint\limits_{-\infty}^{+\infty}\frac{\epsilon^{(p)}\Delta\epsilon^{(p)}}{\epsilon_0 n^2}\mathbf{E}^{(p)}_{zi}\cdot\mathbf{E}^{(p)}_{zj}\,dxdy \tag{A.9}$$

By substitution of Equation A.6 and Equation A.7 into Equation A.8,

$$\frac{dU_{(m)}}{dz} + \frac{dV_{(n)}}{dz}C_{(m)} = iU_{(m)}(\beta^{(a)}_{(m)} + \hat{\kappa}^{(a)}_{(m)}) + iV_{(n)}(C_{(m)}\beta^{(a)}_{(m)} + C_{(m)}\hat{\kappa}^{(a)}_{(m)}) + iA_{(r)}\hat{\kappa}^{(a)}_{(r)}$$

in order to accurately calculate the coupling factor, lets add and subtract the radiation modes $V_{(n)}C_{(m)}\hat{\kappa}^{(a)}_{(r)}$ from the above equation and after some manipulations,

$$\begin{aligned}\frac{dU_{(m)}}{dz} + \frac{dV_{(n)}}{dz}C_{(m)} = iU_{(m)}(\beta^{(a)}_{(m)} + \hat{\kappa}^{(a)}_{(m)}) + iV_{(n)}(C_{(m)}\beta^{(a)}_{(m)} + \tilde{\kappa}_{ab}) \\ + i(A_{(r)} - V_{(n)}C_{(r)})\hat{\kappa}^{(a)}_{(r)}\end{aligned} \tag{A.10}$$

where,

$$\tilde{\kappa}_{ab} = \left[C_{(m)} \quad | \quad C_{(r)}\right]\begin{bmatrix}\hat{\kappa}^{(a)}_{(m)} \\ - \\ \hat{\kappa}^{(a)}_{(r)}\end{bmatrix} = C\hat{\kappa}^{(a)} \tag{A.11}$$

Now, $\tilde{\kappa}_{ab}$ needs to be calculated. By substituting Equation A.9 into Equation A.11, the elements of the coupling matrix can be written as,

$$\begin{aligned}\tilde{\kappa}_{ab}^{(ij)} = \sum_l C_{il}\hat{\kappa}_{lj}^{(a)} = \omega \iint\limits_{-\infty}^{+\infty} \Delta\epsilon^{(a)} \left[\sum_l C_{il}\mathbf{E}_{tl}^{(a)}\right] \cdot \mathbf{E}_{tj}^{(a)} dxdy \\ - \iint\limits_{-\infty}^{+\infty} \frac{\Delta\epsilon^{(a)}}{\epsilon_0 n^2}\mathbf{E}_{zj}^{(a)} \cdot \left[\epsilon^{(a)} \sum_l C_{il}\mathbf{E}_{zl}^{(a)}\right] dxdy\end{aligned} \tag{A.12}$$

The first summation in Equation A.12 is given by Equation A.2a and the second summation is evaluated using Maxwells equation and the H-field expansion similar to Equation A.2a as shown here,

$$\epsilon^{(b)}\mathbf{E}_{zi}^{(b)} = (i/\omega)\nabla_t \times \sum_l C_{il}\mathbf{H}_{tl}^{(a)} = \epsilon^{(a)} \sum_l C_{il}\mathbf{E}_{zl}^{(a)}$$

Thus $\tilde{\kappa}_{ab}$ could simply be written as

$$\tilde{\kappa}_{ab} = \omega \iint\limits_{-\infty}^{+\infty} \Delta\epsilon^{(a)}\mathbf{E}_t^{(b)} \cdot \mathbf{E}_t^{(a)} dxdy - \iint\limits_{-\infty}^{+\infty} \frac{\Delta\epsilon^{(a)}\epsilon^{(b)}}{\epsilon_0 n^2}\mathbf{E}_z^{(b)} \cdot \mathbf{E}_z^{(a)} dxdy \tag{A.13}$$

where $\mathbf{E}_t^{(p)}$, $p = a, b$ is a matrix consisting of all modes for each of the waveguides. Also, $\tilde{\kappa}_{ba}$ can be written by the same expression as Equation A.13 with (a) and (b) interchanged. As shown, in deriving $\tilde{\kappa}_{ab}$ the contributions of radiation modes have been considered. It is only at this point that we neglect the higher order terms in Equation A.10. In a similar fashion, the differential equations concerning waveguide (b) can also be written. To summarize, after neglecting the higher order radiation modes, the two differential equations would become:

$$\frac{dU_{(m)}}{dz} + \frac{dV_{(n)}}{dz}C_{(m)} = iU_{(m)}\left(\beta_{(m)}^{(a)} + \hat{\kappa}_{(m)}^{(a)}\right) + iV_{(n)}\left(C_{(m)}\beta_{(m)}^{(a)} + \tilde{\kappa}_{ab}\right) \tag{A.14a}$$

$$\frac{dV_{(n)}}{dz} + \frac{dU_{(m)}}{dz}D_{(n)} = iV_{(n)}\left(\beta_{(n)}^{(b)} + \hat{\kappa}_{(n)}^{(b)}\right) + iU_{(m)}\left(D_{(n)}\beta_{(n)}^{(b)} + \tilde{\kappa}_{ba}\right) \tag{A.14b}$$

Solving the above equations simultaneously and after some mathematical manipulations, Equation 2.12 can be obtained with corrected propagations constants given in Equation 2.13 and coupling coefficients as in Equation 2.14.